U. S. Department of Commerce
National Oceanic and Atmospheric Administration
National Weather Service
National Centers for Environmental Prediction
5200 Auth Road Room 207
Camp Springs, MD 20746

Technical Note

Optimum Discrete Interaction Approximations for wind waves. Part 4: Parameter optimization.[†]

Hendrik L. Tolman [‡]

Environmental Modeling Center
Marine Modeling and Analysis Branch

December 2010

[†] MMAB Contribution No. 288.

[‡] e-mail: Hendrik.Tolman@NOAA.gov

This page is intentionally left blank.

Abstract

A generalized Multiple DIA (GMD) for accurate description of nonlinear interactions in wind waves has been developed in a previous phase of this study (Tolman, 2008b). The present study focuses on the objective optimization of the free parameters of the GMD, using genetic optimization techniques, augmented with more traditional error mapping and steepest descent search algorithms. In the so-called holistic optimization, full wave model results rather than interactions for selected spectra are considered, using model results obtained with the exact Webb-Resio-Tracy (WRT) algorithm as reference. The genetic optimization is shown to be able to optimize more than 20 parameters in the GMD simultaneously, which would be economically unfeasible with any previously suggested optimization technique. A cascade of GMD configurations is presented with increasing complexity and decreasing error compared to the full exact interaction computations. It is shown that a configuration with five quadruplets, each defined with three free parameters, removes most of the (deep water) model errors associated with the traditional DIA. A model based on this configuration will require approximately 4 times as much computational time as the default wave model using the DIA, but is roughly two orders of magnitude cheaper to run than a model using the WRT approach. It is shown that the traditional DIA may result in wave height errors as large as 25% for hurricanes, and 15% for enclosed areas like Lake Michigan, identifying errors in nonlinear interactions are a potentially significant contributor to overall wave model errors. The present study presents a first ever attempt to optimize a GMD-type nonlinear interaction approximation for (extremely) shallow water. It is shown that the GMD indeed can improve shallow water model behavior, but has some minor spurious behavior in extremely shallow water $kd < 0.1$. The latter will need to be addressed before the GMD can be applied to arbitrary water depths in operational wave models.

Acknowledgments. The author thanks Gerbrant Van Vledder for many discussions during the development of this work, and Arun Chawla and Andre van der Westhuysen for comments on early drafts of this manuscript. Special thanks are due to D.B. Rao and Steve Lord of EMC, for their support of this project for over a decade.

This report is available as a pdf file from

http://polar.ncep.noaa.gov/mmab/notes.shtml

Contents

1 Introduction

This study represents the fourth part of a study into the potential of the Discrete Interaction Approximation (DIA) to represent nonlinear interactions in a wind wave model. For a justification of this study reference is made to Tolman (2003, henceforth denoted as Part 1), Tolman (2005, henceforth denoted as Part 2), Tolman (2008b, henceforth denoted as Part 3), and to Tolman (2004) and Tolman and Krasnopolsky (2004). In Part 1 and Tolman (2004), existing DIA approaches are analyzed, and optimum parameters settings of various DIAs are assessed using inverse modeling techniques based on individual spectral and the corresponding exact interactions. In Part 2 and Tolman and Krasnopolsky (2004), a holistic optimization approaches using genetic optimization techniques is introduced to better optimize nonlinear interactions in the context of the full behavior of a numerical wave model. The latter studies indicate the potential of DIA variations to provide accurate and economical estimates of nonlinear interactions in a practical wave model. In Part 3, a rigorous derivation of DIA approaches for arbitrary water depth has been developed, and this approach is numerically optimized and implemented in the WAVEWATCH III® wave model.

The starting point of the present study is the Generalized Multiple DIA (GMD) as was developed in Part 3, and as described here in Section 2. No documentation of previous work will be provided here. For this, see previous reports in this study. The GMD is optimized here using a holistic optimization procedure, where results of model integration instead of interactions for individual spectra are optimized. The optimization procedure is described in Section 3. Results of various optimization experiments for the GMD are presented in Section 4. The most promising approaches are applied to some realistic applications in Section 5. Finally a brief discussion and conclusions are provided in Section 6.

This page is intentionally left blank.

2 The wave model

Traditionally, wind wave models have been based on some form of the spectral wave energy balance equation for deep water of Hasselmann (1960). In such models the evolution of the wave energy or variance spectrum $F(f,\theta)$ as a function of the spectral frequency f and direction θ can be expressed as

$$\frac{\partial F(f,\theta)}{\partial t} + \boldsymbol{c}_g \cdot \nabla F(f,\theta) = s_{in}(f,\theta) + s_{nl}(f,\theta) + s_{ds}(f,\theta) \quad , \tag{2.1}$$

where the right side of the equation represents the sources and sinks, consisting of wind input (s_{in}), nonlinear interactions (s_{nl}) and dissipation (s_{ds}) source terms. Furthermore, $\boldsymbol{c}_g$ is the group velocity with magnitude $c_g = \partial\sigma/\partial k$ and direction θ, and where $\sigma = 2\pi f$ and k ($\boldsymbol{k}$) is the wavenumber (vector). Note that formally, F is a slowly varying function of space and time $F(f,\theta;\boldsymbol{x},t)$. For brevity of notation, the dependency of F on $(\boldsymbol{x},t)$ is not expressed explicitly in the present equations. In shallow water, additional source terms arise, and in cases with mean ambient currents, wave action rather than wave energy is conserved (Bretherthon and Garrett, 1968). Modern models, therefore are based on a spectral action balance equation.

In the present study the WAVEWATCH III model is used for modeling wave conditions (Tolman, 1991b, 2009b). This model solves the action balance equation

$$\frac{\partial N}{\partial t} + \nabla_x \cdot \dot{\mathbf{x}} N + \frac{\partial}{\partial k}\dot{k} N + \frac{\partial}{\partial \theta}\dot{\theta} N = S \,, \tag{2.2}$$

$$\dot{\mathbf{x}} = \mathbf{c}_g + \mathbf{U} \,, \tag{2.3}$$

$$\dot{k} = -\frac{\partial \sigma}{\partial d}\frac{\partial d}{\partial s} - \boldsymbol{k} \cdot \frac{\partial \mathbf{U}}{\partial s} \,, \tag{2.4}$$

$$\dot{\theta} = -\frac{1}{k}\left[\frac{\partial \sigma}{\partial d}\frac{\partial d}{\partial m} - \boldsymbol{k} \cdot \frac{\partial \mathbf{U}}{\partial m}\right] \,, \tag{2.5}$$

where N is the action spectrum as a function of the wavenumber k and direction θ, which is related to the corresponding energy spectrum as

$$N(k,\theta) = \frac{F(k,\theta)}{\sigma} \quad , \tag{2.6}$$

and where σ is the intrinsic frequency ($\sigma = 2\pi f_r$). Furthermore, $\dot{\mathbf{x}}$, $\dot{k}$ and $\dot{\theta}$ are the characteristic velocities in physical and spectral space, d is the mean water depth, $\mathbf{U}$ is the mean current (not used in this study), s is a coordinate in the direction θ and m is a coordinate perpendicular to θ. The parameters describing spectral space are related in a dispersion and a Doppler relation

$$\sigma^2 = gk \tanh kd \,, \tag{2.7}$$

$$\omega = \sigma + \boldsymbol{k} \cdot \mathbf{U} \, . \tag{2.8}$$

The spectra described as a function of frequency or wavenumber are related through a Jacobian transformation

$$F(f_r, \theta) = \frac{\partial k}{\partial f_r} F(k, \theta) = \frac{2\pi}{c_g} F(k, \theta) \, . \tag{2.9}$$

Several options are available for the source terms S on the right side of Eq. (2.2). As used in this study

$$S = S_{in} + S_{nl} + S_{ds} + S_{bt} + S_{db} \quad , \tag{2.10}$$

where $S_{in} = s_{in}/\sigma$, etc. Note that transition to other spectral domains will require a Jacobian transformation as in Eq. (2.9). Input and dissipation (whitecapping) are modeled using Tolman and Chalikov (1996), bottom friction (S_{bt}) is modeled using Hasselmann et al. (1973), and depth limited breaking is modeled using Battjes and Janssen (1978). See Tolman (2009b) for details and default model settings as used here. Various versions of the nonlinear interactions are used as described below.

The nonlinear interactions considered here describe the resonant exchange of energy, momentum and action between a "quadruplet" of four spectral components with wavenumber vectors $\boldsymbol{k}_1$ through $\boldsymbol{k}_4$ and (radian) frequencies σ_1 through σ_4, satisfying the following resonance conditions (Hasselmann, 1962, 1963) :

$$\boldsymbol{k}_1 + \boldsymbol{k}_2 = \boldsymbol{k}_3 + \boldsymbol{k}_4 \quad , \tag{2.11}$$

$$\sigma_1 + \sigma_2 = \sigma_3 + \sigma_4 \quad . \tag{2.12}$$

The interactions are conventionally expressed in terms of the rate of change of the action spectrum $n(\boldsymbol{k}) \equiv F(\boldsymbol{k})/\sigma$ as

$$\begin{aligned} \frac{\partial n_1}{\partial t} &= \iiint G\left(\boldsymbol{k}_1, \boldsymbol{k}_2, \boldsymbol{k}_3, \boldsymbol{k}_4\right) \, \delta_k \, \delta_\sigma \\ &\times \quad \left[n_1 n_2 \left(n_3 + n_4\right) - n_3 n_4 \left(n_1 + n_2\right)\right] \, d\boldsymbol{k}_2 \, d\boldsymbol{k}_3 \, d\boldsymbol{k}_4 \quad , \end{aligned} \tag{2.13}$$

where n_i is the action density at component i, $n_i = n(\boldsymbol{k}_i)$, G is a complex coupling coefficient (Webb, 1978; Herterich and Hasselmann, 1980), and δ_k and δ_σ are delta functions corresponding to the resonance conditions (2.11) and (2.12). This 'exact' approach represents the baseline for optimizing the GMD. In this study the Webb-Resio-Tracy (WRT) (Webb, 1978; Tracy and Resio, 1982; Resio and Perrie, 1991) method is used for computing the exact interactions. Calculations are performed with the portable package developed by Van Vledder (2002, 2006)[1].

[1] Model version 5.04 used here.

Whereas the benchmark is provided by the WRT method, errors of the GMD are relevant with respect to previous approximations to the exact computations. The previous standard is the Discrete Interaction Approximation (DIA) of Hasselmann et al. (1985). This approach simplifies the computations of the interactions in two main ways. First, only a single resonant quadruplet configuration is considered, satisfying Eqs. (2.11), (2.12) and

$$\left.\begin{array}{rcl} \boldsymbol{k}_1 & = & \boldsymbol{k}_2 \\ \sigma_3 & = & (1+\lambda)\sigma \\ \sigma_4 & = & (1-\lambda)\sigma \end{array}\right\} \quad , \tag{2.14}$$

where λ is a constant, typically set to $\lambda = 0.25$. Second, a discrete equivalent to Eq. (2.13) for the spectrum $F(f,\theta)$ is developed, where discrete contributions to the source term $\delta s_{nl,i}$ for the four quadruplet components are computed as

$$\begin{aligned} \begin{pmatrix} \delta s_{nl,1} \\ \delta s_{nl,3} \\ \delta s_{nl,4} \end{pmatrix} &= D \begin{pmatrix} -2 \\ 1 \\ 1 \end{pmatrix} C g^{-4} f_{r,1}^{11} \times \\ &\left[F_1^2 \left(\frac{F_3}{(1+\lambda)^4} + \frac{F_4}{(1-\lambda)^4} \right) - \frac{2F_1F_3F_4}{(1-\lambda^2)^4} \right] , \end{aligned} \tag{2.15}$$

where $F_i = F(f_{r,i},\theta_i)$, and $\delta s_{nl,1} = \delta s_{nl}(f_{r,i},\theta_i)$, and C is a proportionality constant. In WAVEWATCH III, the default setting is $C = 1.00\ 10^7$. Finally, D is a scaling function to account for effects of limited water depths (Hasselmann and Hasselmann, 1985)

$$D = 1 + \frac{5.5}{\bar{k}d} \left[1 - \frac{5}{6}\bar{k}d \right] e^{-1.25\bar{k}d} . \tag{2.16}$$

where $\bar{k}d$ is the mean relative water depth. Note that Eq. (2.15) implies a logarithmic frequency grid

$$\sigma_{i+1} = X_\sigma\, \sigma_i \quad , \tag{2.17}$$

where X_σ is the discrete frequency increment factor and i is the discrete frequency grid counter.

To compute the nonlinear interactions according to the DIA, discrete contributions $\delta s_{nl,i}$ are computed for a quadruplet with $\boldsymbol{k}_1$ coinciding with each discrete spectral grid point in turn (extending the grid to higher frequencies), after which all discrete contributions are combined to get the total nonlinear interactions. Note that the evaluation of F_i in Eq. (2.15) requires interpolation in spectral space, and that $\delta s_{nl,i}$ needs to be distributed over adjacent discrete spectra grid points. Note, finally, that deep water is assumed in all computations for the DIA, except for the evaluation of D.

*Table 2.1: One two or three parameter definitions of the representative quadruplet from Part 2. $\boldsymbol{k}_d$ represents the discrete spectral grid point for which the discrete interaction contributions are evaluated. *) $\Delta\theta$ implicit in definition of quadruplet.*

	$\boldsymbol{k}_d$	σ	$\Delta\theta$	a_1	a_2	a_3	a_4
(λ)	$\boldsymbol{k}_1$	σ_1	0	1	1	$1+\lambda$	$1-\lambda$
(λ,μ)	$\frac{1}{2}(\boldsymbol{k}_1+\boldsymbol{k}_2)$	$\frac{1}{2}(\sigma_1+\sigma_2)$	*)	$1+\mu$	$1-\mu$	$1+\lambda$	$1-\lambda$
$(\lambda,\mu,\Delta\theta)$	Eq. (2.19)	σ_1	$\Delta\theta$	$1+\mu$	$1-\mu$	$1+\lambda$	$1-\lambda$

The present study aims to optimize the parameter settings of the Generalized Multiple DIA (GMD) as developed in Part 3. This approach expands upon the traditional DIA in several ways. First, it is expressed directly in terms of the action spectrum $N(k,\theta)$ as used in WAVEWATCH III. Note that this has some impact on interpolations in spectral space in the computation of discrete interactions, which in turn has a notable impact on the resulting interactions (see Part 3 and below). Second, the definition of the representative quadruplet is expanded, to become a one, two or three parameter definition, where

$$\left.\begin{array}{rcl} \sigma_1 &=& a_1\sigma \\ \sigma_2 &=& a_2\sigma \\ \sigma_3 &=& a_3\sigma \\ \sigma_4 &=& a_4\sigma \\ \theta_2 &=& \theta_1 \pm \Delta\theta \end{array}\right\} \quad , \tag{2.18}$$

The definitions of a_i depend on the relation of the quadruple components to the discrete wavenumbers $\boldsymbol{k}_d$ of spectral grid point for which the discrete interactions are evaluated, and are given in Table 2.1. For the three-parameter definition of the quadruplet,

$$\boldsymbol{k}_d = \frac{||\boldsymbol{k}_1||}{||\boldsymbol{k}_1+\boldsymbol{k}_2||}\,(\boldsymbol{k}_1+\boldsymbol{k}_2) \quad . \tag{2.19}$$

Note that, unlike in the traditional DIA, the quadruplet layout is evaluated for the actual depth for each discrete spectral grid point.

Third, multiple representative quadruplets are used. Interactions for individual quadruplets are added, and normalized with the number of representative quadruplet definitions. Fourth, the discrete interactions are reformulated to be expressed in terms of discrete contributions $\delta S_{nl}(k,\theta)$ corresponding to the basic spectrum $N(k,\theta)$ as used in Eq. (2.2), and is properly scaled for arbitrary water depths. This results in the following discrete contributions to S_{nl}

$$\begin{pmatrix} \delta S_{nl,1} \\ \delta S_{nl,2} \\ \delta S_{nl,3} \\ \delta S_{nl,4} \end{pmatrix} = \begin{pmatrix} -1 \\ -1 \\ 1 \\ 1 \end{pmatrix} \left(\frac{1}{n_{q,d}} C_d B_d + \frac{1}{n_{q,s}} C_s B_s \right) \times \left[\frac{N_1}{k_1} \frac{N_2}{k_2} \left(\frac{N_3}{k_3} + \frac{N_4}{k_4} \right) - \frac{N_3}{k_3} \frac{N_4}{k_4} \left(\frac{N_1}{k_1} + \frac{N_2}{k_2} \right) \right], \quad (2.20)$$

where $n_{q,d}$ and $n_{q,s}$ represent the number of deep and shallow water quadruplet definition used (representing the above rescaling for multiple representative quadruplets), and where B_d and B_s represent the asymptotic deep and shallow water scaling functions

$$B_d = \frac{k^{4+m}\, \sigma^{12-2m}}{(2\pi)^9\, g^{4-m}\, c_g} \quad , \quad (2.21)$$

$$B_s = \frac{g^2\, k^{10}}{(2\pi)^9\, c_g} (kd)^n \quad , \quad (2.22)$$

where m and n are free parameters to be optimized. Finally, C_d and C_s are proportionality constants for the two scaling functions, corresponding to the proportionality constant C in the DIA [Eq. (2.15)]. Note that Eq. (2.21) differs from Eq. (2.107) in Part 3 by a factor of $(2\pi)^3$, to ensure that equations reduce to the original DIA equations for deep water.

In the numerical integration of the source terms in WAVEWATCH III, the diagonal terms of the partial derivatives of the source term with respect to the spectrum $\partial S_{nl,i}(k,\theta)/\partial N_i(k,\theta) \equiv D_i(k,\theta)$ are needed. The discrete increment of the spectrum $\Delta N_i(k,\theta)$ is calculated as

$$\Delta N_i(k,\theta) = \frac{S_i(k,\theta)\Delta t}{1 - \alpha D_i(k,\theta)\Delta t} \quad , \quad (2.23)$$

where $\alpha = 1$ determines the centricity of the scheme. The diagonal term D follows from Eq. (2.20) as

$$\begin{pmatrix} \delta D_1 \\ \delta D_2 \\ \delta D_3 \\ \delta D_4 \end{pmatrix} = \begin{pmatrix} -K_1' \\ -K_2' \\ K_3' \\ K_4' \end{pmatrix} \left(\frac{1}{n_{q,d}} C_d B_d + \frac{1}{n_{q,s}} C_s B_s \right) \quad , \quad (2.24)$$

where

$$K_1' = k_1^{-1} \left[\frac{N_2}{k_2} \left(\frac{N_3}{k_3} + \frac{N_4}{k_4} \right) - \frac{N_3 N_4}{k_3 k_4} \right] \quad , \quad (2.25)$$

$$K_2' = k_2^{-1}\left[\frac{N_1}{k_1}\left(\frac{N_3}{k_3}+\frac{N_4}{k_4}\right)-\frac{N_3N_4}{k_3k_4}\right] \quad , \tag{2.26}$$

$$K_3' = k_3^{-1}\left[\frac{N_1N_2}{k_1k_2}-\frac{N_4}{k_4}\left(\frac{N_1}{k_1}+\frac{N_2}{k_2}\right)\right] \quad , \tag{2.27}$$

$$K_4' = k_4^{-1}\left[\frac{N_1N_2}{k_1k_2}-\frac{N_3}{k_3}\left(\frac{N_1}{k_1}+\frac{N_2}{k_2}\right)\right] \quad , \tag{2.28}$$

In Fig. 5.1 of Part 3 it is shown that the choice of the spectral description can have a significant impact on the resulting nonlinear interactions. In particular, expressing the interaction in terms of $N(k,\theta)$ instead of $F(f,\theta)$ results in clear differences in resulting interactions, and in clearly different model integration (see Part 3, Figs. 5.9 and 5.10). Originally, the GMD is expressed in terms of the internal spectrum $N(k,\theta)$ of WAVEWATCH III. Here, we will also consider the more conventional description in terms of the energy spectrum $F(f,\theta)$ from the original DIA, to address possible impact on the potential of the optimization. The energy spectrum $F(f,\theta)$ follows from the action spectrum $N(k,\theta)$ as

$$F(f,\theta) = \frac{2\pi\sigma}{c_g}\,N(k,\theta) \quad , \tag{2.29}$$

where $c_g = \partial\sigma/\partial k$ is the group velocity of the spectral component following from the dispersion relation (2.7). For this spectrum, the contributions $\delta s_{nl}(f_i,\theta_i) = \delta s_{nl,i}$ to the nonlinear interactions $s_{nl}(f,\theta)$ for $F(,f,\theta)$ become

$$\begin{aligned}
\begin{pmatrix} \delta s_{nl,1} \\ \delta s_{nl,2} \\ \delta s_{nl,3} \\ \delta s_{nl,4} \end{pmatrix} \;=\; & \begin{pmatrix} -1 \\ -1 \\ 1 \\ 1 \end{pmatrix}\left(\frac{1}{n_{q,d}}C_dB_d+\frac{1}{n_{q,s}}C_sB_s\right) \\
\times\; & \left[\;\frac{c_{g,1}F_1}{k_1\sigma_1}\frac{c_{g,2}F_2}{k_2\sigma_2}\left(\frac{c_{g,3}F_3}{k_3\sigma_3}+\frac{c_{g,4}F_4}{k_4\sigma_4}\right)\right. \\
& \left.-\;\frac{c_{g,3}F_3}{k_3\sigma_3}\frac{c_{g,4}F_4}{k_4\sigma_4}\left(\frac{c_{g,1}F_1}{k_1\sigma_1}+\frac{c_{g,2}F_2}{k_2\sigma_2}\right)\;\right] \quad ,
\end{aligned} \tag{2.30}$$

where

$$B_d = \frac{k^{4+m}\sigma^{13-2m}}{(2\pi)^{11}\,g^{4-m}\,c_g^2} \quad , \tag{2.31}$$

$$B_s = \frac{g^2\,k^{11}}{(2\pi)^{11}\,c_g}(kd)^n \quad , \tag{2.32}$$

Note that in the traditional DIA, F_i in Eq, (2.30) are obtained by bi-linear interpolation in the discrete spectral space, whereas the terms $[c_g(k\sigma)^{-1}]_i$ are computed for the actual components of the quadruplet. In Eq. (2.20), the latter terms are effectively obtained by linear interpolation from the discrete spectral space. Therefore, in order to retain the original DIA results, interpolation should be performed on F rather than $Fc_g(k\sigma)^{-1}$, and $c_g(k\sigma)^{-1}$ should be evaluated at the quadruplet components rather than at the discrete spectral grid points. The diagonal terms for this source term description are computed according to Eq. (2.24) with

$$K'_1 = \frac{c_{g,1}}{k_1\sigma_1}\left[\frac{c_{g,2}F_2}{k_2\sigma_2}\left(\frac{c_{g,3}F_3}{k_3\sigma_3}+\frac{c_{g,4}F_4}{k_4\sigma_4}\right)-\frac{c_{g,3}F_3}{k_3\sigma_3}\frac{c_{g,4}F_4}{k_4\sigma_4}\right] \quad , \tag{2.33}$$

$$K'_2 = \frac{c_{g,2}}{k_2\sigma_2}\left[\frac{c_{g,1}F_1}{k_1\sigma_1}\left(\frac{c_{g,3}F_3}{k_3\sigma_3}+\frac{c_{g,4}F_4}{k_4\sigma_4}\right)-\frac{c_{g,3}F_3}{k_3\sigma_3}\frac{c_{g,4}F_4}{k_4\sigma_4}\right] \quad , \tag{2.34}$$

$$K'_3 = \frac{c_{g,3}}{k_3\sigma_3}\left[\frac{c_{g,1}F_1}{k_1\sigma_1}\frac{c_{g,2}F_2}{k_2\sigma_2}-\frac{c_{g,4}F_4}{k_4\sigma_4}\left(\frac{c_{g,1}F_1}{k_1\sigma_1}+\frac{c_{g,2}F_2}{k_2\sigma_2}\right)\right] \quad , \tag{2.35}$$

$$K'_4 = \frac{c_{g,4}}{k_4\sigma_4}\left[\frac{c_{g,1}F_1}{k_1\sigma_1}\frac{c_{g,2}F_2}{k_2\sigma_2}-\frac{c_{g,3}F_3}{k_3\sigma_3}\left(\frac{c_{g,1}F_1}{k_1\sigma_1}+\frac{c_{g,2}F_2}{k_2\sigma_2}\right)\right] \quad , \tag{2.36}$$

Note that the diagonal terms are identical for both spectral descriptions, since the Jacobian transformations for the spectrum and source terms are identical and hence cancel in the derivatives.

The impact of the choice of the spectral description and interpolation is illustrated in Fig. 2.1. Figures 2.1a and b are taken directly from Part 3, and show the differences in the interactions between the traditional DIA and the GMD where $N(k,\theta)/k$ is interpolated in the discrete spectral space. Figure 2.1c shows results where $N(k,\theta)$ is interpolated and the corresponding factor $1/k$ is evaluated at the actual quadruplet. The differences between the latter two panels are minimal. Finally, panel (d) shows the GMD using Eq. (2.30) with $F(f,\theta)$ interpolated in spectral space and $c_g(k\sigma)^{-1}$ evaluated at the quadruplet. The interactions according to this GMD are virtually identical to those of the traditional DIA (panel a), clearly illustrating the large impact of the choice of spectral interpolation versus evaluation of quadruplets on the resulting nonlinear interactions. Note that the change back to a description of the interactions in terms of the spectrum $F(f,\theta)$ has virtually no impact on the numerical optimization considerations in Section 5.1 of Part 3. Note, furthermore, that the GMD based on Eqs. (2.30) through (2.36) results in model integrations with virtually identical results when compared to the DIA. By contrast, figures (5.9) and (5.10) in Part 3 show that the DIA and the original GMD resulted in very different wave conditions ($H_s = 2.92$m and 2.43m, respectively). With the alternative formulation of the GMD of Eqs. (2.30) through (2.36), model integration for deep water is now virtually identical to that of the DIA ($H_s = 2.91$m).

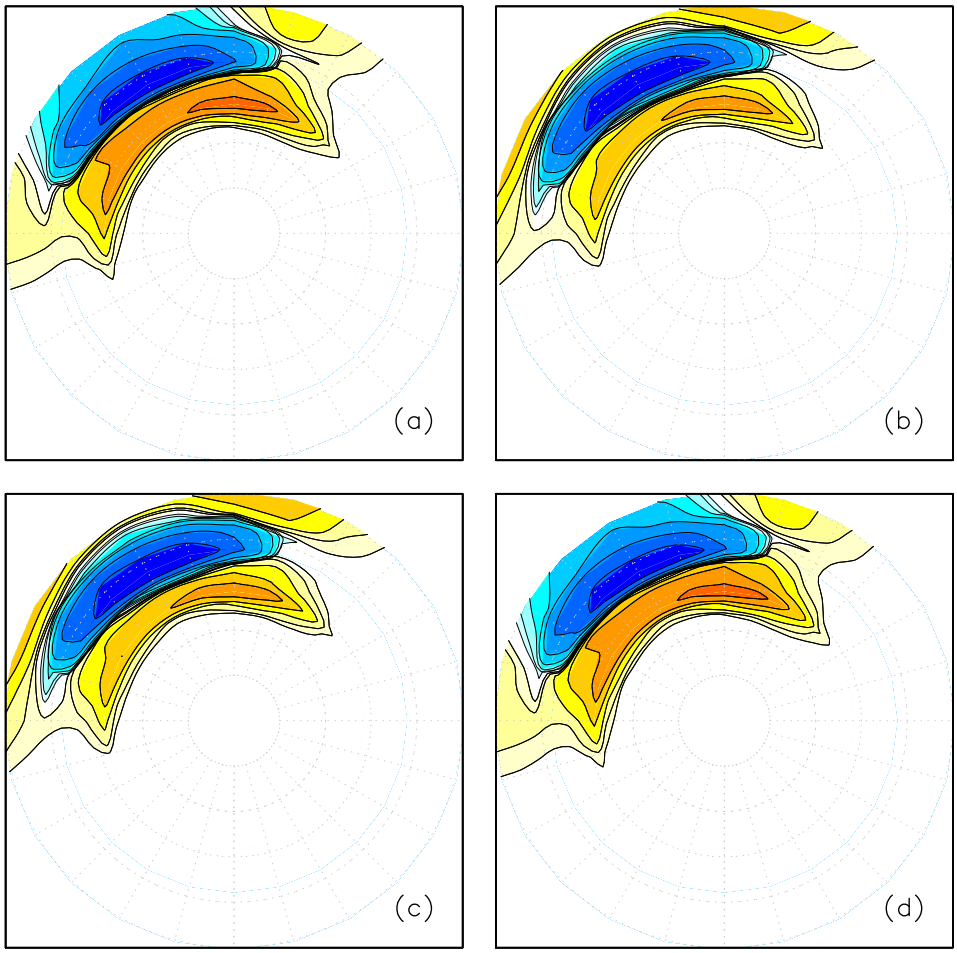

Fig. 2.1 : Like Fig. 5.1 from Part 3. (a) Traditional DIA, (b-d) GMD with parameter settings from traditional DIA. (b) $N(k,\theta)/k$ in product term interpolated in spectral space. (c) Idem $N(k,\theta)$. (d) Idem $F(f,\theta)$. (a,b) from Part 3

Initial comparisons of the two GMD approaches with respect to potential of model optimization are presented in Tolman (2009a), where it is shown that the GMD based on the $F(f)$ spectral description is far superior to the GMD based on $N(k)$. The latter approach results in model errors that are typically twice as large as those of the former approach. Furthermore, the latter GMD is hard pressed even to outperform the traditional DIA. Considering this, only the GMD based on the $F(f)$ spectrum [Eqs. (2.30) - (2.36)] will be used in the remainder of this report.

Part 3 also introduced a filter function for high frequencies in the spectrum based on the nonlinear interactions, and similar to a diffusion term. This term is based on the traditional quadruplet layout of the DIA, with λ chosen small enough not to be resolved by the discrete spectral grid. With the spectral grid given by Eq. (2.17), and defining a_{34} as the offset in the discrete grid of quadruplet components 3 and 4 in the frequency space, normalized with the frequency increment, a_{34}, λ and the frequency increment factor X_σ are related as

$$a_{34} = \frac{\lambda}{X_\sigma - 1} \quad , \tag{2.37}$$

and the quadruplet is not resolved by the discrete spectral grid if $a_{34} < 1$. In the present implementation of this filter in WAVEWATCH III, the default setting is $a_{34} = 0.05$, with a requirement that $a_{34} \leq 0.25$. For the corresponding value of λ and using the one-parameter definition of the quadruplet layout, a normalized discrete change of action density for the two possible realizations of the quadruplet at the central point of the quadruplet $\Delta\tilde{N}_{1,2}$ is computed as

$$\Delta\tilde{N}_{1,2} = -M_c \, \Phi(f) \, C \, \frac{k^8 \, \sigma^4}{(2\pi)^9 \, c_g} \, P_{1234} \, \Delta t \, N^{-1} \quad , \tag{2.38}$$

where the product term is taken from Eq. (2.20), M_c represents the cumulative interpolation factors of all quadruplet components inside the nine point stencil from Part 3, C is the conventional proportionality constant, Δt is the numerical time step and N represents the action density at the discrete grid point considered. $\Phi(f)$ is a filter function introduced to apply these changes only for high frequencies

$$\Phi(f) = \exp\left[-c_1 \left(\frac{f}{c_2 f_p} \right)^{-c_3} \right] \quad , \tag{2.39}$$

with c_1 through c_3 as tunable parameters, in addition to a_{34} and C. Consistent with a diffusion-based filter, the normalized change is limited to a maximum change $\Delta\tilde{N}_{\max}$, distributed over the two quadruplet contributions as

$$\Delta\tilde{N}_{m,1} = \frac{|\Delta\tilde{N}_1|\Delta\tilde{N}_{\max}\,\Phi(f)}{|\Delta\tilde{N}_1| + |\Delta\tilde{N}_2|} \quad , \Delta\tilde{N}_{m,2} = \frac{|\Delta\tilde{N}_2|\Delta\tilde{N}_{\max}\,\Phi(f)}{|\Delta\tilde{N}_1| + |\Delta\tilde{N}_2|} \quad . \tag{2.40}$$

and the discrete changes of action density are limited as

$$-\Delta\tilde{N}_{m,1} \leq \Delta\tilde{N}_{c,1} \leq \Delta\tilde{N}_{m,1} \quad , \quad -\Delta\tilde{N}_{m,2} \leq \Delta\tilde{N}_{c,2} \leq \Delta\tilde{N}_{m,2} \tag{2.41}$$

The maximum allowed change corresponds to the Peclet number. Practical values of $\Delta\tilde{N}_{\max} \approx 0.25$ are used. Note that the above arguments only consider the rate of change in the quadruplet at the center bin in the discrete grid stencil, but that in practice, the quadruplet contributions to all relevant discrete spectral grid points are considered. Using the full implementation of this filter, an effective $S_{nl,e}$ source term can be defined as

$$S_{nl,e} = (N_f - N)\,\Delta t^{-1} \quad , \tag{2.42}$$

where N_f is the spectrum after filtering, and N is the original spectrum.

This additional filter has not been used in the optimization study, but was found to be beneficial both qualitatively and quantitatively when added to selected optimized GMD configurations as will be shown in Section 4.6.

3 Holistic optimization

3.1 Basic approach

The traditional approach to optimizing parameterizations of S_{nl} is to optimize the interactions for given spectra to optimally represent the corresponding exact interactions (e.g., WRT). Such an approach was used in Part 1 and in Tolman (2004). However, it was also shown that a better fit for interactions for individual spectra does not necessarily result in better model results. In fact, a DIA with a single representative quadruplet using the new two-parameter quadruplet definition significantly improved the description of individual interactions, but resulted in unstable model integration with spurious two-peaked spectra. This behavior, where better individual interactions do not result in better model integration is attributed to the strong nonlinearity of the interactions.

The above behavior implies that interactions should be optimized in such a way that full model behavior instead of interactions for selected spectra are optimized. Such a 'holistic' optimization procedure was introduced in Part 2 and in Tolman and Krasnopolsky (2004). With this approach, an optimized DIA with multiple representative quadruplets and an extended quadruplet definition (MDIA) was indeed shown to represent model integration based on the WRT method much better than a model based on the traditional DIA. A second issue is the optimization procedure applied. For an MDIA with a small number of free parameters, the optimization can be performed by brute force mapping of all model errors in parameter space (Part 2), but for larger numbers of free parameters this is not economically feasible. For such a case, a genetic optimization algorithm was designed to effectively find optimal parameter settings in a multi-dimensional parameter space with multiple local minima for errors (Appendix B of Part 2 and Tolman and Krasnopolsky, 2004).

The optimization procedure contains several elements. A set of representative test cases needs to be designed for which the GMD is to be optimized. From these test cases, test parameters and metrics need to be defined to quantify how well a realization of the GMD performs. With this, a genetic optimization procedure can be designed. Before test cases are discussed in Section 3.3, test parameters are discussed in Section 3.2. After this, metrics are discussed in in Section 3.4. Finally, the general design of the genetic algorithm is discussed in Section 3.5. Note that strategies for the actual genetic optimization are deferred to Section 4.

3.2 Test parameters

All tests as described in the following section produce a set of spectra at various times and or locations. These spectra are the basis of test parameters and metrics in the optimization procedure. Inside the wave model the action density spectrum as a function of wavenumber and direction $N(k, \theta)$ is used. However, the output

of the model is the more generally used energy[2] density spectrum as a function of frequency and direction $F(f,\theta)$. The conversion between the spectra follows directly from the definition of the spectra and the Jacobian corresponding to the conversion of spectral space as in Eq. (2.29). Because these spectra contain the full description of the sea state in the model, one could simply define the metric of an optimization algorithm as some direct error measure of the entire two-dimensional spectrum. However, this does not acknowledge that some features of the spectrum may be important, and should be explicitly accounted for in the optimization (as was done in Part 2). For instance, the full spectrum generally contains too much information for practical wave forecasting problems, and hence is generally reduced to one or more mean descriptive parameters of the spectrum such as a representative wave height. For forecast practices, it then makes sense that the wave height error is minimized explicitly. For this reason, error measures considered in Part 2 were based on the wave height, the one- and two-dimensional spectrum, and the one- and two-dimensional steepness spectrum ($G = k^2 F$). In this study a much broader range of spectral parameters is considered in the optimization and validation of the GMD.

The obvious first mean wave parameter to be considered is the total energy (variance) E or the significant wave height H_s,

$$H_s = 4\sqrt{m_0} \quad , \quad E = m_0 = \iint F(f,\theta)\, df\, d\theta \quad , \tag{3.1}$$

where m_0 is the zeroth moment of the spectrum. Traditionally, the significant wave height H_s has the most direct implication for safety at sea and is therefore the preferred of these two parameters to address. The next step is to identify some representative measure for the wave period (or length) and the wave direction. For wave period measures, a choice can be made between a peak period based on the spectral shape, or a mean period based on spectral moments. The peak period in WAVEWATCH III is traditionally estimated from the one-dimensional wave energy spectrum

$$F(f) = \int F(f,\theta)\, d\theta \quad . \tag{3.2}$$

To obtain a continuous estimate of the peak frequency (f_p) or the corresponding peak period ($T_p = f_p^{-1}$) from the discrete frequency spectrum $F(f)$, a parabolic fit is made to the shape of the peak of the spectrum. Mean periods or frequencies are generally obtained from moments of the spectrum

$$m_i = \iint f^i\, F(f,\theta)\, df\, d\theta \quad , \tag{3.3}$$

[2] Formally wave variance rather than energy, but this nomenclature is used throughout wind wave literature.

or similar moments based on the period $T = f^{-1}$. Several definitions of mean frequencies or periods from the first or second spectral moments m_1 and m_2 can be defined. Using peak or mean measures both has advantages. The peak frequency assesses if the dominant feature of the spectrum is 'in the right place', but assessment is less straightforward in multi-peaked spectra. Mean measures tend to focus more on the details of the spectrum at higher frequencies, particularly if higher spectral moments are used. Considering previous issues with the shape of the peak of the spectrum in WAVEWATCH III (see Tolman and Krasnopolsky, 2004, Fig. 4b), and because details of the shape of the spectrum at high frequencies will be addressed with separate parameters below, the present study will focus on the peak frequency and period. Note that the new partitioning algorithm based on the Vincent and Soille (1991) algorithm is available in WAVEWATCH III (Hanson and Jensen, 2004; Hanson et al., 2006; Tolman, 2009b). This algorithm allows for a direct assessment of mean wave parameters of individual wave fields in a multimodal wave field.

Mean directions $\overline{\theta}_{1,2}$ are typically obtained from the directional Fourier components of the spectrum

$$\overline{\theta}_{1,2} = \mathrm{atan}\left(\frac{b}{a}\right) \quad , \tag{3.4}$$

$$a = \int_0^{2\pi} \int_{f_1}^{f_2} \cos(\theta) F(\sigma,\theta)\, d\sigma\, d\theta \quad , \tag{3.5}$$

$$b = \int_0^{2\pi} \int_{f_1}^{f_2} \sin(\theta) F(\sigma,\theta)\, d\sigma\, d\theta \quad . \tag{3.6}$$

By integrating over the entire frequency space ($[f_1, f_2] = [0, \infty]$) the total mean direction $\overline{\theta}$ is obtained, whereas the mean direction at the spectral peak $\overline{\theta}_p$ is obtained by integrating over the discrete spectral band around the discrete peak frequency $f_{p,i}$ only ($[f_1, f_2] = [f_{p,i} \pm 0.5\Delta f_{p,i}$). Together with the mean direction, a mean directional spread $\sigma_{\theta,1,2}$ can be defined from the Fourier components as (Kuik et al., 1988)

$$\sigma_{\theta,1,2} = \left[2 \left\{ 1 - \left(\frac{a^2 + b^2}{E^2} \right)^{1/2} \right\} \right]^{1/2} \quad , \tag{3.7}$$

which can also be applied to the entire spectrum or to selected frequency ranges based on the choice of $f_{1,2}$. Due to the pronounced asymmetric behavior of the spectral shape in frequency space, mean spread parameters of spectral energy in frequency space are not commonly used.

The next level of detail is obtained when one-dimensional spectral descriptions are addressed. Conventional one-dimensional spectral measures are the one-dimensional spectrum $F(f)$ from Eq. (3.2), and the spectral mean directions

$\overline{\theta}(f)$ and directional spread $\sigma_\theta(f)$ obtained by applying Eqs. (3.4) through (3.7) for each discrete spectral frequency band individually. Apart from these spectral measure the steepness spectrum $G(f)$,

$$G(f) = k^2\, F(f) \tag{3.8}$$

provides additional insight in the behavior of the spectrum by focusing more on the high-frequency part of the spectrum.

More detailed behavior of the one-dimensional spectrum to be tested (and later optimized) are the energy level of the parametric tail, the energy level in the transition from the spectral peak to the parametric tail, and the best fit spectral slope in the latter area. The first of these parameters (α, Phillips, 1958) is computed as

$$\alpha = (2\pi)^4 g^{-2}\, F(f)\, f^5 \quad , \tag{3.9}$$

which in the parametric tail by definition is constant, and can therefore be assessed locally, typically at the highest discrete frequency in the spectral grid. The second and third parameter assess the expectation that this part of the spectrum follows an f^{-4} functional behavior, or that the steepness spectrum $k^2\, F(f)$ is constant in this range. Since this is a dynamic range of the spectrum, the level of this part of the spectrum is easily assessed by directly assessing the steepness spectrum. The functional behavior requires an optimal fit estimate of the slope factor m in f^{-m}. Alternately, the fit to the exact steepness spectrum in this frequency range can be addressed directly.

Finally, the full two-dimensional spectrum remains obviously relevant, as is the two-dimensional steepness spectrum

$$G(f,\theta) = k^2\, F(f,\theta) \tag{3.10}$$

This generally covers the holistic model behavior. However, even if the focus is on the holistic model behavior, an accurate instantaneous description of the nonlinear interactions remains a desirable feature of a wave model. Therefore, the actual interactions obtained from the test cases also need to be addressed. Apart from the full interactions $s_{nl}(f,\theta)$, it is worth while to address the one-dimensional interactions

$$s_{nl}(f) = \int s_{nl}(f,\theta)\, d\theta \quad , \tag{3.11}$$

which identifies some of the critical features of the interaction, in particular the redistribution of wave energy over frequencies. From the one-dimensional interaction, an energy flux in frequency space M can be identified as

$$M(f) = \int_0^f s_{nl}(f_i)\, df_i \quad . \tag{3.12}$$

This flux can be interpreted as the nonlinear energy flux to lower frequencies passing the frequency f. Whereas the interactions $s_{nl}(f)$ typically have a three-lobed structure, the flux M has a two-lobed structure, with, by definition $M(0) = M(\infty) = 0$. This implies that there exists a third frequency where $M = 0$. This so-called zero-frequency f_0 for which $M(f_0) = 0$ is important, as it forms a natural separation between low and high frequencies across which nonlinear interactions have no nett impact.

This completes the description of parameters used to asses model behavior in test cases, and to be the basis of optimization metrics in the present study. Error metrics based on these parameters will be defined in Section 3.4.

3.3 Test cases

For the holistic optimization test cases need to be designed, representing realistic an relevant wave model behavior. Considering the importance of nonlinear interactions in terms of wave growth, most if not all tests will consider conditions with active wave growth. As mentioned in Section 1 the WAVEWATCH III model with its default settings is used here. The following additional considerations were made when setting up the test cases.

i) To avoid that the spectral and physical grid directions coincide (enhancing numerical directional anisotropy), the first discrete spectral direction is offset by $0.5\Delta\theta$. Note that this wave model option was not available in Part 2.

ii) To ensure sufficient resolution for the WRT computations, the spectral grid consists of 36 directions ($\Delta\theta = 10^\circ$) and the frequency increment factor of Eq. (2.17) is set to $X = 1.07$.

iii) The WRT computations are known to be somewhat sensitive to the extend of the discrete grid in high frequencies. To ensure accurate WRT computations, a frequency grid ranging from 0.040 Hz to 0.785 Hz with 45 frequencies is used, and for each computation initial conditions are chosen such that the dynamic cut-off frequency between the prognostic part of the spectrum and the diagnostic tail is always well within the discrete spectral range. Typically, initial conditions consists of a JONSWAP spectrum (Hasselmann et al., 1973) with a peak frequency $f_p = 0.25$ Hz.

iv) For maximum consistency with operational model behavior, the third-order propagation scheme using averaging to alleviate the Garden Sprinkler Effect is used. Note that in Part 2 a first order scheme was used to more rapidly achieve stationary conditions in idealized test cases.

v) All spatial propagation tests are performed in Cartesian rather than spherical space.

Note that these model settings are either controlled by the user when compiling the wave model, or are set up centrally for all test cases with a shared environment file (see Tolman, 2010).

In Part 2 only two deep water test cases where considered. In the present study, the number of test cases is expanded dramatically, both to cover additional (deep water) wave growth situations, and to add shallow water conditions. Even now, a major focus is still on deep water wave growth. The corresponding test cases are presented in Section 3.3.1. Additional shallow water tests are described in Section 3.3.2. Finally, some tests are performed to illustrate model behavior after the optimization has been completed. Such tests will be described in Section 5. Additional information on executing test cases can be found in Tolman (2010). Test names correspond to their script names in the test package and identified here with the file font.

3.3.1 Deep water tests

The deep water tests all consider wave growth. They can broadly be divided in several categories

1) Traditional time- and fetch-limited growth curve computations for constant (offshore) wind speed (test_01 and test_02). These are the traditional idealized test conditions considered in numerous studies, and these tests were the only two tests used in Part 2.

2) Conditions with turning winds or waves that are not aligned with the wind. Considered are a time-limited case representing a frontal passage (from Tolman, 1992), a time-limited case with a constantly turning wind, and a so-called 'slanting fetch' case with a uniform wind blowing offshore under an angle with a straight coast. (test_03 through test_05).

3) A case with wave growth in the presence of swell. (test_06).

The test cases will be discussed in some detail below. The wave model behavior in all test cases will be illustrated using the parameters as defined in the previous section. To illustrate the importance of the nonlinear interactions, and the potential improvement to be achieved by the optimizations of the GMD, results from the exact (WRT) interactions and the conventional DIA will be presented side-by-side. Tested are the default WAVEWATCH III settings with $\lambda = 0.25$ and $C = 1 \times 10^7$ (henceforth denoted as WW3), and the traditional WAM settings from WAMDIG (1988) with $\lambda = 0.25$ and $C = 3 \times 10^7$, henceforth denoted as WAM[3].

[3] Note: this identifies WAM DIA settings in WAVEWATCH III, not the full WAM model.

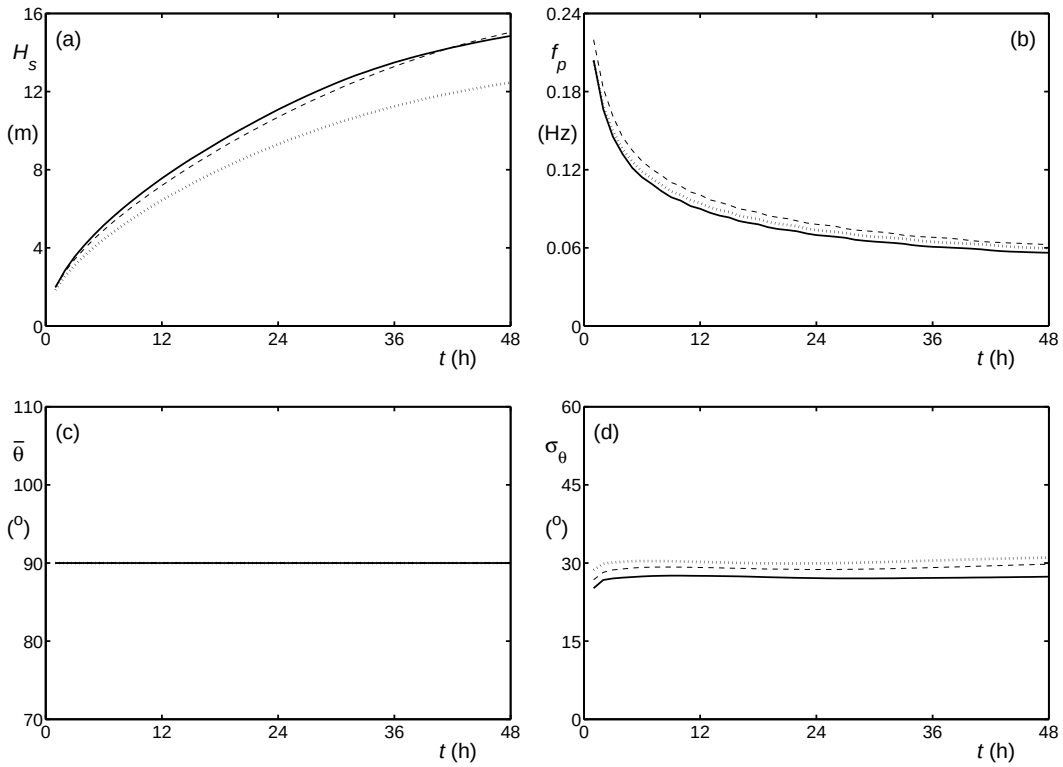

Fig. 3.1 : Evolution in time of a) significant wave height H_s, b) peak frequency f_p, c) mean direction $\overline{\theta}$, and d) directional spread σ_θ for the time-limited growth test test_01. *Solid line: WRT. Dashed line: WW3. Dotted line: WAM. Chain line: wind direction (in this figure, wind and wave direction are identical).*

Test case test_01 considers a conventional time-limited growth situation in otherwise homogeneous conditions. The model consists of one grid point, and all wave propagation is switched off to represent homogeneous conditions. The wind speed is set to $U_{10} = 20$ ms^{-1}, and computations are performed for 48 h. Test data are saved every hour, excluding the initial conditions. This results in 48 sets of test spectra etc. for this test case.

Figure 3.1 shows mean wave parameters resulting from this test for the exact WRT method (solid lines) and the DIA approximations (WW3 dashed lines, WAM dotted lines). Wave heights (panel a) of the WW3 approximation are close to the exact (WRT) results, whereas results from the WAM approach are systematically low. Conversely, the WAM approach reproduces WRT peak frequencies closer than the WW3 approach (panel b). This test lines up wind and wave directions naturally, and hence no differences are found in the mean direction (panel c). Finally, directional spread of both the WAM and WW3 approach overestimate the exact WRT results (Fig. 3.1d).

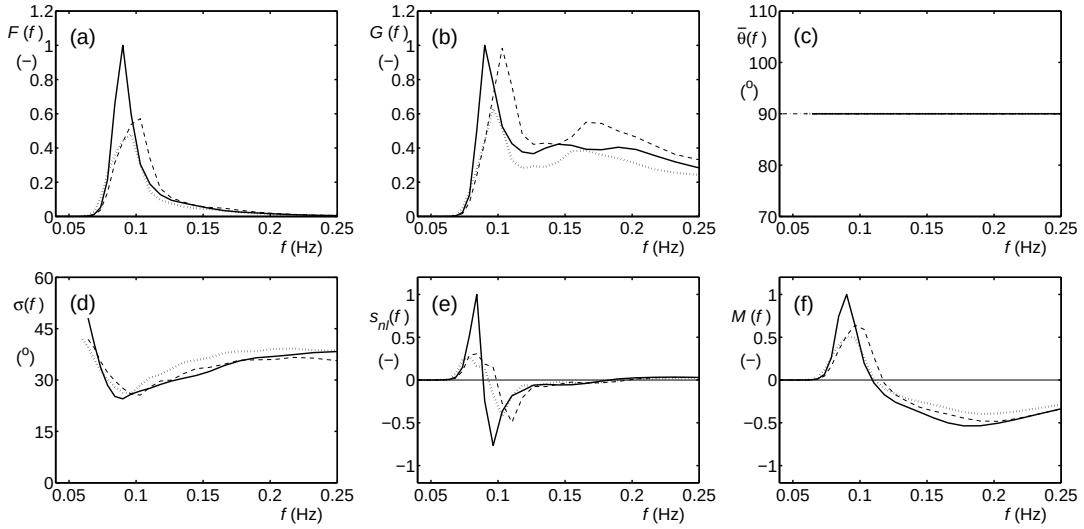

Fig. 3.2 : One-dimensional spectral quantities after 12 h of model integration corresponding to Fig. 3.1. a) energy spectrum $F(f)$, b) steepness spectrum $G(f)$, c) mean direction $\overline{\theta}(f)$, d) directional spread $\sigma_\theta(f)$, e) nonlinear interactions $s_{nl}(f)$, f) nonlinear energy flux $M(f)$, Legend as in Fig. 3.1. All variables normalized with the absolute maximum of the WRT results.

Figure 3.2 shows one-dimensional spectral parameters after 12 h of model integration for this test. These results are representative for the entire model integration. The results for the spectrum $F(f)$ (Fig. 3.2a) indicate that neither the WW3 nor the WAM approach accurately described the sharp spectral peak. The differences in shape for the WW3 and WAM approaches indicate why the former gives a better representation of the wave height H_s, whereas the latter represents the peak frequency f_p better. The steepness spectrum $G(f)$ (panel b) furthermore indicates that neither the WW3 nor the WAM approach describe the constant steepness range for intermediate frequencies particularly well, and that the WAM approach underestimates the energy level at high frequencies α whereas the WW3 approach overestimates it. Due to the setup of the test, the spectral direction $\overline{\theta}(f)$ (panel c) provides no information. The directional spread $\sigma(f)$ is fairly similar between the three approaches, with some overestimation by the WAM approach. The nonlinear interactions (panel e) according to the WW3 and WAM approaches are not as sharply defined as in the exact approach, but corresponding fluxes (panel f) result in fairly similar zero-flux frequencies f_0.

Figures 3.3 and 3.4 show the corresponding two-dimensional spectra $F(f, \theta)$ and source terms $s_{nl}(f, \theta)$. The results of the exact approach are generally sharper and more detailed. Note that the interactions are surprisingly similar, considering the large differences found in previous parts of this study. This can be attributed to the dynamic response of the model, where small changes in spectral shape

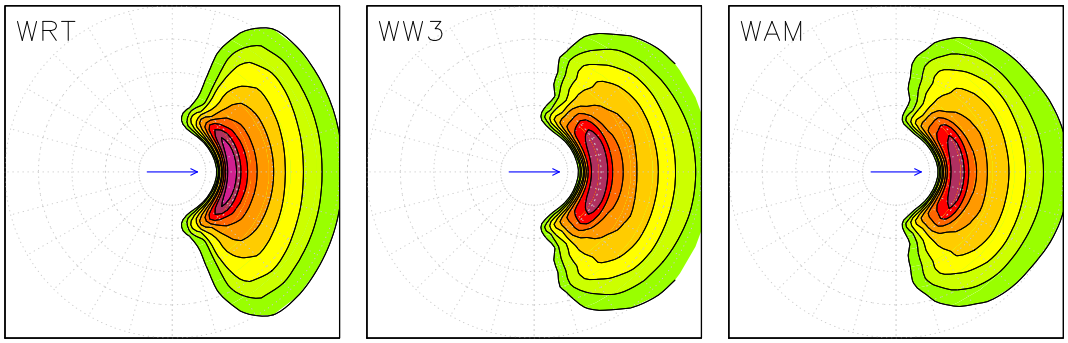

Fig. 3.3 : Two-dimensional energy spectral $F(f,\theta)$ from exact WRT computations (left) and WW3 (center) and WAM DIA approximation (right) corresponding to Fig. 3.1 after 12 h of model integration. Logarithmic scaling with factor 2 between contours and lowest contour at 0.25 $m^2 s$. Frequencies ranging from 0 to 0.25 Hz, frequency grid lines at 0.05 Hz intervals.

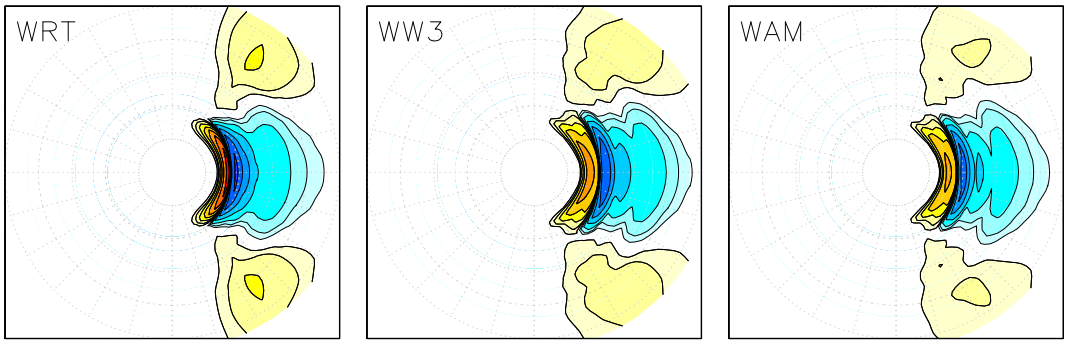

Fig. 3.4 : Nonlinear interactions $s_{nl}(f,\theta)$ from exact WRT computations (left) and WW3 (center) and WAM DIA approximation (right) corresponding to Fig. 3.1 after 12 h of model integration. Logarithmic scaling with factor 2 between contours and lowest contour at $\pm 10^{-4}$ m^2. Grid as in Fig. 3.3.

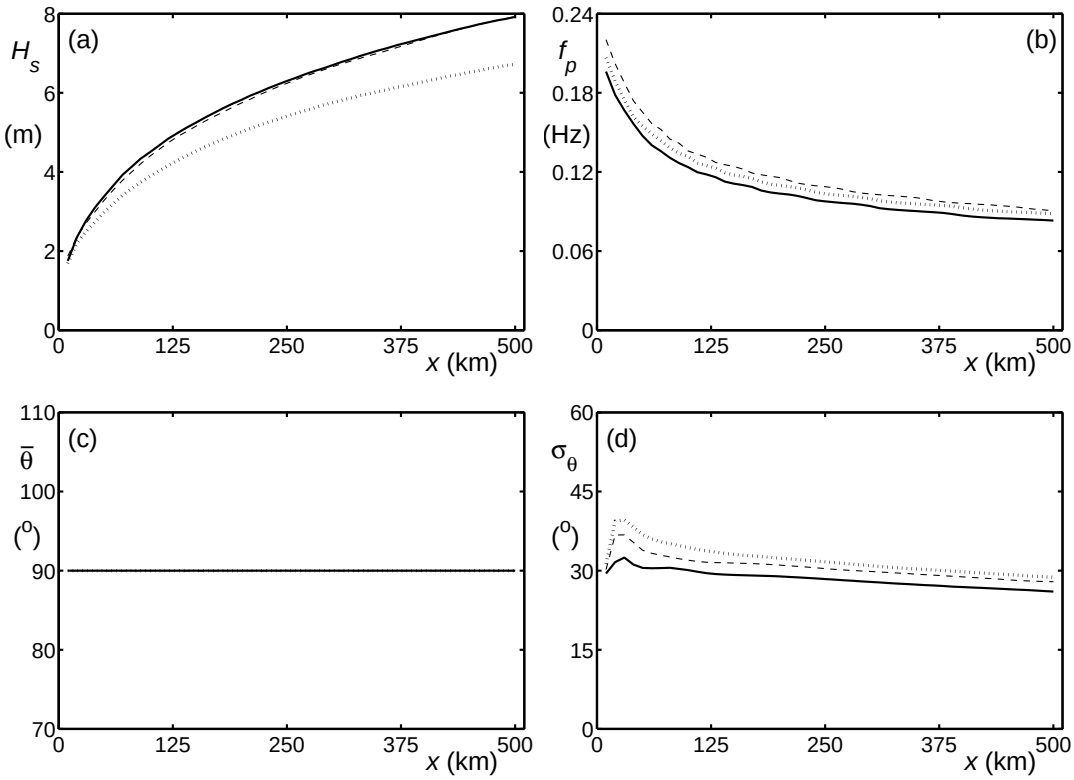

Fig. 3.5 : Like Fig. 3.1 for the fetch-limited growth test test_02.

result in similar energy balances, and therefore in similar interaction shapes. The WW3 and WAM approaches, however, do not have sufficient flexibility to reproduce the sharp features of the WRT interactions.

Test case test_02 represents a conventional fetch-limited growth test in (quasi-) stationary conditions. The grid consists of 50 active offshore grid points with a spacing of 10 km. Perpendicular to the shore, three grid points are considered with a grid spacing of 250 km. Spectral output is produced only for the central grid line. The wind direction is offshore, with a wind speed of $U_{10} = 20$ ms^{-1}. Computations are performed for 24 h to reach quasi-stationary conditions. After 24 h, data for 50 grid points at the center of the coast are saved for evaluation.

Figure 3.5 shows mean wave parameters resulting from this test. The results are similar to those of the time-limited growth test in Fig. 3.1, with two main differences for all models. First, wave heights are significantly smaller in the fetch-limited test. Qualitatively, however, the behavior of the WW3 and WAM version of the DIA relative to the WRT approach are similar. Second, directions spreads of the WW3 and WAM approaches (Fig. 3.5d) deviate more from the WRT results for the shortest fetches. The one- and two-dimensional spectral results

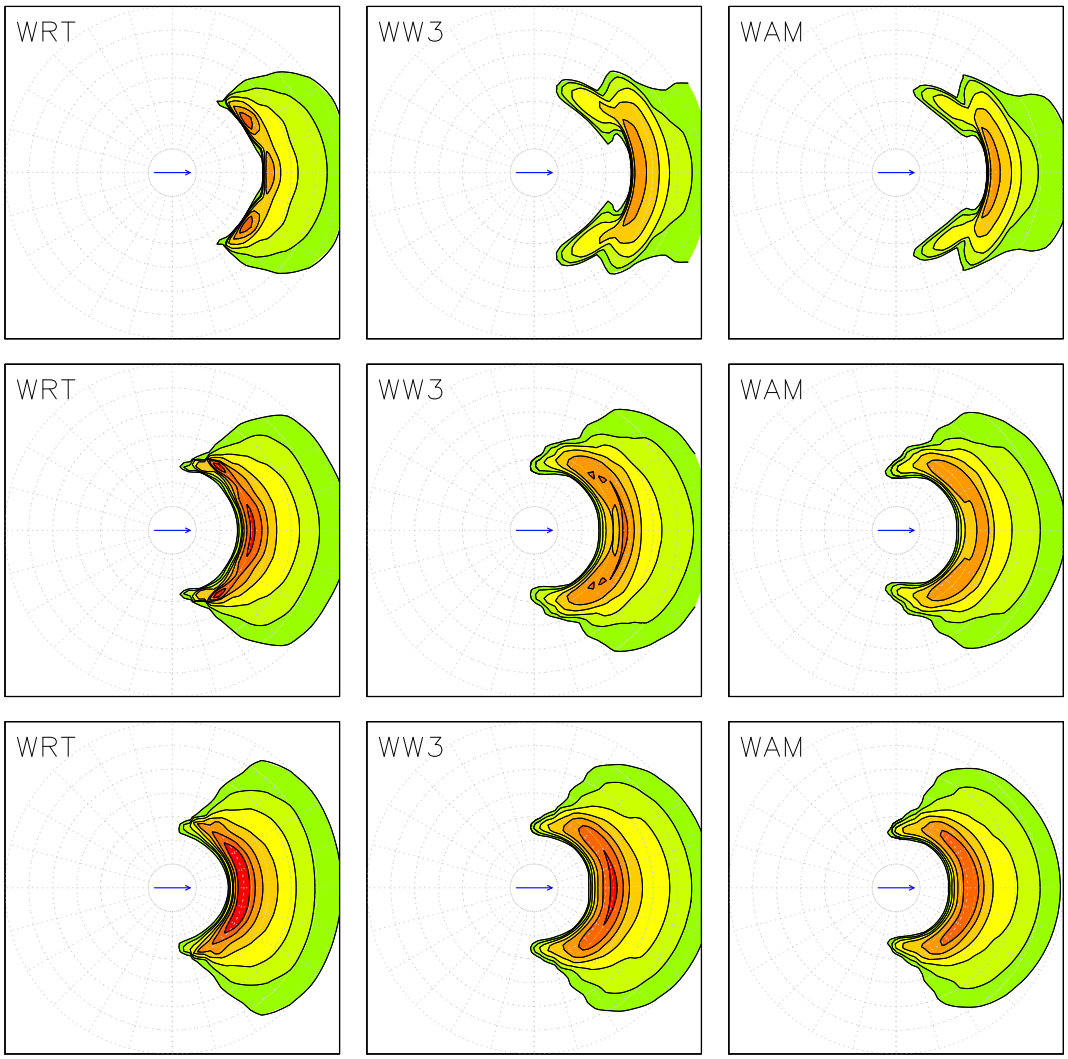

Fig. 3.6 : Like Fig. 3.3 for test test_02. *Top panels for fetch of 10 km. Center panels for fetch of 30 km. Bottom panels for fetch of 50 km. Note that frequencies of up to 0.35 Hz are displayed. Lowest contour at 0.10* m^2s.

from this test are also very similar between the two tests, and will therefore not be illustrated individually for test_02 here, with the exception of two-dimensional spectra for short fetches, which are presented in Fig. 3.6.

For the shortest fetches in the model (10 km, upper panels), the computations using the exact interactions (WRT) result in a bi- or tri-modal spectrum. The DIA-based results (WW3 and WAM) cannot reproduce these spectra, and instead result in very different tri-modal spectra. At the third offshore grid point (30 km, center panels), the exact interactions produce a trimodal spectrum, and the WRT and WAM approaches become more aligned with the WRT results. At the fifth grid point (50 km, bottom panels), all model versions result in a convention unimodal wind sea spectrum, and results have become compatible with the results of the time-limited growth computations.

Test case test_03 represents the 'homogeneous front' case of Tolman (1992). A one-point model without propagation is considered. Initially, the wind speed $U_{10} = 10\text{ms}^{-1}$ is aligned with the waves. After 4 h, the wind speed increases to $U_{10} = 20\text{ms}^{-1}$ and simultaneously turns by 90° during a 2 H period. The wind then stays constant from 6 to 12 h, after which it decreases to $U_{10} = 10\text{ms}^{-1}$ in the next 12 h. Spectra are retained every 30 min, resulting in 48 test spectra.

Figure 3.7 shows mean wave parameters resulting from this test. Whereas the actual evolution of the wave height H_s and peak frequency f_p clearly differ from those of previous test, the relative behaviors of the models based on the WRT, WW3 and WAM approaches are essentially the same. For this case, the evolution of the mean direction ($\overline{\theta}$), Fig. 3.7c) is not trivial. Both the WW3 and WAM approaches turn the wave field too fast. As before, the WW3 and WAM approaches produce directional distributions that are too broad.

Figure 3.8 shows one-dimensional spectral parameters after 6 h of model integration. The one-dimensional spectrum $F(f)$ and steepness spectrum $G(f)$ (Fig. 3.8a,b) show results similar to those of previous test cases. The spectral mean direction $\overline{\theta}(f)$ (Fig. 3.8c) shows that for high frequencies, the mean wave direction lines up with the wind direction (chain line). For lower frequencies, the waves are still oriented more in the previous wind directions, with the WAM and WW3 approaches turning the waves too fast compared to the WRT results. Results for the nonlinear interactions (Fig. 3.8e,f) again are similar to those of the previous tests. Note the the dual peaks in the positive lobe for low frequencies in $s_{nl}(f)$ according to the WRT method is unique for this particular model output time, and is not seen at other output times.

Figures 3.9 and 3.10 show the corresponding two-dimensional spectra $F(f,\theta)$ and source terms $s_{nl}(f,\theta)$. The spectra and source terms again are qualitatively similar for all three approaches, with significantly more detail in the exact (WRT) solutions.

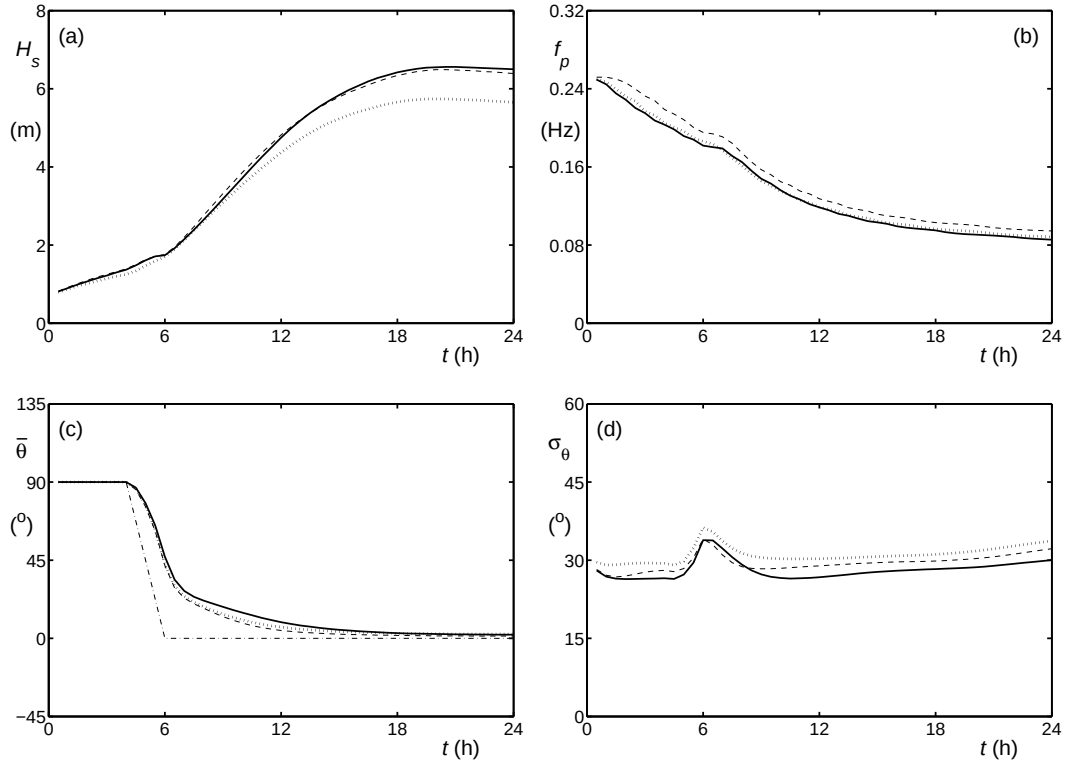

Fig. 3.7 : Like Fig. 3.1 for time-limited 'frontal passage' test test_03.

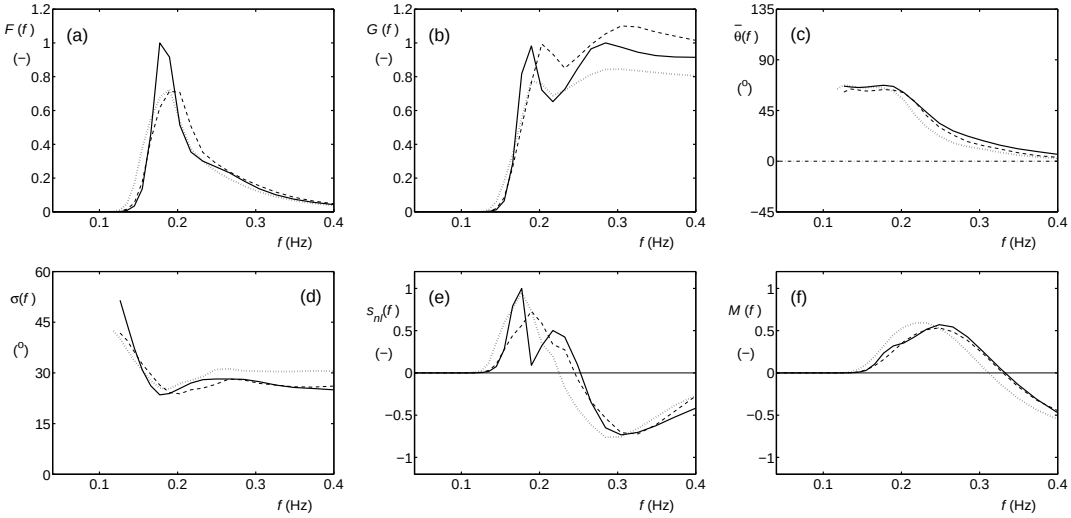

Fig. 3.8 : Like Fig. 3.2 for test_03 *after 6 h of model integration.*

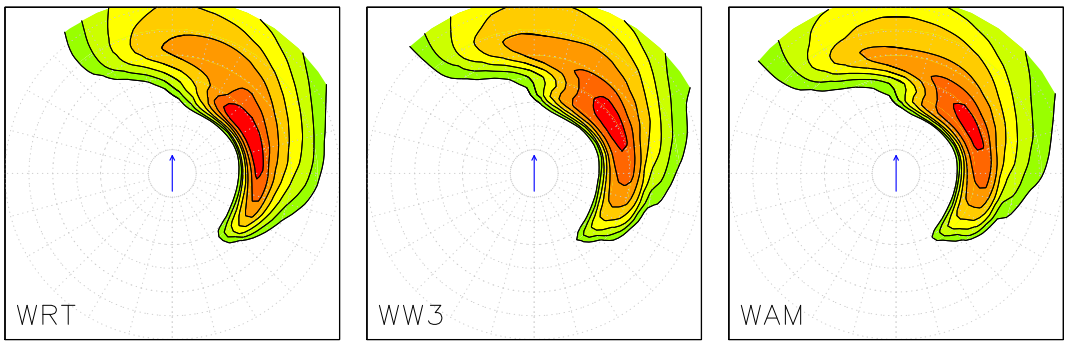

Fig. 3.9 : Like Fig. 3.3 for test_03 *after 6 h of model integration. Lowest contour at 0.02* $m^2 s$.

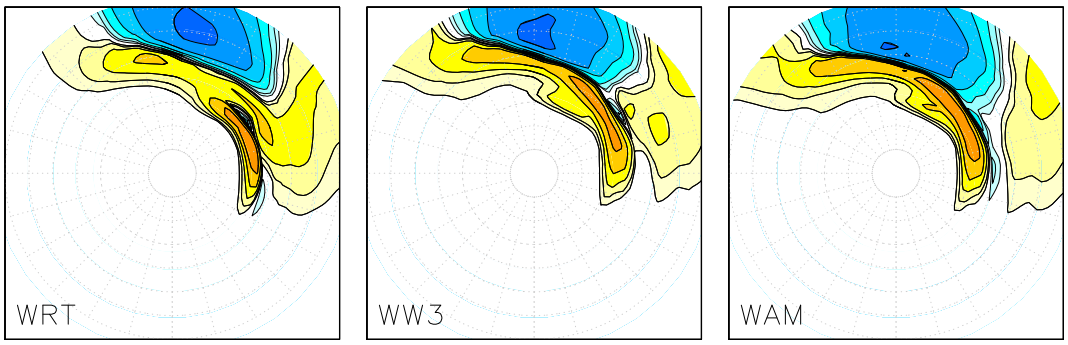

Fig. 3.10 : Like Fig. 3.4 for test_03 *after 6 h of model integration. Lowest contour at* $\pm 10^{-5}$ m^2.

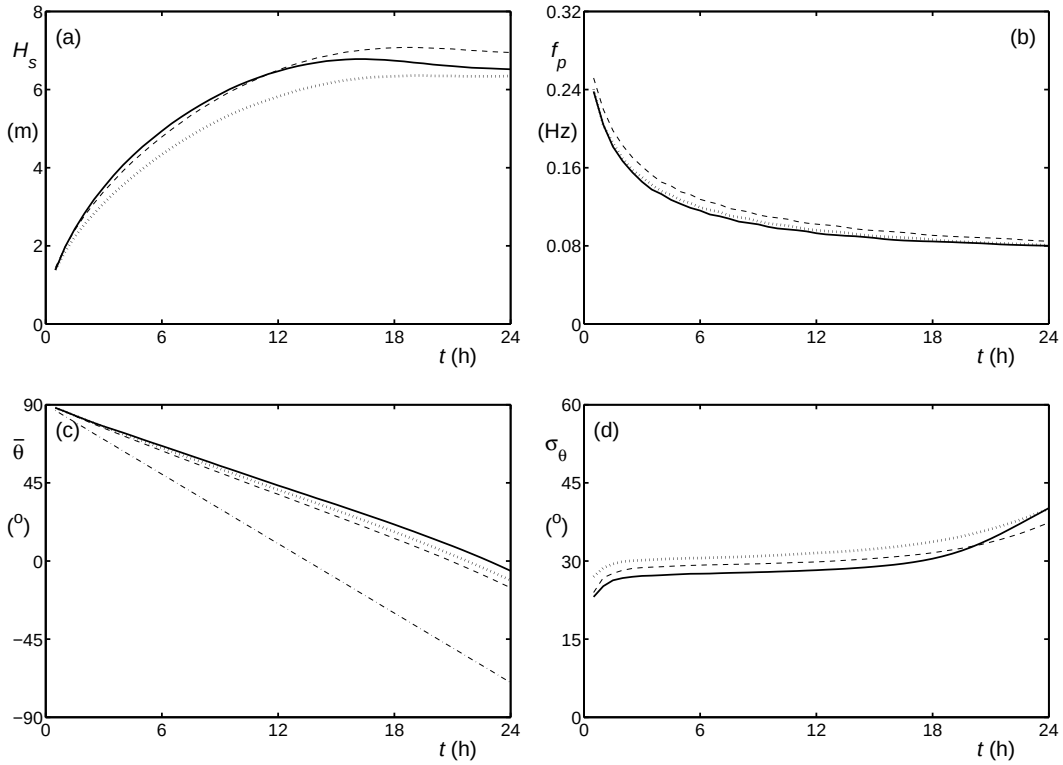

Fig. 3.11 : Like Fig. 3.1 homogeneous rotating wind test test_04.

Test case test_04 is a one-point model without propagation and is characterized by a wind with constant speed ($U_{10} = 10\text{ms}^{-1}$), which rotates with a constant speed (see Fig. 3.11c). The rotation is slow enough for the model not to separate wind seas from swell in a 24 h model run. As before, data are saved every 30 min, resulting in 48 test spectra and source terms.

Figure 3.11 shows the mean wave parameters for this test case. The mean wave direction (Fig. 3.11c) systematically lags more and more behind the wind direction. Eventually, this will result in a separation of wind sea and swell. This however, occurs outside the duration of the present model run. Up to 15 h of model integration, the other mean wave parameters shown in Fig. 3.11 show behavior similar to that of other test cases. After that, the wave height H_s obtained by the WRT methods decreases compared to those of the approximate methods, whereas the directional spread σ_θ increases. This makes the latter part of the model integration the most interesting part of this test.

Figure 3.12 shows one-dimensional spectral parameters at the end of the model integration (24 h). The spectra ($F(f)$ and $G(f)$) obtained with the WRT approach (solid lines) start showing a second spectral peak at a frequency of approximately 0.12 Hz. The WW3 and DIA approximations fail to show this initial

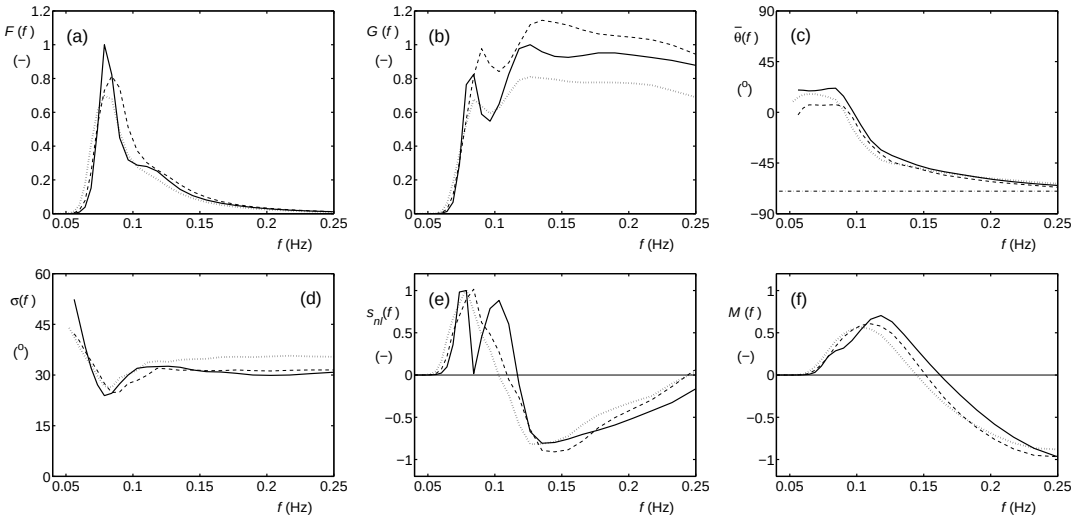

Fig. 3.12 : Like Fig. 3.2 for test_04 *after 24 h of model integration.*

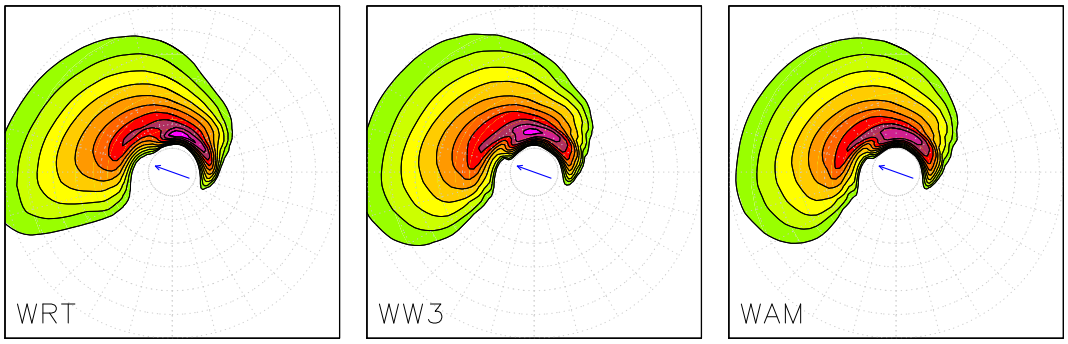

Fig. 3.13 : Like Fig. 3.3 for test_04 *after 24 h of model integration. Lowest contour at 0.10 m^{2}s.*

stage of separation between the wind sea and a swell. The mean directions of the WW3 and WAM methods turn low-frequency waves too fast in the direction of the wind, and show too little change of the directional spread as a function of the wave frequency (Figs. 3.12c,d). The WRT method shows a distinct dual positive lobe for $s_{nl}(f)$ at low frequencies (solid line in Fig. 3.12e), which in this test is a persistent feature. This feature is not reproduced by the WW3 and WAM methods. This feature also has a distinguished impact on the nonlinear fluxes in Fig. 3.12f.

Figure 3.13 shows the corresponding two-dimensional spectra $F(f, \theta)$. The spectra again are qualitatively similar for all three approaches, with significantly more detail in the exact (WRT) solutions, and a more clearly developing wind-sea and swell separation. Note that this separation is mostly due to a much more

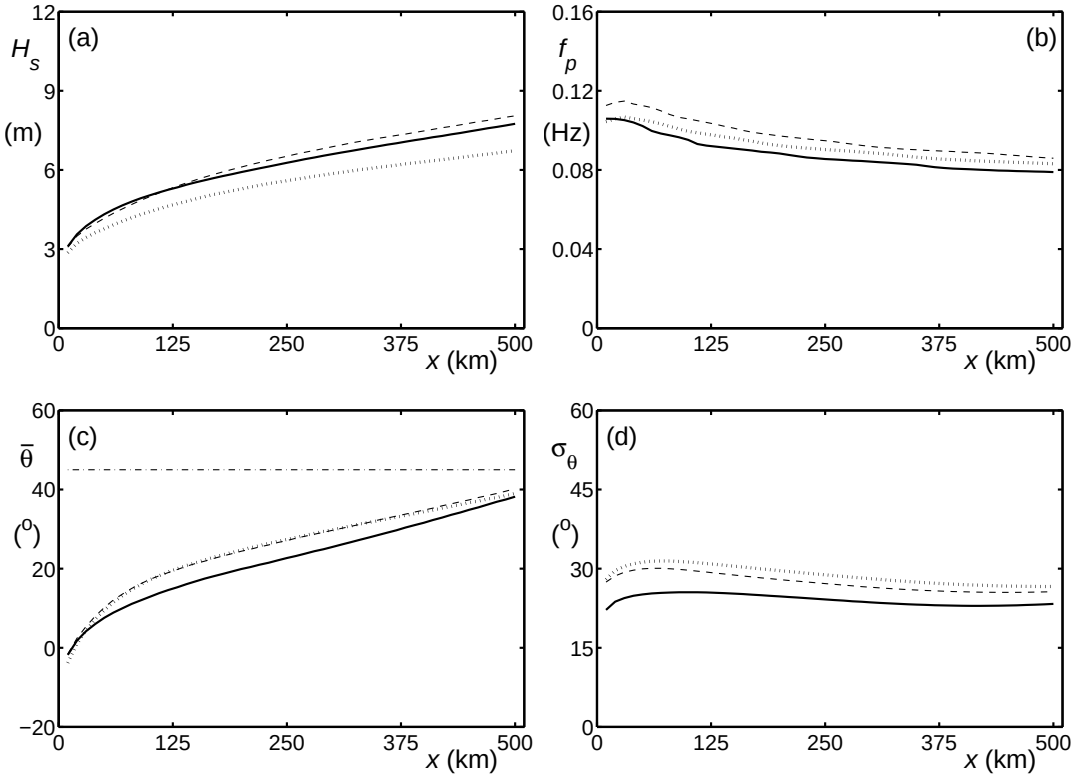

Fig. 3.14 : Like Fig. 3.1 for slanting fetch test test_05.

sharply defined spectral shape in the 'swell' peak for the WRT results.

Test case test_05 represents a slanting fetch case. This test is identical to the fetch-limited growth test test_02 with two exceptions. First, the wind is not directly offshore, but is at a 45° angle with the shoreline. Second, the computational domain is extended another 250 km offshore, to avoid artificial effects of an artificial coastline on the offshore end of the line of output points. As in test test_02, spectra and source terms are saved for 50 grid points at 10 km intervals at the end of the computations (24 h).

Figure 3.14 presents mean wave parameters for this test. Whereas values of wave height and peak frequency vary, behavior of these parameters for the WRT, WW3 and WAM runs are compatible with those of previous test, although the WW3 result now slightly but systematically overestimate the WRT wave heights. Mean wave directions $\overline{\theta}$ deviate greatly from the wind direction (Fig. 3.14c). In fact, for the shortest fetches, the mean wave direction is onshore rather than offshore ($\overline{\theta} < 0°$). As with the previous tests, the WAM and WW3 approaches turn the waves toward the wind direction too fast. Note that directional spreads σ_θ (Fig. 3.14d) are somewhat smaller than with most previous tests.

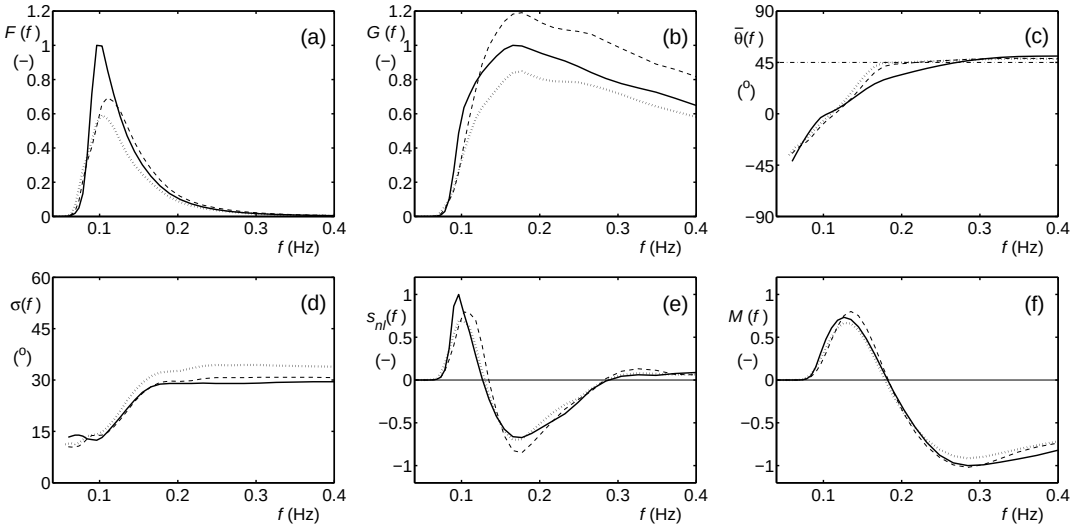

Fig. 3.15 : Like Fig. 3.2 for test_05 *at 20 km offshore.*

In a slanting fetch case, he most interesting model behavior occurs close to the coast. For this reason one-dimensional spectral parameters for the second grid point (20 km offshore) are presented in Fig. 3.15. In this case the spectrum and particularly the steepness spectrum ($F(f)$ and $G(f)$, Fig. 3.15a,b) do not show the distinctly enhanced spectral peak. As with previous test, the mean spectral direction $\overline{\theta}(f)$ (Fig. 3.15c) lines up with the wind for high frequencies, but for low frequencies, the waves line up with the coast, and for the lowest frequencies, wave energy actually travels to the coast under angles as large as 45°. As before, the WW3 and WAM approaches line up the waves too strongly with the wind. The directional spread $\sigma(f)$ (Fig. 3.15d) behaves differently than in all previous tests. For frequencies around and below the spectral peak, the directional spread becomes uncharacteristically narrow. The nonlinear interactions and fluxes (Fig. 3.15e,f) are very similar for all three approaches.

Figure 3.16 shows full two-dimensional spectra of the three approaches at fetches of 10, 50 and 250 km. As before, the WRT approach provides a more sharply defined spectrum. Note the persistence of the spectral rotation relative to the wind. Even at fetches of 250 km (bottom line of plots) this can still be observed, particularly at the spectral peak.

Test case test_06 is equivalent to the time-limited growth case test_01 but now in the presence of a swell field. The initial swell wave height $H_s = 6$ m and peak period $f_p = 0.06$ Hz, and the swell propagates under an angle of 135° relative to the wind direction.

Figure 3.17 shows the evolution of mean wave parameters for this test. The behavior for the wind sea (green lines) is essentially identical to the behavior in

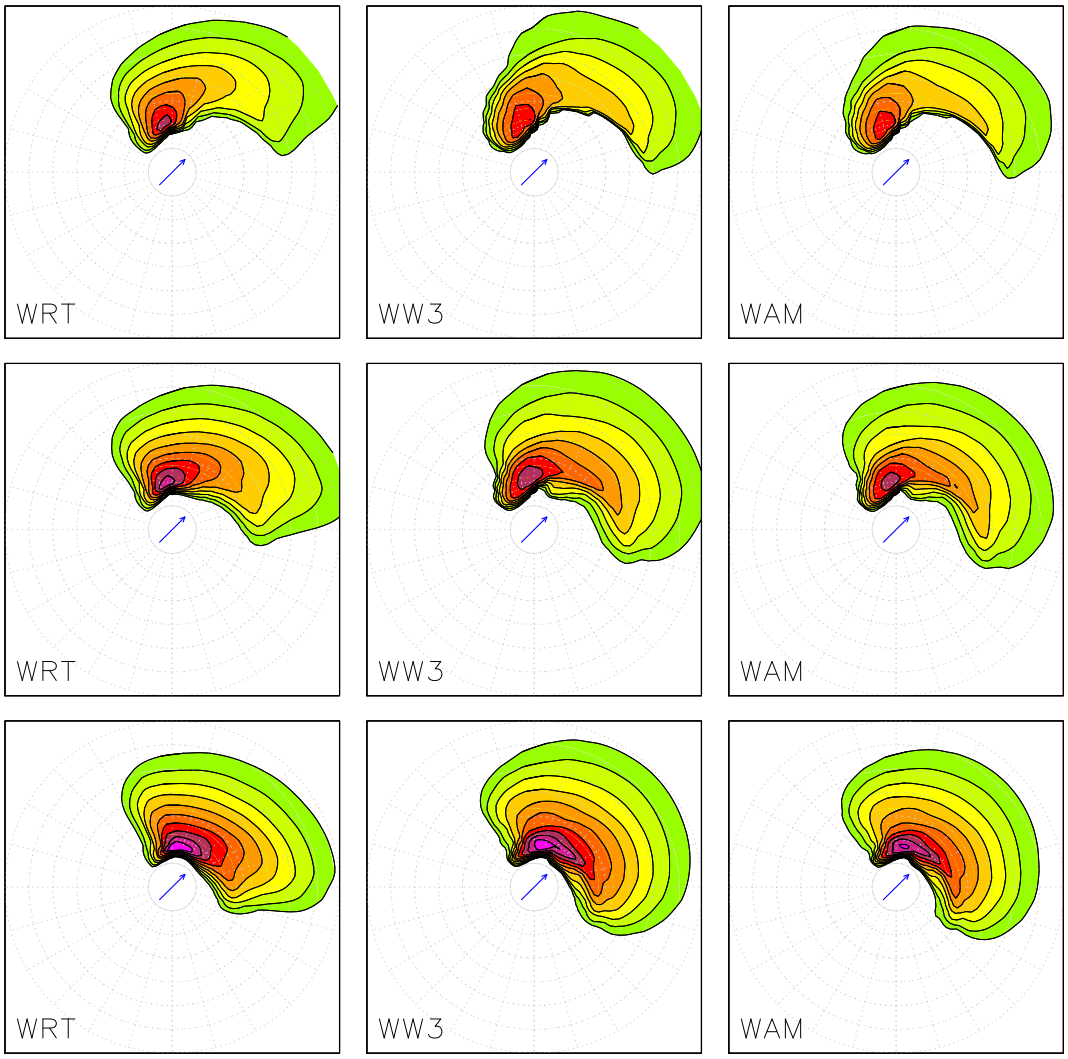

Fig. 3.16 : Like Fig. 3.3 for test_05 *at fetches of 10 km (first line), 50 km (second line) and 250 km (third line). Lowest contour at 0.10* $m^2 s$.

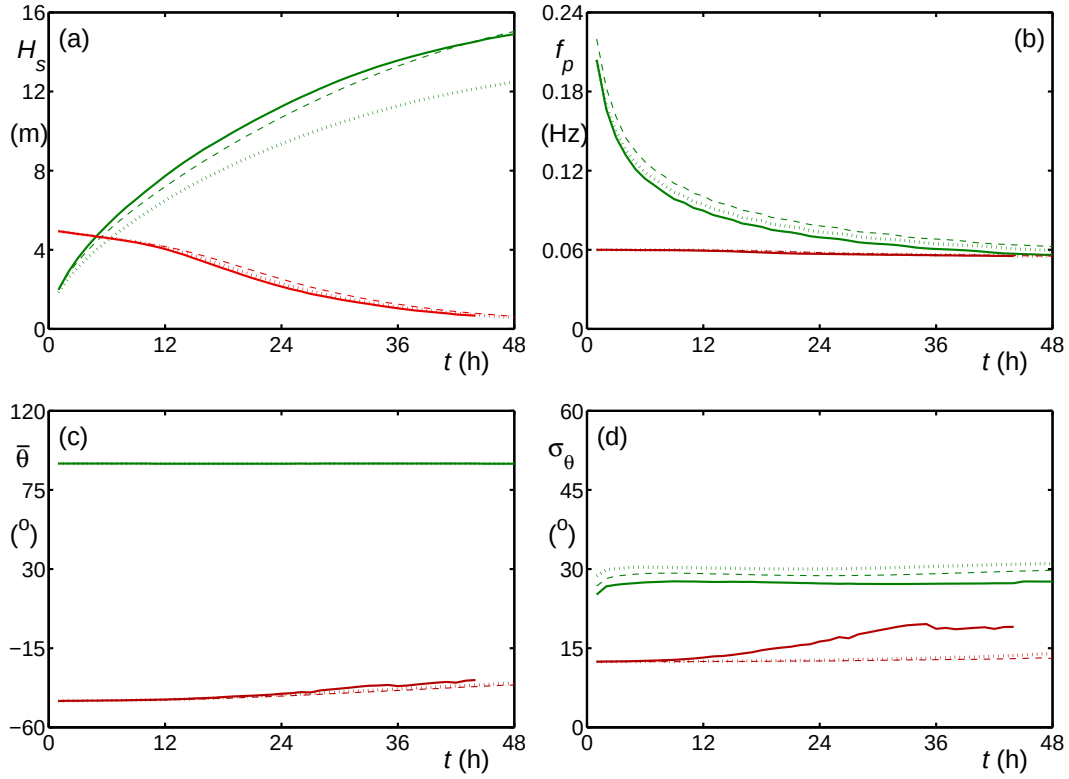

Fig. 3.17 : Like Fig. 3.1 for wave growth in the presence of swell test_06. *Green: wind sea. Red: swell*

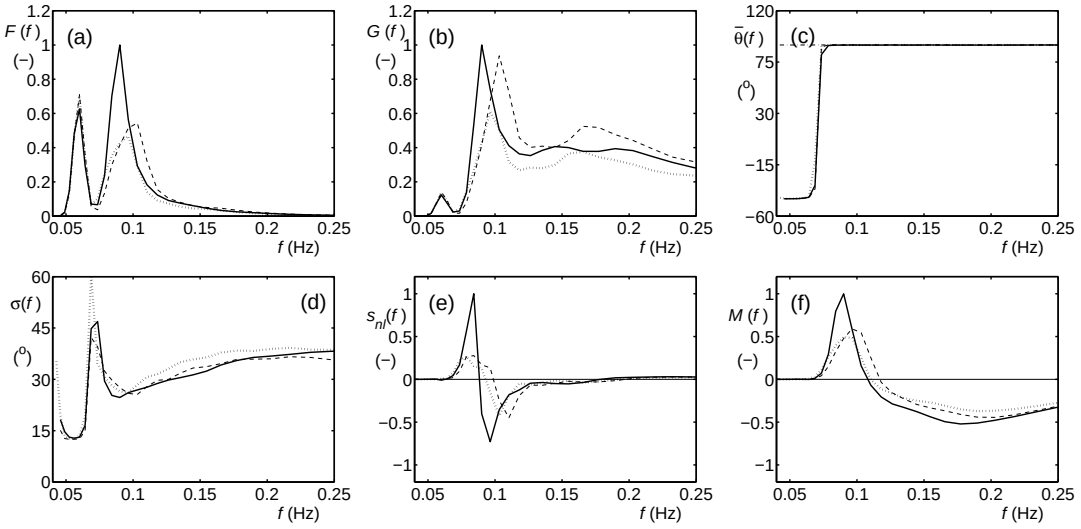

Fig. 3.18 : Like Fig. 3.2 for test_06 *after 12 h of model integration.*

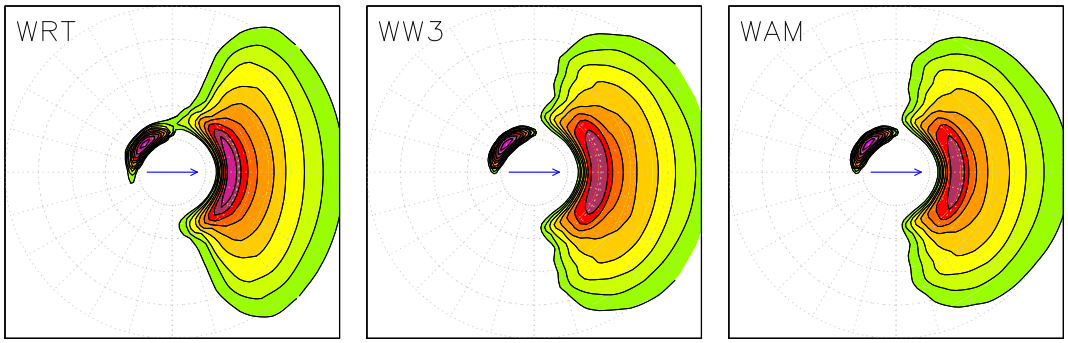

Fig. 3.19 : Like Fig. 3.3 for test_06 *after 12 h of model integration.*

test_01. The red lines in this figure represent the behavior of the swell. During the model integration, the swell height decays, the frequency shifts downward from 0.060 to 0.056 Hz, the mean direction shifts by 10°, and the directional spread increases dramatically. The decay in wave height for the swell (red lines in Fig. 3.17a) accelerates after 12 h of model integration using the WRT method (solid line). This acceleration is not reproduced by the WW3 method, and underestimated by the WAM method. All three methods show similar down shifts in the peak frequency and directional shifts. The WW3 and WAM methods, however, do not reproduce the (dramatic) increase in direction spread for the swell as displayed when using the full WRT interactions.

Figure 3.18 shows the corresponding one-dimensional spectral parameters after 12 h of model integration. The spectra in Fig. 3.18a,b show that the swell is significant in absolute energy but moderate in steepness. Due to the latter, the impact of the swell on the interactions and nonlinear flux is small (Fig. 3.18e,f). The rapid change of direction in the transition from the wind sea to the swell is associated with a large directional spread (Fig. 3.18c,d).

Figure 3.19 shows the corresponding two-dimensional spectra. A subtle but important detail of these spectra is that in the WRT results the swell and wind sea spectra have started to become connected due to the nonlinear interactions, whereas in the WAM and WW3 results, the wind sea and swell remain more separated.

3.3.2 Shallow water tests

Shallow water test cases need to address conditions with small relative depths $k_p d$. For $k_p d > 10$, water depths are uniformly deep. For $k_p d > 3$, conditions at the spectral peak are deep water, but some of the longer components of the spectrum will start to feel the bottom. For $k_p d > 1$, most of the spectrum is in weak (four-wave) interactions conditions, whereas for $k_p d < 0.5$, most of the spectrum is in strong (four-wave) interaction conditions (see Part 3).

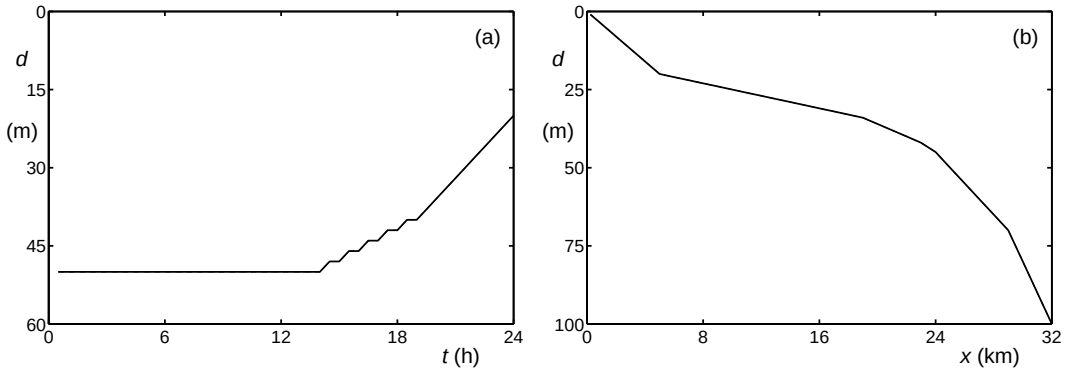

Fig. 3.20 : Water depth (d) for test case test_11 *(panel a) and test cases* test_12 *and* test_13 *(panel b).*

A simple way to generate conditions that are depth limited is to apply the time-limited growth test test_01 in limited water depths. This will result in reduced relative depths $k_p d$, but the smallest relative depth than can be achieved in this way is typically $k_p d \approx 1.0-1.5$. For the purpose of the present study, this is not sufficiently shallow. Smaller relative depths can be achieved by incrementally decreasing the water depth after some initial growth. This reduction needs to be rapid enough to avoid that the model returns to an equilibrium wind sea for that depth. Even then, the model will tend to produce a bimodal sea by growing a new wind sea at higher frequencies. Relative depths that can be attained in this way without generating double peaked spectra are typically $k_p d \approx 0.85$. This describes the general design of depth-limited test test_11. The depths used in this test are shown in Fig. 3.20. The initial water depth $d = 50$ m was chosen to result in $k_p d \approx 10$ for the initial conditions with $f_p = 0.25$ Hz.

Note that, with exception of the nonlinear quadruplet interactions, all depth-limited test cases are run with the default settings of WAVEWATCH III version 3.14. This includes depth-limited breaking (Battjes and Janssen, 1978), but it does note include nonlinear triad interactions. Not modeling a shift of energy to higher frequencies due to triad interactions is beneficial in the present study as it allows for smaller relative depths to evolve.

Figure 3.21 shows the evolution of mean wave parameters for test_11 according to the WRT, WW3 and WAM approaches to the nonlinear interactions. Initially, the WW3 method shows sightly lower wave heights than the WRT method. However, peak frequencies or relative depths are underestimated by the WW3 method. Therefore, the spectra obtained with the WW3 method feel the bottom at a later time than the spectra from the WRT methods. hence, the WW3 method shows higher wave heights later in the integrations. The WAM method again shows systematically lower wave heights at near identical peak frequencies or nondimensional depths $k_p d$. Directional spreads behave similar between

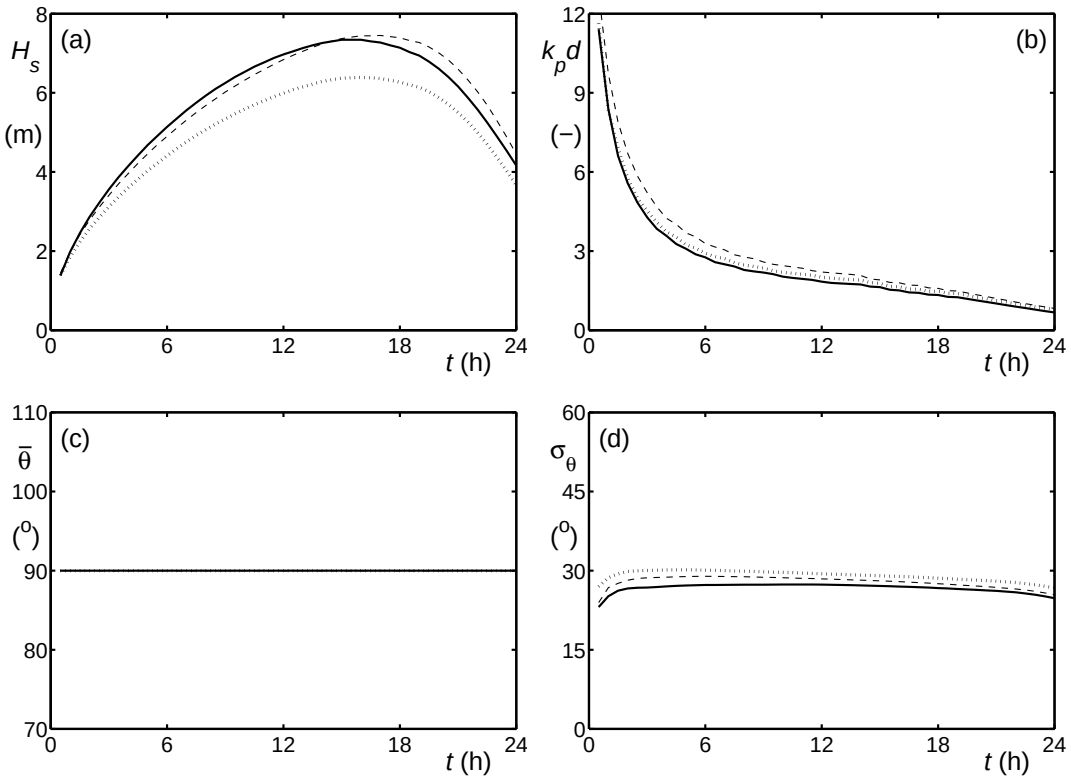

Fig. 3.21 : Evolution in time of a) significant wave height H_s, b) relative depth $k_p d$, c) mean direction $\overline{\theta}$, and d) directional spread σ_θ for the depth- and time-limited growth test test_11. *Solid line: WRT. Dashed line: WW3. Dotted line: WAM. Chain line: wind direction.*

nonlinear approaches as in the deep water tests.

After 12 h of model integration, the relative depth $k_p d \approx 2$, and the spectral shapes are compatible with those of deep water model runs. This is illustrated in Fig. 3.22 (compare to Fig. 3.2). This is not surprising, since the water depth is only moderately limited. After 24 h of model integration, however, the water depth is becoming notably restricted, with $k_p d \approx 0.7$. This does have a distinct impact on the spectral shapes as illustrated in Fig. 3.23. Spectral shapes and the directional spread have changed drastically, and the signature of the nonlinear interactions is significantly broadened in the frequency space.

Reducing the water depth in a quasi-homogeneous model run is somewhat artificial, although it can be representative for a wind wave field riding on a significant tidal wave (e.g., Tolman, 1990, 1991a). A more conventional description of waves in extremely shallow water is found on the beach on lee shores. An idealized description of such a condition is presented in Fig. 3.20b, which is modeled here with the mosaic or multi-grid wave model driver of WAVEWATCH III (Tolman,

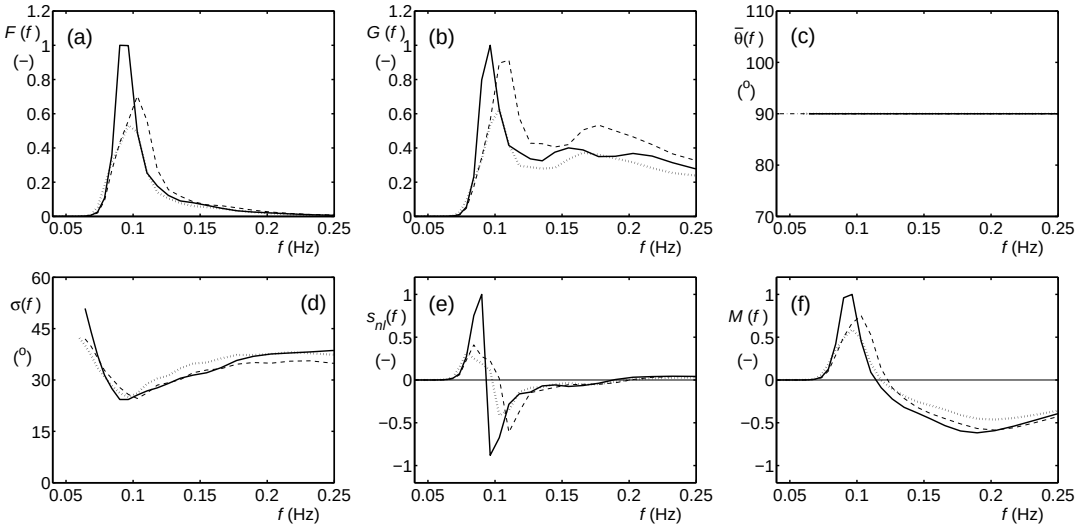

Fig. 3.22 : Like Fig. 3.2 for test_11 *after 12 h of model integration.*

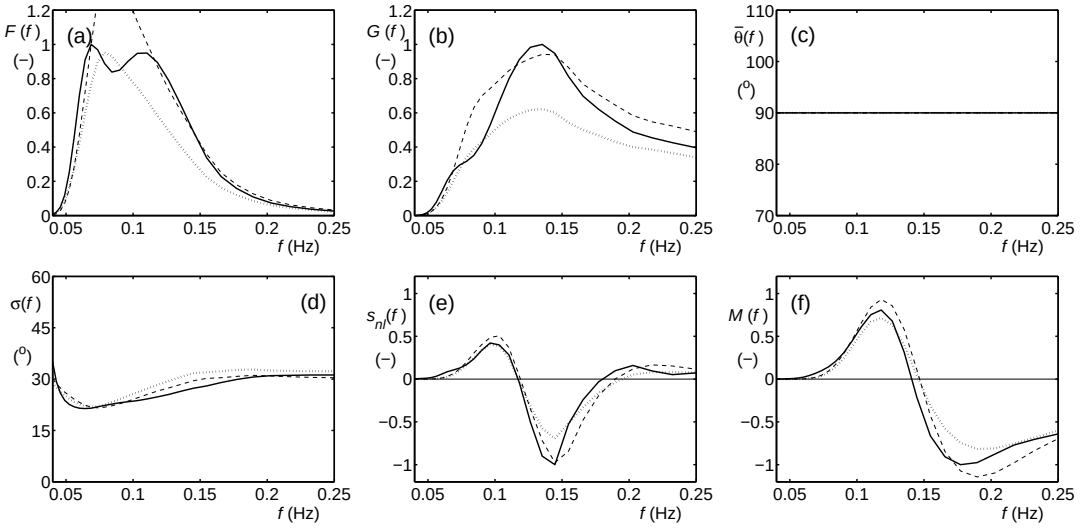

Fig. 3.23 : Like Fig. 3.22 after 24 h of model integration.

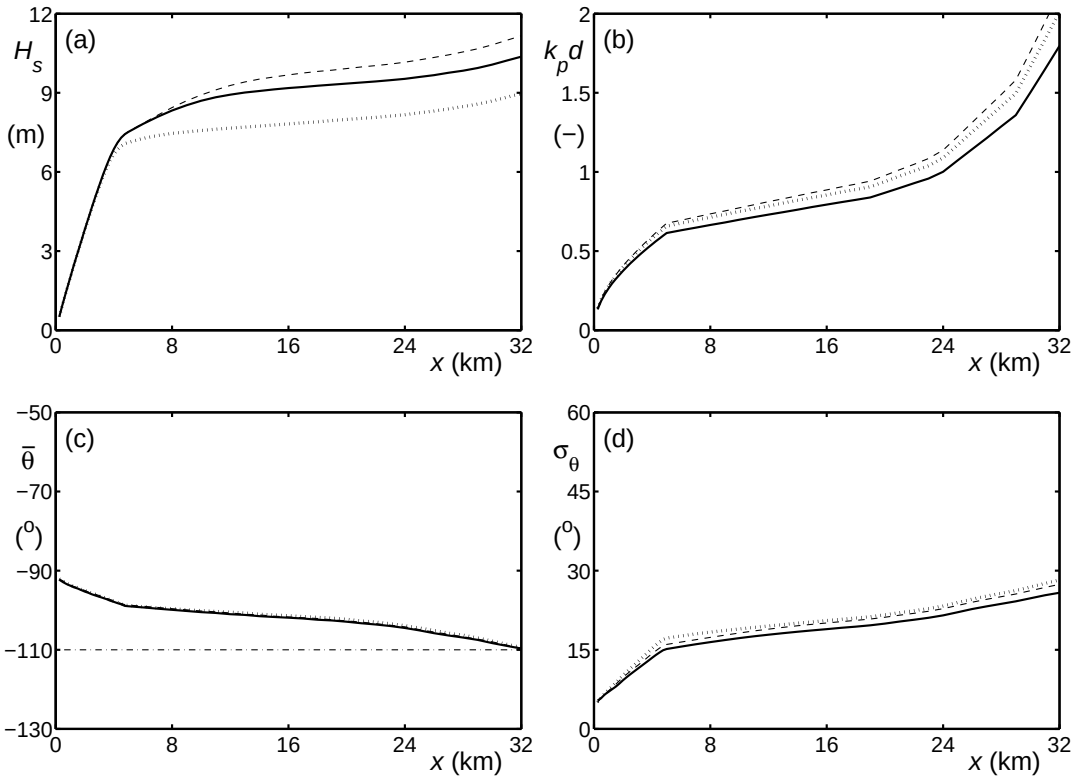

Fig. 3.24 : Evolution in space of a) significant wave height H_s, b) relative depth $k_p d$, c) mean direction $\overline{\theta}$, and d) directional spread σ_θ for the coastal wind sea test test_12. *Solid line: WRT. Dashed line: WW3. Dotted line: WAM. Chain line: wind direction.*

2008a). On the left side of the domain ($x = 0 - 5$ km) a beach exists with a slope of 1:250. This beach is modeled with a first grid with a horizontal resolution of $\Delta x = 250$ m and hence with a depth resolution of $\Delta d = 1$ m. From this grid, 20 output points are generated. For $x = 5 - 32$ km a foreshore model is used with a spatial resolution of $\Delta x = 1$ km. Close to the beach, the bottom slope is 1:1000, on the offshore side, the slope increases to a depth of 100 m at $x = 32$ km. This second grid adds 27 more output grid points with depths increasing up to 100 m. The input boundary point of this nearshore grid is at $x = 33$ km. For a swell case, swell conditions are directly applied at this input point. For a wind sea case, a third grid with quasi-homogeneous conditions is linked in to provide dynamically computed offshore boundary conditions.

Test test_12 is a wind sea case based on the spatial grid of Fig. 3.20b. The wind speed $U_{10} = 20$ ms^{-1} under an angle of 20° with shore normal. The offshore boundary conditions are spun up with a 48 h model run, after which the resulting wind sea spectrum is kept constant. After this, the nearshore grid model is run for 5 hours, and the combined beach and nearshore model is run for an additional

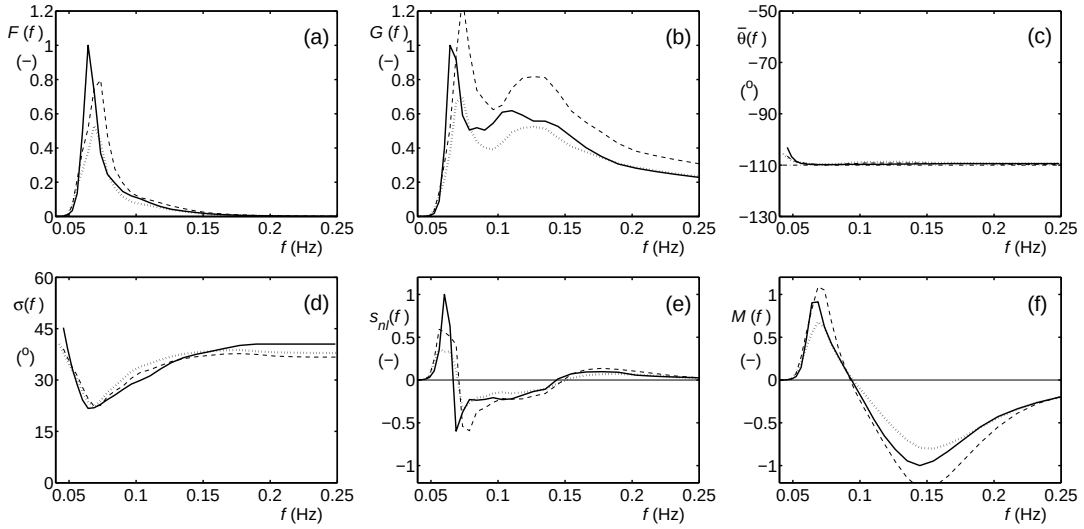

Fig. 3.25 : Like Fig. 3.2 for test_12 *at the offshore model boundary ($x = 33$ km, $d = 100$ m).*

hour. Test spectra for 47 grid points at the end of these runs are used as a quasi-steady solution in the model testing and optimization. Mean wave conditions for these test conditions are presented in Fig. 3.24.

Figure 3.24 shows offshore wave directions lined up with the wind direction, after which refraction turns the waves to shore-normal directions. The peak frequency (not shown here) remains nearly constant at $f_p \approx 0.07$, indicating that wave conditions are mostly determined by the offshore boundary conditions. Correspondingly, the relative depths range from $k_p d \approx 2.0$ at the offshore boundary point to as small as $k_p d < 0.15$ at the shore most grid point. For $x < 4$ km and $d < 15$ m surf zone conditions exist where the wave heights become closely linked to the local water depths. All parameters clearly show a change of wave regime between this surf zone and conditions offshore of this surf zone.

This change of wave regime is also clear in the wave spectra. At the offshore boundary (Fig. 3.25), spectral wave data are very similar to those of the time-limited test test_11. Because the offshore conditions are computed as time-limited wave conditions, this similarity is obviously expected. At the toe of the beach (Fig. 3.26, $x = 5$ km, $d = 20$ m) the wave field is starting to transform into a swell field characteristic as determined mostly by boundary conditions. The spectrum becomes more peaked and loses some of the high-frequency signature. This is somewhat clear in the spectrum $F(f)$, and is obvious in the steepness spectrum $G(f)$. On the coast (Fig. 3.27, $x = 0.25$ km, $d = 1$ m) the transition to swell has been complete. Also, behavior between different nonlinear approaches becomes large. In the WRT approach, interactions have transitioned to the strong interactions in extremely shallow water. This has a distinct spreading impact

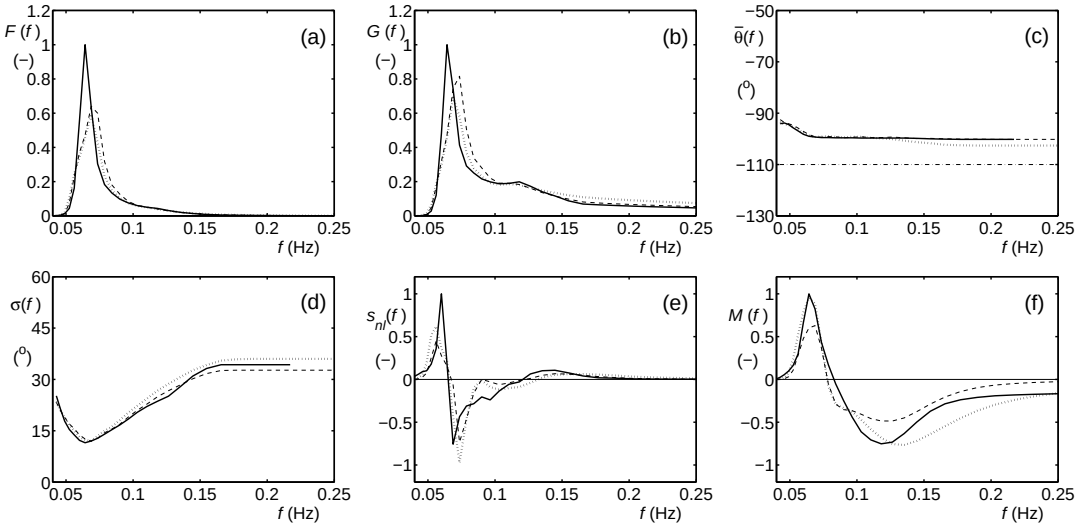

Fig. 3.26 : Like Fig. 3.2 for test_12 *at the toe of the beach ($x = 5$ km, $d = 20$ m).*

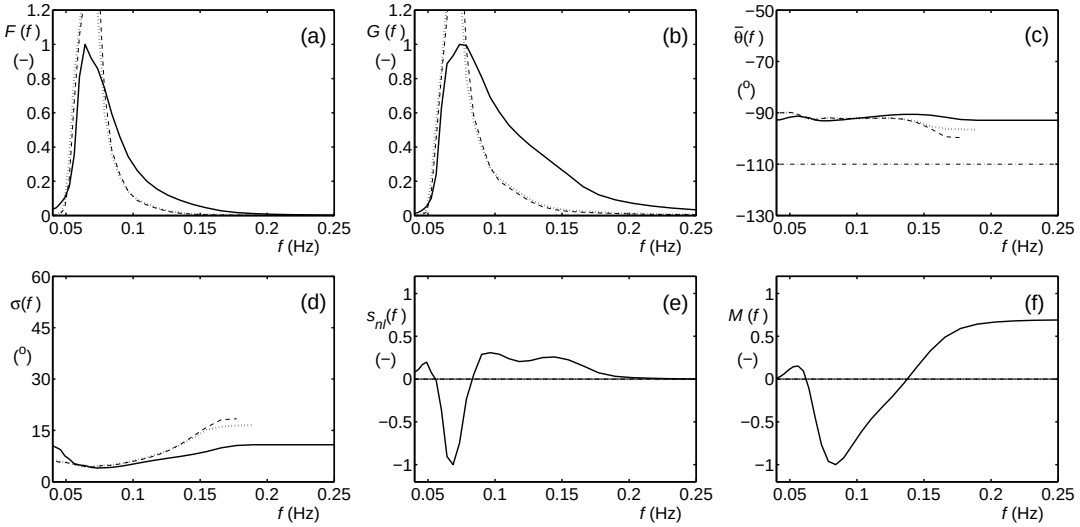

Fig. 3.27 : Like Fig. 3.2 for test_12 *at the shore ($x = 250$ m, $d = 1$ m).*

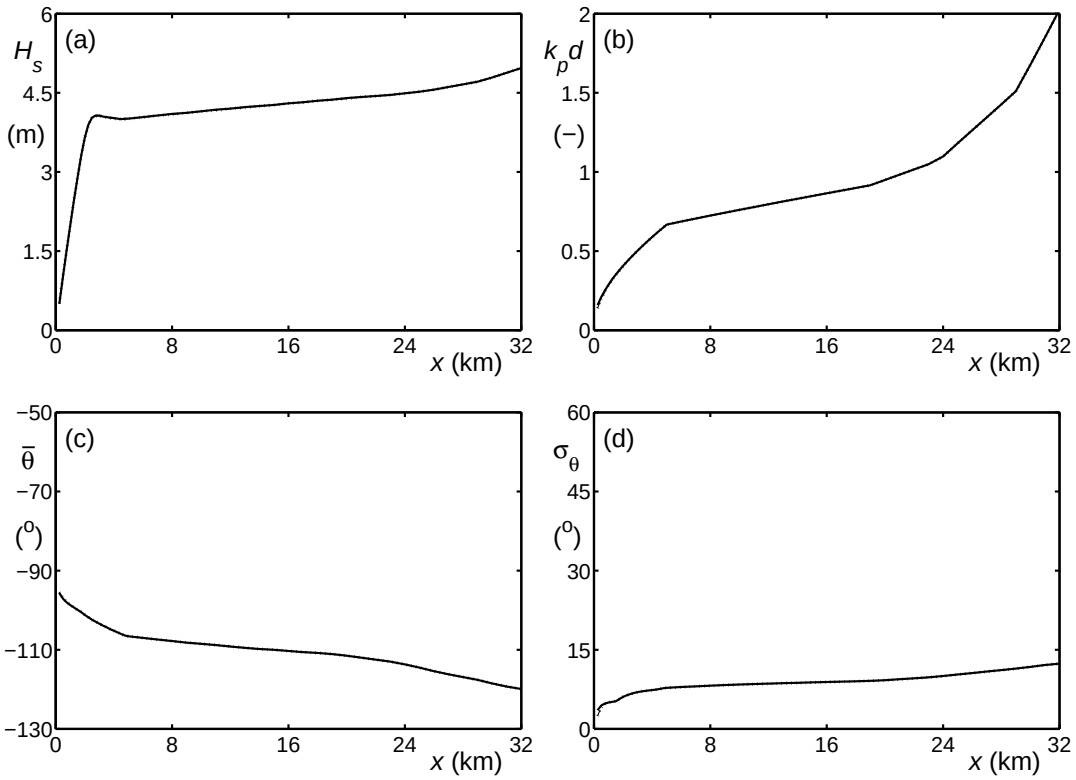

Fig. 3.28 : Like Fig. 3.24 for the swell propagation test test_13.

on the spectra. In the WW3 and WAM approaches the signature of strong interactions is absent (see Part 3, Fig. 3.27e,f), and the swell remains too sharply defined in frequency space (Fig. 3.27a,b).

The final test test_13 is a pure swell case for the idealized beach. The swell peak frequency is set to $f_p = 0.07$ Hz and the wave height at the offshore boundary is set to $H_s = 5$ m. The beach and nearshore grid models are run for one hour only to obtain a stationary solution. Mean wave conditions for these test conditions are presented in Fig. 3.28.

Upon casual inspection, Fig. 3.28 appears to support the general view that swells are not influenced by nonlinear interactions, since all three approaches (WRT, WW3 and WAM) appear to give identical results. Close inspection of the spectral result shows that this is indeed the case for depths $d > 10$ m. At shallower depths, however, the WRT method results in a nonlinear interactions that is orders of magnitude stronger than that of the WW3 and WAM approximations, and that has a significant impact on the spectral shape. this impact is not limited to extremely shallow depths in the last one or two grid points, as is illustrated for the water depth of $d = 5$ m in Fig. 3.29.

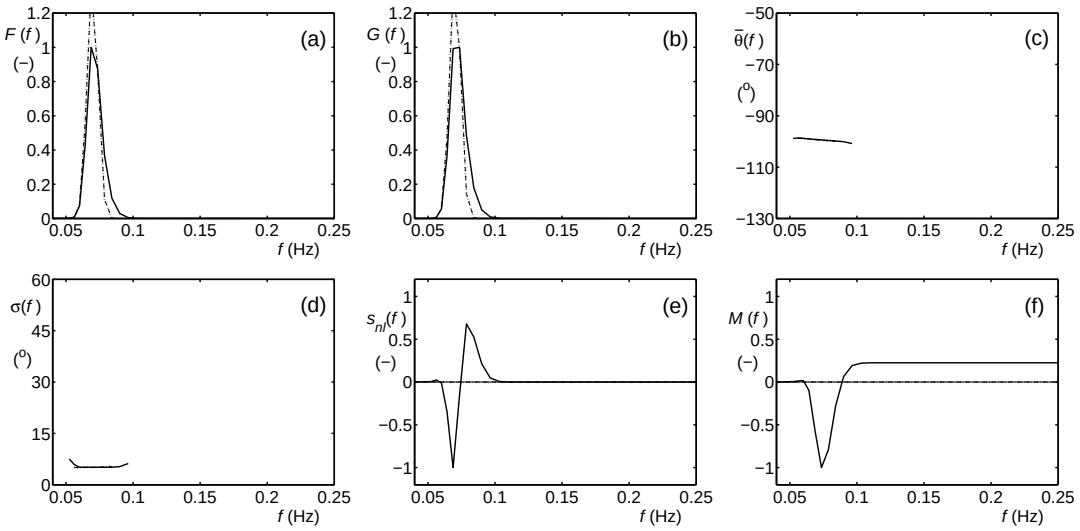

Fig. 3.29 : Like Fig. 3.2 for test_13 *at* $x = 1.25$ *km,* $d = 5$ *m).*

3.4 Metrics

Metrics used in the optimization methods presented here are based on the parameters defined in Section 3.2. To be able to combine individual errors for individual parameters in a single error metric, all errors are normalized, and can hence be expressed as a fraction or a percentage. Furthermore, within test cases, errors for individual locations or times are normalized locally to ensure that errors in all stages of wave development are weighted in a similar way. For instance, the wave height error is addressed locally as

$$\frac{H_{s,p} - H_{s,b}}{H_{s,b}} \quad , \tag{3.13}$$

where the indices p and b represent the results from the parameterization and the baseline (WRT), respectively. This local error can be defined for the N test spectra per test case. The overall wave height error ϵ_H for the test case can then be defined as a conventional rms error

$$\epsilon_H = \sqrt{\frac{1}{N} \sum_N \left(\frac{H_{s,p} - H_{s,b}}{H_{s,b}} \right)^2} \quad . \tag{3.14}$$

Similar errors can be defined for the peak frequency (f_p, ϵ_{fp}), mean direction ($\overline{\theta}$, $\epsilon_{\overline{\theta}}$), and directional spread (σ_θ, $\epsilon_{\overline{\sigma}}$)

$$\epsilon_{fp} = \sqrt{\frac{1}{N} \sum_N \left(\frac{f_{p,p} - f_{p,b}}{f_{p,b}} \right)^2} \quad , \tag{3.15}$$

$$\epsilon_{\overline{\theta}} = \sqrt{\frac{1}{N}\sum_{N}\left(\frac{\overline{\theta}_p - \overline{\theta}_b}{\Delta\theta_n}\right)^2} \quad , \tag{3.16}$$

$$\epsilon_{\overline{\sigma}} = \sqrt{\frac{1}{N}\sum_{N}\left(\frac{\sigma_{\theta,p} - \sigma_{\theta,b}}{\sigma_{\theta,b}}\right)^2} \quad . \tag{3.17}$$

Note that there is no natural normalization for the mean direction error. Instead a normalization angle $\Delta\theta_n$ needs to be defined. Somewhat arbitrarily $\Delta\theta_n = 90°$ is chosen here. These errors can be defined for the entire spectrum of for separate spectral partitions (i.e., wind sea and swell). In the latter case, N represents the number of output points for the test for which the parameter can be defined. If the parameter is defined for the base case only, the corresponding local normalized error cf. Eq. (3.13) is set to ± 1. Similar errors are defined for the high-frequency energy level (α, ϵ_α) and the nonlinear zero-frequency (f_0, ϵ_{f0})

$$\epsilon_\alpha = \sqrt{\frac{1}{N}\sum_{N}\left(\frac{\alpha_p - \alpha_b}{\alpha_b}\right)^2} \quad , \tag{3.18}$$

$$\epsilon_{f0} = \sqrt{\frac{1}{N}\sum_{N}\left(\frac{f_{0,p} - f_{0,b}}{f_{0,b}}\right)^2} \quad . \tag{3.19}$$

Unlike the previous errors, the latter two errors are not relevant for spectral partitions. Finally, Section 3.2 identifies the energy level and the functional shape of the spectrum at intermediate high frequencies as a potential metric to be used. Considering that such parameters correspond to the expectation that the steepness spectrum $G(f)$ is nearly constant in this range, a simple error measure to address this is the direct comparison of steepness spectra in this frequency range

$$\epsilon_\beta = \frac{1}{N}\sum_{N}\frac{\sqrt{\int_{1.5f_p}^{3.0f_p}\left[G_p(f) - G_b(f)\right]^2 df}}{\int_{1.5f_p}^{3.0f_p} G_b(f)\, df} \quad , \tag{3.20}$$

where the integration bounds represent the part of the spectrum to be considered. This type of error measure is also applicable to the one-dimensional spectral parameters, particularly the spectrum ($F(f)$, ϵ_{F1}), steepness spectrum ($G(f)$, ϵ_{G1}), and the source term ($s_{nl}(f)$, ϵ_{nl1})

$$\epsilon_{F1} = \frac{1}{N}\sum_{N}\frac{\sqrt{\int_{0}^{f_2}\left[F_p(f) - F_b(f)\right]^2 df}}{\int_{0}^{f_2} F_b(f)\, df} \quad , \tag{3.21}$$

$$\epsilon_{G1} = \frac{1}{N} \sum_{N} \frac{\sqrt{\int_0^{f_2} \left[G_p(f) - G_b(f)\right]^2 df}}{\int_0^{f_2} G_b(f)\, df} \quad , \tag{3.22}$$

$$\epsilon_{nl1} = \frac{1}{N} \sum_{N} \sqrt{\frac{\int_0^{f_2} \left[s_{nl,p}(f) - s_{nl,b}(f)\right]^2 df}{\int_0^{f_2} s_{nl,b}^2(f)\, df}} \quad . \tag{3.23}$$

The upper integration bound f_2 is explicitly defined to ensure that errors in the parametric tail, which for $F(f)$ are constant, do not dominate the error measure, and that the integration range does not influence the results (as for a steepness measure). Considering this, f_2 should be linked to the transition from the prognostic part of the spectrum to the parametric tail. To allow for part of the tail to be in the integration range, $f_2 = 3.5 f_p$ is chosen, where f_p is taken from the wind sea partition of the spectrum. The error measures for the spectral direction and spread ($\theta(f)$, ϵ_θ and $\sigma(\theta)$, ϵ_σ) can be defined similarly as

$$\epsilon_\theta = \frac{1}{N} \sum_{N} \frac{\sqrt{\int_{f_1}^{f_2} \left[\theta_p(f) - \theta_b(f)\right]^2 df}}{\Delta\theta_n (f_2 - f_1)} \quad , \tag{3.24}$$

$$\epsilon_\sigma = \frac{1}{N} \sum_{N} \frac{\sqrt{\int_{f_1}^{f_2} \left[\sigma_p(f) - \sigma_b(f)\right]^2 df}}{\sigma_{\theta,1,2} (f_2 - f_1)} \quad , \tag{3.25}$$

where the directional error is normalized as in Eq. (3.16), and the spread is normalized with the mean directional spread over the integration range from Eq. (3.7). These directional parameters are defined even for spectral frequencies with virtually no energy. To ensure that the error measure focuses on a spectral range with energy, f_1 and f_2 are chosen to include frequencies only for which $F(f) > 0.001 F_{\max}$, where $F_{\max}$ is the maximum energy of the corresponding spectrum. Furthermore, these last two error measures do not address density functions. Therefore, the integral needs to be divided by the frequency range of integration to obtain a proper error measure.

Finally, the two-dimensional spectral and source term errors are defined as

$$\epsilon_{F2} = \frac{1}{N} \sum_{N} \frac{\sqrt{\int_0^{2\pi} \int_0^{f_2} \left[F_p(f,\theta) - F_b(f,\theta)\right]^2 df\, d\theta}}{\int_0^{2\pi} \int_0^{f_2} F_b(f,\theta)\, df\, d\theta} \quad , \tag{3.26}$$

$$\epsilon_{G2} = \frac{1}{N} \sum_{N} \frac{\sqrt{\int_0^{2\pi} \int_0^{f_2} \left[G_p(f,\theta) - G_b(f,\theta)\right]^2 df\, d\theta}}{\int_0^{2\pi} \int_0^{f_2} G_b(f,\theta)\, df\, d\theta} \quad , \tag{3.27}$$

$$\epsilon_{nl2} = \frac{1}{N} \sum_{N} \sqrt{\frac{\int_0^{2\pi} \int_0^{f_2} \left[s_{nl,p}(f,\theta) - s_{nl,b}(f,\theta) \right]^2 df \, d\theta}{\int_0^{2\pi} \int_0^{f_2} s_{nl,b}^2(f,\theta) \, df \, d\theta}} \quad . \tag{3.28}$$

with f_2 defined as with the corresponding one-dimensional spectral error measures. This only leaves the model run time as a possible metric. There are two main components to the run time. The first is the intrinsic cost of running the parameterization, which is directly related to the complexity of the MDIA. The second is related to the dynamic time step allowed by the parameterization. The first impact of the time step is implicitly assumed in the complexity of the parameterization to be optimized. This run time will be used after optimization to address the economic impact and justification for using more complex parameterizations. The second contribution to the run time can be used to indirectly address the stability of the model integration, and will be used only to effectively filter out poorly performing parameter choices.

Equations (3.14) through (3.28) provide fifteen individual error measures (up from the five used in Part 2). Note that even more error measure are actually used if the error measures based on mean parameters are applied to individual wave fields. For each individual test case, these errors are combined into a single error measure

$$\epsilon_{nn} = \sum \epsilon_p a_p / \sum a_p \quad , \tag{3.29}$$

where nn represents the number of the test from Section 3.3, ϵ_p represents the above fifteen error measures, and a_p represent corresponding weights. Finally, the total error metric for all test cases is computed as

$$\epsilon_{\text{tot}} = \sum \epsilon_{nn} b_{nn} / \sum b_{nn} \quad , \tag{3.30}$$

where b_{nn} are the corresponding relative weights.

With errors and error metrics defined, it is essential to understand which kind of errors to expect, to properly set weights factors in Eqs. (3.29) and (3.30). Tables 3.1 and 3.2 show the individual error measures for the WW3 and WAM approaches relative to the exact WRT approach for all nine test cases.

For both the WW3 and WAM approaches, mean errors including ϵ_α and ϵ_{f0} are generally in the 10% range or smaller, with the expception of ϵ_α for the WW3 approach. The WW3 approach results in more accurate wave heights H_s, whereas the WAM approach results in more accurate peak frequencies f_p and high-frequency energy levels α. For both approaches one- and two-dimensional spectral error measures are much larger and generally in the 100% range. Particularly the spectral error measure increase for the shallow water tests. Note that

*Table 3.1: Individual parameter errors in percent of the DIA using the WAM model settings relative to the exact (WRT) approach for all test cases. Two values for the first four error measures indicate errors for wind sea and swell separately (*test_06*). Note that some of the error measures have no meaning for the swell case* test_13*.*

	test case								
	01	02	03	04	05	06	11	12	13
ϵ_H	15.4	13.9	9.1	8.9	11.7	16.1 5.5	12.6	10.5	0.4
ϵ_{fp}	5.4	6.0	2.1	2.8	5.1	5.8 0.8	6.2	6.2	2.0
$\epsilon_{\overline{\theta}}$	0.0	0.0	2.3	3.6	4.1	0.1 1.6	0.0	0.5	0.1
$\epsilon_{\overline{\sigma}}$	11.4	13.1	10.8	10.5	19.8	11.0 21.1	9.1	9.8	4.5
ϵ_α	9.4	6.4	15.9	17.1	9.1	10.0	11.4	5.0	—
ϵ_{f0}	2.0	3.3	4.1	7.0	5.0	2.5	3.7	9.1	—
ϵ_β	70.0	61.0	60.6	62.8	64.2	70.8	66.2	83.3	—
ϵ_{F1}	151.	146.	117.	119.	115.	145.	130.	152.	82.0
ϵ_{G1}	80.3	76.1	63.5	64.5	62.9	81.1	73.9	108.	79.6
ϵ_{nl1}	87.8	89.7	81.8	83.5	65.0	88.5	82.0	93.6	99.5
ϵ_θ	0.1	18.1	18.1	25.8	34.0	26.3	0.0	17.0	10.8
ϵ_σ	46.3	40.7	45.9	48.5	56.0	43.4	41.3	50.9	74.7
ϵ_{F2}	138.	133.	109.	116.	133.	132.	118.	163.	112.
ϵ_{G2}	59.5	58.0	56.5	58.7	60.2	60.0	56.3	105.	107.
ϵ_{nl2}	87.5	89.3	81.6	82.2	74.6	88.2	81.1	96.3	99.5

even for the shallow water swell test, where most of the errors are concentrated in the 5 to 10 grid points close to the coast, these errors are large.

The 136 error measures presented in Tables 3.1 and 3.2 are combined into errors per test case using Eq. (3.29). The corresponding weights are presented in Table 3.3. As discussed in Part 2, it is preferable to ensure that bulk parameters such as the wave height H_s are well described. This can be achieved by assigning large relative weights to the corresponding error measures. Somewhat arbitrarily, this has lead to the error measures as indicated for the first test case (test_01). Note that these error measures can be refined later, to focus the optimization on selected features of the model integration. This will be considered outside the scope of the present study.

The error weights for test_01 can be applied to all other test cases with two

Table 3.2: Like table 3.1 for WW3 settings of the DIA.

	test case								
	01	02	03	04	05	06	11	12	13
ϵ_H	3.3	1.9	2.0	3.9	3.6	4.6 14.5	4.4	4.3	0.4
ϵ_{fp}	11.3	10.8	8.4	9.1	10.3	11.8 1.1	11.8	9.1	2.0
$\epsilon_{\overline{\theta}}$	0.0	0.0	3.4	6.8	4.3	0.1 2.2	0.0	0.3	0.1
$\epsilon_{\overline{\sigma}}$	6.8	8.3	5.7	5.2	13.7	6.3 22.3	4.5	5.6	4.6
ϵ_α	24.6	29.9	16.4	19.1	26.9	24.0	25.4	31.7	—
ϵ_{f0}	5.3	5.9	3.1	6.5	4.4	6.1	6.0	7.9	—
ϵ_β	83.5	79.2	66.2	67.3	78.7	82.7	77.3	84.6	—
ϵ_{F1}	156.	151.	121.	129.	114.	150.	141.	157.	82.1
ϵ_{G1}	93.0	90.9	71.5	75.0	74.8	93.6	87.8	121.	79.7
ϵ_{nl1}	94.4	95.7	88.7	92.6	72.3	94.8	90.22	95.5	99.8
ϵ_θ	0.1	14.1	18.5	28.1	30.6	24.8	0.0	14.2	10.6
ϵ_σ	43.3	40.3	33.8	34.1	40.5	41.8	42.4	49.2	75.9
ϵ_{F2}	144.	138.	114.	129.	130.	139.	128.	168.	113.
ϵ_{G2}	66.1	67.7	57.5	58.2	59.6	66.3	65.5	114.	107.
ϵ_{nl2}	95.5	96.2	89.6	91.9	80.5	96.0	90.4	98.4	99.8

exceptions. First, in test_06 separate weights need to be assigned to mean parameters for wind sea and swell. To obtain a similar error balance as in the other tests, these are set to half the corresponding values for tests with a single wave field. Second, test_13 deals with swell only. Three parameters are irrelevant in this case, and hence the error weights for these measures are set to 0. Furthermore, errors occur almost exclusively in the spectral space in this test case. Hence, the overall error is computed without taking into account the error measures for mean wave parameters,

Resulting mean error measures for all 9 test cases are presented in Table 3.4. Error measures for all tests are comparable, with the exception of those for test_13. The latter could be expected due to the rather different weighting of individual errors in this test. In computing the overall total error measure in Eq. (3.30), all tests considered will be weighted equally with the exception of test_13. The latter test will be weighted at 30% compared to all other tests, to avoid artificial dominance of this test in the overall error measure.

Table 3.3: Error weights in Eq. (3.29) as used in the optimization procedure for all nine test cases.

	test case								
	01	02	03	04	05	06	11	12	13
ϵ_H	10	10	10	10	10	5 5	10	10	0
ϵ_{fp}	5	5	5	5	5	2.5 2.5	5	5	0
$\epsilon_{\overline{\theta}}$	5	5	5	5	5	2.5 2.5	5	5	0
$\epsilon_{\overline{\sigma}}$	5	5	5	5	5	2.5 2.5	5	5	0
ϵ_α	5	5	5	5	5	5	5	5	0
ϵ_{f0}	3	3	3	3	3	3	3	3	0
ϵ_β	3	3	3	3	3	3	3	3	0
ϵ_{F1}	1	1	1	1	1	1	1	1	1
ϵ_{G1}	1	1	1	1	1	1	1	1	1
ϵ_{nl1}	1	1	1	1	1	1	1	1	1
ϵ_θ	1	1	1	1	1	1	1	1	1
ϵ_σ	1	1	1	1	1	1	1	1	1
ϵ_{F2}	1	1	1	1	1	1	1	1	1
ϵ_{G2}	1	1	1	1	1	1	1	1	1
ϵ_{nl2}	1	1	1	1	1	1	1	1	1

Table 3.4: Overall errors in % for each test case based on the error in Tables 3.1 and 3.2 and the error weights in Table 3.3.

	test case								
	01	02	03	04	05	06	11	12	13
WAM	26.2	25.2	23.1	24.2	25.4	26.2	23.9	29.0	83.2
WW3	27.4	27.6	22.6	25.0	26.4	29.8	26.1	31.2	83.5

3.5 Parameter optimization

3.5.1 General considerations

.

The main goal of the present study is to objectively optimize the parameters of several GMD configurations. For a GMD with a small number of free parameters, this can be done by brute force mapping of model errors in parameter space. This was done for a simple DIA with one representative quadruplet defined by one parameter in Part 2. However, even for simple MDIA with two representative quadruplets, brute force error mapping already becomes prohibitively expensive (Part 2). Alternatively, (local) search algorithms can be employed to find error minima in parameter space. A popular search method is the steepest descent method, where the search pattern attempts to follow the steepest gradients of the errors in parameter space. Such a requires that the error gradients are well behaved (i.e., differentiable), and that there are well defined global minima. The brute force mapping in Part 2 has shown that neither is the case for parameter optimization in an MDIA. Hence, (local) steepest descent optimization can at best be used here to refine a search once a near-optimum solution has been found. Th presence of many local error minima in parameter space requires an efficient global search algorithm such as multi-start descent algorithms, (directed) random search or genetic algorithms.

In Part 2, genetic optimization techniques have been used successfully to optimize MDIAs. A general description of such techniques can be found in Eiben and Smith (2003). Genetic algorithms are loosely based on principles of natural selection, and can be interpreted as directed random search. In Part 2, the genetic optimization procedure was combined with a steepest descent method to improve final convergence of the search algorithm, and test were performed to check the sensitivity of the error to the final parameter settings. By and large, the steepest descent method resulted in marginally better model errors, and sensitivities to rounding off of parameter values were found to be minor. Nevertheless, descent methods can be supplemental to genetic search, as they can indicate the level of (local) convergence reached by the genetic search, and because they are generally more effective in terms of final convergence. In Part 2 a relatively simple and traditional genetic search algorithm was used. In the present study, the algorithms have been refined further, as will be discussed in the following sections.

Genetic algorithms form a subset of what is generally identified as Evolutionary Computing (e.g., Eiben and Smith, 2003). In such methods, populations are described with the genome of individuals. Individuals in the population generate offspring using rules loosely based on natural reproduction, and the population retains only the most successful members, loosely following ideas of natural selection (see Fig. 3.30). The description of a single member of the population will be

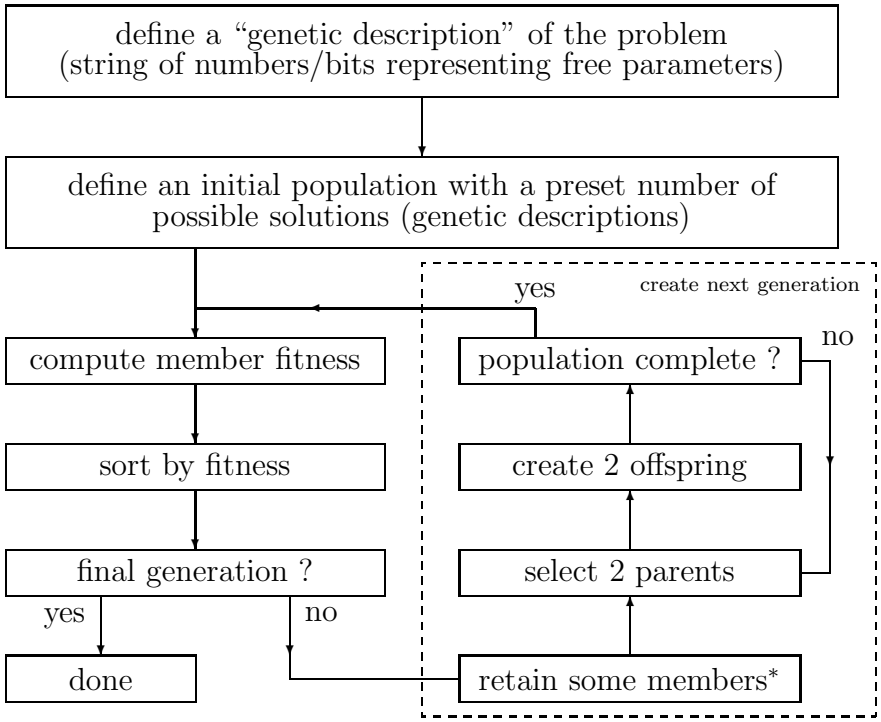

Fig. 3.30 : General layout of a genetic search algorithm (: optional).*

discussed in Section 3.5.2. Section 3.5.3 describes the construction of the initial population, and Section 3.5.4 describes the evolution of consecutive populations.

3.5.2 Describing the genome

The description of individual members of a population contains two elements. First, the problem considered needs to be described adequately. Second, each member of the population needs to be evaluated to obtain a fitness or score, to be used to rank the members of a population, and to be used in procreation.

The basic elements of the description of a member of the population are the free parameters in the GMD. Possibly added to this are free parameters in the high-frequency S_{nl}-based filter. Additional parameters ordering and defining GMD layouts related to optimization strategies can also be added (see Section 4).

In Part 2, the free parameters of the MDIA were represented by a bit string, following traditional concepts of Genetic Optimization (e.g., Holland, 1992). The description of real-valued parameters by integer numbers or bits implies a build-in accuracy or round-off of parameter values. For real-valued parameter optimizations as considered here, it is more natural to describe members of the population with real numbers.

Table 3.5: Basic description of members of a population. i_g is the sequence number of the parameter in the description. n_q is the number of representative quadruplets and i_q is the quadruplet number. Accuracy refers to fixed format description of parameter in data files. Note that $\Delta\theta < 0°$ is used to identify (one- or) two parameter quadruplet definitions. std and β refer to perturbation mutation in Table 3.6

i_g	Par.	Eq. / Table	range	acc.	type	std
$5(i_q-1)+1$	λ	(2.18)/2.1	0-0.5	0.001	lin	$0.25\,\beta$
$5(i_q-1)+2$	μ	(2.18)/2.1	0-0.5	0.001	lin	$0.25\,\beta$
$5(i_q-1)+3$	$\Delta\theta$	(2.18)/2.1	0-90°	0.1°	lin	$45°\,\beta$
$5(i_q-1)+4$	C_d	(2.30)	10^5-10^{10}	3 digit	exp	βC_d
$5(i_q-1)+5$	C_s	(2.30)	10^4-10^9	3 digit	exp	βC_s
$5n_q+1$	m	(2.31)	0-8	0.01	lin	$4.\,\beta$
$5n_q+2$	n	(2.32)	(-6) - 2	0.01	lin	$4.\,\beta$

An elementary description of a member of the population includes the five free parameters per representative quadruplet and two additional scaling parameters in Eqs. (2.18) through (2.32) and in Table 2.1. In principle, the two scaling parameters can be defined for each representative quadruplet separately, but somewhat arbitrarily, m and n will be kept the same here for all quadruplets. With n_q representative quadruplets, this results in $n_g = 5n_q+2$ numbers describing a member of the population. The definition of the sequence of real numbers describing a member of the population is given in Table 3.5.

In any computer description of real numbers, a round-off or accuracy error exists due to the binary description of all numbers. Here, the population information is stored in human-readable formated data files (for practical reasons). This effectively creates an accuracy at which the parameters are described, as is documented in Table 3.5.

To finalize the description of a member of the population, a fitness value needs to be defined. As in Part 2, the fitness ζ is defined as the inverse of the total error of Eq. (3.30)

$$\zeta = \frac{1}{\epsilon_{\text{tot}}} \quad . \tag{3.31}$$

Two additional remarks need to be made on the definition of the genome. First, not all five quadruplet parameters will be considered in each optimization experiment. Therefore, a mask is added to the the genome description identifying which element i_q of each member of the population is to be optimized dynamically. With this mask, default values for each i_g are also given. Second, following

Part 2, acceptable relations between λ, μ and $\Delta\theta$ are enforced explicitly in the generation of the initial and subsequent generations. Combinations of λ, μ and $\Delta\theta$ for which the deep water resonance conditions cannot be satisfied are not allowed in the population. Before being applied to the wave model λ and μ are interchanged to ensure that $\mu < \lambda$ in the wave model, and $\Delta\theta$ is modified accordingly to leave the deep water quadruplet layout unchanged. This ensures that in the wave model all quadruplets are valid without unduly restricting diversity in the population (e.g., Eiben and Smith, 2003)

3.5.3 Initial population

The initial population is generated by a simple random initialization. For λ, μ and $\Delta\theta$ direct physical limitations of the parameter settings are available, and for the initial population, values for each member are set randomly assuming a uniform distribution of values in the valid range of the parameter. The ranges used in the optimization are presented in Table 3.5, and were determined as part of the optimization process. Note that for the three-parameter definition of the quadruplet not all combinations $(\lambda, \mu, \Delta\theta)$ result in a valid quadruplet. Invalid quadruplets resulting from random initialization are not added to the initial population.

Values for C_d and C_s are not naturally bounded. The valid range here is set subjectively, based on the initial experiments from Section 4. After each individual optimization, the accepted range is checked against optimum values found in the optimization. Optimum values close to the extrema are considered to indicate a poor choice of the parameter range. Because large ranges of parameters are considered here, either linear of exponential distributions are considered. In the first case a uniform distribution is assumed, in the second a uniform distribution of $\log(C_d)$ and $\log(C_s)$ are assumed.

The scaling parameter m is naturally bounded as derived in Part 3[4]. The scaling parameter n is not, and bounds as presented in Table 3.5 are based on practical experience from Part 2 and from experiments described in Section 4.

3.5.4 Subsequent populations

Generating the next generation involves several activities; generation of children from parents by mutation and recombination, parent selection, population models and survivor selection.

Mutation and recombination are needed to create offspring that differs from the parents. In the traditional Genetic Algorithm approach mutation corresponds to random switching of selected bits in a child after the child is defined from the genetic material of the parent, whereas recombination takes part of the genetic

[4] Note that a wider range of values was deemed necessary in subsequent sections.

description of the child from each parent, using a crossover process consistent with biological genetic recombination. Using a bit string to describe the 'genetic material' of parent and child, the implementation of these processes is fairly unambiguous. Describing this genetic material with a set of real numbers somewhat complicates the definition of recombination and mutation.

In the process of recombination, a crossover point is determined. Left of this crossover point information from one parent is obtained by the child. Right of the crossover point, the child receives information from the other parent. When this procedure is performed for a bit string representation of the parent and the child, the crossover point will often appear inside the bit string describing a single parameter. Consequent, this parameter in the child will be different from the parameter value in each parent, whereas all other parameter values are directly inherited from one of the two parents. With a real valued description of the parameters in the parents, the simplest approach (denoted as simple recombination in Eiben and Smith, 2003, section 3.5.3), all parameter values are directly taken from one of the two parents, depending on the position of the parameter relative to a randomly chosen crossover point. This process ignores modification of the parameter at the crossover point. Another process denoted as single arithmetic recombination describes this second process by taking a single parameter in the child, and defining it as a weighted average of the parameter values of the two parents. Defining the parents as x and y, the child as c, and the index i representing the crossover parameter value index, the parameter value of the first child is determined as

$$c_i = \alpha x_i + (1 - \alpha) y_i \quad , \tag{3.32}$$

and the parameter value for the second child is obtained by exchanging x and y. Note that for $\alpha \in [0, 1]$ this always represents a smoothing operator that reduces the genetic diversity of the population. In previous studies random values for α have been used, but due to the general smoothing nature of Eq. (3.32) many studies simply use $\alpha = 0.5$.

In the present study, simple recombination is used with 0, 1 or 2 crossover points, and with simple recombination or single arithmetic recombination left or right of the crossover point with randomly selected α. This procedure is designed to closely follow the successful bit string recombination of Part 2. The corresponding parameter values used in the final optimization experiments are gathered in Table 3.6.

In traditional mutation, each individual bit describing a parameter can be changed in value. This effectively means that mutation can reset the parameter value anywhere in its predefined valid range. For real numbers, a simple way to duplicate this process it to reinitialize the parameter values consistent with the way in which it was defined in the initial population (denoted as uniform mutation in Eiben and Smith, 2003, section 3.4.3). The real value description

Table 3.6: Parameters used in the generation of children from parents in the genetic optimization procedure. See Table 3.5 for computation of std from β in perturbation mutation from spread parameter.

Fraction of old population retained	0.20
Error factor for parent selection (γ)	2.00
Minimum parent fraction	0.25
Maximum parent fraction	0.50
Probability of 0 crossovers	0.50
Probability of 1 crossover	0.25
Probability of 2 crossovers	0.25
Probability of arithmetic recombination	0.50
Expected number of mutations	1.25
Probability of uniform mutation (otherwise perturbation mutation)	0.30
Spread parameter in perturbation (β)	0.10

of parameter used here makes it simple to alternatively perturb the parameter values slightly, typically by using a normal distribution with a small predefined standard deviation. This represents a localized random search, or, in case of integer representation of members of a population, it is also identified as creep mutation.

In the present study, the expected number of mutations is predefined. The probability of mutation for each individual parameter is defined as this expectation divided by the number of parameters to be optimized. For each parameter to be mutated, a predefined fraction will undergo uniform mutation, and the remainder will undergo a perturbation mutation. As an additional mutation option mutation is allowed to switch off selected parameters in the GMD definition. μ and $\Delta\theta$ are allowed to be switched off so that a three-parameter quadruplet definition can degenerate to a simpler definition. C_d and C_s are allowed to switch off to use deep or shallow scaling only. If the parameter is subsequently switched back on by mutation, uniform mutation is automatically used. The corresponding parameter values used in the bulk of the optimization experiments are gathered in Tables 3.6 and 3.5.

Two general population models can be used (Eiben and Smith, 2003, section 3.6). The first is the 'generational model', where for each next generation, all parents are replaced by their children. The second is a 'steady state' model where a fraction of the population is replaced by offspring.

Closely related to the population model is the survivor selection scheme used. This can be either age-based, fitness based or a combination of both (Eiben

and Smith, 2003, section 8.8). In Part 2, a scheme was used where the best members of the population were retained, but where identical solutions were not permitted in the population (steady state population model). In the present study this successful approach is used again. With the real number description of parameters, this requires the definition of a tolerance to identify identical solutions. This tolerance is set as typically twice the parameter accuracy in Table 3.5. Note that by stetting the fraction of the population that is to be retained to 0, this will revert to a generational population model.

This leaves only the parent selection scheme to be defined. The selection of parents allowed to produce offspring is (as in Part 2) defined as a fraction of the total population. Here, the group of parents allowed to reproduce is defined by their error

$$\epsilon \leq \gamma \epsilon_{\min} \quad , \tag{3.33}$$

where $\epsilon_{\min}$ is the error of the fittest member of the population. This results in a fraction of the population that is allowed to become parent. This fraction is furthermore limited by a minimum and a maximum fraction of the population. After this fraction is established, a limiting fitness ($\zeta_{\lim}$) according to Eq. (3.31) is defined as the fitness of the fittest member of the population that is not allowed to become a parent, or, if l members of a ranked population are allowed to have offspring, $\zeta_{\lim} = \zeta_{l+1}$. The probability p_i of each parent with index $i \leq l$ to be chosen as a parent is then defined as

$$p_i = (\zeta_i - \zeta_{\lim}) \left(\sum_{i=1}^{l} \zeta_i - \zeta_{\lim} \right)^{-1} \quad , \tag{3.34}$$

with indices i for parents determined by a straightforward random selection. Parameter settings for this procedure are largely taken from Part 2, and are presented in Table 3.6. From each set of parents two offspring are created by first applying crossover recombination and subsequently applying mutation. Only those children that do not represent (near-) duplicates of already accepted members of the population are added to the population.

3.5.5 Descent methods

In Part 2, steepest descent methods were used in combination with the genetic optimization procedures. Whereas such procedures are not suitable to search for optimal nonlinear parameterizations due to the behavior of the errors in parameter space (local minima and semi-discontinuous behavior, see Part 2), this method is nevertheless useful to complement genetic optimization by checking the level of convergence for high-scoring members of the population in the genetic optimization procedure. In selected experiments, this has lead to significant

reduction in the optimum error of the optimum GMD configuration, as will be shown in the following section. With the modular elements used in the genetic optimization package described in Tolman (2010), it is relatively simple to construct a steepest descent search method starting from members of populations. The steepest descent method used here has the following basic elements.

1) Perturb each parameter to be optimized both positively and negatively to estimate the partial derivative of the model error with respect to the parameter to be optimized.

2) Gather the partial derivatives (or discrete error changes for the parameter perturbations) with a positive impact on the model error into a vector, and normalize this vector with its norm.

3) Use the normalized vector as the search direction in parameter space and evaluate the model errors for a discrete set of parameter settings along this line (Note: because the optimization packages heavily uses parallelization of computations on a cluster, a discrete set of parameter realizations is used instead of a dynamic search along the line).

This procedure is nested into two loops. In the inner loop the increments used to estimate partial derivatives and discrete distances along the search line are systematically reduced after progress has stopped with a given increment. A second loop is repeated until the inner loop as a whole does not result in improved model behavior.

3.5.6 Mapping of error space

In Part 2 mapping of errors in parameter space has been used to address error behavior and to set reasonable parameter ranges in the genetic optimization procedure. With the genetic optimization package described in Tolman (2010), errors can be mapped in parameter space simply by generating a single population on a regular discrete grid in parameter space and compute the errors for this population with the modular elements of the optimization package.

This page is intentionally left blank.

4 Optimizing the GMD

4.1 Previous work

Previous holistic optimizations of multiple DIAs have been presented in Tolman and Krasnopolsky (2004), Tolman (2005) and Tolman (2009a). Of these papers, particularly the latter is relevant for two reasons. First, it presents initial results corresponding to the present report; second, it is used to select the formulation of the GMD in terms of $F(f)$ as used in the present report. Representing early results of the present report, Tolman (2009a) differs from the present report in various important ways.

1) In Tolman (2009a) the swell hight in test_06 in the WRT computations was set to $H_s = 5$m as in the present report, but in all other computations it was erroneously set to $H_s = 2.5$m. This accounts for the much larger errors for test_06 in Table 3 of Tolman (2009a) compared to the present Table 3.4.

2) Error weights for individual tests and details of the genetic optimization approach have been fine-tuned since Tolman (2009a) to improve convergence, economy and final results of the genetic optimization algorithm. Thus, results of Tolman (2009a) are not expected to be completely reproducible with the present genetic optimization procedure.

Considering this, detailed optimization results from Tolman (2009a) should be considered only as 'quick-and-dirty' initial results, to be superseded by results presented in this study.

4.2 Strategies

The GMD leaves an almost infinite number of configurations to be tested for their accuracy and economy. To realistically reduce the amount of optimization work done, optimization strategies need to be considered.

As a first step to designing optimization strategies, it is important to acknowledge that the GMD is excellently suitable for incremental optimization. First and foremost, the GMD needs to perform well in deep water. If this is not the case, there is no hope for the GMD to be applicable in a practical wave model. This means that C_s, m, and n can initially be ignored while optimizing the quadruplet parameters and C_d. This optimization needs to consider tests test_01 through test_06 only. Some optimized deep water GMD configurations can then be used as the starting point of the shallow water optimization using test cases test_11 though test_13.

Another principle to be considered is that the simplest approaches are most economical, and that improvement in accuracy is only acceptable at a reasonable

increase in computational cost. Therefore, single quadruplet GMDs need to be considered as a baseline. From Part 2, it is understood that only the traditional quadruplet layout can be used in a single-component GMD. For this GMD, parameter settings can be assessed by full mapping of error space. This will be done in Section 4.3. After this, the same GMD will be optimized with the genetic optimization approach (Section 4.4) for two reasons. First, to assess how to perform the shallow water optimization, which has never been done before. Second, to 'test-drive' the genetic optimization techniques.

Following the principle of simplicity, the one-parameter quadruplet and single quadruplet approach should be expanded incrementally. Considering that the traditional quadruplet definition can be stable with any number of representative quadruplets, adding quadruplets to this configuration will be assessed first (Section 4.5). The logical next step after this is to use more complex quadruplet definitions (Section 4.6). Based on the results presented in Part 2, this approach should start with a minimum of three quadruplets.

The incremental increase of complexity naturally adds individual representative quadruplets one at a time, as was done in Part 2. However, alternatively, quadruplets could be laid out to sample spectral space by setting (part of) a fixed number of quadruplet configurations, while optimizing the strength of each quadruplet. This approach is somewhat similar to the approach used in the SRIAM algorithm (e.g., Komatsu, 1996; Tamura et al., 2008). Both strategies for adding quadruplets will be considered here.

4.3 Mapping for a single-component GMD.

For a single-component GMD with the traditional one-parameter quadruplet definition in deep water, only values of λ and C_d need to be optimized. For such an optimization process, full mapping of error space is economically feasible. It is furthermore interesting to address the behavior of errors in (λ, C_d) space. Note that such an error mapping was already preformed in Part 2, showing, amongst others, the somewhat discontinuous behavior of errors in (λ, C_d) space. The latter justifies using a genetic optimization algorithm (or other random search methods) to deal with limited possibility of using derivatives of errors in parameter space. Note that it is prudent to repeat the mapping experiments from Part 2 due the increased number of test parameters and test cases.

In Part 2, ranges of λ from 0.12 to 0.30 with increments of 0.005 and ranges of C_d from $0.9\,10^7$ to $4.0\,10^7$ with increments of $0.1\,10^7$ were considered. Because the somewhat noisy behavior of errors in this space has already been established in Part 2, a larger parameter range with somewhat lower resolution will be considered mostly here. In the mapping, values of λ from 0.10 to 0.35 are considered with increments of 0.01, and values of C_d are considered from 10^6 to 10^9 with a logarithmic discretization with 31 discrete values. The overall errors ϵ_{tot} for the

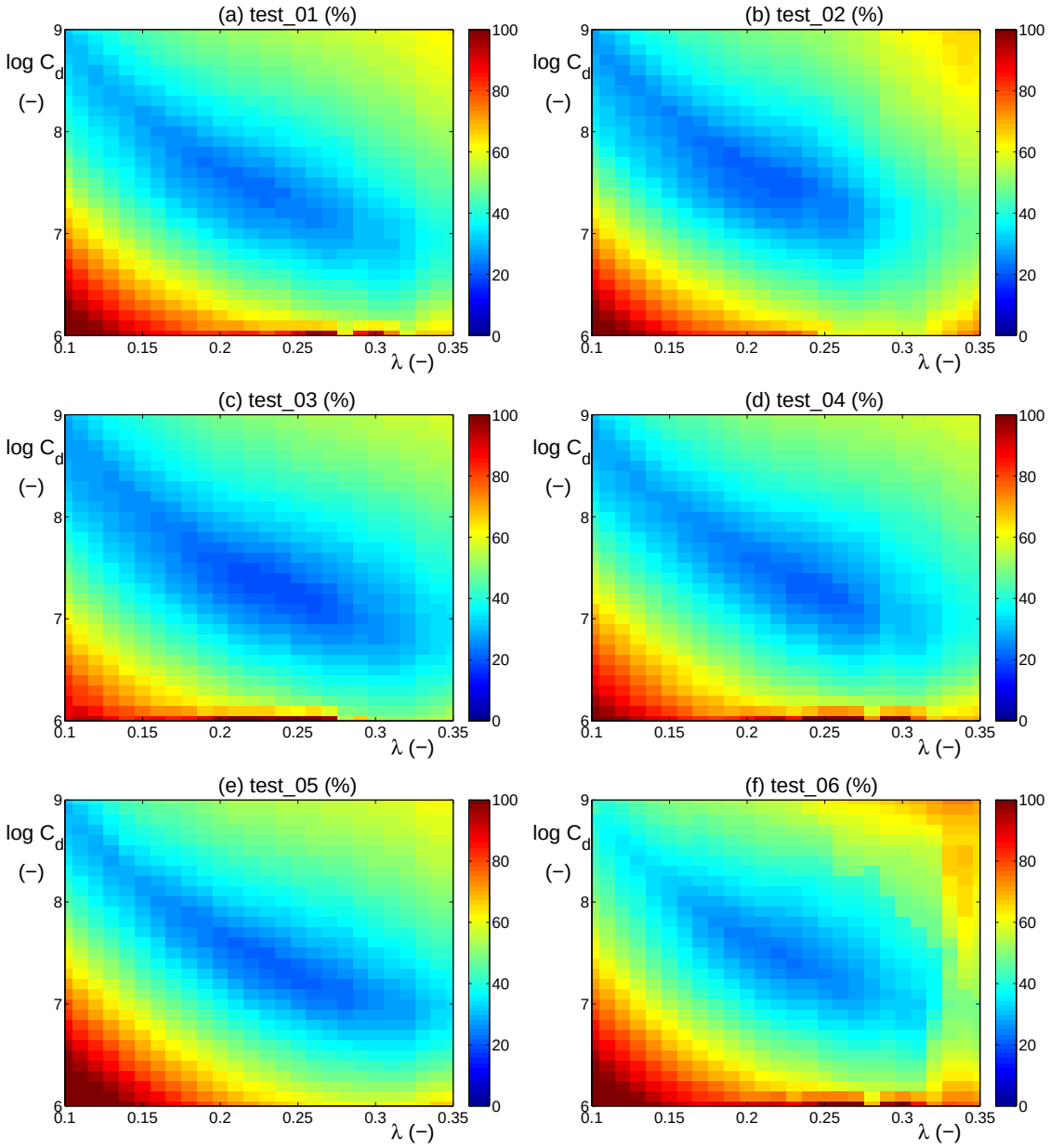

Fig. 4.1 : Total error ϵ_{tot} as a function of λ and C_d for GMD with single quadruplet and traditional quadruplet definition for deep water tests test_01 *through* test_06.

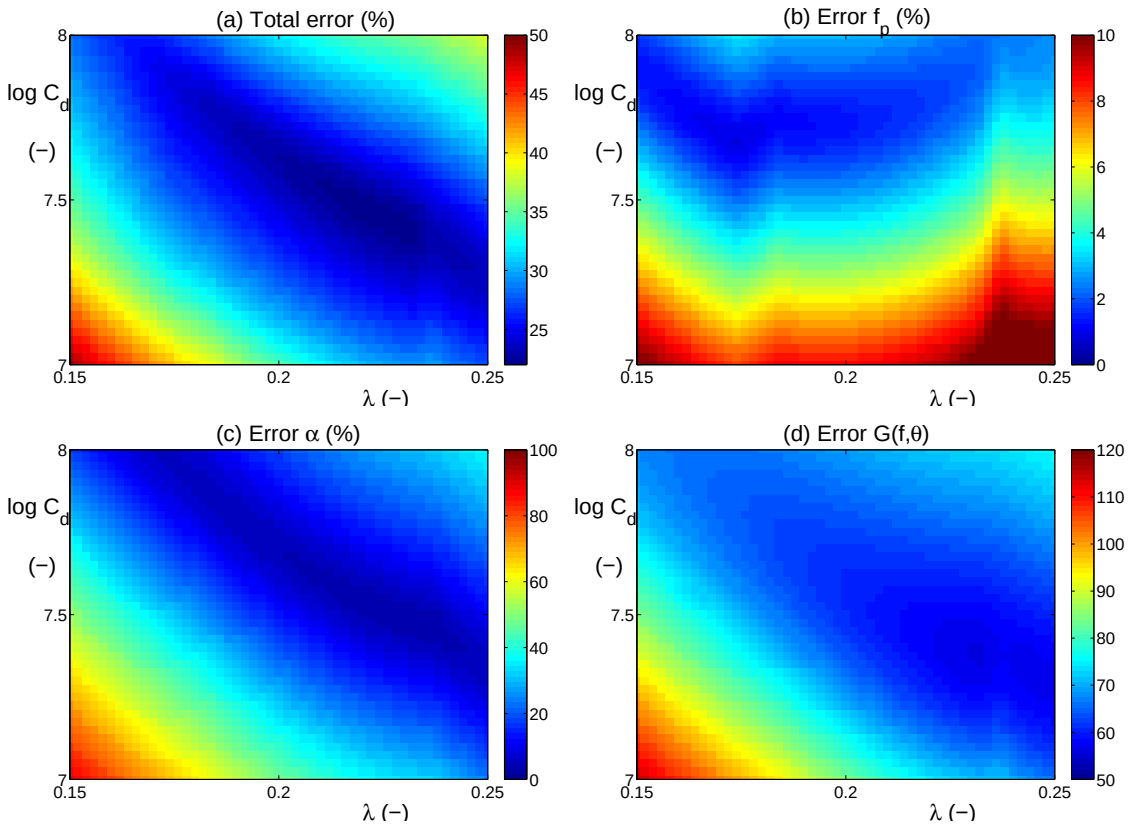

Fig. 4.2 : Results of high-resolution error mapping for test test_01. *(a) Total error ϵ_{tot} as in Fig. 4.1. (b-d) Errors for selected individual error metrics.*

six deep water tests are presented in Fig. 4.1.

Figures 4.1a and b are closely related to the two error mapping cases presented in Part 2 (Figs. 7.12 and 7.13), and show compatible results. All six test cases show qualitatively and quantitatively similar results, with some test cases showing some irregular error behavior for the lowest values of C_d considered here, and with test_06 showing different results for the largest values of λ. The latter can be attributed to the error behavior of the swell, as will be discussed below. In general, there is a large area of near-optimal model behavior, with poorly defined local error gradients. This makes steepest descent methods less effective.

Figure 4.2 presents results for high-resolution error mapping for a reduced (λ, C_d) space, which has been performed for test_01 (time-limited growth) only, and for illustration purposes only. The total error (Fig. 4.2a) shows two local minima. The error of the peak frequency (Fig. 4.2b) has a rather complicated structure. The error for α has a large but narrow area of optimal errors, where close inspection reveals many local error minima. Finally, the error in $G(f, \theta)$ shows several local error minima, as well as a large area of near-optimal errors. All these features are detrimental for steepest descent optimization algorithms,

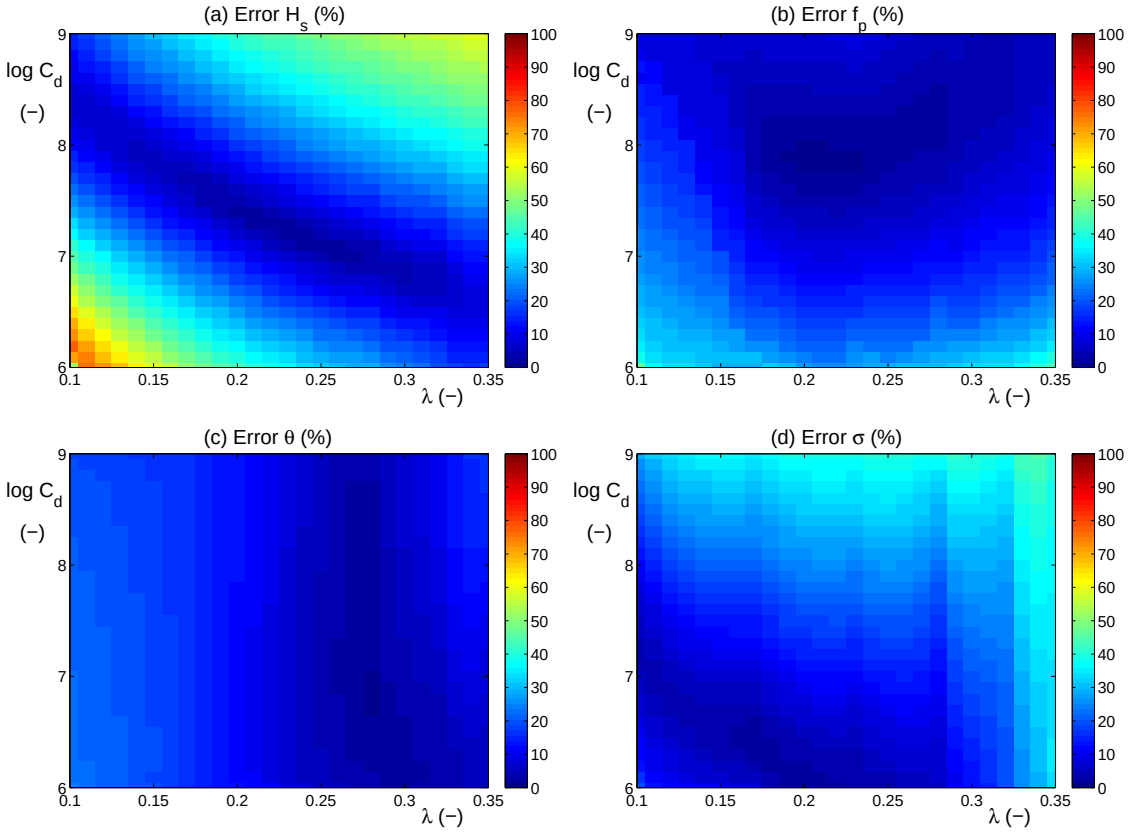

Fig. 4.3 : Error maps as a function of λ and C_d for a GMD with a single quadruplet and traditional quadruplet definition for deep water test test_05*. (a) Wave height. (b) Peak frequency. (c) Mean direction. (d) Directional spread.*

and justify the development of the genetic optimization approaches. Furthermore, the latter algorithm can be parallelized easily, unlike the former. All this, together with its general economy, justifies using the genetic optimization approach here.

Figures 4.3 through 4.6 present individual error measures for all individual error metrics for test test_05 (slanting fetch). This test was chosen as representative for all tests. As far as this is not the case, additional error measures for additional tests will also be presented.

Figure 4.3 presents errors for the mean wave parameters H_s, f_p, $\overline{\theta}$ and σ_θ. For the significant wave height H_s (Fig. 4.3a), the error map shows a well-defined area of optimal model behavior. However, this is a narrow and elongated area. Rather than having a clear optimum parameter setting, there appears to be a well-defined line in (λ, C_d) space with near optimal model behavior. For the peak period f_p and mean direction $\overline{\theta}$ (Figs 4.3b and c), the area in parameter space with near optimal model behavior is not as well-defined, and generally does not

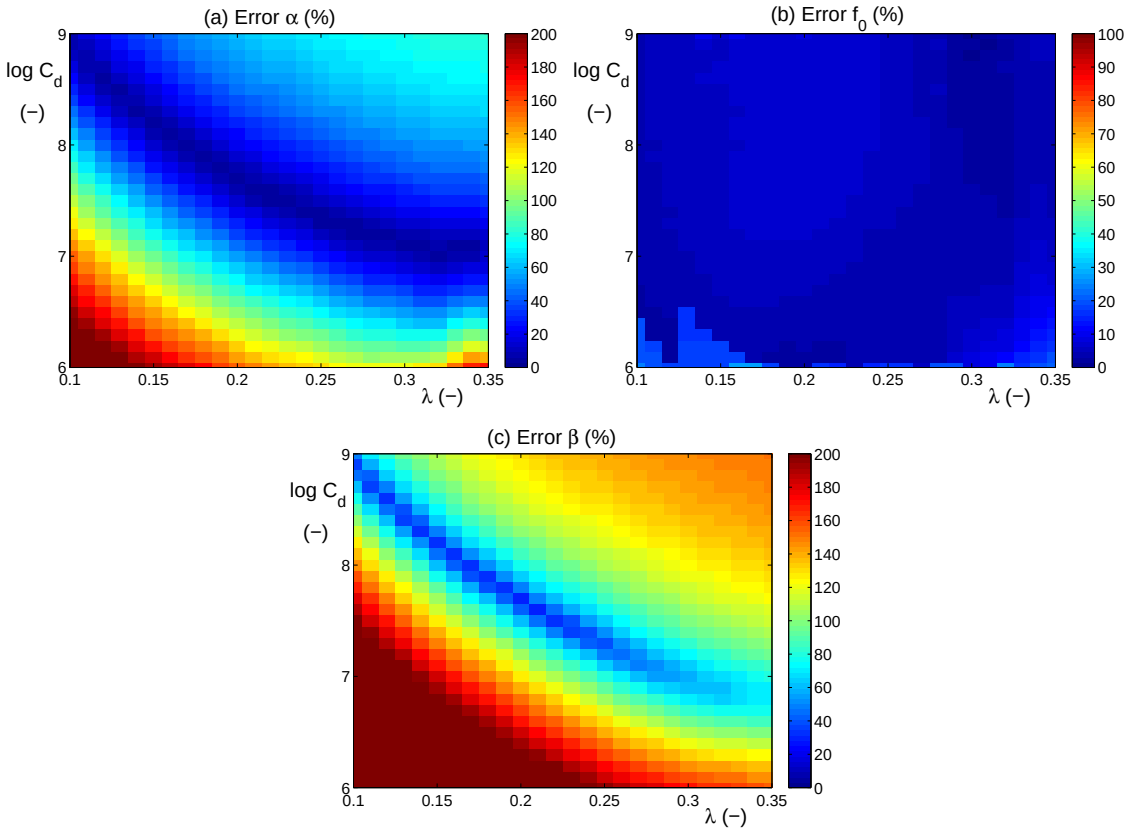

Fig. 4.4 : Like Fig. 4.3 for (a) the nondimensional energy level α, (b) the nonlinear zero-flux frequency f_0, and (c) the nonlinear energy level β.

coincide with the area of optimal behavior for the significant wave heights H_s. For the directional spread σ_θ, the optimum area is also poorly defined and not coincident with the optimum area for H_s, and furthermore shows discontinuous behavior in the upper right corner of the figure.

Figure 4.4 presents the other derived scalar parameters of the spectrum α, f_0 and β. Of these, the errors for α and β show a clear near-optimum function between λ and C_d, similar to the one found for the error in H_s. The zero-flux frequency f_0, on the other hand, shows very little error variability in parameter space, with multiple optimal error locations in parameter space. Note that errors in f_0 are generally small throughout parameter space.

Figure 4.5 presents error maps of the one-dimensional spectral parameters used in the error metrics (spectrum, steepness spectrum, direction and spread as function of frequency and nonlinear source term). The spectrum and steepness spectrum (Figs. 4.5a and b) show rather large errors, but again with a clearly defined relation between λ and C_d with near-optimal behavior. Note that the error of the spectrum is particularly high, which is understandable because these

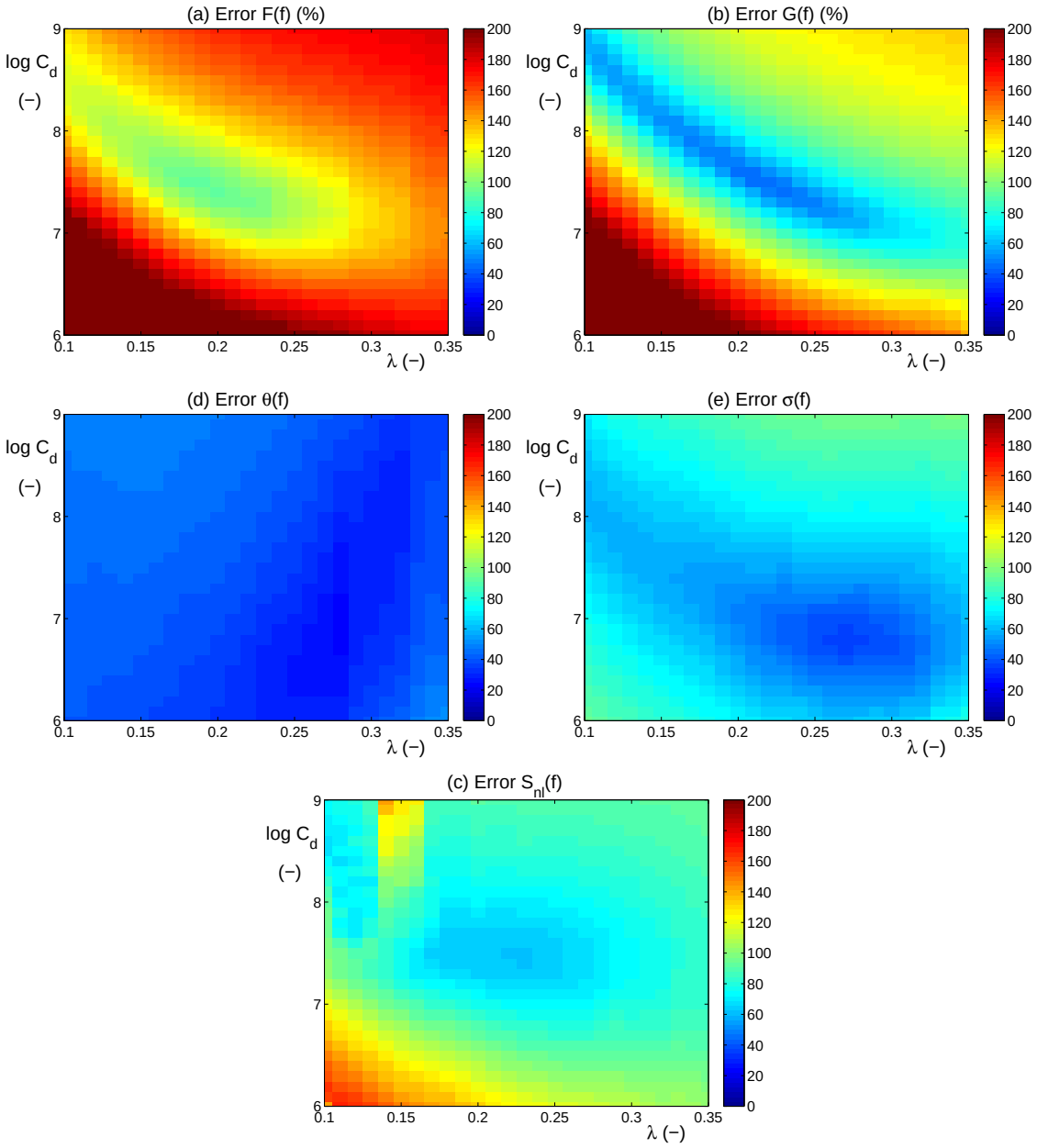

Fig. 4.5 : Like Fig. 4.3 for (a) one-dimensional spectrum $F(f)$ and (b) steepness spectrum $G(f)$, (c) mean direction θf and (d) directional spread $\sigma(f)$, and (e) one-dimensional interactions $s_{nl}(f)$.

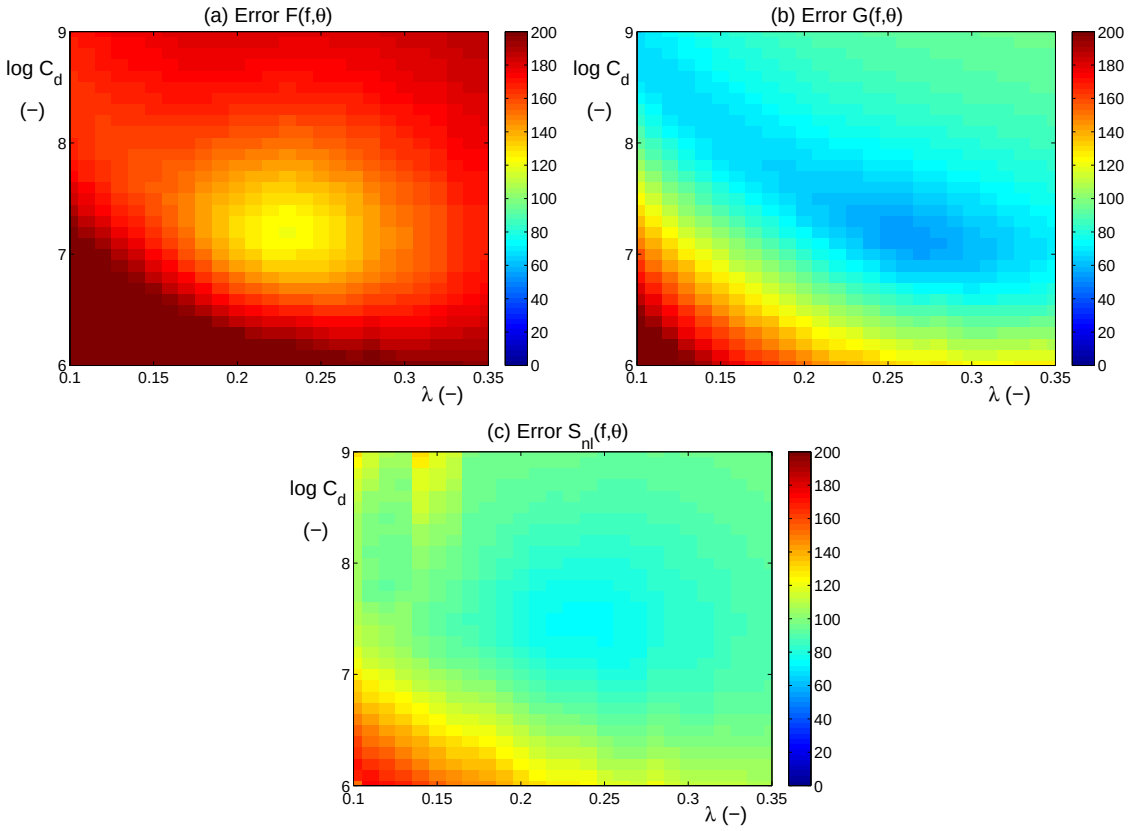

Fig. 4.6 : Like Fig. 4.3 for (a) two-dimensional spectrum $F(f,\theta)$, (b) steepness spectrum $G(f,\theta)$, and (c) source term $s_{nl}(f,\theta)$.

errors are dominated by errors in representing the spectral peak. For the steepness spectrum, errors are smaller, since they focus on energy levels for a much larger range in frequency space. The spectral direction and directional spread (Figs. 4.5c and d). show much smaller errors, and particularly for the direction do not show a well defined area of optimum model behavior. The interactions $s_{nl}(f)$ (Fig. 4.5e) show smaller errors than the spectral parameters, with a clearly defined area of near-optimal model behavior, as well as some discontinuous error behavior in the upper left corner of the figure.

Finally, Fig. 4.6 presents results for the two-dimensional spectra and source term. Resulting error maps are similar to the error maps for the corresponding one-dimensional spectra and source term in Fig. 4.5, however, with a better defined area of optimal model behavior, particularly for the conventional wave spectrum.

For all other tests, error maps per parameter show some differences, but generally show the same behavior. Only for test_06 (wave growth with swell) different errors occur due to the separation in mean parameter error for wind sea and

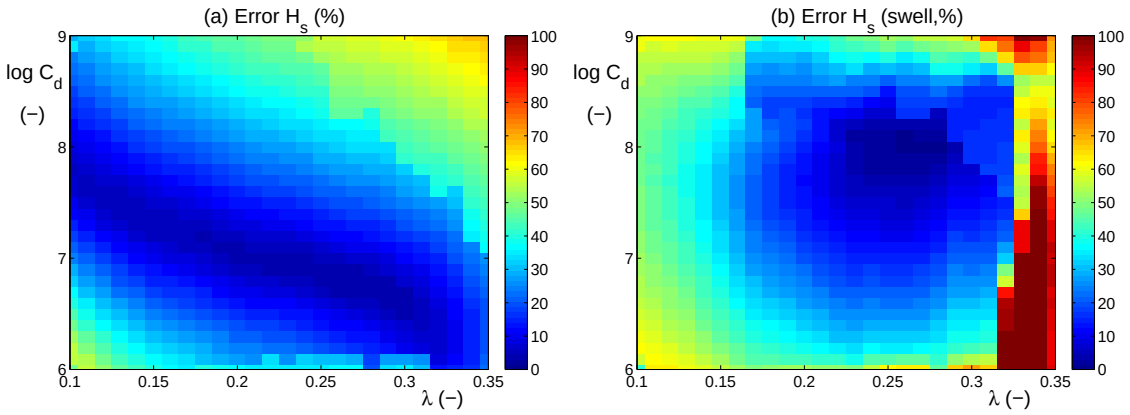

Fig. 4.7 : Like Fig. 4.3 for test test_06 *(a) wave height H_s for wind sea and (b) for swell.*

swell. This becomes particularly evident in the wave height error maps, as shown in Fig. 4.7. For wind seas, the wave height error map is very similar to the maps of the other test cases. For the swell, the wave height errors are clearly different, with discontinuously high errors for large λ, which are responsible for the somewhat different total errors at high λ for test_06 in Fig. 4.1.

Figures 4.3 through 4.7 indicate which error parameters contribute most to the optimization process; this will generally be the error parameters with well-defined optimal error areas in parameter space, and with a large range of the errors in parameter space. Inspection of the figures suggests that the wave height H_s, energy levels α and β and one and two dimensional variance and steepness spectra will dominate the error estimates and therefore the optimization. Correspondingly, the errors of the peak frequency, directional measures and the zero-flux frequency do not have clear signals in parameter space, and hence will not have a big impact on the error or optimization process. This also implies that these parameters do not have a big potential in terms of being optimized in the optimization process.

Another observation that can be made from these figures is that areas in parameter space of optimum model behavior for different model parameters generally do not coincide. This was also observed in the experiments performed in Part 2 (see Fig. 1 of Tolman and Krasnopolsky, 2004). This implies that for a DIA or a GMD with a single representative quadruplet defined as in the DIA it is impossible to optimize all metrics simultaneously, and the choices of error weights in Eq. (3.29) Table 3.3 will influence the resulting optimum λ and C_d. Note that in test_06 wind sea and swell wave height cannot be optimized simultaneously.

So far, error mapping has been considered for deep water only. In shallow water, many more parameters need to be optimized than in deep water. In its simplest

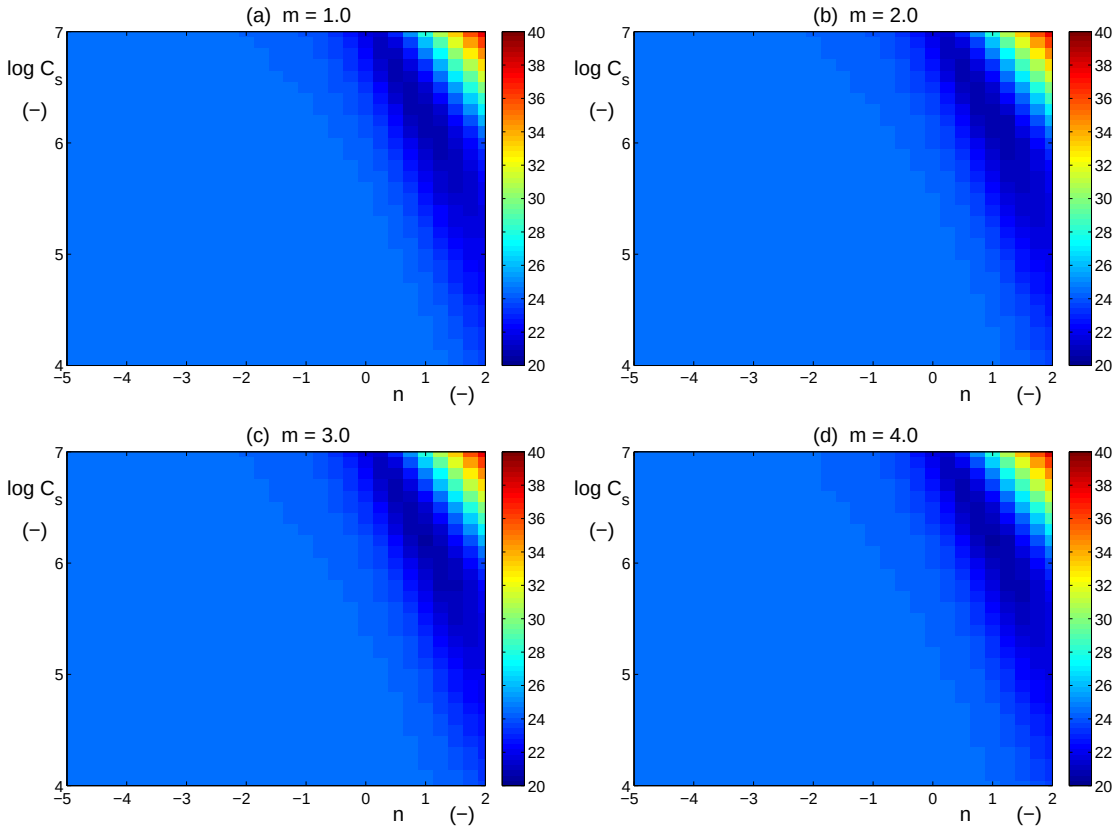

Fig. 4.8 : Total error distribution in (n, C_s) space for test_11 *for various values of m.*

form, the GMD then needs estimates for λ, C_d, C_s, m and n in Eqs. (2.30) through (2.32), possibly with separate values of λ for C_d and C_s. In its full form, the corresponding mapping exercise is of too high dimensionality to be economically feasible. The dimensionality can be reduced by using 'standard' settings of deep water parameters of the wave model ($\lambda = 0.25$, $C_d = 1.0\ 10^7$) with a single estimate for λ. This leaves only a three-dimensional parameter space (C_s, m, n). Furthermore considering that Part 3 suggests that the scaling is only moderately influenced by the choice of m, the first error mapping efforts for shallow water will consider the C_s, n parameter space for a very coarse discretization of m ($m \in [0, 1, 2, 3, 4]$).

Maps of the total error as a function of n and C_s for tests test_11 through test_13 for various values of m are presented in Figs. 4.8 through 4.10. Two observations can be made directly from these figures. First, error maps per test case are largely insensitive to the choice of m, as was expected. However, the radical differences between error maps for different test cases may not have been expected, and suggest that the tests rely on different aspects of the GMD for optimal model behavior. A first observation can be that the error maps for

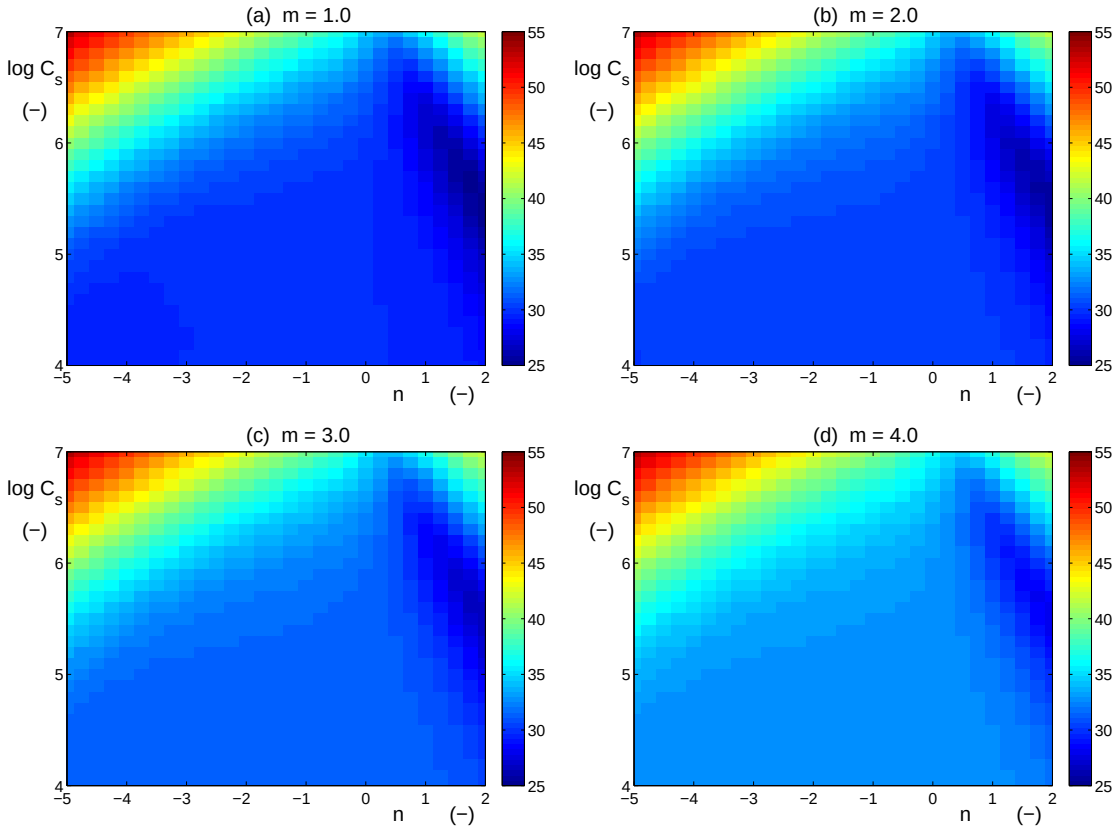

Fig. 4.9 : Like Fig. 4.8 for test_12.

test_12 can loosely be interpreted as the combination of the error maps for test_11 and test_13.

The differences in error behavior between the the three tests can tentatively be attributed to significant differences in the conditions in the three tests. the most extreme shallow water conditions are encountered in the beach test, particularly when only severely depth-limited swells are considered (test_13, Fig. 4.10). In this case, optimum errors are found for a range of values of n and C_s, centered around expected values for $n \approx -3.5$, as is expected to produce proper scaling behavior of S_{nl}. For test_11, however, optimum value for n deviate greatly from the expected value. In the latter test, however, truly shallow water conditions do not occur, and, furthermore, some of the errors are related to errors in the deep water conditions of initial growth. In this case, n is not required to produce proper shallow water scaling behavior, and hence, n and C_s produce optimum behavior in unexpected parameter ranges. For the remaining test, both shallow water growth and severe depth-limited growth occur, and optimum parameter values correspond to both parts of parameter space found before.

The differences in error behavior between the three test cases poses the ques-

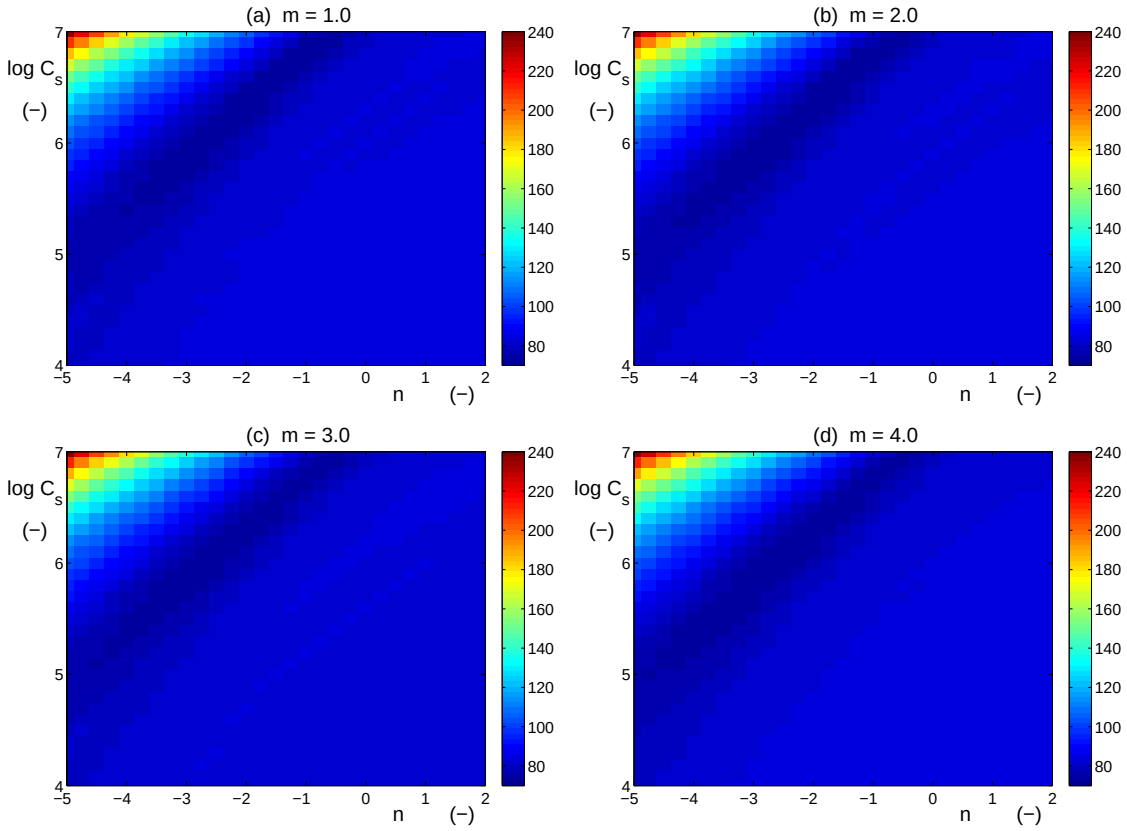

Fig. 4.10 : Like Fig. 4.8 for test_13.

tion on how to optimize the free shallow water parameters in the GMD. If test_11 results in optimized parameter values of n inconsistent with shallow water scaling as found in Tolman (2009a) and in Figs. 4.9 and 4.10, should this test still be used? There are three options to deal with this behavior. (i) Do not consider this test. This does not appear to be advisable, since the test does provide practical shallow water conditions, and since this would imply that test_12 should be abandoned too. (ii) n can be preset to $n \approx -3.5$ based on Tolman (2008b) to ensure proper scaling behavior, without dynamic optimization. (iii) n can be optimized in a limited range only, typically $-5 < n < -1$ to ensure optimization in a proper scaling range only.

The individual error measures for individual error metrics again display different behavior as with the deep water test. Generally, conclusions are similar as compared to the deep water test cases, and therefore additional figures are not reproduced here.

The above assessment of optimizing n, and the insensitivity of errors to the values of m, suggest another mapping exercise. Keeping $m = 2$ and $n = -3.5$ constant, errors as a function of C_s and a separate λ for shallow water can be

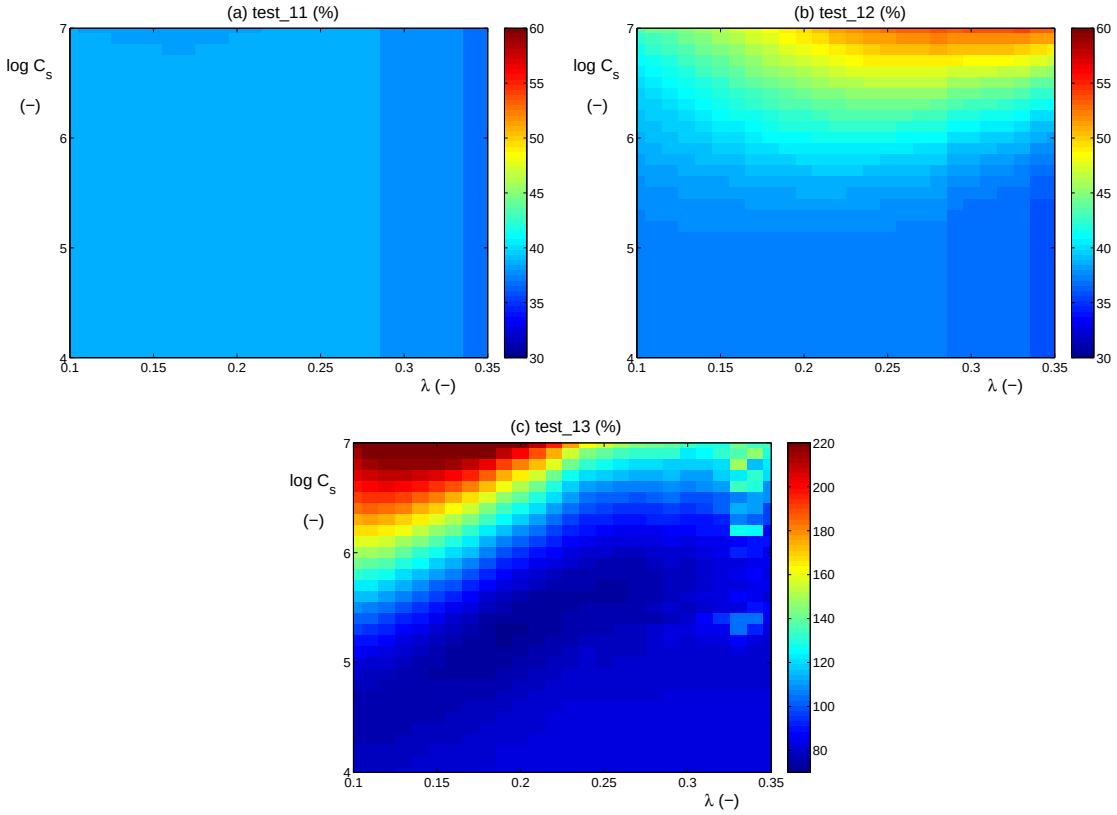

Fig. 4.11 : Total error ϵ_{tot} as a function of a shallow water λ and C_s for GMD with deep water quadruplet with $\lambda = 0.25$ and $C_d = 1.\,10^7$ and with shallow water quadruplet with $m = 2$ and $n = -3.5$ for tests test_11 *through* test_13.

mapped. As with the other shallow water tests, $\lambda = 0.25$ for the deep water quadruplet with $C_d = 1.0\,10^7$, as in the default setting of the wave model. Note that this model setting in fact requires two quadruplets, one with deep water scaling exclusively ($C_s \equiv 0$), and one with shallow water scaling only ($C_d \equiv 0$).

Figure 4.11 shows the total error maps as a function of λ (shallow water) and C_s for the three shallow water tests. Test test_11 (Fig. 4.11a) shows virtually no sensitivity of the error to the two parameters. This suggests that this test is not suitable for identifying optimum settings of these parameters, when m and n are set and represent reasonable scaling behavior in shallow water. Note that these results are tentatively consistent with the lack of sensitivity to C_s in the corresponding range of n in Fig. 4.8a. Test test_12 (Fig. 4.11b) shows more sensitivity to the mapping parameters, with clear areas with poorer model behavior, but with a fairly undefined area of optimum model behavior. Finally, test test_13 (Fig. 4.11c) shows clear sensitivity of the model to parameter choices, with a well defined area of optimum parameter settings. Note that the errors in

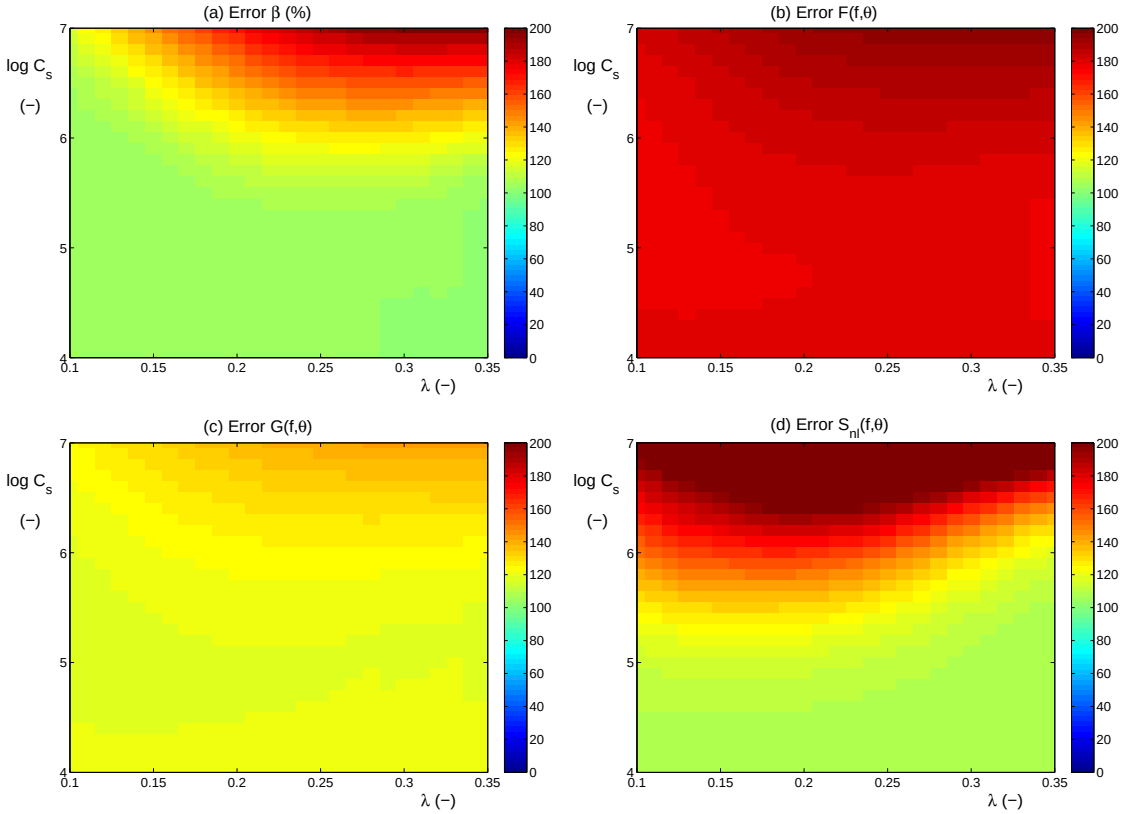

Fig. 4.12 : Selected individual error measures corresponding to Fig. 4.11 for test_12.

the latter figure are much larger due to the different composition of the total error as outlined in Tables 3.3 and 3.4.

The total error for test_12 in Fig. 4.11 is dominated by the errors in β and the one and two dimensional spectra and source terms. This is illustrated in Fig. 4.12 with some selected error maps.

The total error for test_13 is entirely made up of spectral and source term errors. The spectral direction and directional spread are not sensitive to the choice of the GMD parameters, but all spectral and source term errors are. This is illustrated in Fig. 4.13. The spectral errors clearly define areas in parameter space with optimal model behavior, the interaction errors more clearly identify areas with poor model behavior, particularly for small λ and large C_s.

This concludes the discussion of the mapping exercises. For deep water, previous conclusions for a less complete holistic optimization have been confirmed, as have been reasonable parameter ranges for the free parameters in the GMD. For shallow water, new ground has been broken. It has been shown that test_11 is dominated by 'deep water' error growth behavior, and has limited usefulness for

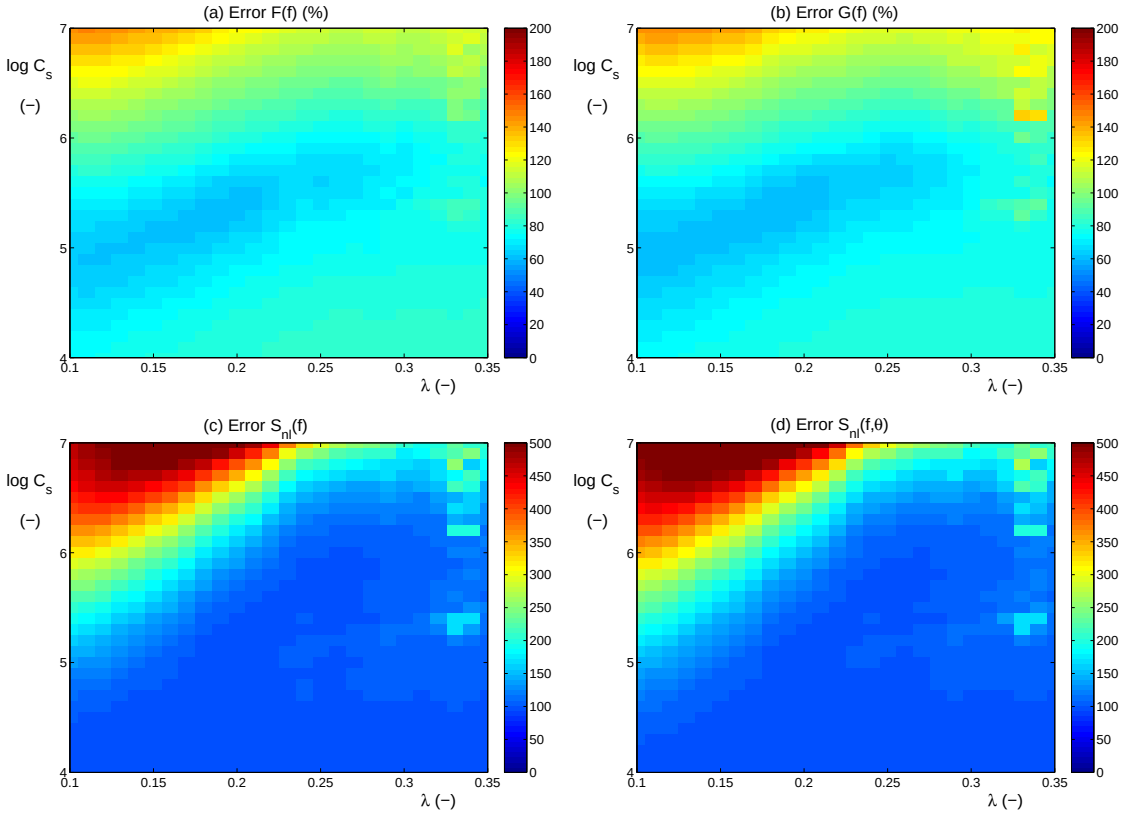

Fig. 4.13 : Like Fig. 4.12 for test_12.

the shallow water optimization, other than possibly eliminating negative impacts on intermediate water depth wave growth behavior. Test test_12 mixes deep water growth behavior with shallow water behavior, whereas test_13 is dominated by shallow water (swell) conditions. The mapping particularly identified that the GMD is not expected to be particularly sensitive to the choice of m, and that a full free choice of n may negatively impact the shallow water scaling behavior. These findings will be discussed in more detail in the following sections.

4.4 Single component GMD

As has been shown in previous parts of this study, a single component GMD can only work if it uses the quadruplet of the conventional DIA. For this GMD layout the error mapping of the previous section can be used to determine optimum parameter settings, and the genetic optimization is not needed to make the optimization feasible. However, the genetic optimization is used here to test its behavior against the mapping exercise. Deep and shallow water optimization will be addressed in Sections 4.4.1 and 4.4.2, respectively. A summary of optimization

results will be given in Section 4.4.3.

4.4.1 Deep water

The deep water optimization for this quadruplet considers all six deep water tests, and optimized λ and C_d for a single representative quadruplet as in the mapping exercises of Section 4.3. Because only two parameters need to be optimized, only a small population and a small number of generations are needed. Here, the population size is set to 50, and 10 generations are considered. Several initial random populations are considered, and a steepest descent search is initiated from the best members of the last generation of each experiment. The experiments result in the same optimum model setting with $\lambda = 0.231$ and $C_d = 2.54\,10^7$ after the steepest descent search, although best results for the genetic search algorithm differ by negligible amounts between experiments with different random initial populations.

With the genetic optimization, the focus will be on two things; first, on the evolution of the individual generations towards near-optimal solutions, and second on the evolution of the minimum model errors and the simultaneous loss of diversity of (near-optimal) generations.

Figures 4.14 and 4.15 illustrate the evolution of populations for one of theses optimization procedures. In the former figure, members are colored according to their total error ϵ_{tot}, making this figure in essence a sparse sampling of the error mappings produced in the previous sections. In the latter figure, members are colored according to their rank in the population, rank 1 being the member with the smallest error, and rank 50 the member with the largest error.

The first generation in Figs. 4.14 and 4.15 by definition randomly samples the parameter space, with the figures showing the entire parameter space considered in the optimization. In generations 2 and 3, the population rapidly moves toward a general area with lower model error. In generations 5 through 10, the area covered the 1/3 of the population with the lowest errors (blue colors in Fig. 4.15) contracts until it focuses on the best possible solution with the smallest model error. In generation 10, diversity for this part of the population is hence clearly reduced or effective lost.

For this simple optimization problem, meaningful error maps as presented in Figs. 4.14 and 4.15 are easily defined and analyzed. For more complex problems with more free parameters, such plots cannot easily be designed, yet an assessment of model convergence and population diversity is essential to assess the success of the optimization approach. Alternately, the evolution of the best performing member of the population (smallest error ϵ_{tot}) gives some indication of the convergence of the genetic optimization routine, whereas multiple random initial conditions give some indication of how well the optimization problem is posed (i.e., are there multiple near-optimal solutions). Comparing the error of the

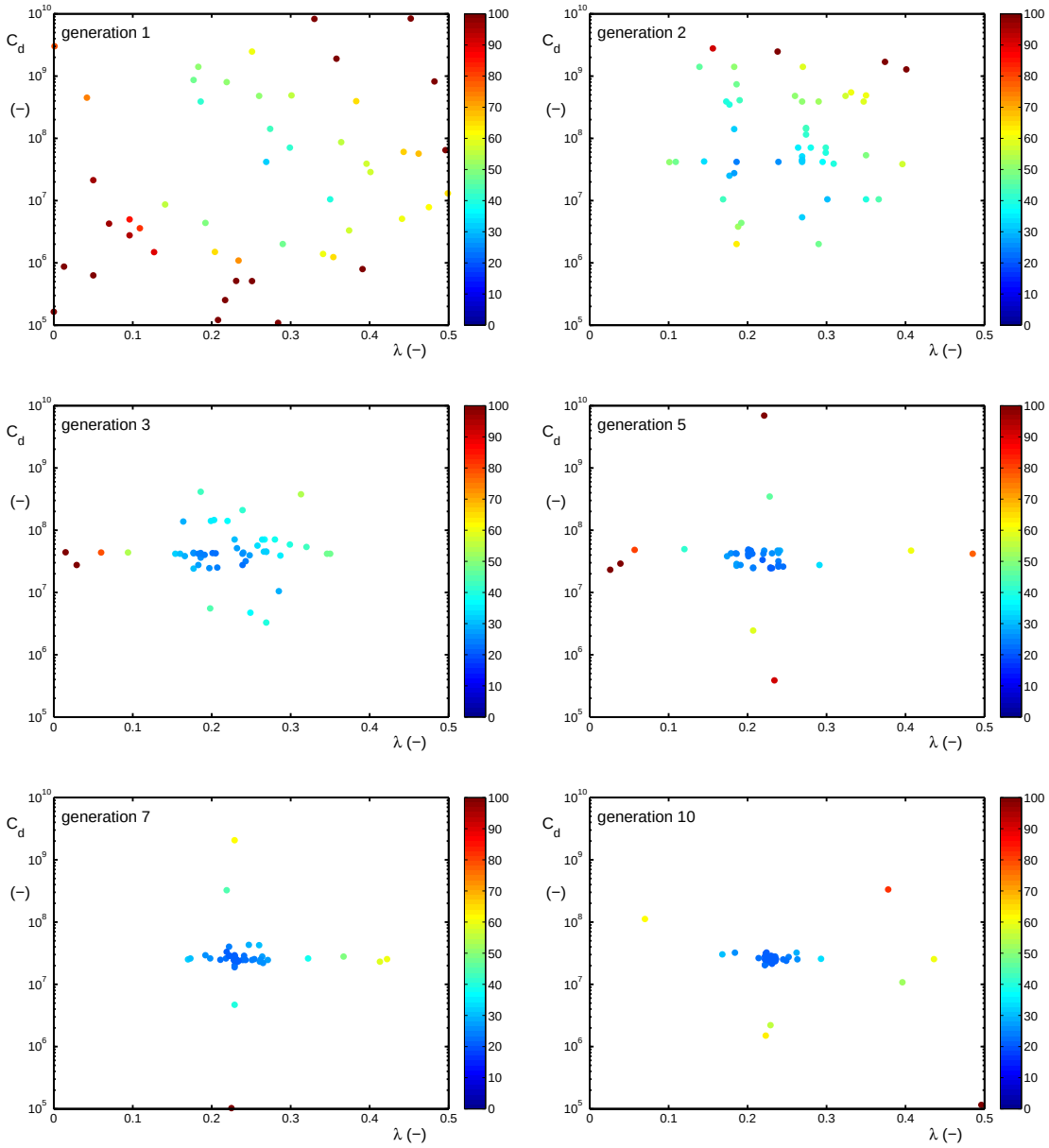

Fig. 4.14 : Example populations for deep water single component GMD. Simultaneous optimization of λ and C_d, 50 members in population, 10 generations in optimization. Color scale identifies total error for six deep water tests

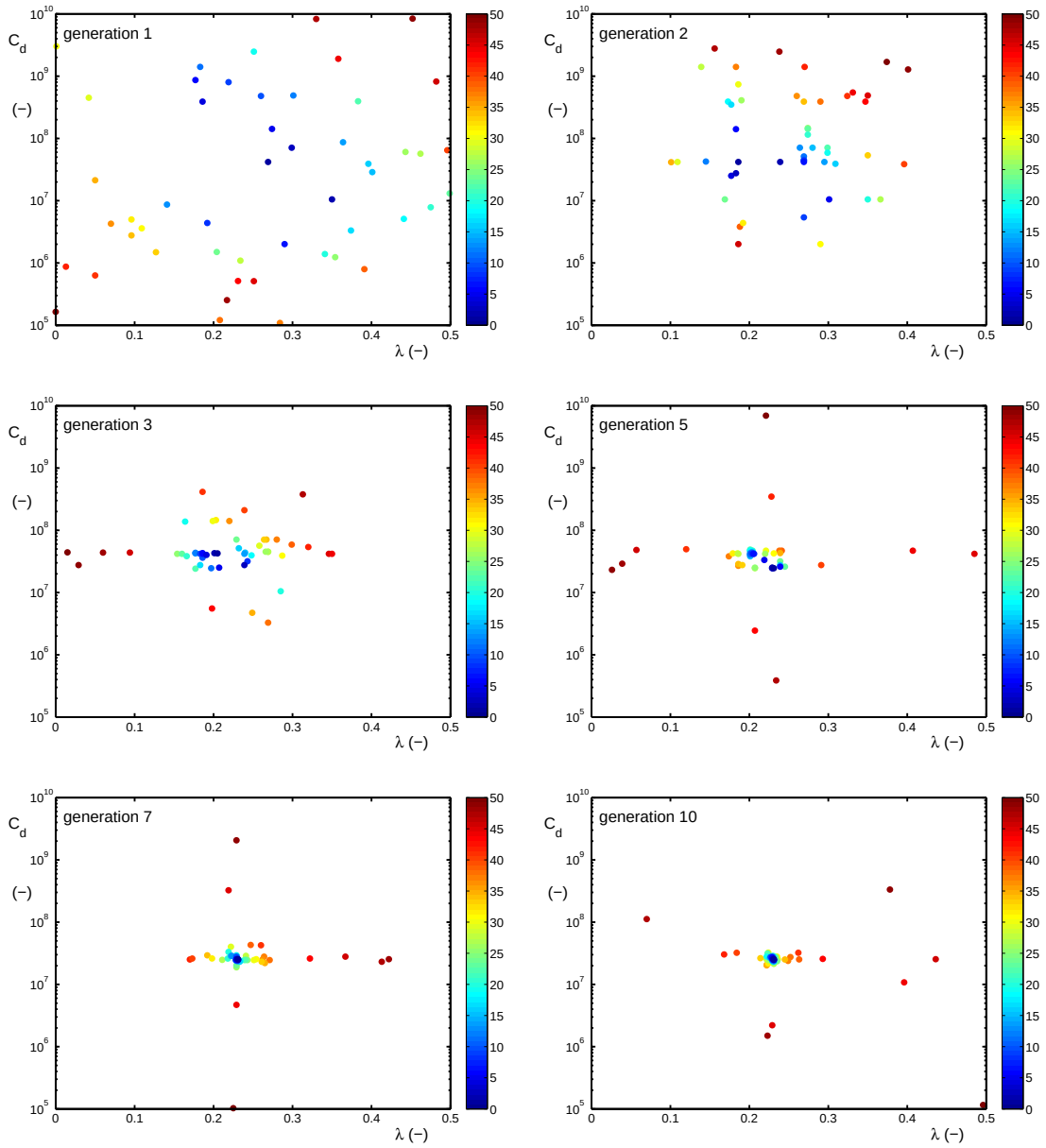

Fig. 4.15 : Like Fig. 4.14, color representing rank in the population.

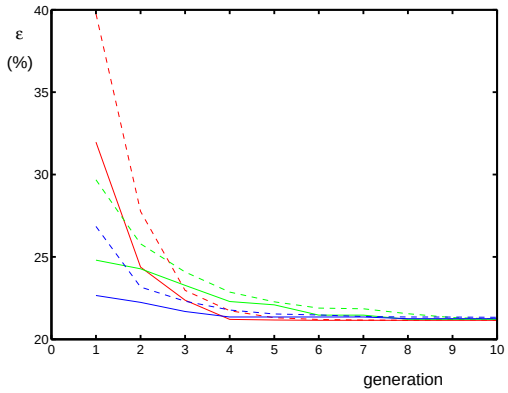

Fig. 4.16 : Minimum errors (ϵ_{min}, solid lines) and average errors for fittest half of population (ϵ_{avg}, dashed lines) as a function of the generation for various optimization experiments (identified by color) with traditional quadruplet definition and one representative quadruplet.

best performing member of the population with the average of, for instance, the 50% best performing members of the populations (ϵ_{avg}), gives a quick assessment of diversity of the population, assuming that there is a reasonably well defined area of best model performance in parameter space.

Figure 4.16 shows the evolution of ϵ_{min} (solid lines) and ϵ_{avg} (dashed lines) for the optimization of λ and C_d for three different initial populations (red, green and blue).

The three experiments show drastically different errors for the initial population, but convergence to the same optimum error in less than 10 generations. Initially, ϵ_{avg} is significantly larger than ϵ_{min}, indicating diversity in the initial populations. For the later generations, $\epsilon_{avg} \approx \epsilon_{min}$, indicating a lack of diversity, suggesting that considering more generations is not likely to produce better parameter estimates.

Note that the green population appears to have reach an asymptotic solution in the fifth generation, but then again moves to better solutions. This behavior can be expected with genetic optimization, as it focuses on near-optimal solutions, with no guarantee that 'the' optimal solution is found. This makes it useful to (i) try optimization with various initial populations, and (ii) augment the genetic optimization with steepest descent methods. The latter is needed if diversity is lost without reaching the (local) minimum.

4.4.2 Shallow water

In shallow water, there are more than two free parameters that could be optimized. These are the m and n parameters in the scaling functions, the shallow water proportionality constant C_s, and possibly a separate value of λ associated

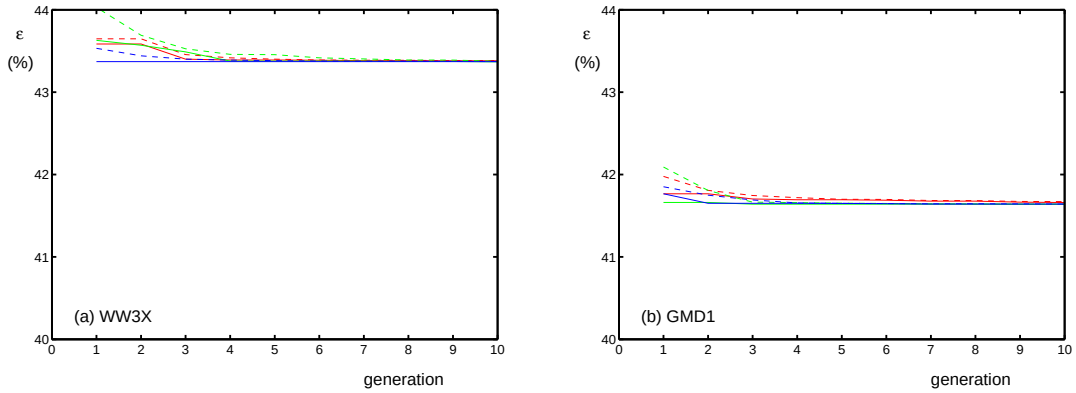

Fig. 4.17 : Like Fig. 4.16 for shallow water optimization of n and C_s, with deep water settings of λ and C_d from (a) the WW3X and (b) the GMD1 model setup.

with C_s. In the latter case, there will be two representative quadruplets, one for asymptotic deep water scaling only, and one for asymptotic shallow water scaling only. On top of this, a deep water setting for λ and C_d needs to be adopted to start with the optimization. For the latter deep water setup, the logical choice is to adopt the optimum model settings from Section 4.4.1, i.e., $\lambda = 0.231$ and $C_d = 2.54\,10^7$. Another sensible setting to consider is the default setting of the wave model, i.e., $\lambda = 0.250$ and $C_d = 1.00\,10^7$. In the latter case, introducing the GMD does not influence the wave model in deep water, but modifies the model results in extremely shallow water by introducing more accurate scaling functions. The deep water setting for the optimized GMD and extended WAVEWATCH III model setting will be denoted as 'GMD1' and 'WW3X' setting in the remainder of Section 4.4.

From the initial shallow water optimization experiments reported in Tolman (2009a), it is clear that the model results are fairly insensitive to the choice of the scaling parameter m. Furthermore, optimum values of m as found in the latter paper ($m < 1$) are much smaller than tentative choices of m based on the results from Part 3 ($m \approx 4$). To explore this issue further, the GMD1 and WW3X model setups are optimized for the three shallow water test cases with an essentially deep water model setup with $C_s \equiv 0$, while optimizing m only. Both optimization tests result in an optimum value of $m = 0$. Considering the relative insensitivity of the results to m, and in order to simplify the optimization procedures, $m = 0$ will therefore be used in all other optimization experiments reported in this Section.

With m set, the simplest optimization procedure is to dynamically optimize C_s and n. Due to the low dimensionality of this problem, this could again be done using the mapping reported in Section 4.3. However, in order to test the

Table 4.1: Optimal GMD setting for traditional quadruplet layout and single deep quadruplet optimizing C_s and n with given λ and C_d. Combined error for shallow water tests only, $m = 0$.

WW3X	λ	C_d	C_s	n	ϵ_{tot} (%)
Exp. 1	0.250	$1.00\,10^7$	$4.94\,10^5$	-3.23	43.4
Exp. 2			$3.77\,10^5$	-3.49	43.4
Exp. 3			$3.55\,10^5$	-3.55	43.4
Fixed n			$3.74\,10^5$	-3.50	43.4

GMD1	λ	C_d	C_s	n	ϵ_{tot} (%)
Exp. 1	0.231	$2.54\,10^7$	$3.43\,10^5$	-3.43	41.7
Exp. 2			$2.31\,10^5$	-3.77	41.6
Exp. 3			$2.55\,10^5$	-3.69	41.6
Fixed n			$3.12\,10^5$	-3.50	41.7

genetic optimization schemes, and in order to test how well posed the optimization problem is, the optimization again is performed using the genetic optimization procedure, augmented with a steepest descent algorithm. Note that, based on the mapping experiments, values of n are not allowed to be larger than -2, which is different from the base setup started with in Table 3.5. These experiments have been performed with the GMD1 and WW3X base model settings, using 10 generations with 50 members each, and starting each experiment with three different randomly selected initial generations, and are identified as GMD1a and WW3Xa, respectively.

Error evolution for these experiments is shown in Fig. 4.17. Errors change little per generation, suggesting an ill-posed optimization problem (or a large enough initial population to randomly find optimum values). The ill-posed nature of these experiments is further illustrated in Table 4.1, which shows that experiments with different initial populations result in clearly different optimum values but with near-identical model errors. The table furthermore shows that if n is preset to $n = -3.5$, which was shown to result in near-optimal scaling in Part 3, consistent results are also found. These first shallow water optimization experiments suggest that $m = 0$ and $n = -3.5$ could be used without further attempts at optimization. This leaves two optimizations that have been considered. In the first, only C_s needs to be optimized. This is done using five generations with 20 members each. This trivial optimization experiment will not be discussed in more detail, and the results are identified as WW3Xa and GMD1a in Table 4.2. Finally, a separate shallow water quadruplet can be defined, optimizing λ to-

Table 4.2: Optimal GMD setting for traditional quadruplet layout and single deep and/or shallow quadruplet. Combined error for shallow water tests only, $m = 0$, $n = -3.5$.

model	λ	C_d	C_s	ϵ_{tot} (%)
WW3X	0.250	$1.00\,10^7$	—	45.8
WW3Xa	0.250	$1.00\,10^7$	$3.74\,10^5$	43.4
WW3Xb	0.250	$1.00\,10^7$	—	42.2
	0.184	—	$1.63\,10^5$	
GMD1	0.231	$2.54\,10^7$	—	44.2
GMD1a	0.231	$2.54\,10^7$	$3.12\,10^5$	41.7
GMD1b	0.231	$2.54\,10^7$	—	40.7
	0.184	—	$1.63\,10^5$	

gether with C_s, using 10 generations with 50 members. Resulting model settings are shown as WW3Xa and GMD1b in Table 4.2, and the error evolution of these experiments are presented in Fig. 4.18.

Table 4.2 shows error reductions when going from a deep water only model setup, to a single quadruplet with deep and shallow water scaling, to a GMD with a single deep and a single shallow water quadruplet. This error reduction occurs for both the WW3X and GMD1 deep water settings. Note that the table presents the total error for the shallow water tests only. The basis of these errors are the accuracy with which the deep water settings of the approximations are able to provide the 'deep water' wave growth boundary conditions in test test_11 and test_12.

Finally, Fig. 4.18 shows the error evolution of the last optimization tests. The error evolutions are more similar to the evolution of errors for the deep water model setup, and hence suggest a better posed optimization problem. The better posed nature is also evident in the fact that the steepest descent methods for all three experiments results in identical or near identical parameter settings. Note that for the green experiment in Fig. 4.18a population diversity is lost before the optimum error is found. However, the steepest descent method applied after generation 10 did find the unified optimum solution, and running this experiment for more generations did eventually converge of the solution of the other two experiments. This again illustrates the random and near-exact nature of the genetic optimization procedures. Note also, that the latter descent method proved as costly as running several generations in the genetic algorithm, illustrating the general efficiency of the genetic algorithm to get near-optimal solutions.

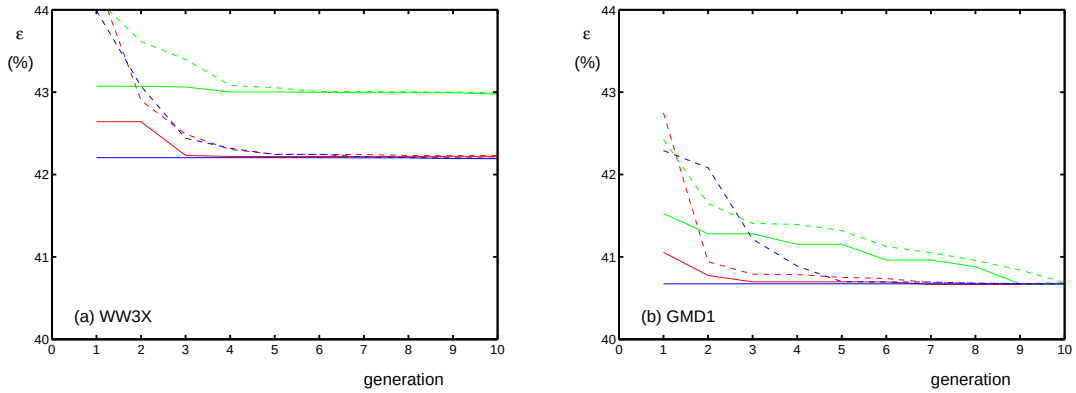

Fig. 4.18 : Like Fig. 4.17 optimizing λ and C_s as a second shallow water only quadruplet.

4.4.3 Summary

Six viable single-quadruplet GMD settings are presented in Table 4.2. They represent a GMD with deep water scaling only, a GMD with mixed deep and shallow water scaling, and a GMD with separate deep and shallow water quadruplets. For these three options, the default deep water quadruplet settings of WAVEWATCH III are used, or the separately optimized deep water GMD settings from Section 4.4.1. For these six model settings, errors for each individual test as well as composite errors are presented in Table 4.3. Note that the total errors in the Tables 4.2 and 4.3 differ, since the total errors in Table 4.2 refer to the shallow water tests only, whereas the total errors in Table 4.3 refer to all test cases. Note, furthermore, that the results for WW3 in Table 3.4 differ slightly from the results for WW3X presented in Table 4.2, because the former are computed using the traditional DIA whereas the latter are computed using the GMD. In deep water, minor differences occur due to different implementations of essentially identical equations, whereas in shallow water, quadruplet layout are evaluated differently.

For deep water (tests test_01 through test_06) the optimization results in significantly smaller errors for the GMD1 models than for the WW3X models. Resulting model behavior will be presented in more detail in Section 4.7. Sufficeth to say here that smaller errors in some ways can be misleading. In Sections 3.3.1 and 3.3.2, it is shows that the WW3(X) approach gives a very good representation of the wave height, but at a cost of rather large errors in the spectral shape. The GMD1 approach reduces errors significantly by reducing errors in spectral shape, but at the cost of a poorer description of the wave height. Since the wave height is the first and often the only parameter from the wave model seen by users, the GMD1 approach might therefore be perceived as being of poorer quality than the WW3X approach.

In shallow water, adding shallow water scaling to the existing quadruplet, or

Table 4.3: Overall errors in % for each test case for the configurations in Table 4.2. Error for deep water test cases are identical for all WW3X or GMD1 cases, and are therefore not repeated in the Table.

	test case									
	01	02	03	04	05	06	11	12	13	tot
WW3X	27.4	27.7	22.5	25.1	26.5	29.8	24.6	29.4	83.5	32.9
WW3Xa							24.7	31.0	74.5	32.1
WW3Xb							24.7	29.9	72.0	31.7
GMD1	22.2	21.7	19.1	20.4	20.5	23.1	21.1	28.3	83.3	28.8
GMD1a							21.1	29.9	74.3	28.0
GMD1b							21.1	28.8	72.0	27.7

adding a shallow water quadruplet ('a' and 'b' approaches) reduces composite model errors. Error reduction is significant for the swell propagation test test_13, but for the wind sea tests, moderate increases of the errors are observed. This can be attributed to the fact that forcing $n = -3.5$ to force shallow water scaling for extremely shallow water automatically focuses the optimization on the swell test, but will not necessarily allow for improvement of the wind seas in more intermediate water depths.

Considering the limited experience with shallow water optimization, and considering experiences presented in Tolman (2009a), it is important to address the quality of GMD in shallow water in some detail. Considering the above, the most extreme shallow water conditions occur in the surf zone for the swell propagation onto a beach. In Fig. 4.19, spectra from various test for a water depth of 3 m are presented. The results for the deep-water scaling only WW3X and GMD1 approaches (dashed red lines in figure) in effect have no nonlinear interactions, and hence represent shoaling only. In the exact interactions (green solid lines) energy is significantly spread in spectral space, resulting in a reduction of the spectral peak energy level by a factor of nearly 2. The shallow water 'a' and 'b' approaches reproduce this reduction adequately. However, these approaches also result in a spurious second spectral peak at lower frequencies. Hence, it remains to be seen if this shallow water approach should be used in practical models.

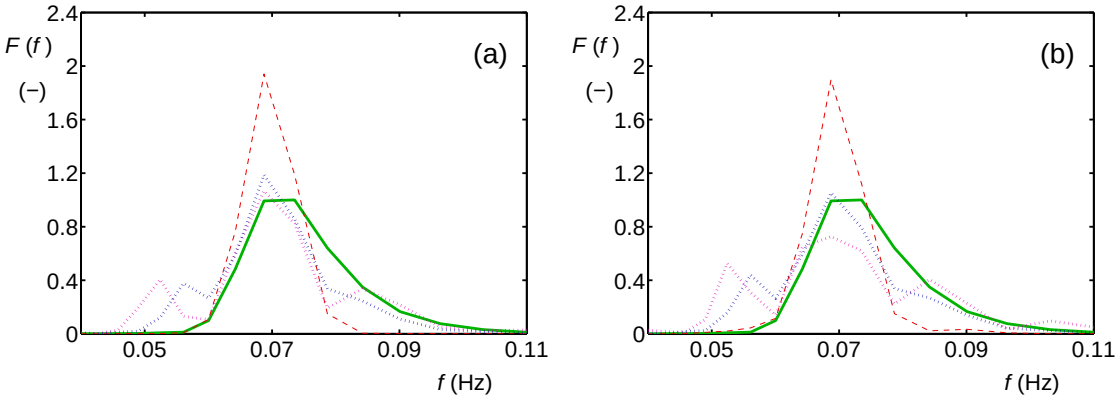

Fig. 4.19 : One-dimensional spectra $F(f)$ for test test_13 *at 3 m water depth for (a) WW3X and (b) GMD1. Solid green; WRT. Dashed red: deep water scaling only. Dotted magenta: deep and shallow water scaling. Dotted blue: separate shallow water quadruplet.*

4.5 Multi-component traditional quadruplet GMD

The next step is to introduce multiple representative quadruplets, as was done in Part 2. The deep water experiments of the latter paper are reproduced in Section 4.5.1. Additional experiments with sampling spectral space are discussed in Section 4.5.2, and the corresponding shallow water optimization experiments are presented in Section 4.5.3 through 4.5.5, and a summary of these experiments is given in Section 4.5.6.

4.5.1 Deep water, increasing number of quadruplets

Following the experience gained in Part 2, experiments with a conventional quadruplet definition and 2, 3 or 4 representative quadruplets are considered, with the expectation that the latter experiments will show no gain in accuracy compared to the experiments with 3 representative quadruplets. Population sizes used are 125, 200 and 350, respectively, and the number of generations considered are 40, 70 and 100, respectively. As expected, the experiment with 4 quadruplets gained no more accuracy, hence the discussion will concentrate on models with 2 or 3 representative quadruplets only.

Figure 4.20 presents the evolution of the minimum and average errors for cases with 2 or 3 representative quadruplets, and for three separate randomly chosen initial conditions for each configuration. The relatively early stabilization of ϵ_{min} and ϵ_{avg} suggests that fewer generations could have been used. Furthermore, not all three initial conditions result in the same 'final' errors. This may be due either to the well-known fact that final convergence of genetic methods is notoriously slow, or that distinctly different local optimal solutions in error space

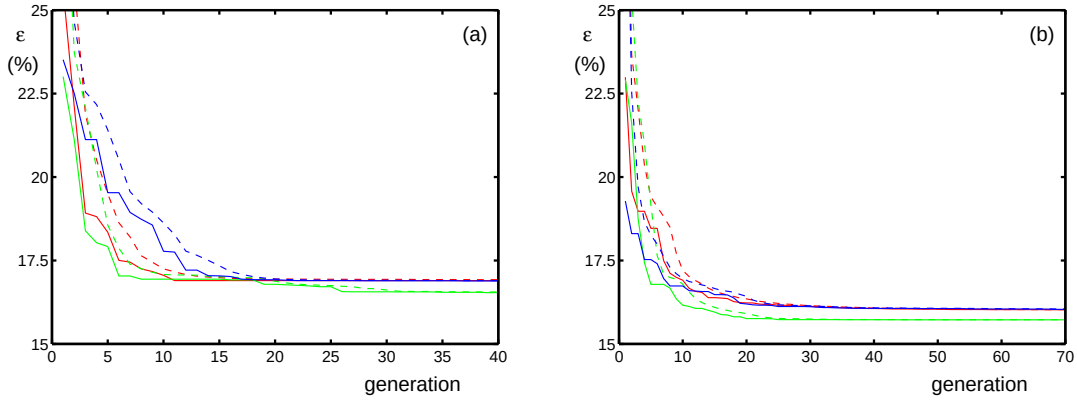

Fig. 4.20 : Like Fig. 4.16 optimizing λ and C_d using 2 representative quadruplets (panel a) or 3 representative quadruplets (panel b).

are found. An assessment can be made on which of the two reasons is responsible for this behavior when the descent method is applied to the best solutions of each genetic optimization experiment. Table 4.4 presents the optimum GMD parameter settings for deep water parameters and tests corresponding to the six optimization experiments from Fig. 4.20 after the steepest descent method was applied to the best member of the last population in the genetic optimization.

Table 4.4 shows that for both the experiments with 2 or 3 representative quadruplets ($n_q = 2$ or 3) different initial conditions can result in different optimal parameters settings. However, the fact that the experiments for $n_q = 2$ (r) and (g) result in essentially the same optimum parameter settings, as do the experiments for $n_q = 3$ (r) and (b) suggest that there are a limited number of near-optimal solutions, and that the genetic optimization results in a reasonable level of reproducibility.

An additional observation can be made from Fig. 4.20 and Table 4.4. For the experiments with $n_q = 2$ the red and green experiments result in the smallest model errors and in essentially the same GMD settings as shown in Table 4.4. However, Fig. 4.20a shows that the red experiment focused on poorer model behavior than the green experiment. This apparently is a case where the red experiment displays the difficulty of the genetic approach to effectively produce final convergence, which in this case is remedied by the subsequent steepest descent method. In contrast, the green experiment for the $n_q = 3$ in Fig. 4.20b shows the best genetic optimization results, which is also confirmed by the subsequent steepest descent method (results presented in Table 4.4). Hence, for the experiments with $n_q = 3$, the different results for the green experiment in Fig. 4.20b identifies that a different local optimum of the model errors in parameter space has indeed been found. This again illustrates the strength of the method where a genetic approach is used to find (multiple) near-optimum parameters settings,

Table 4.4: Optimal GMD setting for traditional quadruplet layout and 2 or 3 deep water quadruplets based on deep water tests only. Genetic optimization followed by steepest descent. (r), (g), and (b) refers to red, green and blue, respectively, in Fig. 4.20.

model	λ	C_d	ϵ_{tot} (%)
$n_q = 2$ (r)	0.127	$4.12\,10^7$	16.5
	0.280	$1.91\,10^7$	
$n_q = 2$ (g)	0.127	$4.09\,10^7$	16.5
	0.279	$1.95\,10^7$	
$n_q = 2$ (b)	0.181	$3.51\,10^7$	16.9
	0.318	$9.43\,10^6$	
$n_q = 3$ (r)	0.066	$5.80\,10^7$	16.0
	0.184	$4.32\,10^7$	
	0.318	$1.43\,10^7$	
$n_q = 3$ (g)	0.126	$4.79\,10^7$	15.7
	0.237	$2.20\,10^7$	
	0.319	$1.10\,10^7$	
$n_q = 3$ (b)	0.066	$5.63\,10^7$	16.0
	0.184	$4.33\,10^7$	
	0.318	$1.44\,10^7$	

which then can be used as starting point of a steepest descent method to economically perform parameter optimization.

A synopsis of the optimization results in this section is given in Fig. 4.21, which shows the optimum quadruplet (λ, C_d) settings for deep water for a GMD with the traditional quadruplet definition and $n_q = 1$ through 4 representative quadruplets. Also shown in the figure are the optimum C_d for a given λ from the mapping experiments with $n_q = 1$ in Section 4.3 (dashed lines) and the corresponding areas where such a GMD has errors less than 10, 20, 30 or 40% more than the minimum model error.

As expected, the optimum setting for the GMD with $n_q = 1$ (green symbol) coincides with the optimum results from the mapping experiments. There are clearly preferred settings of λ utilized by GMDs with different numbers of quadruplets. Moreover, optimum C_d settings for individual quadruplets for GMDs with multiple quadruplets are similar to the corresponding optimum single quadruplet GMD for the corresponding λ, but may differ by close to an order of magnitude. This suggests that multiple DIAs are not simply an averaging of optimum single DIAs, but in fact represent a more subtle interaction between quadruplets in a

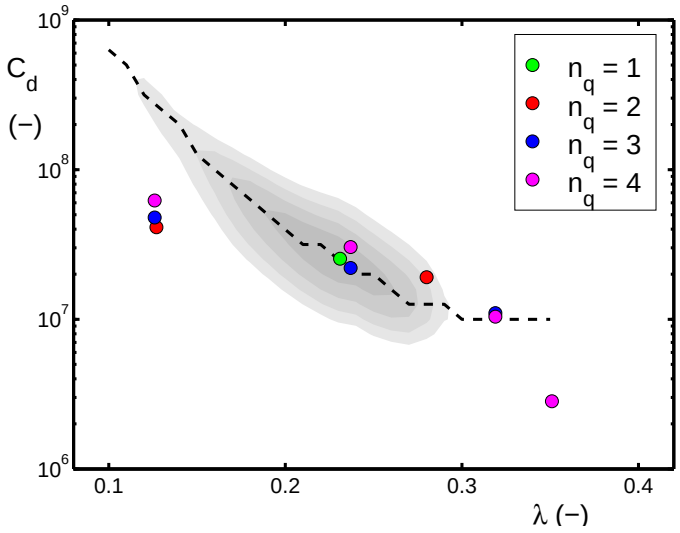

Fig. 4.21 : Synopsis of results of optimizing λ and C_d for deep water with n_q ranging from 1 to 4. Settings for optimum model only. Dashed line represents optimum C_d for given λ from mapping experiments from Section 4.3 for all deep water tests combined. Shaded areas depict areas bounded by 10% increases from minimum ϵ_{tot} for $n_q = 1$.

multiple DIA. Note that the GMD with four representative quadruplets does not add accuracy compared to the one with three quadruplets. The "fourth" quadruplet with $\lambda = 0.35$ is significantly weaker with respect to the value of C_d than expected from the single-component GMD (dashed line), which suggests that this quadruplet contributes little to this GMD.

4.5.2 Deep water, sampling of spectral space

As mentioned in Section 4.2, the next attempt to optimize the GMD is to use the quadruplet layout to sample spectral space, while optimizing the strength of the representative quadruplet (C_d) only. Initial experiments with this optimization approach showed that for several representative quadruplets C_d gravitated to its lowest allowed value in Table 3.5. This suggests that the optimum solution for such a quadruplet layout would be to not use it at all. To allow for this to happen in the optimization approach, the genetic optimization procedure has been modified slightly to allow for the quadruplet to be switched off by setting $C_d \equiv 0$ if and only if the quadruplet layout (λ, μ, and $\Delta\theta$) are predefined, and C_d drops below its minimum value allowed in Table 3.5. This switching off can occur if the drift mutation drops C_d below this value, or in 5% of the cases of re-initialization by mutation. Quadruplets are switched back on in the opposite way, allowing shift mutation to start from C_d at its minimum value.

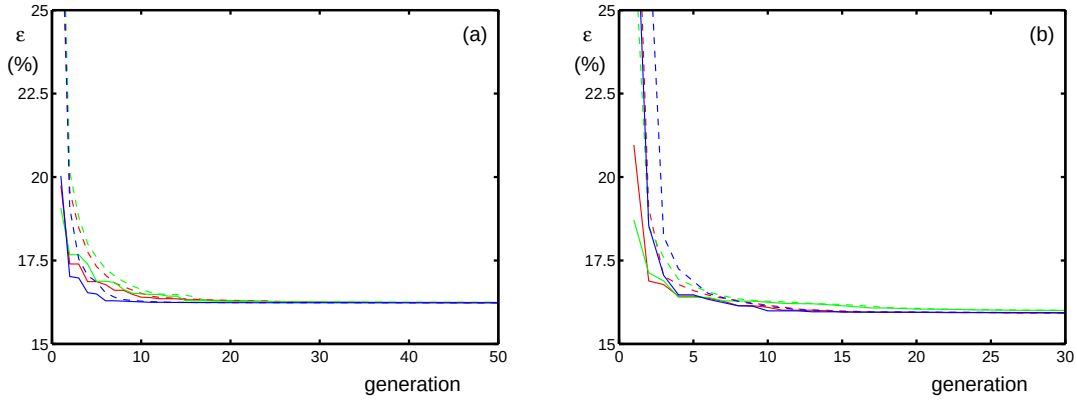

Fig. 4.22 : Like Fig. 4.16 optimizing C_d only with λ preset to sample spectral space with (a) 7 or (b) 13 quadruplets (see Tables 4.5 and 4.6).

One complication occurs if quadruplets are switched off, since this influences the normalization factor $n_{q,d}^{-1}$ in Eq. (2.30), effectively rescaling the strength of all quadruplets. To avoid that switching off one quadruplet effectively influences all other quadruplets, the strength of all other quadruplets is rescaled so that $C_d/n_{q,d}$ remains unchanged in Eq. (2.30). Experiments are performed with 7 or 13 quadruplets, as outlined in Tables 4.5 and 4.6. Population sizes are set to 300 and 500, respectively. For the first experiment, 50 generations have been used. Based on error evolution of the first experiment, and considering the increasing costs of the experiments, the second experiment was first conducted with 30 generations, and later expanded to 40. As before, the genetic optimization is followed by a steepest descent algorithm.

Error convergence plots for both experiments are presented in Fig. 4.22. For the experiment with 7 quadruplets (Fig. 4.22a), convergence of errors appears to have been reached after approximately 25 generations, although some minor improvement is seen in later generations. Final error behavior of the three sub-experiments seems to be nearly identical, with the blue experiment reaching optimum behavior somewhat faster that the red and green experiments.

The optimum results for the red, green and blue experiments with 7 conventional quadruplets sampling spectral space are presented in Table 4.5 and Fig. 4.23a. All experiments show that the optimum solution for some of the pre-selected quadruplet layouts is to not use them at all. For the red and blue experiments this is the case for the quadruplets with $\lambda = 0.300$ or 0.400. In the green experiment, the quadruplet with $\lambda = 0.400$ is also switched off, whereas the quadruplet with $\lambda = 0.150$ has an optimum setting that is several orders of magnitude smaller than that of its neighbors, and therefore for practical purposes is also switched off. With respect to the optimum settings of the other quadruplets, the red and blue experiments also as generally similar, with the green experiment

Table 4.5: Optimum C_d values for deep water optimization for 7 conventional quadruplets sampling spectral space. i_q represents the quadruplet number. Number of generations $n_g = 50$.

		experiment		
i_q	λ (-)	red	green	blue
1	0.100	$7.07\,10^7$	$9.09\,10^7$	$5.49\,10^7$
2	0.150	$1.98\,10^7$	$2.97\,10^5$	$3.36\,10^7$
3	0.200	$6.23\,10^6$	$3.87\,10^7$	$1.84\,10^6$
4	0.250	$3.96\,10^7$	$2.81\,10^7$	$3.96\,10^7$
5	0.300	—	$4.90\,10^6$	—
6	0.350	$1.00\,10^7$	$1.20\,10^7$	$1.02\,10^7$
7	0.400	—	—	—
ϵ_{tot} (%)		16.2	16.2	16.2

resulting in a distinctly different optimum setting. The resulting total errors ϵ_{tot} differ by less than 0.02%, indicating that there are several optimum solutions with near identical resulting total errors. For the red and blue experiments, the resulting error is virtually identical (difference of 0.01%) and slightly better than for the green experiment. For $\lambda = 0.250$ and 0.350 the red and blue experiments show identical optimum settings, whereas for lower values of λ the results clearly differ. This suggests that the behavior of the interactions is dominated by the former λ, and is less sensitive to the latter. This is also consistent with the results from the error mapping experiments. These indicate that dominant interactions require larger C_d for smaller λ, inconsistent with the results of Table 4.5.

Note that the minimum errors of these experiments ($\epsilon_{tot} = 16.2\%$) are lower than the optimum errors for two fully optimized quadruplets, but slightly larger than for the three fully optimized quadruplets (16.5 and 15.7%, respectively, see Table 4.4). Added complexity by considering more quadruplets therefor does not appear to pay off, consistent with the experience of fully optimizing additional quadruplets. Fixing λ rather than optimizing it dynamically results in 5 or 6 quadruplets, and hence a more expensive approximation than the approximation with three fully optimized quadruplets. At least for deep water, this added complexity and computational costs cannot be justified based on the resulting accuracy.

The optimum results for the red, green and blue experiments with 13 conventional quadruplets sampling spectral space and using $n_g = 30$ generations are presented in Table 4.6 and Fig. 4.23b. As with the experiments with 7 quadruplets, various quadruplets are switched off by the optimization. Some are actu-

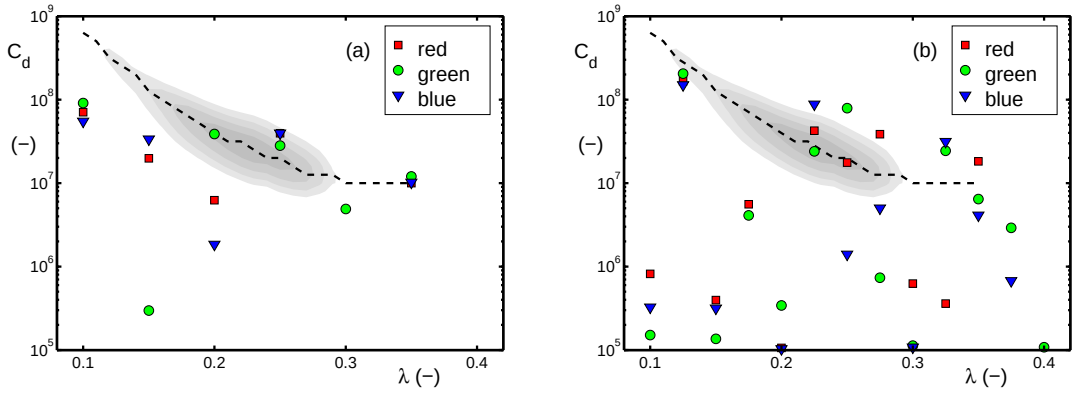

Fig. 4.23 : Like Fig. 4.21 for approach with sampling spectral space with either 7 (panel a) or 13 (panel b) quadruplets.

Table 4.6: Like Table 4.5 for 13 representative quadruplets. $n_g = 30$

		experiment		
i_q	λ (-)	red	green	blue
1	0.100	$8.17\ 10^5$	$1.51\ 10^5$	$3.25\ 10^5$
2	0.125	$1.66\ 10^8$	$2.05\ 10^8$	$1.50\ 10^8$
3	0.150	$3.97\ 10^5$	$1.36\ 10^5$	$3.16\ 10^5$
4	0.175	$5.58\ 10^6$	$4.10\ 10^6$	—
5	0.200	$1.06\ 10^5$	$3.42\ 10^5$	$1.03\ 10^5$
6	0.225	$4.24\ 10^7$	$2.40\ 10^7$	$8.80\ 10^7$
7	0.250	$1.76\ 10^7$	$7.91\ 10^7$	$1.40\ 10^6$
8	0.275	$3.85\ 10^7$	$7.35\ 10^5$	$5.00\ 10^6$
9	0.300	$6.26\ 10^5$	$1.13\ 10^5$	$1.08\ 10^5$
10	0.325	$3.60\ 10^5$	$2.44\ 10^7$	$3.14\ 10^7$
11	0.350	$1.82\ 10^7$	$6.43\ 10^6$	$4.11\ 10^6$
12	0.375	—	$2.91\ 10^6$	$6.75\ 10^5$
13	0.400	—	$1.88\ 10^5$	—
ϵ_{tot} (%)		15.922	16.003	15.932

Table 4.7: Like Table 4.5 for 13 representative quadruplets. $n_g = 40$

		experiment		
i_q	λ (-)	red	green	blue
1	0.100	$6.59\,10^5$	$1.41\,10^5$	$2.05\,10^5$
2	0.125	$1.51\,10^8$	$2.06\,10^8$	$1.23\,10^8$
3	0.150	—	$1.37\,10^5$	—
4	0.175	$5.07\,10^6$	$4.36\,10^6$	$1.66\,10^5$
5	0.200	$9.62\,10^4$	$7.05\,10^5$	—
6	0.225	$3.85\,10^7$	$2.83\,10^7$	$7.20\,10^7$
7	0.250	$1.41\,10^7$	$7.31\,10^7$	$1.14\,10^6$
8	0.275	$3.37\,10^7$	$7.35\,10^5$	$4.10\,10^6$
9	0.300	$5.69\,10^5$	$1.13\,10^5$	—
10	0.325	$2.85\,10^5$	$2.41\,10^7$	$2.58\,10^7$
11	0.350	$1.75\,10^7$	$7.71\,10^6$	$3.36\,10^6$
12	0.375	—	$2.67\,10^6$	$5.34\,10^5$
13	0.400	—	$1.08\,10^5$	—
ϵ_{tot} (%)		15.911	15.986	15.930

ally switched off, some are effectively switched off by the resulting low values of C_d. Many of the latter quadruplet strengths C_d are several orders of magnitude smaller than expected based on the optimum C_d value for a GMD with only one representative quadruplet, as is illustrated in Fig. 4.23b. Results in general follow the results from the experiments with 7 equally spaced quadruplets. For some values of λ, the red, green and blue experiments result in near identical solutions, yet for others they are large enough to contribute, yet significantly different per experiment, This again indicates that there is no clear "best" solution. As with the previous experiment, the resulting total error of approximately 16% is no better than the total error obtained with three fully optimized quadruplets, which does not justify the use of this much more expensive approach.

The present expensive approach can be made cheaper by switching off quadruplets that do not contribute to the solution. To this end, two additional experiments have been performed. First, the existing experiment was extended to include 40 generations, to assess if additional optimization switches off additional quadruplets, or conversely, switches them back on. The resulting optimum quadruplet settings for the red green and blue experiments are presented in Table 4.7. Additional optimization indeed switches off a few more components, but also leaves most components with very small C_d in the optimum settings. The latter could be expected based on the characteristics of the optimization procedure.

Table 4.8: Like Table 4.5 reducing the number of quadruplets interactively and re-optimizing by steepest decent only. the starting point is the red experiment in Table 4.7.

i_q	λ (-)	$n_q = 10$	$n_q = 9$	$n_q = 8$	$n_q = 7$	$n_q = 6$	$n_q = 5$
1	0.100	$6.59\,10^5$	$5.93\,10^5$	—	—	—	—
2	0.125	$1.51\,10^8$	$1.36\,10^8$	$1.21\,10^8$	$1.06\,10^8$	$9.09\,10^7$	$7.84\,10^7$
3	0.150	—	—	—	—	—	—
4	0.175	$5.07\,10^6$	$4.67\,10^6$	$4.16\,10^6$	$3.73\,10^6$	$3.20\,10^6$	—
5	0.200	$9.62\,10^4$	—	—	—	—	—
6	0.225	$3.85\,10^7$	$3.47\,10^7$	$3.09\,10^7$	$2.70\,10^7$	$2.34\,10^7$	$2.12\,10^7$
7	0.250	$1.41\,10^7$	$1.27\,10^7$	$1.13\,10^7$	$9.89\,10^6$	$8.51\,10^6$	$7.12\,10^6$
8	0.275	$3.37\,10^7$	$3.03\,10^7$	$2.69\,10^7$	$2.35\,10^7$	$2.03\,10^7$	$1.66\,10^7$
9	0.300	$5.69\,10^5$	$5.25\,10^5$	$4.68\,10^5$	$4.09\,10^5$	—	—
10	0.325	$2.85\,10^5$	$2.57\,10^5$	$2.28\,10^5$	—	—	—
11	0.350	$1.75\ 10^7$	$1.57\,10^7$	$1.40\,10^7$	$1.25\,10^7$	$1.08\,10^7$	$9.00\,10^6$
12	0.375	—	—	—	—	—	—
13	0.400	—	—	—	—	—	—
ϵ_{tot} (%)		15.911	15.911	15.910	15.908	15.905	15.905

If such quadruplets do not contribute to the solution, changing them (including switching them off) will not improve the solution, and hence will not be identified as a better solution by the genetic optimization algorithms. Alternatively, weak quadruplets can be switched off by hand, while rescaling the remaining quadruplets to conserve $C_d/n_{q,d}$, and followed by a steepest descent method to obtain a new optimum solution. If the quadruplet could be switched off safely, there will be no notable change in the resulting total model error. Results of such an experiment are presented in Table 4.8 and Fig. 4.24.

The strategy to remove quadruplets from this configuration is using the distance of the strength C_d compared to the optimum setting for a single component GMD (dashed line) in Fig. 4.24. The corresponding order of quadruplets to be removed is i_q = 5, 1, 10, 9 and 4, to reduce the number of active quadruplets from 10 out of 13 to 5 out of 13. The corresponding total model errors ϵ_{tot} as re-optimization can be found in Table 4.8. Each quadruplet is disabled by removing it altogether, reducing $n_{q,d}$ in Eq. (2.30). Because the effective magnitude of all remaining quadruplets is $C_d/n_{q,d}$, this effectively increases the effective strength of each quadruplet by

$$\frac{n_{q,d,old}}{n_{q,d}} = \frac{n_{q,d}+1}{n_{q,d}} \quad , \tag{4.1}$$

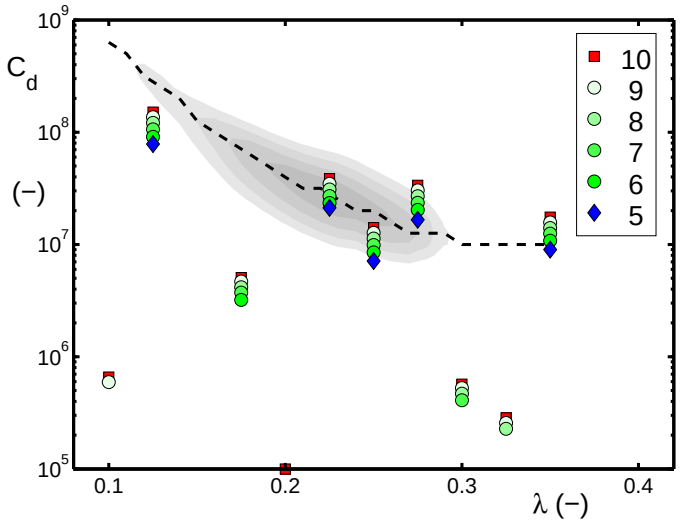

Fig. 4.24 : Like Fig. 4.21 reducing the number of active quadruplets in the 'red' experiment sampling spectral space starting with $n_q = 13$. Legend identifies number of active quadruplets. See also Table 4.8.

where $n_{q,d}$ represents the new number of quadruplets, which here is one less than the old number. To ensure that the removal of quadruplets with negligible strength does not change results, all remaining strengths C_d need to be reduced by the factor in (4.1).

The successive removal of quadruplets with negligible strength down to $n_q = 5$ does have little impact on the errors of the GMD, provided that the the remaining components are rescaled. Subsequent optimization using steepest descent methods generally results in slightly better model behavior, as is shown in Table 4.8. Changes in C_d while reducing n_q $(= n_{q,d})$ are dominated by the rescaling, as is particularly clear in Fig. 4.24. With $n_q = 5$, all remaining quadruplets have strengths close to those expected based on optimization of a model with $n_q = 1$, and hence no clear path to removal of additional quadruplets is available. Note that the results with 5 quadruplets remaining are comparable to the result obtained from full optimization of quadruplets as shown in Fig. 4.21, and that the remaining errors (15.9%) are compatable with the optimum results for $n_q = 3$ with full quadruplet optimization (15.7%). Considering this, the added computational effort for the sampling approach with $n_q = 5$ quadruplets remaining cannot be justified based on deep water only. It does, however, represent a more controlled optimization environment, which will be useful to explore in shallow water also.

Table 4.9: Overall errors in % for each test case for the GMD configurations in Tables 4.2 (GMD1) and 4.4 (GMD2, $n_q = 2$ red; GMD3, $n_q = 3$ green). $C_s \equiv 0$ and $m = 0$ for all experiments.

	test case									
	01	02	03	04	05	06	11	12	13	tot
WW3X	27.4	27.7	22.5	25.1	26.5	29.8	24.6	29.4	83.5	32.9
GMD1	22.2	21.7	19.1	20.4	20.5	23.1	21.1	28.3	83.3	28.8
GMD2	16.9	15.6	15.1	16.5	16.1	19.0	17.1	22.2	103.7	26.9
				($m = -6.87$)			17.0	24.0	83.2	24.8
GMD3	15.2	14.6	15.1	17.1	15.0	17.3	16.1	21.6	97.3	25.5
				($m = -5.07$)			16.0	23.0	82.3	24.0
$s_{nl} \equiv 0$									83.6	

4.5.3 Shallow water, deep water quadruplets

The next step is to optimize the GMD based solely on the traditional quadruplet for shallow water, but with multiple representative quadruplets. Starting points will be the two- and three-quadruplet results from the red and green experiments in Table 4.4, respectively. First, the behavior of a pure deep-water setup in shallow water tests will be addressed, to provide a baseline, and to look at the impact of choosing the value of m in the deep water scaling. Results for such GMDs with $n_q = 1$, 2 and 3, $m = 0$ and $C_s \equiv 0$ are presented in Table 4.9.

With increasing complexity and optimization of the GMD, i.e., going down in Table 4.9, it is expected that errors are systematically reduced. this indeed is the case for the total error, and for the errors of nearly all individual tests. However, it is not the case for the shallow water swell propagation test test_13. For this test, configurations GMD2 and GMD3 have significantly larger errors than WW3X and GMD1, with the latter two tests resulting in errors nearly identical to those obtained by ignoring S_{nl} (last line in the table). Spectra at shallow water for this test (Fig. 4.25a) are virtually identical, and do not account for the increase in error. Close inspection of errors for all parameters shows that the increased error is due to errors in the nonlinear interactions at the deeper water near the offshore boundary of the model (Fig. 4.25b). Since this error is fairly irrelevant for the resulting spectral shape, it could be ignored by reducing the weight for this error parameter for this test. However, one of the ideas behind full holistic optimization is that all errors are accounted for, including these, hence it is worth while to assess if this error can be reduced by optimizing m.

Optimization of m for the GMD2 and GMD3 model setup were performed using a simple genetic optimization with a population size of 20 and 5 generations.

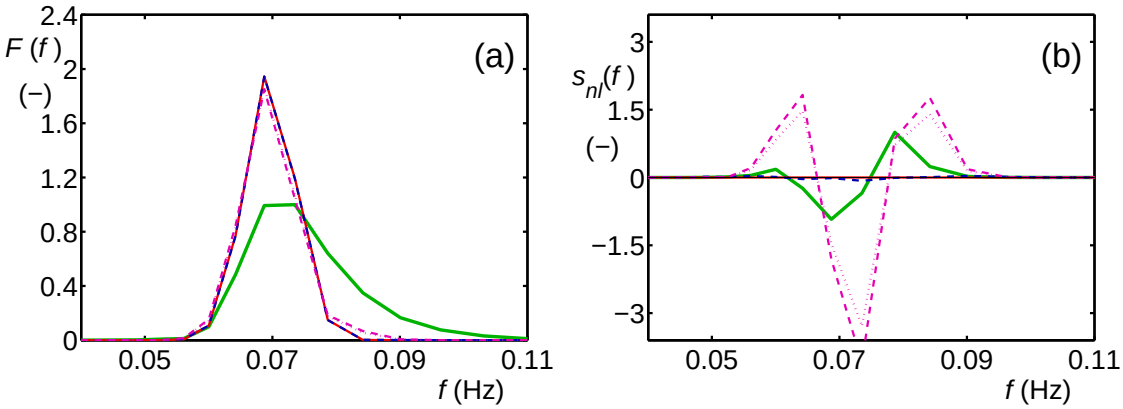

Fig. 4.25 : (a) One-dimensional spectra $F(f)$ at 3 m water depth and (b) source terms $s_{nl}(f)$ at 40 m water depth for test test_13. *Solid green: WRT. Solid red: $S_{nl} \equiv 0$. Dashed blue: GMD1. Dashed magenta: GMD2. Dotted magenta: GMD3.*

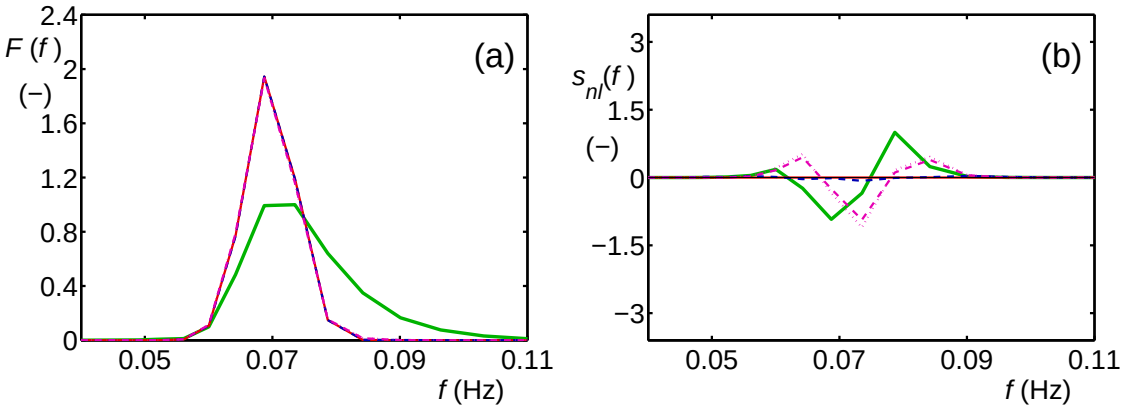

Fig. 4.26 : Like Fig. 4.25 for optimized m in GMD2 and GMD3,

Considering that S_{nl} needs to be suppressed further for intermediate depths, values of $m \in [-8, 4]$ are allowed, well out of the expected range of this parameter (i.e., $m \in [0, 8]$). The resulting values of m are presented in Table 4.9, together with the resulting shallow water test errors, and composite errors. Note that the deep water test errors for these model settings are not repeated, since they are independent of the choice of m. Optimization of m indeed dramatically improves the errors of the swell propagation test test_13, even improving upon the results obtained by ignoring S_{nl} altogether. Note that this improvement comes at the expense of a slight degradation in the performance for the test with wind seas on a beach (test_12). Nonlinear interactions at the deeper part of the domain improve dramatically (see Fig. 4.26).

Considering the above, both C_s and m will need to be optimized for the GMD

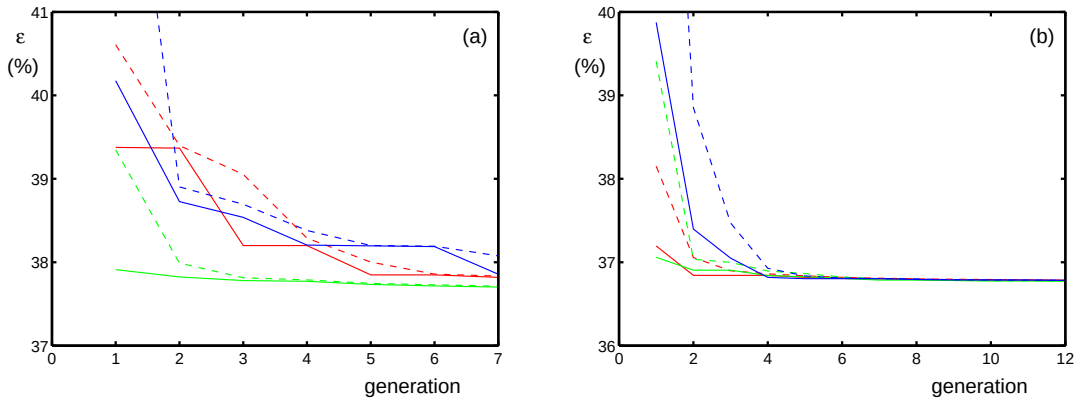

Fig. 4.27 : Like Fig. 4.16 for adding optimal shallow water scaling to previously optimized deep water configurations for cases with (a) two quadruplets ($n_q = 2$) or (b) three quadruplets ($n_q = 3$). Quadruplets and resulting constants are presented in Tables 4.10 and 4.11.

Table 4.10: Optimal GMD setting for traditional quadruplet layout and two deep water quadruplets, adding shallow water scaling to deep water quadruplets, using shallow water tests only. (r), (g), and (b) refers to red, green and blue, respectively, in Fig. 4.27. $n = -3.5$

model	λ	C_d	C_s	m	ϵ_{tot} (%)
GMD2	0.127	$4.12\,10^7$	—	-6.87	41.4
	0.280	$1.91\,10^7$	—		
$n_q = 2$ (r)	0.127	$4.12\,10^7$	$6.31\,10^4$	-10.21	37.6
	0.280	$1.91\,10^7$	$4.74\,10^5$		
$n_q = 2$ (g)	0.127	$4.12\,10^7$	$6.01\,10^4$	-10.27	37.6
	0.280	$1.91\,10^7$	$4.69\,10^5$		
$n_q = 2$ (b)	0.127	$4.12\,10^7$	$6.42\,10^4$	-10.26	37.6
	0.280	$1.91\,10^7$	$4.61\,10^5$		

Table 4.11: Like Table 4.10 for GMD with three representative quadruplets.

model	λ	C_d	C_s	m	ϵ_{tot} (%)
GMD3	0.126	$4.79\,10^7$	—	-5.07	40.4
	0.237	$2.20\,10^7$	—		
	0.319	$1.10\,10^7$	—		
$n_q = 3$ (r)	0.126	$4.79\,10^7$	$7.80\,10^4$	-7.60	36.8
	0.237	$2.20\,10^7$	$4.16\,10^5$		
	0.319	$1.10\,10^7$	$3.87\,10^5$		
$n_q = 3$ (g)	0.126	$4.79\,10^7$	$6.64\,10^4$	-7.10	36.8
	0.237	$2.20\,10^7$	$5.16\,10^5$		
	0.319	$1.10\,10^7$	$2.80\,10^5$		
$n_q = 3$ (b)	0.126	$4.79\,10^7$	$6.53\,10^4$	-7.29	36.8
	0.237	$2.20\,10^7$	$6.27\,10^5$		
	0.319	$1.10\,10^7$	$5.00\,10^4$		

with $n_g = 2$ or 3. Population sizes are set to 50 and 75, respectively, considering 7 and 12 generations. Error evolutions of these experiments are presented in Fig. 4.27, and optimum parameter settings and resulting errors are presented in Tables 4.10 and 4.11.

For the experiments with 2 representative quadruplets, 7 generations appear only borderline sufficient (Fig. 4.27a), but the corresponding final configurations after descent optimization are essentially identical. Note that the optimum values for m after descent optimization in Table 4.10 are smaller than allowed in the genetic optimization. For the experiments with 3 representative quadruplets, 12 generations appear sufficient (Fig. 4.27b). Results after descent optimization are similar for the red and green experiments, but somewhat different for the blue experiments (Table 4.12). All experiments have similar resulting errors, with the green experiment having marginally smaller errors. Note that in this case values of m remained in the preset range for the generic optimization.

The optimized GMDs presented in this section show a clearly reduced error for the shallow water test cases compared to the previously optimized GMDs. Considering that the latter GMDs showed aphysical behavior for swell spectra in shallow water for test `test_13`, it is prudent to consider these conditions for present optimized parameterizations too. The corresponding shallow water spectra and source terms are presented in Fig. 4.28 a and b, respectively. The two optimized GMDs presented here show the same spurious spectral peak at low frequencies, and a corresponding signature in the nonlinear interactions, albeit less pronounced than in previously optimized shallow water GMDs.

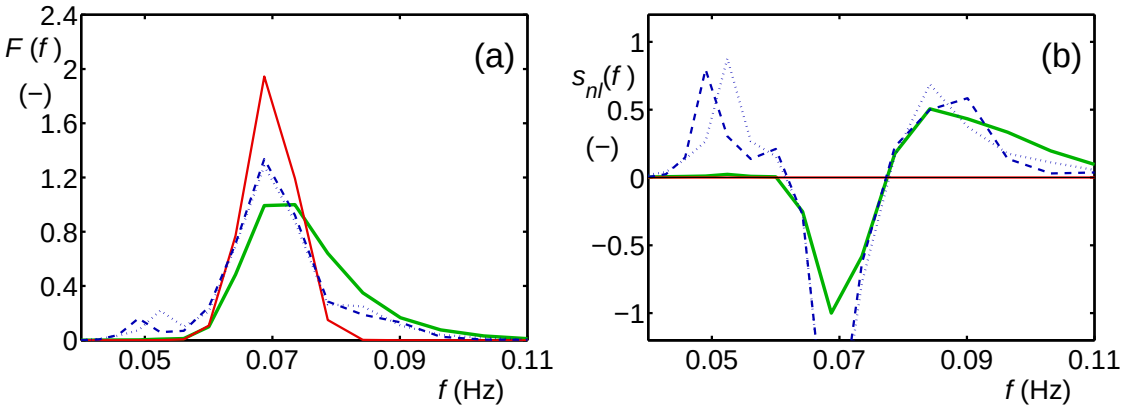

Fig. 4.28 : (a) One-dimensional spectra $F(f)$ for test test_13 *at 3 m water depth and (b) corresponding nonlinear interactions $s_{nl}(f)$ for results of Tables 4.10 and 4.11. green solid line: WRT. red solid line: no S_{nl}. blue dashed line: $n_q = 2$ (green exp.). blue dotted $n_q = 3$ (green exp.).*

4.5.4 Shallow water, separate quadruplets

The next step is to add separate shallow water quadruplets, optimizing both λ and C_s. Following the practice of the previous paragraph, m is optimized simultaneously. This still leaves many possible model configurations, since any number of shallow water quadruplets can be added to the pre-selected number of deep water quadruplets. To limit the number of configurations to be optimized, only configurations with two (three) shallow water quadruplets added to two (three) deep water quadruplets are considered here. Note that the saturation with respect to numbers of shallow water quadruplets will be assessed when considering sampling of spectral space in the following section. As in previous experiments, three initial conditions are considered per experiment. The experiments with '2+2' or '3+3' quadruplets consider populations with 125 and 175 members, and 20 and 25 generations, respectively. Error convergence plots are presented in Fig. 4.29, and resulting quadruplets and total (shallow water) errors are presented in Tables 4.12 and 4.13.

For both experiments, the error plots in Fig 4.29 suggest reasonable convergence for the optimization experiments. Both experiments, however, indicate that there are multiple near-optimal solutions, with the smallest minimum errors found in the green and blue experiments respectively (Tables 4.12 and 4.13. As in the previous section, the value of m for the '2+2' experiments is brought out of the range accepted in the genetic optimization by the steepest descent optimization, whereas the value for the '3+3' remains in this range. For both sets of experiments, fully optimizing the shallow water quadruplet reduces the overall error for shallow water tests by approximately 0.4%, compared to the corresponding experiments where only C_s was optimized.

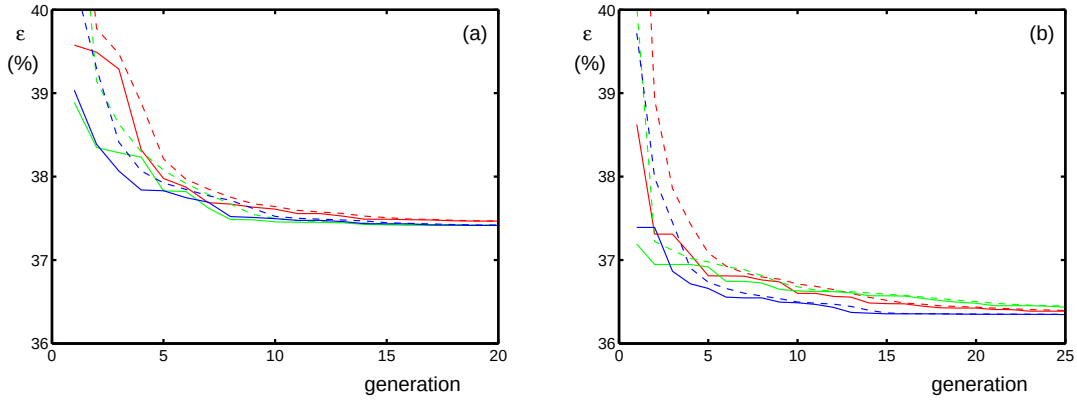

Fig. 4.29 : Like Fig. 4.16 for adding optimal shallow water quadruplets to previously optimized deep water quadruplets for cases with (a) 2+2 quadruplets ($n_q = 4$) or (b) 3+3 quadruplets ($n_q = 6$). Quadruplets and resulting constants are presented in Tables 4.12 and 4.13.

Table 4.12: Optimal GMD setting for traditional quadruplet layout and 2 deep water quadruplets, adding 2 shallow water quadruplets, based on shallow water tests only. Genetic optimization followed by steepest descent.(r), (g), and (b) refers to red, green and blue, respectively, in Fig. 4.29. $n = -3.5$. Deep water quadruplets are identical for all configurations, and are presented only for first configuration.

model	λ	C_d	C_s	m	ϵ_{tot} (%)
$n_q = 4$ (r)	0.127	$4.12\ 10^7$	—	-9.65	37.4
	0.280	$1.91\ 10^7$	—		
	0.079	—	$3.61\ 10^4$		
	0.237	—	$5.06\ 10^5$		
$n_q = 4$ (g)	0.184	—	$2.81\ 10^5$	-9.88	37.3
	0.376	—	$4.03\ 10^5$		
$n_q = 4$ (b)	0.184	—	$2.79\ 10^n$	-9.80	37.3
	0.375	—	$4.07\ 10^n$		

Table 4.13: Like Table 4.12 for three deep water quadruplets adding three shallow water quadruplets.

model	λ	C_d	C_s	m	ϵ_{tot} (%)
$n_q = 6$ (r)	0.126	$4.79\,10^7$	—	-7.47	36.4
	0.237	$2.20\,10^7$	—		
	0.319	$1.10\,10^7$	—		
	0.020	—	$1.65\,10^5$		
	0.184	—	$3.91\,10^5$		
	0.373	—	$6.72\,10^5$		
$n_q = 6$ (g)	0.023	—	$1.31\,10^5$	-7.50	36.4
	0.184	—	$3.85\,10^5$		
	0.375	—	$6.21\,10^5$		
$n_q = 6$ (b)	0.048	—	$4.61\,10^4$	-7.50	36.3
	0.184	—	$3.64\,10^5$		
	0.373	—	$6.65\,10^5$		

Considering that the previous shallow water optimization experiments resulted in spurious spectral peaks at low frequencies for the swell experiment test_13, this test is addressed in some more detail here in Fig. 4.30. Both optimized configurations from this section do show a spurious low-frequency peak in the swell spectra in shallow water, albeit much less pronounced than for the single component GMD1, and shifted compared to the 2 and 3 component GMDs from the previous section (compare Fig 4.28 to Fig 4.19 on page 81).

4.5.5 Shallow water, sampling of spectral space

The final attempt to optimize the GMD based on the traditional quadruplet definition of the DIA will consider sampling of spectral space with preset values of λ. Considering the results of such an optimization experiment for deep water only (Section 4.5.2), only the "high-resolution" case with 13 quadruplets will be considered, and for this experiment consecutive switching off of components with low strength will be considered. A quick initial optimization experiment with 20 population members and 5 generations resulted in a optimum value of $m = -4.96$ and suggests that m should be optimized together with the values of C_s as in the previous sections.

Initial optimization experiments by sampling spectral space start with the deep water setup with $n_{q,d} = 5$ from Table 4.8, while optimizing all 13 values of C_s and a single value for m. As before, three sets of initial conditions are used. The population size was set to 400, and initially 20 generations were considered.

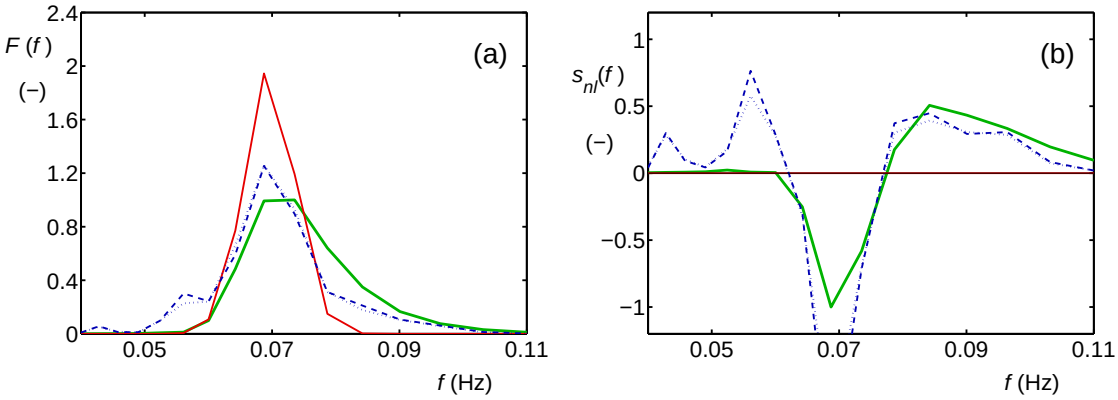

Fig. 4.30 : Like Fig. 4.28 for separate deep and shallow water quadruplets (green and blue experiments, respectively).

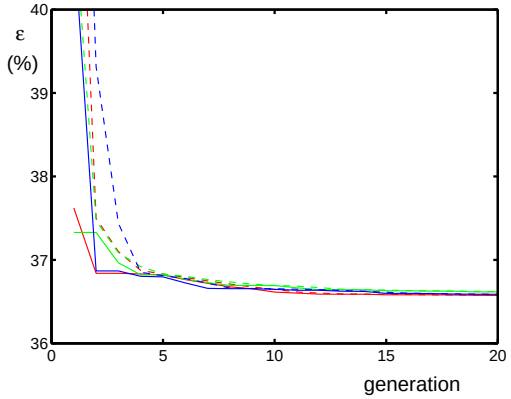

Fig. 4.31 : Like Fig. 4.16 for adding optimal shallow water scaling to 13 quadruplets sampling spectral space. Quadruplets and resulting constants are presented in Table 4.14.

The error evolution is presented in Fig. 4.31. Based on this figure, 20 generations appear adequate, which is confirmed by the small corrections made by the descent algorithm. In fact, the major contribution of the descent algorithm is to switch off many of the quadruplets with small C_s as obtained from the genetic optimization.

The resulting quadruplet configurations for the three experiments (after genetic and descent optimization) are presented in Table 4.14 and Fig. 4.32a. Again, many pre-selected quadruplets are disabled by the optimization procedure. Note that in this case, the genetic optimization resulted in small C_s, whereas the descent optimization switched most of these quadruplets off in the red experiments, but left many switched on in the green and blue experiments. As in deep water experiments, non-contributing quadruplets have been switched off, after which model errors were recalculated (without further descent optimization). The lat-

Table 4.14: Optimum C_s and m values for shallow water optimization for 13 conventional quadruplets sampling spectral space. Deep water settings from Table 4.8, with $n_q = 5$. i_q represents the quadruplet number. Number of generations $n_g = 20$.

			C_s from experiment		
i_q	λ (-)	C_d	red	green	blue
1	0.100	—	$5.95\,10^4$	$1.79\,10^5$	$1.05\,10^5$
2	0.125	$7.84\,10^7$	—	—	—
3	0.150	—	—	$3.16\,10^4$	—
4	0.175	—	—	$1.11\,10^3$	$2.65\,10^4$
5	0.200	—	$7.85\,10^5$	$4.64\,10^5$	$1.23\,10^6$
6	0.225	$2.12\,10^7$	—	$2.63\,10^4$	$3.26\,10^4$
7	0.250	$7.12\,10^6$	—	$1.62\,10^6$	—
8	0.275	$1.66\,10^7$	—	$1.97\,10^5$	$8.08\,10^3$
9	0.300	—	—-	$3.57\,10^3$	$1.24\,10^4$
10	0.325	—	$5.03\,10^3$	$2.51\,10^3$	$1.66\,10^5$
11	0.350	$9.00\,10^6$	$4.22\,10^5$	$1.26\,10^5$	$8.50\,10^4$
12	0.375	—	$6.05\,10^5$	$2.10\,10^3$	$6.02\,10^5$
13	0.400	—	$2.21\,10^5$	$8.10\,10^5$	$1.39\,10^6$
m (-)			-7.41	-7.29	-7.43
ϵ_{tot} (%)			36.568	36.616	36.581

ter results are presented in Table 4.15 and Fig. 4.32b, suggesting that only 5 or 6 of the thirteen quadruplet configurations contribute to the shallow water performance of the GMD. Comparison of total errors presented in Tables 4.14 and 4.15 strongly indicate that the removed weak quadruplets indeed do not contribute to this GMD parameterization.

A comparison of the tables and figure panels suggest that the resulting red and blue configurations are similar, with a distinctly different green configuration, but all result in similar total errors. Because configurations are different, and because the spurious peaks in the swell spectra for `test_13` only contribute to one of many error measures considered, it is interesting to check the resulting spectra and source terms for all three configurations. Some resulting spectra and source terms are presented in Fig. 4.33. Indeed, the green experiment produces notably different spectra and source terms than the red and blue experiments. The differences are most pronounced in the representation of the spurious spectral peak for low frequencies, which is much more pronounced in the green experiment, but also shows differences between the red and blue experiments. Note that for

Table 4.15: Like Table 4.14 after removal of non-contributing quadruplets and additional descent optimization.

i_q	λ (-)	C_d	C_s from experiment red	green	blue
1	0.100	—	$4.96\,10^4$	$8.95\,10^4$	$6.30\,10^4$
2	0.125	$7.84\,10^7$	—	—	—
3	0.150	—	—	—	—
4	0.175	—	—	—	—
5	0.200	—	$6.54\,10^5$	$2.32\,10^5$	$7.38\,10^5$
6	0.225	$2.12\,10^7$	—	—	—
7	0.250	$7.12\,10^6$	—	$8.10\,10^5$	—
8	0.275	$1.66\,10^7$	—	$9.85\,10^4$	—
9	0.300	—	—	—	—
10	0.325	—	—	—	$9.96\,10^4$
11	0.350	$9.00\,10^6$	$3.52\,10^5$	$6.30\,10^4$	$5.10\,10^4$
12	0.375	—	$5.04\,10^5$	—	$3.61\,10^5$
13	0.400	—	$1.84\,10^5$	$4.05\,10^5$	$8.34\,10^5$
m (-)			-7.41	-7.29	-7.43
ϵ_{tot} (%)			36.568	36.617	36.578

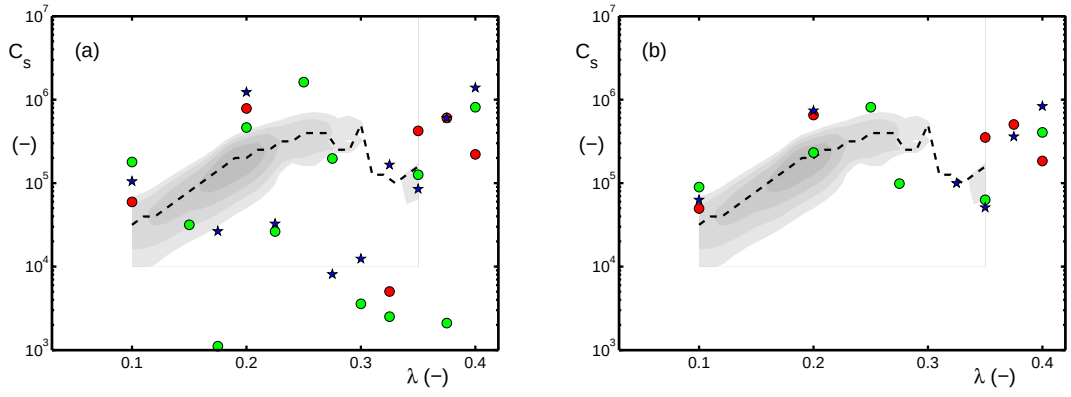

Fig. 4.32 : Synopsis of results of optimizing C_s while sampling spectral space with 13 quadruplets and deep water settings from Table 4.8 with $n_q = 5$. Dashed line represents optimum C_s for given λ from mapping experiments from Section 4.3 for all shallow water tests combined. Shaded areas depict areas bounded by 10% increases from minimum ϵ_{tot} for $n_q = 1$. (a) original optimization. (b) After removal of non-contributing quadruplets.

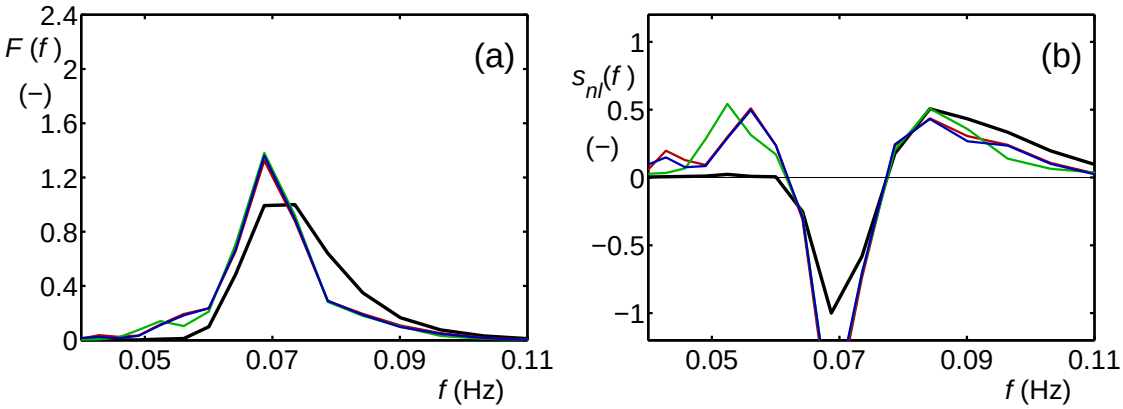

Fig. 4.33 : (a) One-dimensional spectra $F(f)$ for test test_13 *at 3 m water depth and (b) corresponding nonlinear interactions $s_{nl}(f)$ for results of Table 4.15. Black solid line: WRT. Other colors correspond to experiment in the Table.*

shallow water, sampling of spectral space does appear to be able to suppress spurious spectral peaks, although they still appear at the shallowest depths in the test case (not presented here).

4.5.6 Summary

In Sections 4.4 and 4.5 a GMD with the traditional quadruplet layout of the DIA has been optimized using one or more representative quadruplets. The optimization has been performed either by optimizing the full quadruplet layout, or by predetermining the sampling of spectral space by predefining a number of quadruplets with given λ. The experiments indicate that not much accuracy is gained by adding more than 3 or 4 fully optimized quadruplets, and that when sampling spectral space, no more than 5 deep water and 6 shallow water quadruplets contribute to the accuracy of the model, with different quadruplets contributing to deep and shallow water, respectively. A synopsis of the errors for various optimized GMDs with increasing complexity is presented in Table 4.16.

Adding quadruplets (going from GMD to GMD3) systematically reduces the errors for the deep water tests. Sampling of the spectral space (GS13), results in errors comparable to those of GMD3, but shows no further improvement. Total errors per test are reduced by typically 40% compared to the standard DIA approach from the WAVEWATCH III model (WW3X). For shallow water, test_11 and test_12 show a significant benefit from better deep water behavior of the corresponding GMD, suggesting the obvious conclusion that accurate shallow water modeling requires accurate deep water modeling. For the pure swell case of test_13, boundary conditions are predefined, and errors are much less impacted by deep water behavior of the model, although intermediate water depth behavior

Table 4.16: Synopsis of errors in % for optimized configurations for the GMD configurations with traditional quadruplet layout. GMD1 : $n_q = 1$ for deep water only, GMD1s : $n_q = 1$ for deep and shallow water, GMD1s1 : $n_q = 1 + 1$, etc. GMD1 with $m = 0$, others with optimized m. GS13 refers to sampling spectral space with 13 quadruplets.

	test case									
	01	02	03	04	05	06	11	12	13	tot
WW3X	27.4	27.7	22.5	25.1	26.5	29.8	24.6	29.4	83.5	32.9
GMD1	22.2	21.7	19.1	20.4	20.5	23.1	21.1	28.3	83.3	28.8
GMD1s							21.1	29.9	74.3	28.0
GMD1s1							21.1	28.8	72.0	27.7
GMD2	16.9	15.6	15.1	16.5	16.1	19.0	17.0	24.0	83.2	24.8
GMD2s							17.2	23.8	71.6	23.5
GMD2s2							17.2	23.8	70.9	23.5
GMD3	15.2	14.6	15.1	17.1	15.0	17.3	16.0	23.0	82.3	24.0
GMD3s							16.0	22.6	72.3	22.8
GMD3s3							16.2	23.1	69.9	22.6
GS13	15.1	14.7	15.5	18.0	15.0	17.1	15.8	23.1	82.4	24.1
GS13s(b)							16.0	23.1	70.7	22.8

governed by the scaling constant m has some impact here. Apparently, accurate description of effects of nonlinear interactions on swell in shallow water represent the most difficult conditions for a GMD based on the traditional quadruplet to represent, considering the moderate improvements of the errors for this test, and considering the spurious model behavior for this test case as discussed above.

A synopsis of the resulting quadruplets is presented in Fig. 4.34. For deep water, the configurations with multiple representative quadruplets result in quadruplet strengths C_d for the corresponding layout parameter λ (symbols in figure) that are relatively close to the optimal value for C_d for a single given λ (dashed line and shaded areas in figure, well within an order of magnitude difference).

The impact of the optimization with increasingly complex GMD configurations has been assessed by inspecting results for all test parameters for all test cases. The results are illustrated here with selected test cases only. In general, increasing complexity of the GMD will lead to increasing accuracy. However, results for tests evolving in either space or time do differ. Figures 4.35 and 4.36 show mean wave parameters for tests test_05 and test_06, respectively, to illustrate these differences.

The traditional DIA as used in the default wave model settings (WW3X)

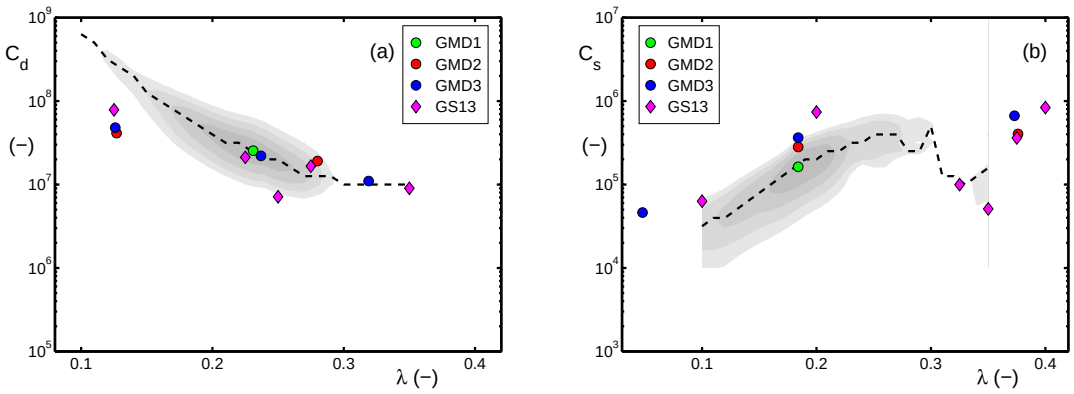

Fig. 4.34 : Synopsis of results of (a) optimizing λ and C_d for deep water or (b) optimizing λ and C_s for shallow water. Dashed line represents optimum C_d or $C_s$for given λ from mapping experiments from Section 4.3. Shaded areas depict areas bounded by (a) 10% and (b) 1% increases from minimum ϵ_{tot} for $n_q = 1$.

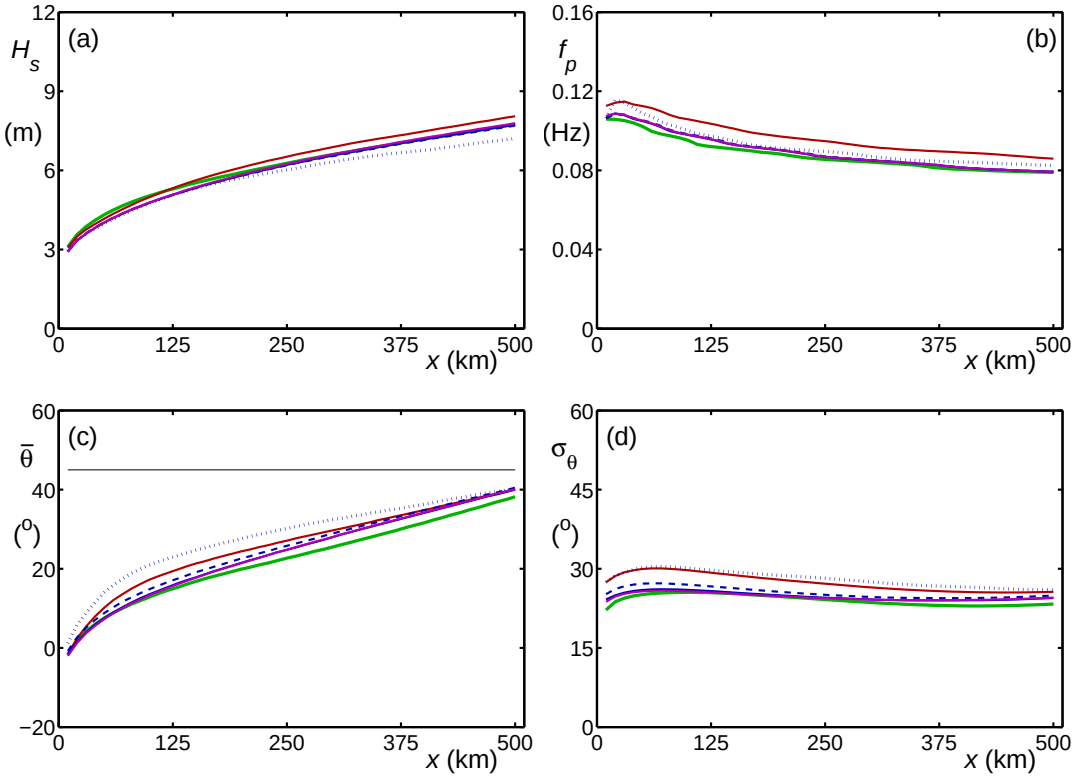

Fig. 4.35 : Evolution in time of a) significant wave height H_s, b) peak frequency f_p, c) mean direction $\overline{\theta}$, and d) directional spread σ_θ for the slanting fetch test test_05*. Green line: WRT. Red line: WW3. Dotted / dashed / solid blue lines: GMD1 / GMD2 / GMD3. Purple line GS13.*

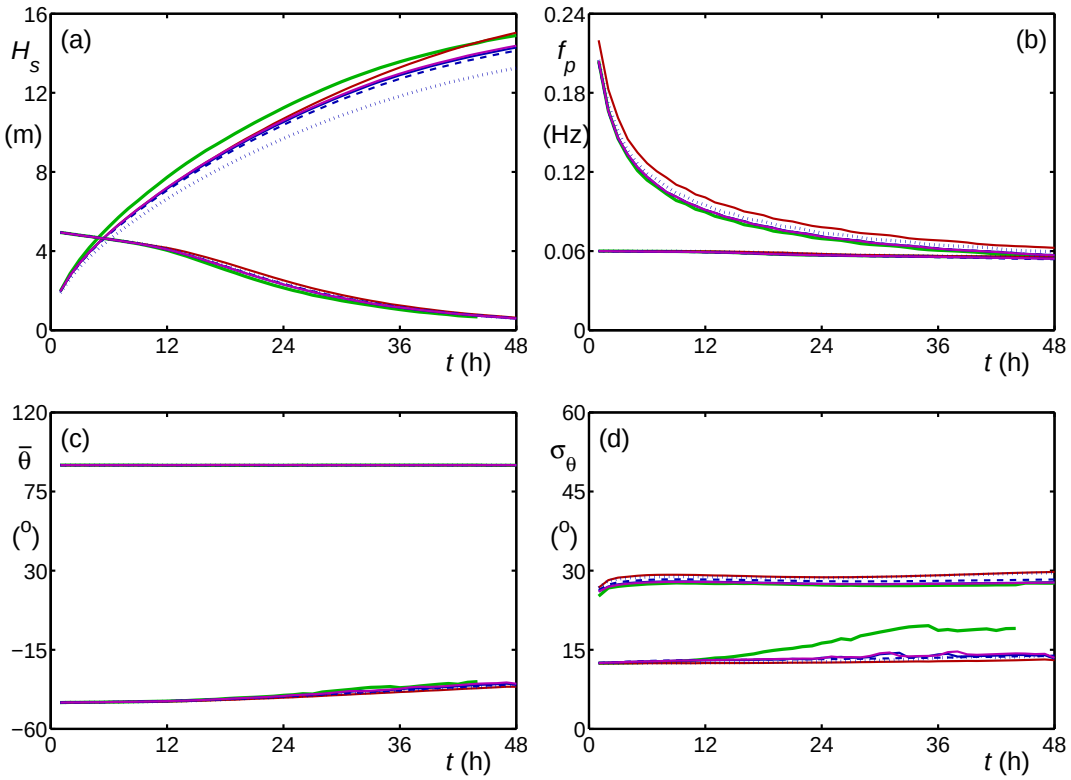

Fig. 4.36 : Like Fig. 4.35 for wave growth with swell test test_06.

represents the wave height H_s accurately at the expense of the representation of the peak frequency f_p. The corresponding optimized GMD (GMD1) improves the representation of the f_p at the expense of the representation of H_s. Adding complexity (GMD2, GMD3, GS13) results in an accurate description of the peak frequency f_p for both wave evolution in space and time. The wave height evolution in space (Fig. 4.35a) also becomes accurate, but the wave height evolution in time (Fig. 4.36a) remains systematically underestimated. The directional spread (σ_θ) shows similar systematic improvement with increasing complexity of thee GMD, with only small remaining errors. The exception is the inability of these GMD parameterizations to reproduce the systematic directional widening of the swell in Fig. 4.36d. The description of the mean direction in cases where the direction actually changes is systematically improved with increasing complexity of the GMD, but also has notable remaining errors. For spectral parameters, increasing complexity of the GMD leads to increasing accuracy as is illustrated in Fig. 4.37. However, clear errors remain particularly in the one-dimensional spectra and source term (panels a, b, e and f).

In shallow water, errors for tests including wind seas are dominated by the 'deep water' errors of the model. This is illustrated here with the wave height and

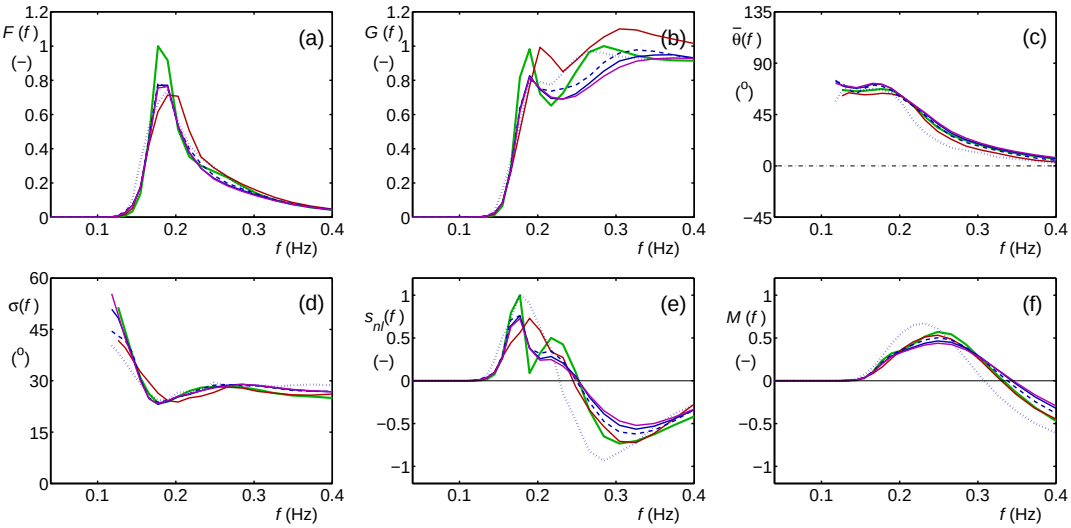

Fig. 4.37 : One-dimensional spectral quantities after 6 h of model integration for test test_03 *a) energy spectrum $F(f)$, b) steepness spectrum $G(f)$, c) mean direction $\overline{\theta}(f)$, d) directional spread $\sigma_\theta(f)$, e) nonlinear interactions $s_{nl}(f)$, f) nonlinear energy flux $M(f)$, Legend as in Fig. 4.35. All variables normalized with the absolute maximum of the WRT results.*

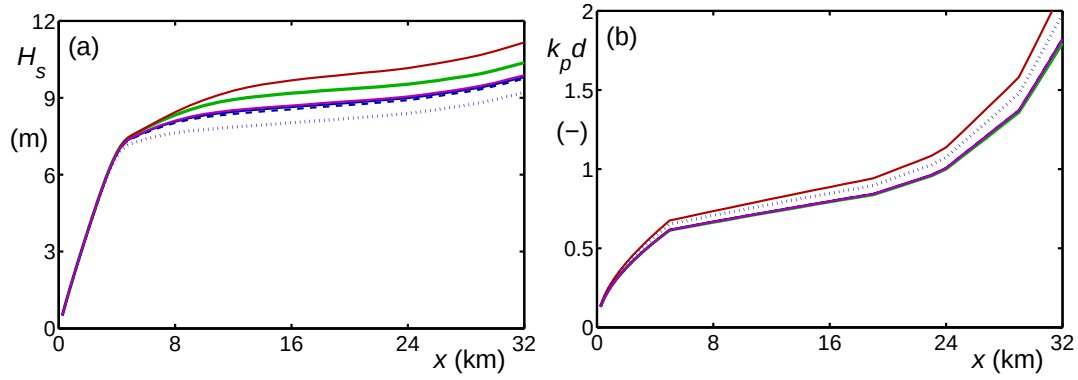

Fig. 4.38 : Evolution in time of a) significant wave height H_s and b) relative depth $k_p d$ for wind sea on beach test test_12. *Legend as in Fig. 4.35.*

relative depth evolution for test_12 in Fig. 4.38. Issues with spectral shapes for the swell case have already been discussed in previous sections. Note that for test_11 the exact interactions generate dual-peaked spectra in the most shallow water depth. Such spectra are not reproduced by any of the new parameterizations.

In spite of the large volume of optimization work presented so far, only a small part of possible optimization approaches and details have been addressed. Some of these concern the (exploratory) shallow water optimization, for instance

- Figure 4.34b shows that that sampling spectral space results in a significant contribution for the smallest λ in the sampling. This λ, however, is significantly larger than some freely optimized λ values. This suggests that better results may be obtained if smaller values for λ are used when sampling spectral space for shallow water optimization.
- It may be worth while to add the shallow water swell test case test_13 to the deep water optimization to consider accuracy of swell for interactions for intermediate water depths.
- Good results might be obtained with full optimization for deep water, combined with sampling for shallow water, or by using a different number of shallow water and deep water representative quadruplets.

Some of these observations will be used in the following sections, others will be left for future research.

4.6 Multi-component expanded quadruplet GMD

The next step of this study is to consider more complex definitions of the quadruplet. In Tolman (2003, 2004, 2005) and Tolman and Krasnopolsky (2004) it has been noted that such quadruplets by themselves do not result in stable model integration, unless multiple representative quadruplets are used. For this reason, the present optimization will start with three representative quadruplets.

The two-parameter (λ, μ) and three parameter $(\lambda, \mu, \Delta\theta)$ definitions of the quadruplet introduce more free parameters in the optimization, and hence require larger populations and/or numbers of generations. For this reason, the optimization of such parameters will be more selective than for the classic quadruplet layout in the previous section. Considering the saturation behavior in the previous section, and the fact that sampling spectral space did not add to accuracy, combined with the additional difficulty of setting sampling strategies for a multi-dimensional parameter space, only full parameter optimization for an increasing number of quadruplets will be considered in this section.

Table 4.17: Population sizes (n_{pop}) and number of generations (n_{gen}) for deep water optimization using two (λ, μ) and three parameter $(\lambda, \mu, \Delta\theta)$ quadruplet definition and number of representative quadruplets (n_q). Size of initial population in parenthesizes if different from general population size.

	(λ, μ)		$(\lambda, \mu, \Delta\theta)$	
n_q	n_{pop}	n_{gen}	n_{pop}	n_{gen}
3	350	45	600 (1200)	60
4	500	60	1200 (2400)	60
5	600	60	1500 (3000)	90
6	750	60	2000 (4000)	150

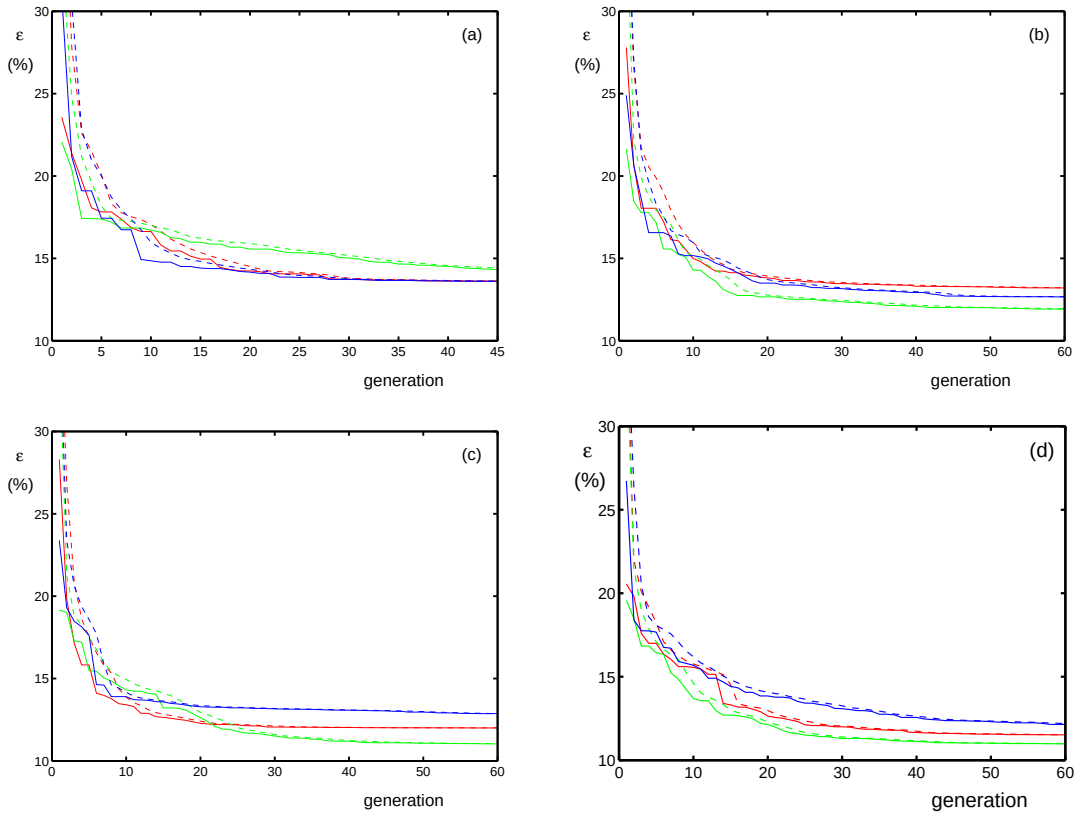

Fig. 4.39 : Minimum errors (ϵ_{min}, solid lines) and average errors for fittest half of population (ϵ_{avg}, dashed lines) as a function of the generation for optimization experiments (identified by color) for deep water with the two-parameter quadruplet definition. (a) Number of quadruplets $n_q = 3$. (b) $n_q = 4$. (c) $n_q = 5$. (d) $n_q = 6$.

4.6.1 Deep water, increasing number of quadruplets

In this section, two and three parameter quadruplet definitions will be optimized for deep water, with three to six representative quadruplets. For each optimization attempt, three different initial conditions will be considered. As in previous sections, these experiments will be denoted as the red, green and blue experiments. Population sizes and number of generations considered are presented in Table 4.17. As before, genetic optimization is augmented with steepest descent optimization for the best performing member of the last generation. First, results for the two-parameter quadruplet definition will be presented and discussed.

Figure 4.39 shows the error evolution as a function of the generation for the four sets of three experiments for the two-parameter quadruplet definition. Corresponding best quadruplets and lowest errors are presented in Tables 4.18 through 4.21. As before, increasing the number of quadruplets systematically improves the quality of the GMD, with apparent diminishing return for increasing numbers of quadruplets. Unlike with the experiments with the one-parameter quadruplet, introducing $n_q = 6$ quadruplets still shows some improvement relative to the experiments with $n_q = 5$. Hence, no plateau with respect to benefit of additional quadruplets seems to have been reached yet. The only exception to this observation is that for the red experiment with $n_q = 6$ the third quadruplet has an anomalously small C_d, and hence could effectively be considered as turned off.

Compared to the error evolution for the optimization of the one-parameter quadruplet in the previous sections, Fig. 4.39 show more erratic optimization behavior, in particular with respect to consistency between the red blue and green experiments for each separate configuration (i.e., n_q). For the experiments with $n_q = 3$ the red and blue experiments effectively result in the same optimum GMD, giving some confidence that this indeed may be a good solution, and possibly close to the global optimal solution. For all other configurations, the three optimum solutions show clearly different configurations, giving less confidence that the best of these indeed is close to the global optimum solution. This more erratic behavior indicates that the setup of the genetic optimization needs to be improved. This has been addressed for the three-parameter quadruplet definition below.

Several other observations can be made from the experiments with the two parameter quadruplet definition. First, the optimization naturally selects one-parameter quadruplets where appropriate. Particularly striking is that all three experiments with $n_q = 3$ results in an optimum solution with a one-parameter quadruplet with $\lambda \approx 0.14$. Second, as already observed above, the experiments with $n_q = 6$ start to display some "degenerate" behavior. One of the resulting quadruplets for the red experiment is effectively switched off, and for the green experiment two quadruplets have near identical λ (but different μ). Third, for all individual experiments presented here, the steepest descent approach applied to the best guess from the genetic optimization resulted in small improvements

Table 4.18: Optimal GMD setting for two-parameter quadruplet layout and three deep water quadruplets based on deep water tests only. Genetic optimization followed by steepest descent.(r), (g), and (b) refers to red, green and blue experiments.

experiment	λ	μ	C_d	ϵ_{tot} (%)
red	0.136	—	$3.06\ 10^7$	13.59
	0.208	0.135	$7.39\ 10^7$	
	0.345	0.101	$1.10\ 10^7$	
green	0.143	—	$3.21\ 10^7$	14.16
	0.237	0.126	$4.65\ 10^7$	
	0.346	0.075	$8.49\ 10^6$	
blue	0.137	—	$3.04\ 10^7$	13.58
	0.208	0.137	$7.91\ 10^7$	
	0.347	0.097	$1.05\ 10^7$	

Table 4.19: Like Fig. 4.18 for $n_q = 4$.

experiment	λ	μ	C_d	ϵ_{tot} (%)
red	0.066	0.025	$2.78\ 10^8$	13.16
	0.215	0.082	$7.19\ 10^7$	
	0.279	0.222	$2.04\ 10^7$	
	0.352	0.075	$9.73\ 10^6$	
green	0.111	0.089	$2.77\ 10^8$	11.89
	0.130	—	$3.63\ 10^7$	
	0.230	0.118	$5.27\ 10^7$	
	0.349	0.109	$1.34\ 10^7$	
blue	0.065	0.014	$8.78\ 10^7$	12.66
	0.115	0.090	$1.95\ 10^8$	
	0.184	0.066	$6.28\ 10^7$	
	0.310	0.127	$3.28\ 10^7$	

Table 4.20: Like Fig. 4.18 for $n_q = 5$.

experiment	λ	μ	C_d	ϵ_{tot} (%)
red	0.127	—	$4.11\,10^7$	12.00
	0.172	0.126	$1.31\,10^8$	
	0.237	—	$2.45\,10^7$	
	0.245	0.184	$2.20\,10^7$	
	0.348	0.116	$1.72\,10^7$	
green	0.068	0.015	$6.39\,10^7$	11.01
	0.115	0.077	$3.58\,10^8$	
	0.192	0.125	$4.35\,10^7$	
	0.248	0.066	$3.23\,10^7$	
	0.349	0.145	$1.87\,10^7$	
blue	0.126	—	$3.87\,10^7$	12.78
	0.195	0.074	$6.61\,10^7$	
	0.224	0.184	$5.52\,10^7$	
	0.320	0.124	$2.55\,10^7$	
	0.399	—	$1.74\,10^6$	

only. Combined with the clearly different optimization results for the experiments for each given n_q, this clearly indicates that for the more complex quadruplet definitions many local minima for model errors exist in parameter space, clearly indicating that the genetic optimization approach is far superior to the descent approach. Fourth, an anomalously large impact of the final descent algorithm was found for the blue experiment with $n_q = 6$. After genetic optimization only, this experiment produced the poorest performing GMD. The descent optimization, however, reduced the error by another 1.5%, producing the best GMD of the three eperiments.

The next step is to optimize GMDs based on the three-parameter quadruplet definition. Initial experiments with this configuration saw the erratic behavior per configuration increase up to a level that the three-parameter configurations in some cases did not outperform the corresponding two-parameter configurations. Because the three-parameter configuration can reproduce the two-parameter configuration exactly, this is a clear indication that these initial optimizations did not perform as expected, and that some additional assessment of the setup of the genetic optimization was needed.

For the initial experiments with the three-parameter quadruplet definition and $n_q = 3$ (Fig. 4.40a and Table 4.22), initial experiments with a population with 600 members could not outperform the corresponding model setup with the

Table 4.21: Like Fig. 4.18 for $n_q = 6$.

experiment	λ	μ	C_d	ϵ_{tot} (%)
red	0.098	—	$5.27\,10^7$	11.47
	0.123	0.092	$4.43\,10^8$	
	0.182	0.120	$8.75\,10^5$	
	0.232	0.068	$5.47\,10^7$	
	0.328	0.145	$2.54\,10^7$	
	0.383	—	$2.37\,10^6$	
green	0.069	0.045	$7.41\,10^8$	10.97
	0.183	0.002	$5.39\,10^7$	
	0.232	0.147	$5.95\,10^7$	
	0.233	0.064	$1.22\,10^7$	
	0.278	0.237	$1.44\,10^7$	
	0.351	0.110	$1.92\,10^7$	
blue	0.059	0.026	$2.59\,10^8$	10.78
	0.132	0.080	$2.60\,10^8$	
	0.227	0.127	$6.30\,10^7$	
	0.279	—	$1.36\,10^7$	
	0.351	0.219	$1.47\,10^7$	
	0.359	0.070	$7.03\,10^6$	

two-parameter quadruplet definition. Close inspection of the initial population showed that only a small fraction of the randomly selected initial population produced viable results. Tentatively, this suppresses (viable) diversity in the initial generation. This can be remedied be taking a larger initial population, and reducing the size of the initial population to the target population size after initial sorting of the population, but before the second population is generated.

Doubling the size of the initial population indeed resulted in significantly better GMD configurations. Making initial populations even larger resulted in poorer optimization results, which can tentatively be attributed to the fact that this would suppress non-viable configurations to a level that the population diversity encapsulated therein was suppressed too much. Figure 4.40a and Table 4.22 show that with this approach two near-identical optimum solutions are found (red and green), whereas the blue solution degenerates to a one-parameter quadruplet dominated configuration from which the genetic optimization cannot reach more accurate configurations in the 60 generations considered.

Initial experiments to optimize the GMD with the three-parameter quadruplet definition and $n_q = 4$ were performed with a population size of 800 (1600 for

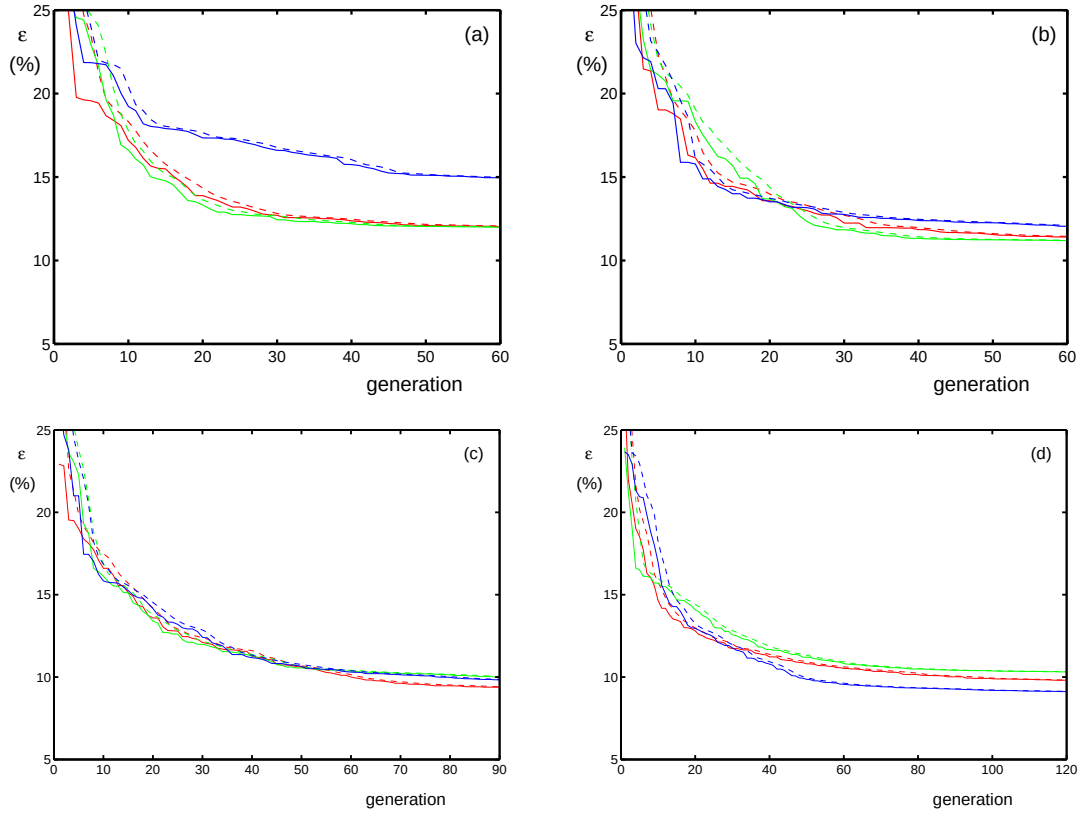

Fig. 4.40 : Like Fig. 4.39 for the three-parameter quadruplet definition. (a) Number of quadruplets $n_q = 3$. (b) $n_q = 4$.(c) $n_q = 5$. (d) $n_q = 6$.

initial population and up to 90 generations. This again lead to an unexpected large difference in results from the red, green and blue experiments. Additional experiments suggest that this population size did not support sufficient diversity. Increasing the population size as indicated in Table 4.17 gave much more uniform results over the three experiments while requiring fewer generations to reach the convergence. Now the red and green experiments show identical errors, with three of four resulting quadruplets for all practical purposes shared. In this case near-identical results suggesting that a near-optimal solution is found proved misleading. In one of the earlier (erratic) results, a minimum error 0.5% smaller was found (results not presented here).

The approach with larger populations, double initial population size and effectively fewer populations was applied to the experiments with $n_q = 5$ and 6, with population sizes shown in Table 4.17 and error evolutions shown in Figs. 4.40c and d. Note that for the last experiments, results again become a little more erratic. Resulting optimum quadruplet settings for $n_q = 3$, 4, 5 or 6 and red green and blue experiments are presented in Tables 4.22 through 4.25.

Table 4.22: Optimal GMD setting for three-parameter quadruplet layout and three deep water quadruplets based on deep water tests only. Genetic optimization followed by steepest descent.(r), (g), and (b) refers to red, green and blue experiments.

experiment	λ	μ	$\theta_{12}(^o)$	C_d	ϵ_{tot} (%)
red	0.072	0.033	23.3	$3.06\ 10^8$	12.01
	0.215	0.067	7.3	$4.10\ 10^7$	
	0.339	0.148	17.4	$1.22\ 10^7$	
green	0.074	0.037	22.8	$2.71\ 10^8$	11.94
	0.204	0.070	8.8	$4.77\ 10^7$	
	0.341	0.162	18.2	$1.29\ 10^7$	
blue	0.184	—	0.0	$4.61\ 10^7$	14.63
	0.315	—	12.5	$1.40\ 10^7$	
	0.477	0.456	10.5	$2.66\ 10^6$	

Table 4.23: Like Fig. 4.22 for $n_q = 4$.

experiment	λ	μ	$\theta_{12}(^o)$	C_d	ϵ_{tot} (%)
red	0.126	0.017	19.3	$5.02\ 10^7$	11.19
	0.161	0.126	20.8	$1.68\ 10^8$	
	0.250	—	0.0	$2.22\ 10^7$	
	0.361	0.205	12.9	$1.09\ 10^7$	
green	0.069	0.045	25.0	$4.67\ 10^8$	11.19
	0.126	0.017	16.6	$4.62\ 10^7$	
	0.237	0.008	3.4	$3.57\ 10^7$	
	0.361	0.223	18.3	$1.26\ 10^7$	
blue	0.081	0.037	22.4	$4.23\ 10^8$	12.00
	0.247	0.072	0.5	$3.68\ 10^7$	
	0.337	0.152	23.4	$4.06\ 10^6$	
	0.373	0.230	18.9	$7.65\ 10^6$	

Table 4.24: Like Fig. 4.22 for $n_q = 5$.

experiment	λ	μ	$\theta_{12}(^o)$	C_d	ϵ_{tot} (%)
red	0.066	0.018	21.4	$1.70\,10^8$	9.25
	0.127	0.069	19.6	$1.27\,10^8$	
	0.228	0.065	2.0	$4.43\,10^7$	
	0.295	0.196	40.5	$2.10\,10^7$	
	0.369	0.226	11.5	$1.18\,10^7$	
green	0.082	0.011	7.5	$5.30\,10^7$	9.31
	0.121	0.070	23.3	$1.80\,10^8$	
	0.184	0.107	26.5	$6.79\,10^7$	
	0.264	0.066	14.9	$2.74\,10^7$	
	0.365	0.217	14.1	$1.26\,10^7$	
blue	0.068	0.025	20.6	$2.22\,10^8$	9.83
	0.145	0.079	17.4	$1.42\,10^8$	
	0.176	0.022	61.8	$3.98\,10^7$	
	0.244	0.075	3.6	$2.71\,10^7$	
	0.345	0.185	15.7	$1.93\,10^7$	

A comparison of results for two- or three-parameter quadruplet definitions shows that the three-parameter quadruplet definition is far superior in terms of minimizing resulting model errors. Whereas the one-parameter quadruplet definition is a factor two cheaper in computation, the two- and three-parameter quadruplet definitions have identical computational costs. Considering this, a three-parameter quadruplet definition should always be favored over a two-parameter quadruplet definition, whereas a one-parameter quadruplet definition might still be considered for its computational economy.

The results obtained with the three-parameter quadruplet definition and n_q increasing from 3 to 6 shows a steady improvement of model results, even for $n_q = 6$. However, with the increasing number of degrees of freedom in the optimization, it becomes more difficult to optimize the quadruplet configurations. Because the present optimizations do not yet consider source terms specifically designed for (near) exact nonlinear interactions, there is little justification to try and obtain even more accuracy by increasing n_q even more. Therefore, such experiments are not considered here. Note that the results for $n_q = 5$ appear to represent a sweet spot in terms of accuracy, as the results are much better than those for $n_q = 4$, but only marginally worse than those for $n_q = 6$.

Considering the above, the results for the red experiment with the three-parameter quadruplet definition with $n_q = 5$ will be used as the basis for the shal-

Table 4.25: Like Fig. 4.22 for $n_q = 6$.

experiment	λ	μ	$\theta_{12}(^o)$	C_d	ϵ_{tot} (%)
red	0.076	0.033	20.6	$4.07\ 10^8$	9.76
	0.183	—	32.2	$3.61\ 10^7$	
	0.237	0.074	0.0	$5.00\ 10^7$	
	0.282	0.218	27.0	$1.48\ 10^7$	
	0.347	0.078	11.7	$9.75\ 10^6$	
	0.372	0.289	2.6	$6.63\ 10^6$	
green	0.065	0.027	45.0	$3.69\ 10^8$	10.25
	0.146	—	—	$5.01\ 10^7$	
	0.237	0.126	16.0	$4.75\ 10^7$	
	0.289	—	19.2	$1.67\ 10^7$	
	0.330	0.282	15.0	$1.45\ 10^7$	
	0.393	0.287	11.7	$8.48\ 10^6$	
blue	0.065	0.023	5.9	$1.75\ 10^8$	9.02
	0.145	0.068	26.5	$1.14\ 10^8$	
	0.156	—	51.6	$3.69\ 10^7$	
	0.225	0.127	16.3	$7.47\ 10^7$	
	0.344	0.145	0.1	$1.82\ 10^7$	
	0.439	0.376	24.2	$1.51\ 10^6$	

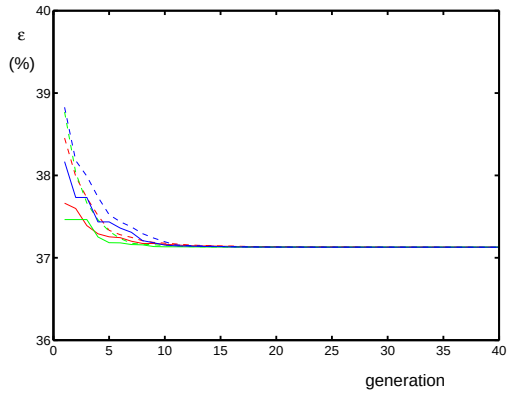

Fig. 4.41 : Minimum errors (ϵ_{min}, solid lines) and average errors for fittest half of population (ϵ_{avg}, dashed lines) as a function of the generation for optimization experiments (identified by color) for shallow water with the three-parameter quadruplet definition. Starting from $n_q = 5$ deep water quadruplets (Table 4.24, red) optimizing m and C_s. $n = -3.5$

Table 4.26: Optimum GMD setting for three parameter quadruplet layout for the three shallow water tests. Starting point is red experiment with $n_q = 5$ from Table 4.24 with additional optimization of C_s and m. $n = -3.5$

experiment	λ	μ	$\theta_{12}(^o)$	C_d	C_s	m	ϵ_{tot} (%)
deep	0.066	0.018	21.4	$1.70\,10^8$	—	0	39.51
	0.127	0.069	19.6	$1.27\,10^8$	—	-3.79	38.75
	0.228	0.065	2.0	$4.43\,10^7$	—		
	0.295	0.196	40.5	$2.10\,10^7$	—		
	0.369	0.226	11.5	$1.18\,10^7$	—		
red	0.066	0.018	21.4	$1.70\,10^8$	$6.71\,10^5$	-6.91	37.13
	0.127	0.069	19.6	$1.27\,10^8$	—		
	0.228	0.065	2.0	$4.43\,10^7$	$2.41\,10^6$		
	0.295	0.196	40.5	$2.10\,10^7$	$2.73\,10^8$		
	0.369	0.226	11.5	$1.18\,10^7$	$2.35\,10^6$		
green	0.066	0.018	21.4	$1.70\,10^8$	$6.38\,10^5$	-6.91	37.13
	0.127	0.069	19.6	$1.27\,10^8$	—		
	0.228	0.065	2.0	$4.43\,10^7$	$2.43\,10^6$		
	0.295	0.196	40.5	$2.10\,10^7$	$2.76\,10^8$		
	0.369	0.226	11.5	$1.18\,10^7$	$2.41\,10^6$		
blue	0.066	0.018	21.4	$1.70\,10^8$	$7.10\,10^5$	-7.08	37.13
	0.127	0.069	19.6	$1.27\,10^8$	—		
	0.228	0.065	2.0	$4.43\,10^7$	$2.40\,10^6$		
	0.295	0.196	40.5	$2.10\,10^7$	$2.78\,10^8$		
	0.369	0.226	11.5	$1.18\,10^7$	$2.38\,10^6$		

low water optimization experiments in the following sections. The two-parameter quadruplet will not be considered for shallow water optimization.

4.6.2 Shallow water, deep water quadruplets

The shallow water optimization using deep water quadruplets starts from the three-parameter quadruplet definition with $n_{q,d} = 5$ quadruplets from the red experiment in the previous section only. First, a quick optimization is performed to address the optimum value of m only with $C_s \equiv 0$. As in previous experiments, an optimum value is found outside the range of initially expected values ($m = -3.79$). To optimize the five values of C_s and the single value of m, three experiments are run again with a population size of 250 and considering 40 generations., followed by a steepest descent optimization for the best performing

member of the last generation. Error evolutions are presented in Fig. 4.41, and optimum quadruplets are presented in Table 4.26.

Figure 4.41 shows highly consistent behavior of the three separate experiments, with identical asymptotic behavior of the resulting model errors. The Figure indicates that 20 rather than 40 generations would have sufficed for this experiment.

For the deep water setting of the quadruplets ($C_s \equiv 0$), optimizing m has a notable impact on model behavior, reducing the total model error for the shallow water tests from $\epsilon_{tot} = 39.51\%$ to $\epsilon_{tot} = 38.75\%$. Optimizing the quadruplets fully for shallow water systematically improves the shallow water behavior, reducing the model error further to $\epsilon_{tot} = 37.13\%$. The three experiments show near-identical optimization results. In all cases the second quadruplet is not used for shallow water, and, based on the value of C_s, the fourth quadruplet is dominant. Negative values of m are found again. These values are outside the range of theoretically expected values, but consistent with earlier optimization results.

4.6.3 Shallow water, separate quadruplets

The final set of optimization experiments considers optimizing additional shallow water quadruplets using a preset set of $n_{q,d} = 5$ deep water quadruplets as obtained in the previous section, together with $n_{q,s} = 3$, 4, 5 or 6 additional shallow water quadruplets. Values of m are also dynamically optimized, where $n = -3.5$ again is preset. Because the number of degrees of freedom to be optimized are nearly identical to the number of degrees of freedom optimized for the corresponding deep water cases, population sizes and numbers of generations are identical to those of the corresponding deep water optimization experiments as presented in Table 4.17, with the exception of the experiments for $n_{q,s} = 6$, for which 120 instead of 150 generations are considered. The error evolution of all experiments is presented in Fig. 4.42 and the corresponding optimum GMD settings (after steepest descent optimization) are presented in Tables 4.27 through 4.30.

Figure 4.42a shows fairly consistent behavior between the three experiments with $n_{q,s} = 3$ shallow water quadruplets, with the red experiment as a (negative) outlier. Resulting optimum model errors range from 33.3% to 33.8%. A further comparison with Table 4.27 indicates that the subsequent steepest descent optimization results in negligible improvements for all three experiments. The differences in optimum results for the three experiments again indicate that there are several near-optimum solutions. Note that the optimum configurations share similar but not identical quadruplets, and that all solutions include quadruplets that are in essence degenerated to the single parameter quadruplet definition ($\mu = 0$, $\theta_{12} \approx 0^\circ$). The resulting model errors are significantly better than the best model errors obtained with the one parameter quadruplet in previous sec-

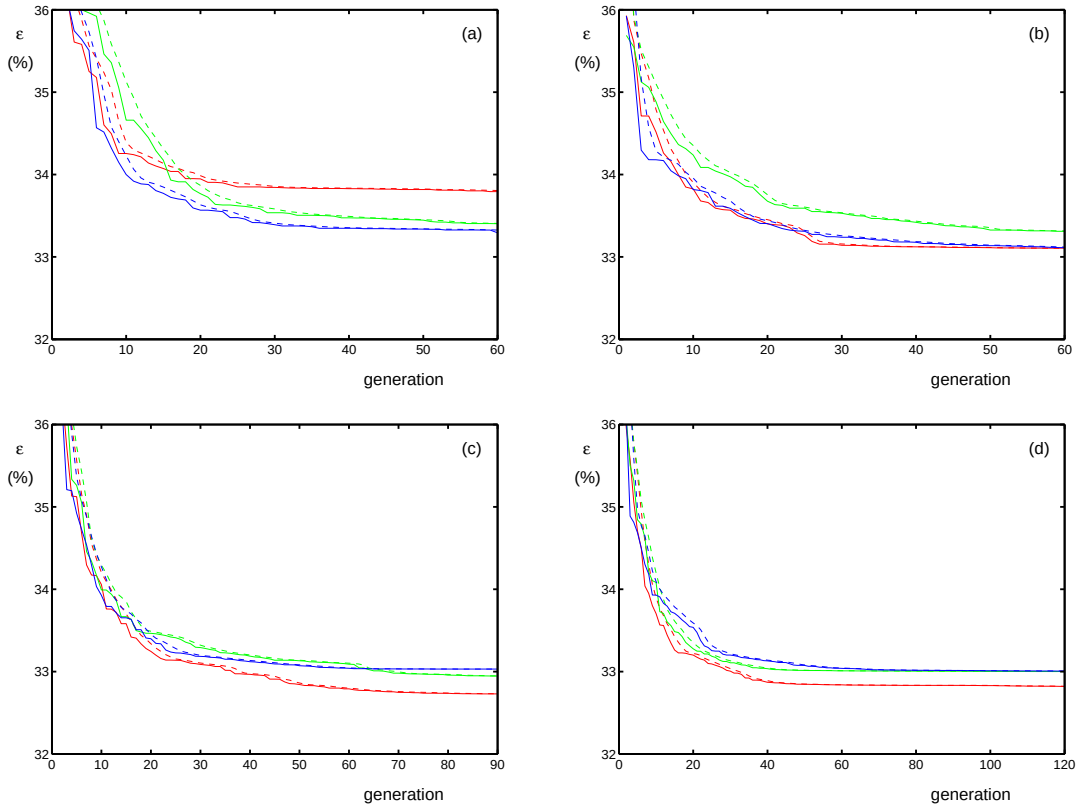

Fig. 4.42 : Minimum errors (ϵ_{min}, solid lines) and average errors for fittest half of population (ϵ_{avg}, dashed lines) as a function of the generation for optimization experiments (identified by color) for shallow water with the three-parameter quadruplet definition and fixed set of $n_{q,d} = 5$ deep water quadruplets. (a) Number of shallow water quadruplets $n_{q,s} = 3$. (b) $n_{q,s} = 4$. (c) $n_{q,s} = 5$. (d) $n_{q,s} = 6$.

tions (i.e., 36.4%), although this is at least partially due to better deep water behavior in test_11 and test_12 as will be illustrated in Section 4.6.4.

Figure 4.42b shows fairly consistent behavior between the three experiments with $n_{q,s} = 4$ shallow water quadruplets, with the green experiment as a (negative) outlier. Resulting optimum model errors range from 33.1% to 33.3%. A further comparison with Table 4.28 again indicates a minor impact of the subsequent steepest descent optimization, similar but not identical preferred quadruplets, as well as several quadruplets that have degenerated to the one-parameter quadruplet definition.

Figures 4.42c and d and Tables 4.29 and Table 4.30 show a similar pattern for $n_{q,s} = 5$ or 6 shallow water quadruplets, with some additional observations. First, the green and blue experiments with 5 shallow water quadruplets introduce an alternative optimum two-parameter quadruplet definition where $\mu = 0$ but θ_{12}

Table 4.27: Optimum GMD setting for three parameter quadruplet layout for the three shallow water tests. Five pre-set deep deep water quadruplets ($n_{q,d} = 5$, shown for red case only) and three additional shallow water quadruplets ($n_{q,s} = 3$) optimized as shown in the table. m is dynamically optimized, $n = -3.5$.

experiment	λ	μ	$\theta_{12}(^o)$	C_d	C_s	m	ϵ_{tot} (%)
red	0.066	0.018	21.4	$1.70\,10^8$	—		
	0.127	0.069	19.6	$1.27\,10^8$	—		
	0.228	0.065	2.0	$4.43\,10^7$	—		
	0.295	0.196	40.5	$2.10\,10^7$	—		
	0.369	0.226	11.5	$1.18\,10^7$	—		
	0.118	—	1.9	—	$1.27\,10^5$	-7.05	33.79
	0.322	0.043	2.7	—	$1.12\,10^6$		
	0.349	0.211	42.9	—	$2.93\,10^8$		
green	0.184	—	2.4	—	$5.74\,10^5$	-7.94	33.39
	0.334	0.213	29.7	—	$2.25\,10^7$		
	0.354	0.222	45.4	—	$3.05\,10^8$		
blue	0.093	—	4.7	—	$9.04\,10^4$	-7.30	33.29
	0.241	—	2.4	—	$8.70\,10^5$		
	0.351	0.216	42.1	—	$2.83\,10^8$		

Table 4.28: Like Table 4.27 for $n_{q,s} = 4$

experiment	λ	μ	$\theta_{12}(^o)$	C_d	C_s	m	ϵ_{tot} (%)
red	0.040	—	4.0	—	$1.35\,10^5$	-8.29	33.03
	0.189	—	2.2	—	$7.42\,10^5$		
	0.321	0.232	40.5	—	$2.07\,10^8$		
	0.433	0.408	57.4	—	$9.99\,10^8$		
green	0.184	—	2.7	—	$7.86\,10^5$	-8.19	33.27
	0.320	0.236	41.9	—	$2.74\,10^8$		
	0.432	0.406	57.3	—	$7.19\,10^8$		
	0.493	0.261	21.3	—	$5.09\,10^8$		
blue	0.182	0.180	17.1	—	$3.50\,10^7$	-7.97	33.05
	0.184	—	2.2	—	$7.62\,10^5$		
	0.334	0.204	36.8	—	$1.20\,10^8$		
	0.387	0.261	49.9	—	$4.66\,10^8$		

Table 4.29: Like Table 4.27 for $n_{q,s} = 5$

experiment	λ	μ	$\theta_{12}(^o)$	C_d	C_s	m	ϵ_{tot} (%)
red	0.036	0.003	4.2	—	$2.54\,10^5$	-7.58	32.72
	0.105	0.104	0.5	—	$1.58\,10^7$		
	0.184	—	1.9	—	$7.40\,10^5$		
	0.360	0.225	44.1	—	$5.04\,10^8$		
	0.375	—	0.0	—	$1.03\,10^6$		
green	0.146	0.005	59.9	—	$1.87\,10^8$	-9.07	32.88
	0.184	—	1.9	—	$9.20\,10^5$		
	0.185	0.184	17.1	—	$6.04\,10^7$		
	0.321	0.236	40.0	—	$2.65\,10^8$		
	0.433	0.405	56.7	—	$1.11\,10^9$		
blue	0.043	—	4.1	—	$1.56\,10^5$	-9.18	32.98
	0.164	—	60.0	—	$1.96\,10^8$		
	0.192	—	2.4	—	$9.60\,10^5$		
	0.323	0.232	40.4	—	$2.76\,10^8$		
	0.434	0.402	55.9	—	$8.02\,10^8$		

Table 4.30: Like Table 4.27 for $n_{q,s} = 6$

experiment	λ	μ	$\theta_{12}(^o)$	C_d	C_s	m	ϵ_{tot} (%)
red	0.032	0.001	3.7	—	$2.77\,10^5$	-8.72	32.80
	0.157	—	60.1	—	$2.26\,10^8$		
	0.184	—	2.0	—	$9.65\,10^5$		
	0.322	0.233	39.4	—	$2.86\,10^8$		
	0.418	—	0.2	—	$1.36\,10^6$		
	0.438	0.401	52.5	—	$6.61\,10^8$		
green	0.035	0.005	5.0	—	$3.91\,10^5$	-8.71	32.98
	0.158	0.007	60.4	—	$2.48\,10^8$		
	0.191	—	2.2	—	$1.13\,10^6$		
	0.319	0.238	38.4	—	$2.20\,10^8$		
	0.371	0.248	50.8	—	$3.64\,10^8$		
	0.442	0.409	54.7	—	$7.34\,10^8$		
blue	0.048	0.004	4.7	—	$2.37\,10^5$	-7.58	32.99
	0.184	—	1.5	—	$6.71\,10^5$		
	0.237	—	3.1	—	$6.49\,10^5$		
	0.315	0.237	39.7	—	$2.33\,10^8$		
	0.406	0.294	52.8	—	$6.81\,10^8$		
	0.459	0.083	0.8	—	$1.61\,10^6$		

Table 4.31: Synopsis of errors in % for optimized configurations for the GMD with the two or three quadruplet layout. Gabc refers to a parameters in the quadruplet and b deep water quadruplets. c as 'd' refers to deep water optimization only, 's' refers to quadruplets optimized for deep and shallow water, while a number refers to the number of separate shallow water quadruplets ($n_{q,s}$). Deep water configurations with $m = 0$ unless specified differently. S25d refers to G25d with high-frequency smoother added.

	test case									
	01	02	03	04	05	06	11	12	13	tot
G23d	12.9	14.4	13.7	16.0	14.1	14.1	—	—	—	14.2
G24d	9.6	14.3	11.4	10.7	14.6	10.8	—	—	—	11.9
G25d	8.9	14.4	10.3	9.2	13.3	9.8	—	—	—	11.0
S25d	8.8	14.4	10.3	9.1	13.2	9.8	—	—	—	10.9
G26d	8.9	12.7	10.5	10.6	11.9	10.0	—	—	—	10.8
G33d	11.6	12.0	11.8	11.3	12.8	12.1	—	—	—	11.9
G34d	9.9	11.2	11.2	10.5	12.6	11.7	—	—	—	11.2
G35d	7.8	9.7	9.4	9.2	10.9	8.6	—	—	—	9.3
G36d	7.0	10.3	9.5	8.2	10.8	8.7	—	—	—	9.1
G35d	7.8	9.7	9.4	9.2	10.9	8.6	13.6	21.2	83.7	19.3
				($m = -3.79$)			13.5	22.1	80.7	19.1
G35s							13.3	20.7	77.4	18,5
G353							12.4	19.3	68.1	17.3
G354							12.9	18.1	68.1	17.2
G355							12.5	18.7	67.0	17.1
G356							12.9	18.0	67.5	17.1

is substantial ($\theta_{12} = 60°$). Second, no further improvement is found for $n_{q,s} = 6$ quadruplets, leaving the optimized configurations with $n_{q,s} = 5$ quadruplets as the preferred configuration when accuracy and economy are considered.

This concludes the present optimization experiments for shallow water. It should be noted that this was a first-ever attempt to optimize the GMD for extremely shallow water, and that hence not the same maturity level can be expected as for deep water. It is expected that shallow water optimization can be improved further by adjusting both the shallow water scaling and the actual optimization techniques. This will be the subject of subsequent studies.

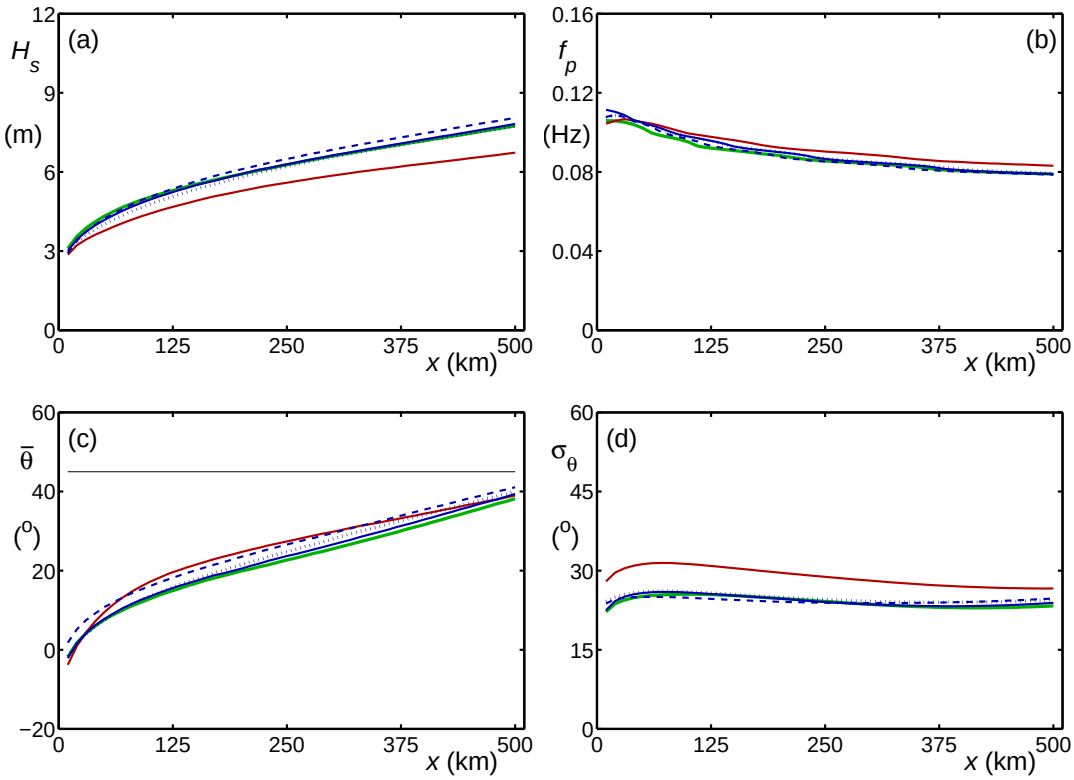

Fig. 4.43 : Evolution in time of a) significant wave height H_s, b) peak frequency f_p, c) mean direction $\overline{\theta}$, and d) directional spread σ_θ for the slanting fetch test test_05. *Green line: WRT. Red line: WAM. Dotted / dashed / solid blue lines: GMD3 / G25d / G35d. Solid line in panel c) represents wind direction.*

4.6.4 Summary

In Section 4.6 a GMD with the two- or three-parameter quadruplet definition has been optimized for deep and shallow water. Based on experiences with the optimization of the traditional quadruplet layout, these versions of the GMD have been optimized using a increasing number of fully optimized quadruplets. First, deep water quadruplets have been optimized, then one of these deep water quadruplet configurations has been used as the starting point for shallow water optimization. The experiments indicate improved model behavior for increasing numbers of deep water quadruplets up to the maximum number considered here (6), whereas no notable improvement was found for shallow water optimization beyond $n_{q,s} = 5$. A synopsis of the errors for various optimized GMDs with increasing complexity is presented in Table 4.31. All model configurations correspond to the best performing configurations from the corresponding tables in Sections 4.6.1 through 4.6.3. For model configurations G23d through G36d above

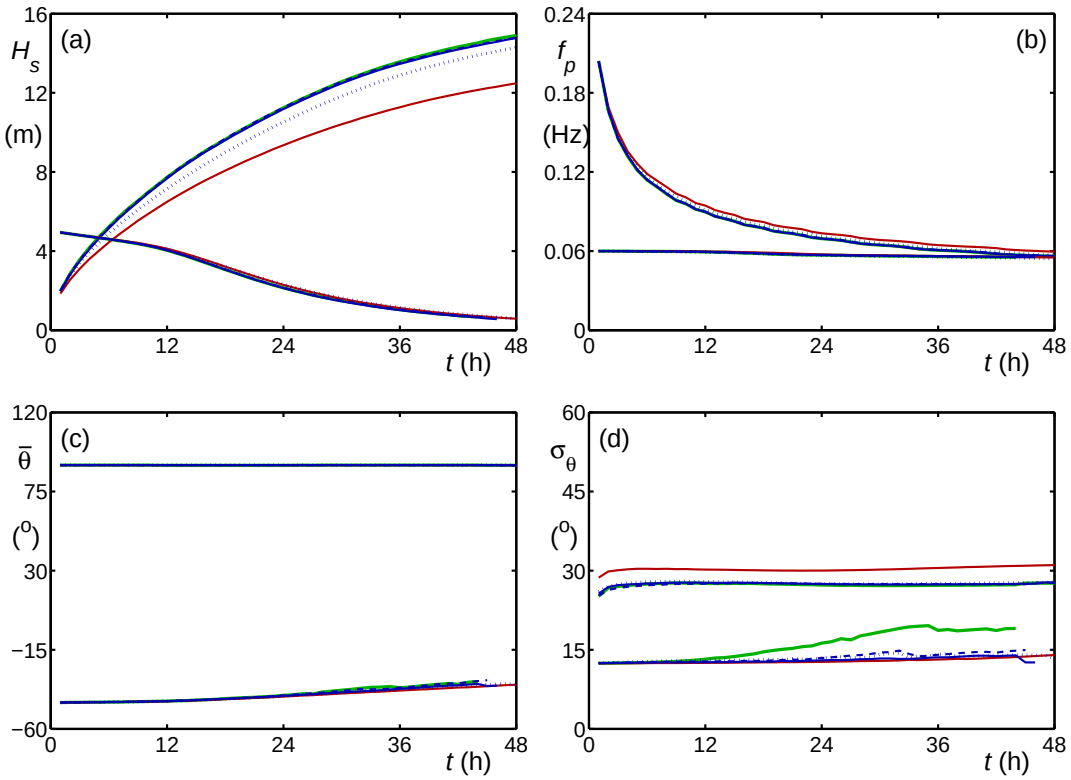

Fig. 4.44 : Like Fig. 4.43 for wave growth with swell test test_06.

the double line in the table, only the deep water tests are considered in the computation of the overall error. For the model configurations below the double line, deep and shallow water tests are considered in the total error. Since the deep water test results are identical for the latter configurations, these errors are not reproduced for each shallow water configuration.

The deep water optimization experiments with increasing numbers of quadruplets for the two-parameter quadruplet definition (configurations G23d through G26d) and for the three-parameter quadruplet definition (configurations G33d through G36d) show a systematic improvement of the overall model error with increased complexity (Table 4.31). For individual tests, however, the improvement is not monotonous with increasing $n_{g,d}$. This could be interpreted as another indication that there are many near-optimum configurations. It also indicates that the genetic optimization approach could easily be used to target more specifically individual tests, or more detailed model behavior by adding additional tests representing such behavior. Although the smallest errors are found for $n_{q,d} = 6$, the additional benefit compared to $n_{q,d} = 5$ is small. For this reason, and somewhat subjectively, the latter configurations will be considered here as the presently optimum approach when considering both accuracy and economy.

Figures 4.43 and 4.44 present mean wave parameters for various deep water configurations for test test_05 (slanting fetch) and test_06 (wave growth in the presence of swell). Presented are the reference results (WRT, green line), previous approach (WW3, red line) and optimized GMD results (blue lines). The latter include a one-parameter (GMD3, dotted line), two-parameter (G25d, dashed line) and three-parameter (G35d, solid line) quadruplet definition. In general the traditional approach and the results for the one-parameter quadruplet definition clearly differ from the reference conditions, but the results for the two and three-parameter quadruplet definitions are, for practical purposes, identical to the reference results. Only for the directional spread at very short fetches in the slanting fetch case (Figure 4.43c) the G35d approach is clearly superior to all others, and only for the directional spread of the swell in the case with wave growth in the presence of swell (Figure 4.43d) do none of the DIA or GMD approaches accurately describe the directional widening of the swell spectrum. The latter may either indicate a systematic limitation of the GMD, or of the representativeness of the test cases to properly describe interactions between wind seas and swell.

Differences between results for the various optimized GMD configurations with respect to spectral parameters are much larger than for the mean wave parameters, as is illustrated in Figs 4.45 through 4.47. The smallest differences are found for the one point models in the time-limited test cases, for which Figs 4.45 is representative. Larger differences are found for the two fetch-limited test cases (Figs 4.46 and 4.47.)

The three parameter quadruplet GMD (solid blue lines) clearly outperforms the two parameter quadruplet GMD with respect to the mean direction directional spread and nonlinear source term (panels c, d and e) for all test cases. For the fetch limited test cases, the three parameter quadruplet definition also outperforms the two parameters definition with respect to the spectral shape (panels a), reproducing a clearly sharper and more accurate spectral peak. For the one-point models, this difference is less pronounced or even negligible. Only for the steepness spectrum (panels b), the behavior is somewhat anomalous. Here, the three parameter quadruplet definition results in an overestimation of the reduction of the steepness just above the spectral peak, potentially resulting in an artificial bi-modality in the steepness spectrum. This behavior will need to be monitored in real life applications to ensure that this does not result in spurious multi-modal spectra.

Two-dimensional spectral results are illustrated in Figs. 4.48 and 4.49 with spectral from the first three offshore grid points of the fetch limited and slanting fetch test cases. Somewhat surprisingly, the two parameter quadruplet definition results in spectral noise in the points closest to shore, which disappears when moving offshore. This behavior is also obvious in the nonlinear interactions. but is not seen in the other test cases (figures not presented here). Note that the G35d

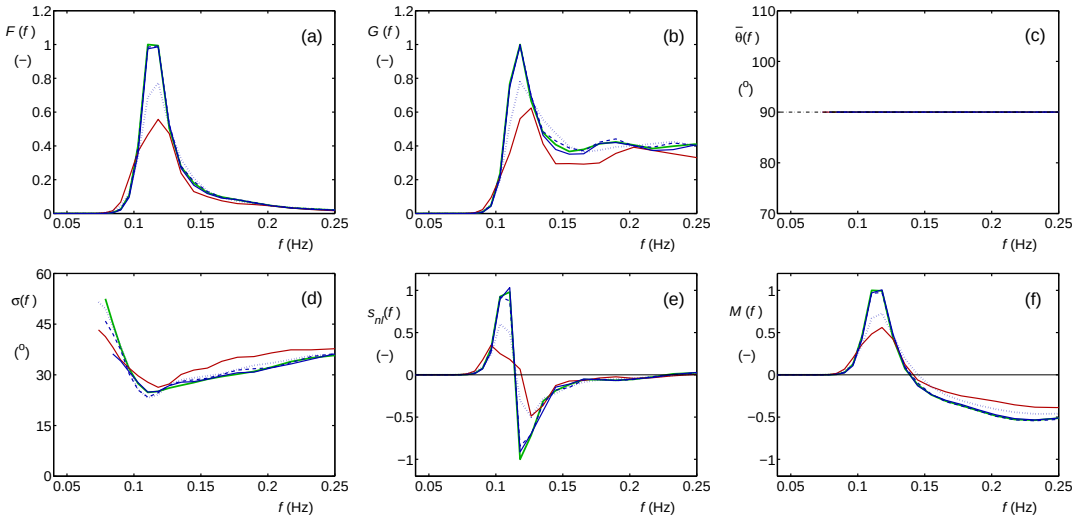

Fig. 4.45 : One-dimensional spectral quantities after 6 h of model integration for test test_01 *a) energy spectrum $F(f)$, b) steepness spectrum $G(f)$, c) mean direction $\overline{\theta}(f)$, d) directional spread $\sigma_\theta(f)$, e) nonlinear interactions $s_{nl}(f)$, f) nonlinear energy flux $M(f)$, Legend as in Fig. 4.43. All variables normalized with the absolute maximum of the WRT results.*

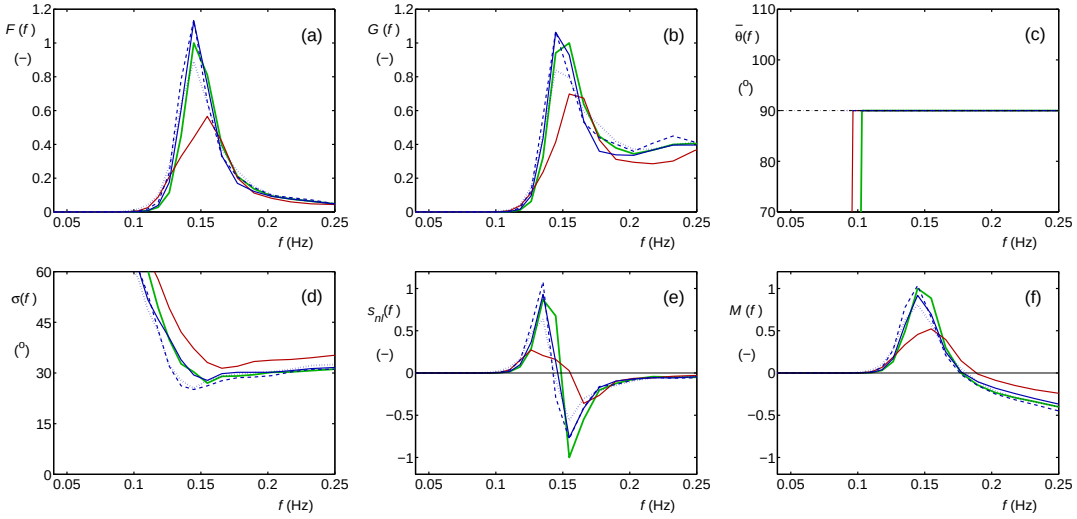

Fig. 4.46 : Like Fig. 4.45 for test_02 *at 50km offshore*

.

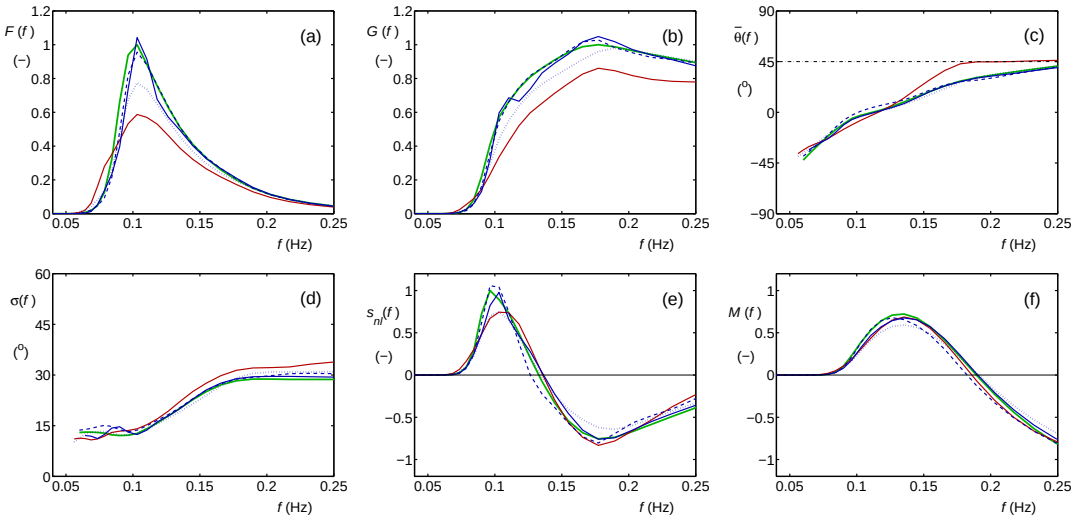

Fig. 4.47 : Like Fig. 4.46 for test_05.

.

configuration is the only configuration that attempts to reproduce spectral multi-modality of the WRT method in the fetch-limited growth test, albeit with limited accuracy. The one-parameter WAM and GMD3 methods result in uniformly unimodal spectra (figures not reproduced here)

The spectral noise in the G25d configuration occurs only at high frequencies. Therefore, it is natural to attempt to suppress it with the high-frequency filter introduced in Part 3 and reproduced in Section 2. The resulting two-dimensional spectra corresponding to those presented in Figs. 4.48 and 4.49 are presented in Fig. 4.50, and the corresponding model errors per test are presented in Table 4.31 and are identified as configuration S25d. A comparison of the three figures shows that the filtering indeed suppresses the high-frequency noise in the spectra, and the table indicates that the resulting model errors are actually slightly better than those of the corresponding unfiltered model configuration (compare configurations S25d and G25d). When comparing the two configurations to each other instead of to the reference WRT results, model differences ('errors') of 3% are found. The fact that these differences are much smaller than the errors of the individual configurations, indicates that the effects of the filtering indeed affect noise in the spectral tail, with minimal impact on other model behavior.

If the filtering is used in combination with the GMD, the filter would ideally be included in the optimization experiments, and not included after the optimization has taken place. For the present feasibility oriented study, and given the small impact of the filter on model behavior other than high-frequency noise, such an optimization has not been considered. For future optimization experiments, however, the filter (with possibly its parameter values, should be included in the

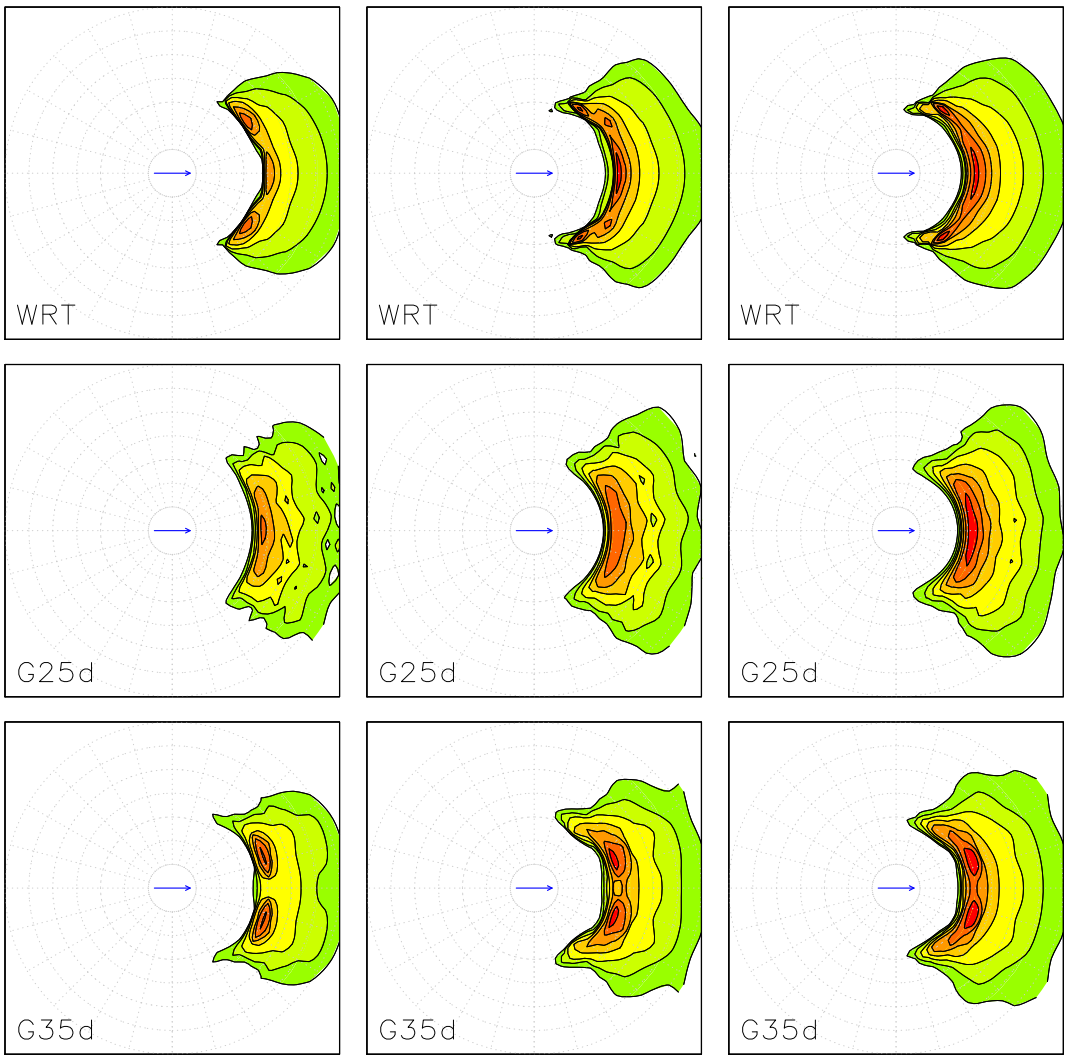

Fig. 4.48 : Two-dimensional energy spectral $F(f,\theta)$ from approaches as indicated in the panels for the fetch-limited growth test test_02 *10km (left panels), 20km (center panels) or 30km (right panels) offshore. Logarithmic scaling with factor 2 between contours and lowest contour at 0.25 m^2s. Frequencies ranging from 0 to 0.25 Hz, frequency grid lines at 0.05 Hz intervals.*

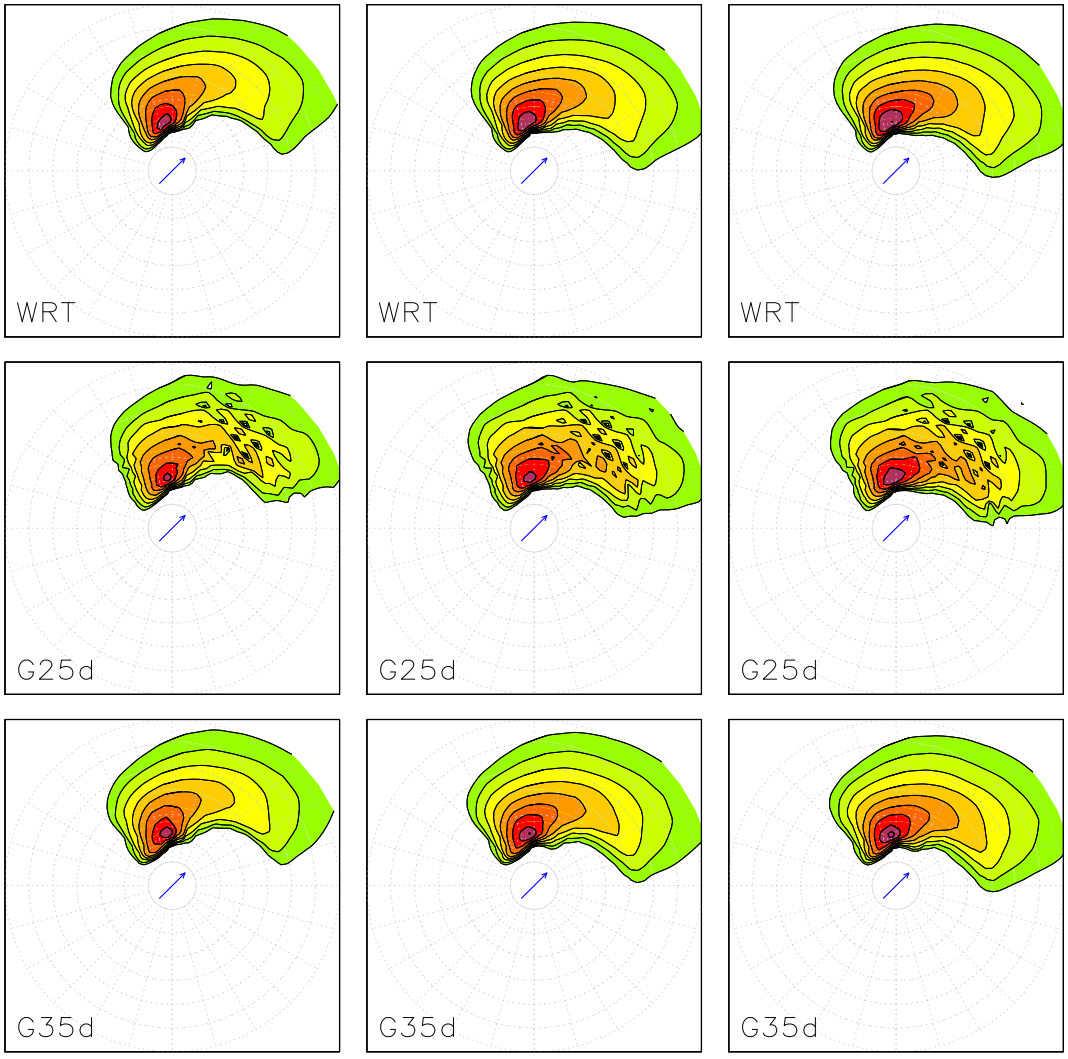

Fig. 4.49 : Like Fig. 4.48 for test test_05.

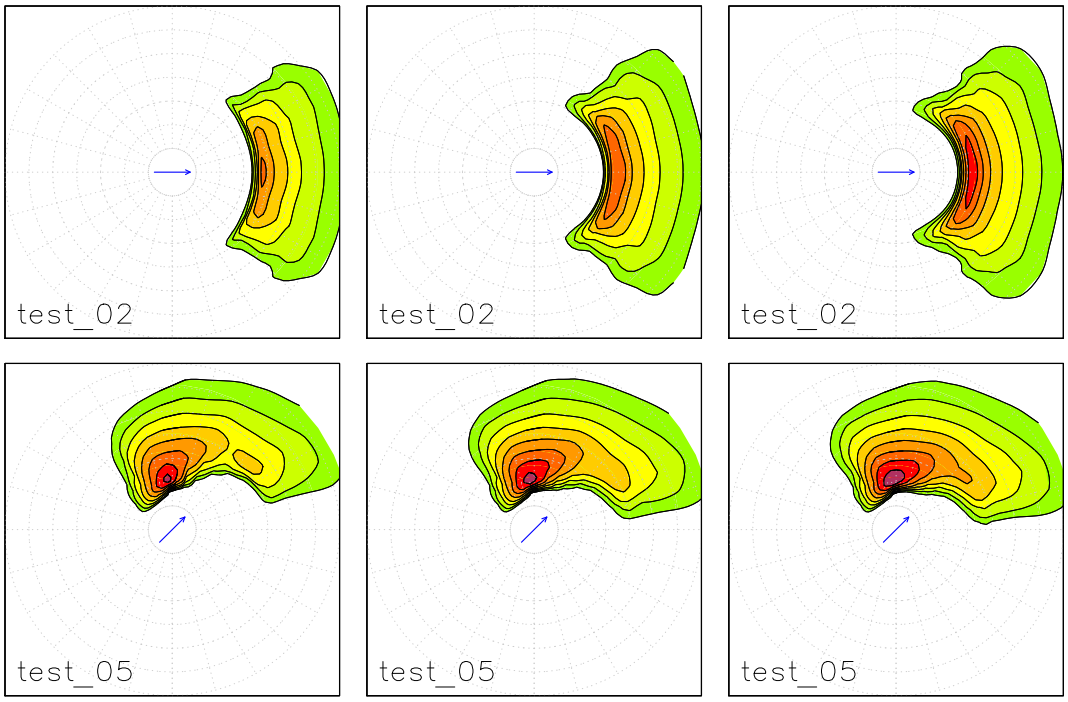

Fig. 4.50 : Like Fig. 4.48 and 4.49 for G25d with high-frequency filtering added.

genetic optimization experiments.

So far, only deep water configurations have been discussed. To minimize the number of optimization experiments, all shallow water optimizations have been performed with a fixed set of deep water quadruplets, for which the G35d configuration was chosen. Table 4.31 shows the impact of subsequent optimization of m, of C_s for the deep water quadruplets (G35s), or adding of 3 to 5 separate shallow water quadruplets (G353 - G356) of errors per shallow water test and on the overall model error. Optimizing m has a small but notable impact on all errors, as does optimization of C_s for each individual deep water quadruplet, incrementally reducing the overall model error by 0.2, and 0.6%, respectively. A larger impact is found when optimizing three independent shallow water quadruplets (G353), which reduces the overall model error by 1.2% compared to the five deep/shallow quadruplets, and by 2.0% compared to the deep water configuration. Subsequent adding of quadruplets has a minor but systematic positive impact on model errors. Note that as with the deep water optimization, errors of individual tests do not monotonically improve with complexity of the GMD configuration.

Figures 4.51 through 4.53 show the mean wave parameters H_s and k_pd for the three shallow water tests, and for the WRT, WW3, GMD3s3 and G354 through

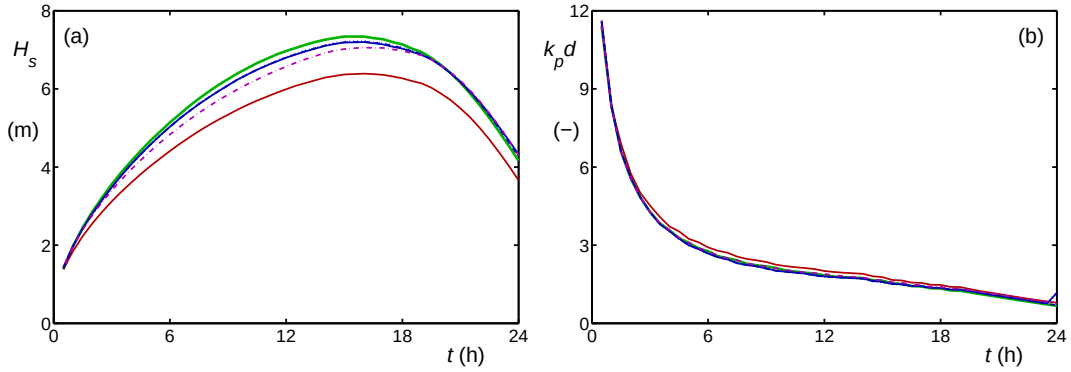

Fig. 4.51 : Evolution in time of a) significant wave height H_s, and b) relative depth $k_p d$ for the shallow water growth test test_11. *Green line: WRT. Red line: WAM. Dotted / dashed / solid blue lines: G354 / G355 / G356. Purple chain line: GMD3s3 based on one-parameter quadruplet definition.*

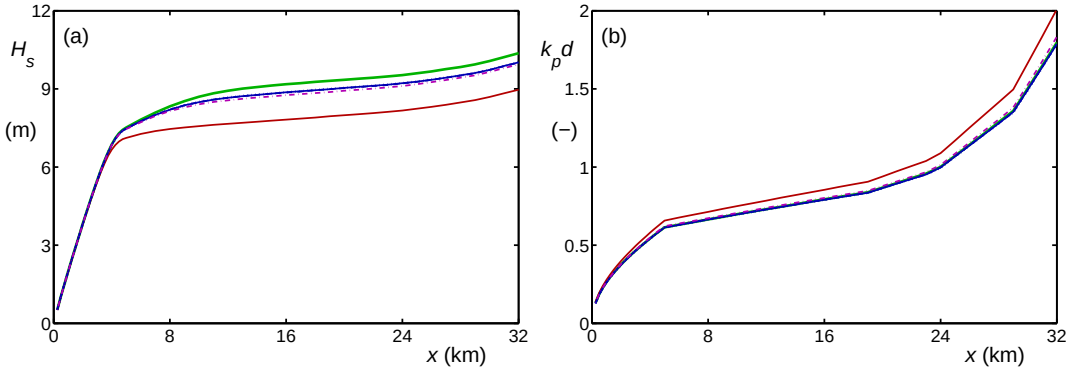

Fig. 4.52 : Evolution in space of a) significant wave height H_s, and b) relative depth $k_p d$ for the wind seas on beach test test_12. *Legend as in Fig. 4.51. Solid black line in c) represent wind direction.*

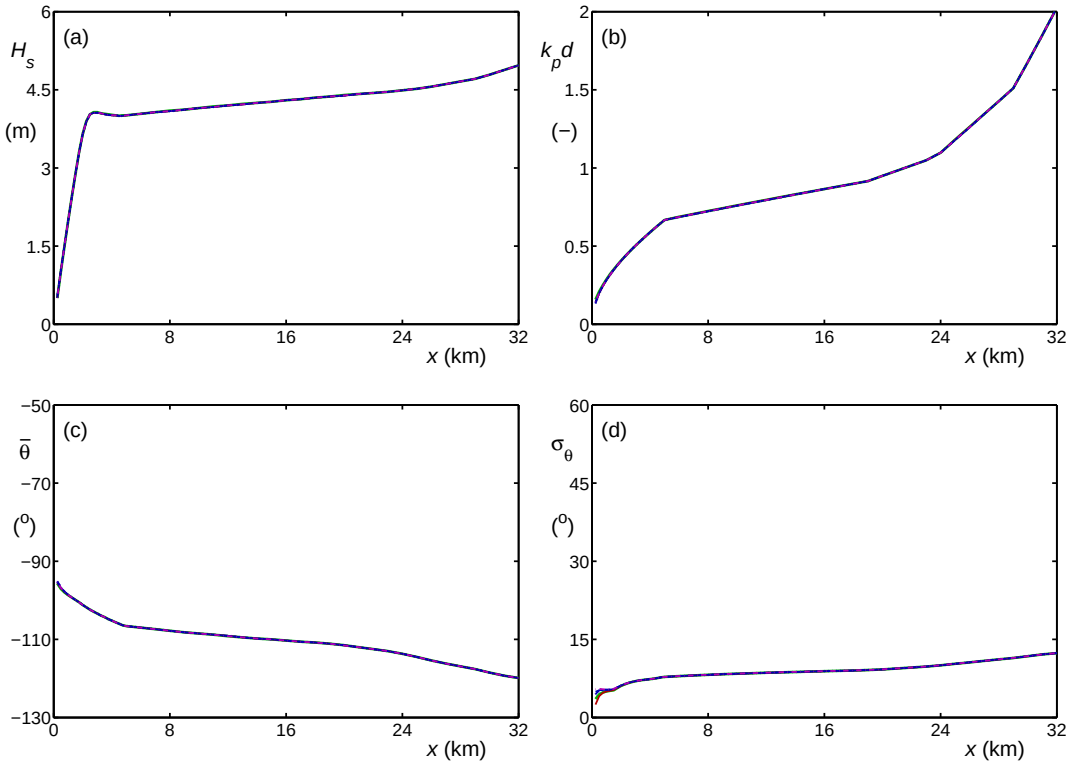

Fig. 4.53 : Like Fig. 4.52 for the swell on beach test test_13*, adding mean direction and directional spread.*

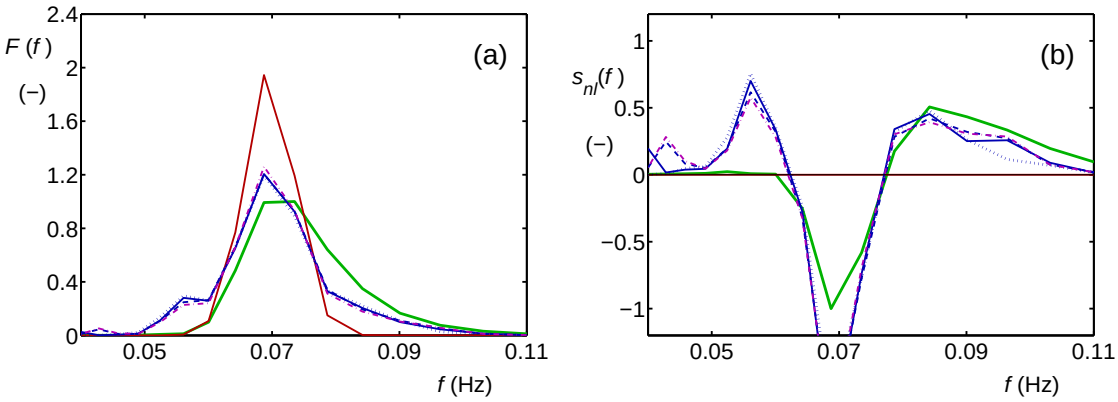

Fig. 4.54 : (a) One-dimensional spectra $F(f)$ for test test_13 *at 3 m water depth and (b) corresponding nonlinear interactions $s_{nl}(f)$ for results of Tables 4.10 and 4.11. green solid line: WRT. red solid line: no S_{nl}. blue dashed line: $n_q = 2$ (green exp.). blue dotted $n_q = 3$ (green exp.).*

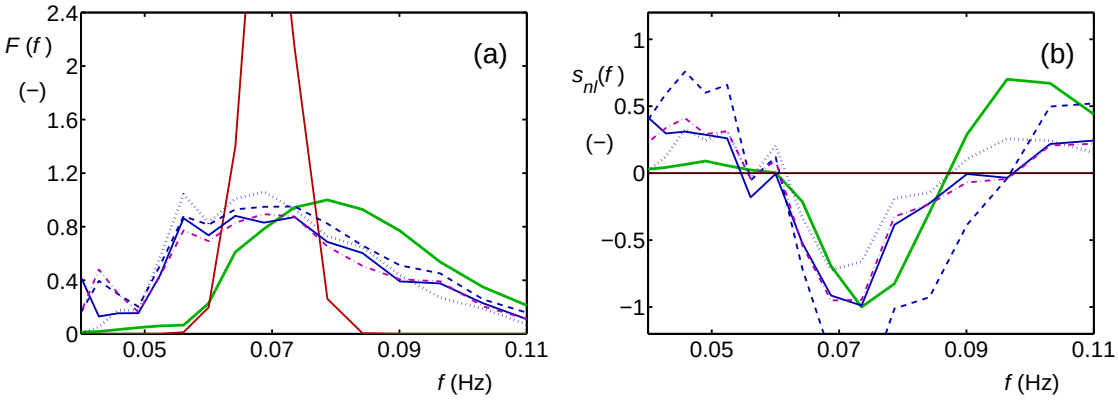

Fig. 4.55 : Like Fig. 4.54 at 1m water depth.

G356 configurations. For test_11 and test_12, the GMD configurations based on the three-parameter quadruplet definition (blue lines) have some advantage over the configurations based on the one-parameter quadruplet definition (GMD3s3, purple line). As before, it is noticed that errors for these two tests are dominated by errors in the deep water / offshore conditions, and hence depend on the accuracy of the deep water quadruplet configuration used as the basis for the shallow water optimization. For the swell test test_13 virtually no differences are found in the wave height and relative depth. In the shallowest grid points in the latter test, however, ($d \leq 5$m) the directional spread and the peak frequency (not shown here) show clear differences between the various approaches.

As in previous optimization experiments, the small divergences of approaches for extremely shallow water is associated with the inability of the present GMD implementation to accurately describe the strong interactions in the shallowest water. Figure 4.54 shows the spectrum and source term at 3m water depth. As with the corresponding results for the optimized one-parameter quadruplets shown in Fig. 4.28, a spurious low-frequency peak is found in both the spectrum and the source term, with the present most complex approach giving only marginal improvements over the latter. The most extreme conditions in the shallowest grid point of this test, however, do indicate the benefit of additional complexity in the GMD configuration. This is illustrated in Fig. 4.55; particularly the interaction source term at this depth is clearly improved by adding quadruplets. This is not evident in the overall model error, as this behavior occurs in only a few of the 47 test spectra for this test case. In spite of the spurious shift of the spectrum to lower frequencies, the capability of the GMD to lower the spectral peak and widen the spectrum is impressive.

Table 4.32: optimum deep water GMD configurations.

configuration	λ	μ	$\theta_{12}(^o)$	C_d
WAM	0.250	—	—	$3.00\,10^7$
WW3	0.250	—	—	$1.00\,10^7$
GMD1	0.231	—	—	$2.54\,10^n$
GMD3	0.066	—	—	$5.80\,10^7$
	0.184	—	—	$4.32\,10^7$
	0.318	—	—	$1.43\,10^7$
G35d	0.066	0.018	21.4	$1.70\,10^8$
	0.127	0.069	19.6	$1.27\,10^8$
	0.228	0.065	2.0	$4.43\,10^7$
	0.295	0.196	40.5	$2.10\,10^7$
	0.369	0.226	11.5	$1.18\,10^7$

4.7 Summary of results

The present section provides a first ever attempt to optimize a full GMD for deep and shallow water, although it can be considered as an expansion of previous work for deep water. The deep water results are in line with previous results and show a massive improvement of model behavior with increasing complexity of the GMD configuration. Preferred deep water configurations will be discussed below. Shallow water optimizations have never been attempted before. The results presented here show the potential of the GMD to improve model behavior in shallow water, but also shows some remaining issues with spurious behavior in extremely shallow water. This behavior indicates a need for re-assessing the scaling of the GMD in such conditions, as well as a need for re-assessing optimization for such conditions. Both are linked, and will be considered outside the scope of the present study. Considering this, only improvements for operational model in deep water will be considered in the remainder of this study. Due to the natural separation of deep and shallow water behavior in the GMD, and considering that the GMD and DIA are traditionally considered only for deep and intermediate water depths, considering deep water improvements is both straightforward and appropriate.

Optimizing a GMD is an exercise in finding balance between accuracy and economy. For this reason, there is no single optimum solution. Accuracy is measured against the reference model configuration with the WRT nonlinear interaction parameterization, whereas economy and accuracy are measured relative to accuracy and computational costs of the original DIA in WAM or WW3 configuration. The traditional DIA configuration is the benchmark for speed, but cannot provide all-round accuracy. The WAM and WW3 configurations should be

used for reference, whereas the GMD1 configuration represents a subjectively optimized configuration. The GMD1 configuration, however, lacks the capability to accurately describe both wave energy and peak frequency. This capability can be introduced by using the GMD3 configuration, in which three traditional quadruplet configurations are used. The experiments with optimizing such a GMD by sampling spectral space with pre-set quadruplets confirms that no accuracy can be gained by using more than 5 or 6 traditional quadruplet configurations, and that a balance between economy and accuracy is found by using a GMD3 configuration. Whereas a GMD3 configuration goes a long way towards accurate mean wave parameters, clear spectral errors remain. Spectral errors can be reduced by introducing two- or three-parameter quadruplet definitions in the GMD. A reasonable balance between cost and accuracy was found in the G25d and G35d configurations. Since the G25d configuration is less accurate, equally expensive, and more sensitive to producing spectral noise, the G35d configuration appears preferable. This leaves the WRT, WAM, WW3, GMD1, GMD3 and G35d configurations to be tested in practical application in Section 5. For convenience, the corresponding GMD configurations are gathered in Table 4.32.

5 Practical applications

So far, only test results that were part of the optimization have been considered. Such tests are not independent, and cover only a limited number of idealized test conditions. Hence, the next step is to test the selected GMD configurations in more realistic conditions. As mentioned in the previous section, only deep water tests will be considered for now. Error metrics will consist of the previously used test metrics for selected points and times, augmented with maps of differences in mean wave parameters. Model run times will also be considered to assess if increases in run times coincide with expectations from Part 3. The realistic test cases considered are a synthetic moving hurricane, and a storm system over Lake Michigan.

Note that the only goal for executing these tests is to see if model results obtained with the GMD closely follow those obtained with the exact WRT method. Since there are no operational wave model physics packages available designed explicitly for the WRT methods[5], a comparison with wave data is somewhat futile.

5.1 Moving idealized hurricane

The first realistic test considers a moving hurricane modeled with a set of three telescoping nests with resolutions of 50, 15 and 5km, respectively. This case (test_hr) is in essence the mww3_test_05 test that is distributed with WAVEWATCH III version 3.14 (with outer output points at 500km rather than 800km from the eye of the hurricane). A total of 33 output points are used to compute the metrics of this study. The grid layout and the output points are illustrated in Fig. 5.1. Note that maps of mean wave parameters for this test will be generated by successive overlay of graphics for the three individual grids, without attempts to smooth the transitions. The model starts from calm conditions and integrates for 24h. Spectra at the end of this period are considered. The maximum wind speed is 45ms^{-1} and the radius of maximum wind is 50km. The hurricane and grid move with a speed of 5ms^{-1} to the right. This test is run with the spectral resolutions used throughout the GMD optimization.

The wave heights at the end of the integration period for the exact WRT computation are presented in Fig. 5.2a. Due to waves and the storm moving in the same direction, and hence having most time to grow, waves at the right side of the storm (or south side of the eye in the figure) are the highest and surpass $H_s = 12.2$m. Conversely, waves at the left (north) side of the eye are lowest and typically $H_s < 6$m, with an 'eye' in the wave field slightly to the NW of the eye of the storm with wave height $H_s < 2$m. Swells with $H_s > 3$m (comparable to

[5] Note that some source term development has bee done with WRT in idealized cases, e.g., Alves and Banner (2003).

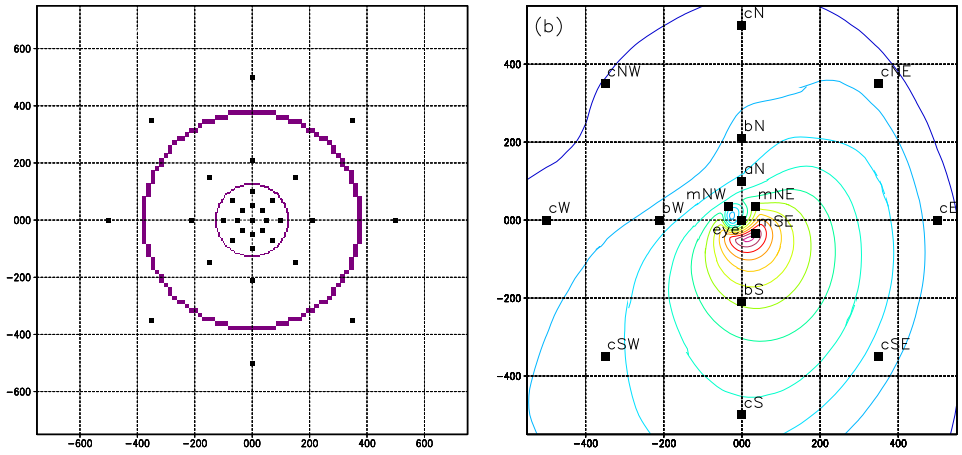

Fig. 5.1 : (a) Grid layout and output points for moving grid hurricane test test_hr. *Purple grid boxes identify boundary points in telescoping grids with resolutions of 50, 15 and 5km, respectively. Offsets in km. Outer grid ranges from -1250 to 1250km, and is not fully displayed.(b) Output point used in following figures, overlaying WRT wave heights.*

the 12ft wave height range monitored by the National Hurricane Center in the US) running ahead and to the right of the storm reach as far as 400km east and 600km south of the storm

Panels (b) through (f) of Fig. 5.2 show the differences in wave heights for the five GMD configurations compared to the exact solution. The WW3, WAM and GMD1 configurations correspond to versions of the traditional DIA. For all three configurations, wave heights on the left (north) of the eye of the storm are overestimated by as much as 1.4m, whereas wave heights on the right (south) of the storm are underestimated by as much as 1.4m. Furthermore, forerunners of the storm (in the east of the plot) are systematically underestimated by more than 0.4m. Figure 5.3b through f show the corresponding relative differences. The traditional DIA configurations result in wide spread errors in wave heights ranging from -20 to 30%.

Figures 5.2e and 5.3e show the absolute and relative wave height errors obtained with the GMD3 configuration. Errors are still widespread but, as expected, much reduced compared to the configurations compatible with the DIA. The maximum wave height errors are less than 1m, and generally less than 10%. Finally, Figs. 5.2f and 5.3f show the absolute and relative wave height errors obtained with the G35d configuration. Errors are much less wide spread, and greatly reduced in magnitude, with maximum local wave height errors uniformly below 0.4m and 10%, and generally below 5%. Hence, as expected, the progression of GMDs with increasing complexity leads to increasing accuracy, with the G35d configurations closely reproducing wave heights from the WRT approach. As the wave heights

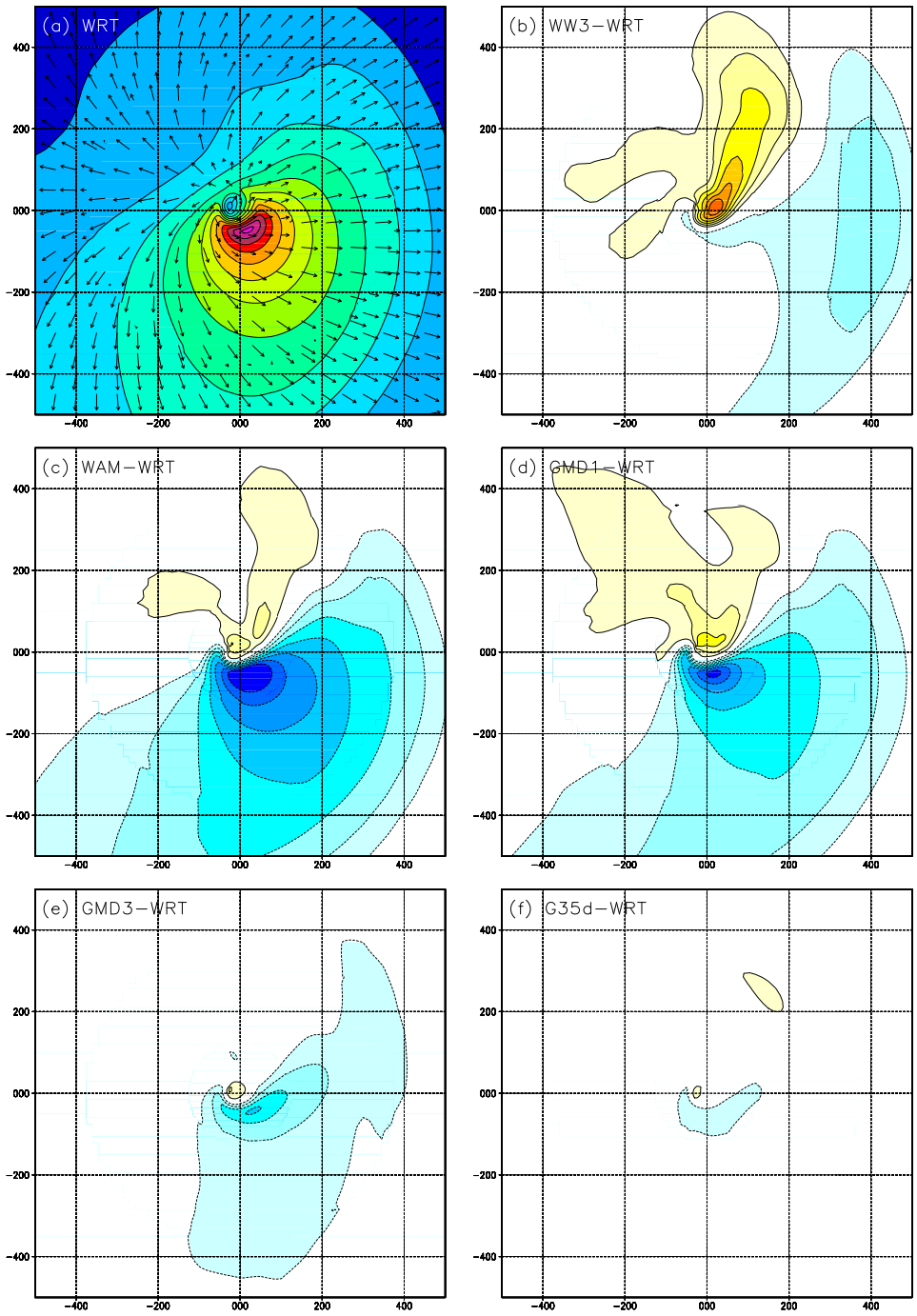

Fig. 5.2 : (a) Significant wave height H_s for the hurricane test test_hr *and the WRT approach. Contour intervals at 1m and maximum wave height larger than 12m (b-f) Wave height difference in m for indicated approaches. Contour levels at 0.2m. Reds indicate positive difference. 0m difference contour not plotted.*

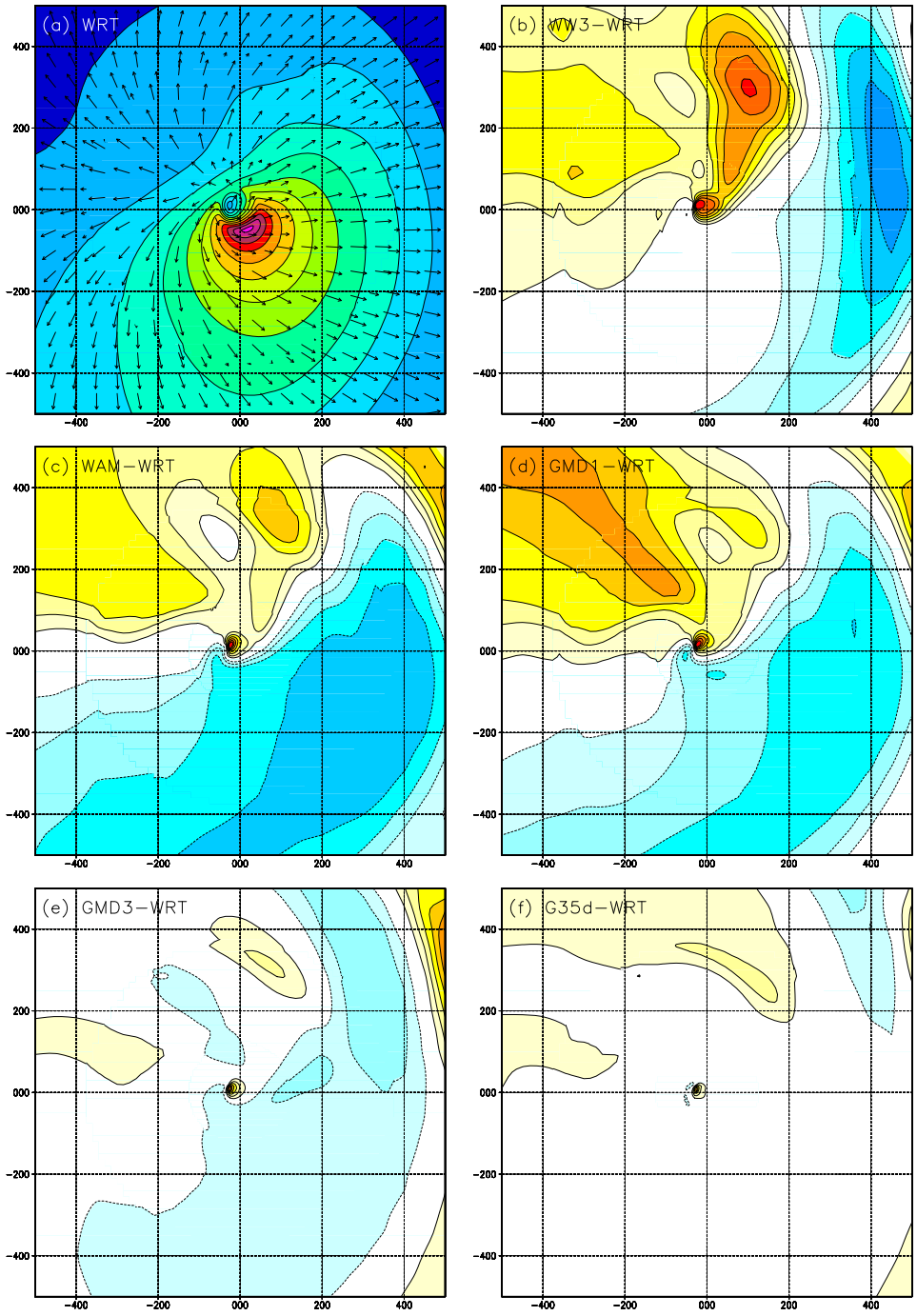

Fig. 5.3 : Like Fig. 5.2 with relative differences of wave heights in percent, and contours at 4% intervals.

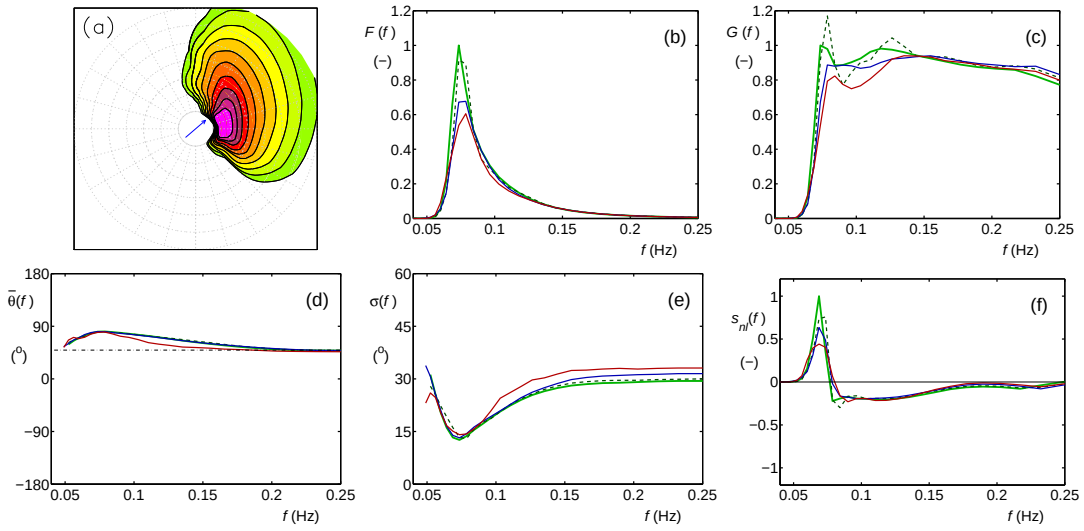

Fig. 5.4 : Spectral behavior of various nonlinear approaches for output point mSW as identified in Fig. 5.1. (a) Two-dimensional spectrum $F(f,\theta)$. (b) One-dimensional spectrum $F(f)$. (c) Steepness spectrum $G(f)$.(d) Spectral direction $\sigma_\theta(f)$. (e) Directional spread $\sigma(f)$. (f) Source term $s_{nl}(f)$. Green line: exact (WRT) solution. Dashed dark green line: G35d. Blue line: GMD3. Red line: GMD1.

in this test case form a mix of wind seas and swells, and since both appear to be reproduced accurately, this also suggests accurate description of spectral shapes.

The next step is to check more detailed spectral model behavior at the output test points. Examples of this are shown in Figs. 5.4 through 5.19. First, wave conditions at the radius of maximum wind will be considered.

The largest waves are found near the radius of maximum winds in the SE sector of the hurricane. In the southern half of the hurricane, winds and waves line up, and result in a slightly rotated wind sea spectrum. The highest waves are found near output point mSW, and resulting spectral parameters are presented in Fig. 5.4. Errors for the various GMD configurations are as expected from the results in the previous sections. Increasing complexity of the GMD results in increasing accuracy, with the G35d configuration being highly accurate but with a slight bi-modality in the steepness spectrum $G(f)$ (Fig. 5.4c).

The lowest wave heights at the radius of maximum winds occur in the NW quadrant of the hurricane, where the hurricane and the winds move in different directions, and where no swells can penetrate from other quadrants of the hurricane. As is illustrated in Fig. 5.5, waves have higher frequencies and result in a directionally skewed wind sea spectrum. In the NE quadrant of the hurricane the spectrum is strongly skewed, with the peak spectral energy at more than 90° off the wind direction (Fig. 5.6a, d). Even here the spectrum retains typical wind sea characteristics with respect to spectral shape and nonlinear interaction, however,

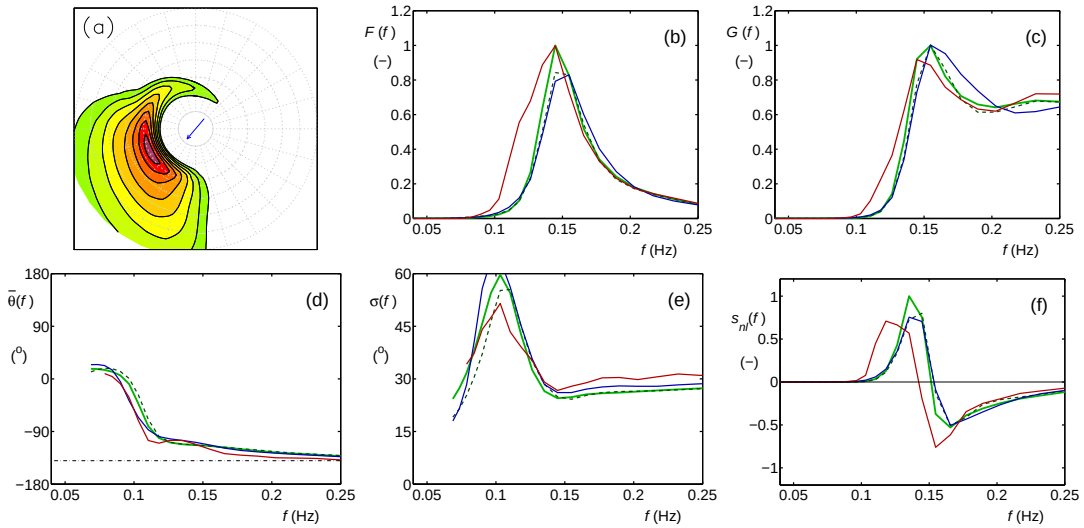

Fig. 5.5 : Like Fig. 5.4 for location mNW

with limited peak enhancement as with the idealized turning wind case.

The next set of output points is located at twice the radius of maximum wind. For most of these output points, spectra are typical skewed wind sea spectra similar to those found at the radius of maximum wind speed. However, in the northernmost three output points, there appears to be a start of wind-sea to swell separation, with the nonlinear interactions loosing the typical three-lobed structure for wind seas. This is illustrated here with spectral output for the point directly north of the eye of the hurricane in Fig. 5.7.

The third set of output points is located at 210km from the eye of the hurricane, or approximately 4 times the radius of maximum wind speed. North of the eye of the hurricane, winds have become light at this distance, and spectra are transitioning to narrow swell shapes. This is illustrated here with spectral data directly north of the eye in Fig. 5.8. Note that in Fig. 5.8c the steepness spectrum does not seem to be normalized properly. This can be attributed to the fact that the low wind speed attempts to build a wind sea at high frequencies at the edge of the discrete spectral grid, but without sufficient spectral resolution to resolve the wind sea spectrum up to $3f_p$. In this case, the WRT approach results in locally unrealistic spectral values, particularly influencing α, β and f_0. hence, in computing objective errors for this case, it is prudent not to include error measures for these three parameters.

South of the eye of the hurricane, winds remain stronger, and spectra retain characteristics of wind seas. This is illustrated here with spectral data directly south of the eye in Fig. 5.9. Note that this spectrum still has the spectral peak enhancement and shape of the nonlinear interactions typical for wind seas. Note that somewhat anomalous behavior at this distance to the eye is found directly

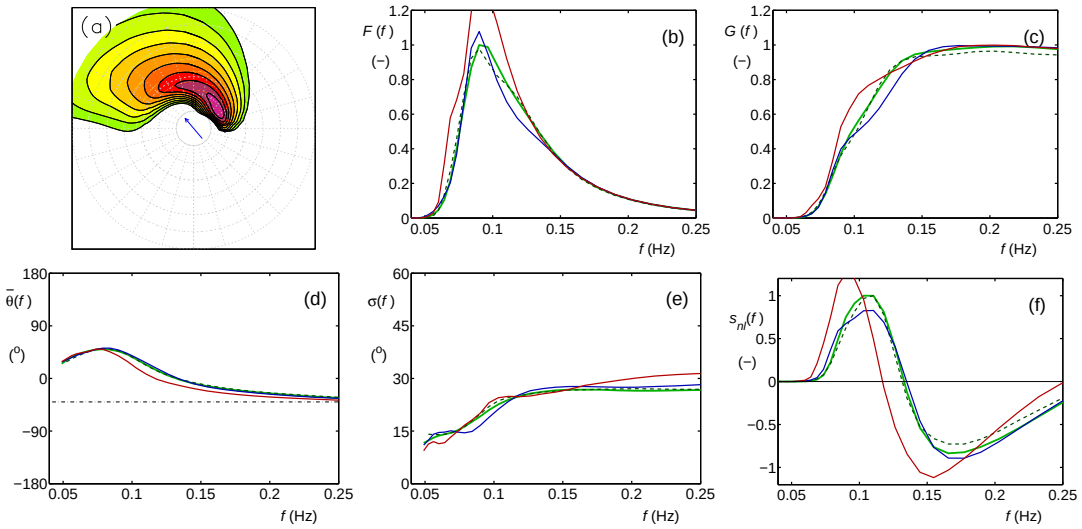

Fig. 5.6 : Like Fig. 5.4 for location mNE

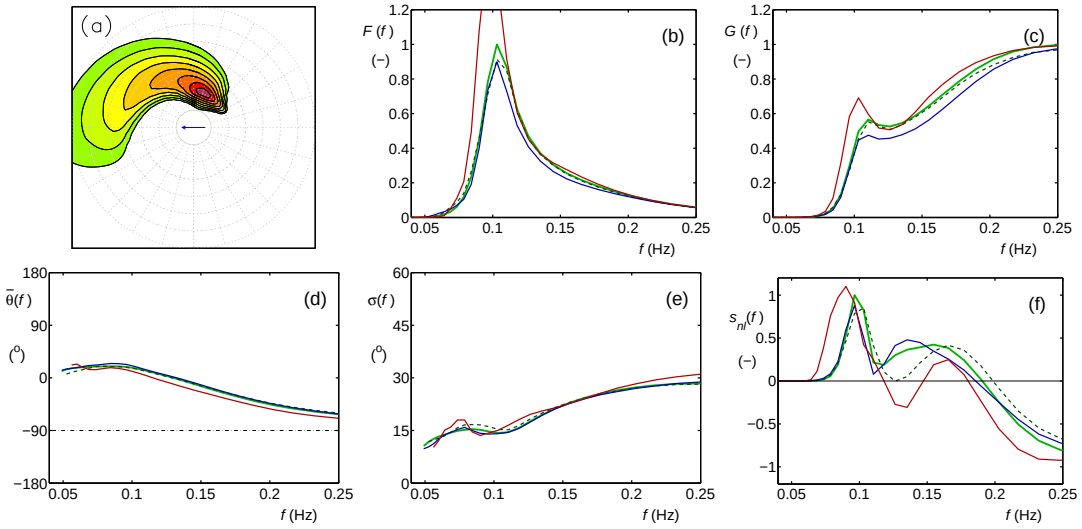

Fig. 5.7 : Like Fig. 5.4 for location aN

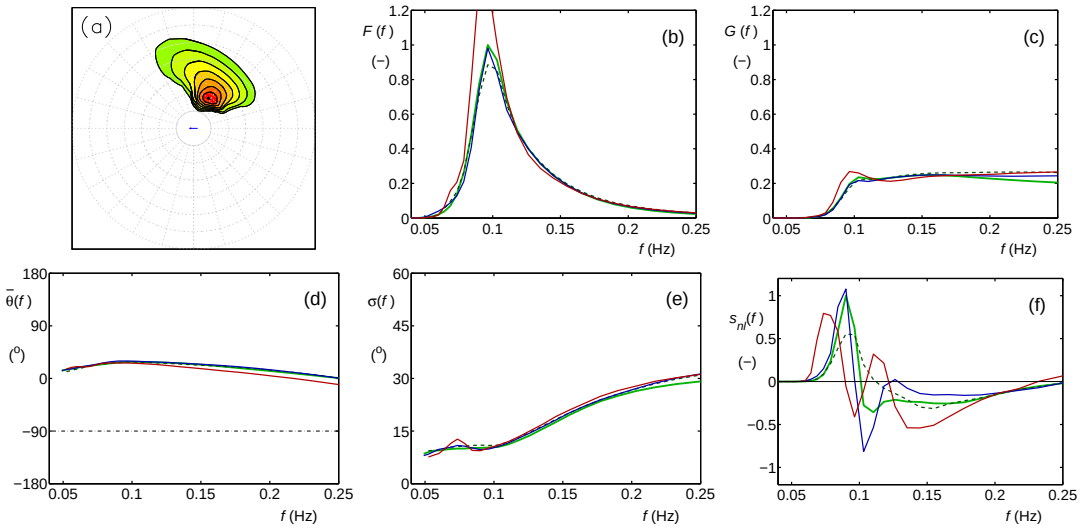

Fig. 5.8 : Like Fig. 5.4 for location bN

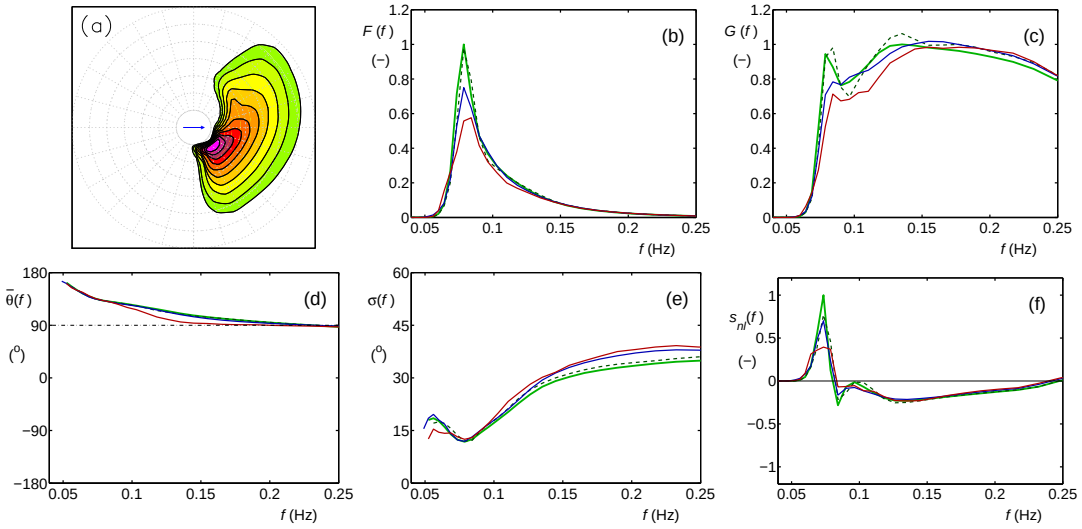

Fig. 5.9 : Like Fig. 5.4 for location bS

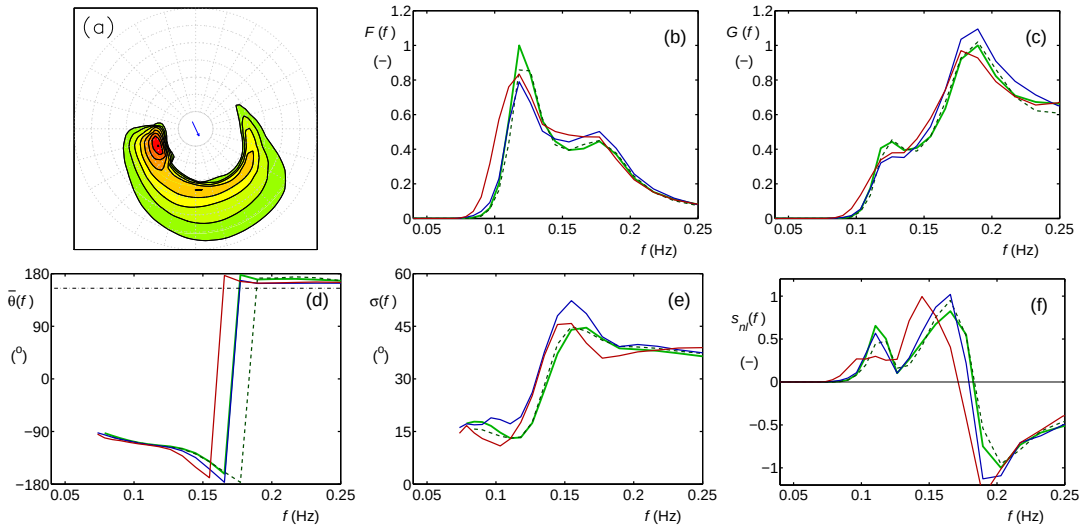

Fig. 5.10 : Like Fig. 5.4 for location bW

behind the hurricane (Fig. 5.10.) Here, the spectrum clearly starts to separate into a swell originating from the northern half of the hurricane, and a wind sea left behind by from the western side of the hurricane.

The fourth and last set of output points is located at 500km from the eye of the hurricane, or 10 times the radius of maximum wind speed. Because all output points show somewhat different behavior here, spectral data are presented here for all 8 points in Figs. 5.11 through 5.18. The discussion of the output at these points will start in the NE quadrant (Fig. 5.11), and will run counterclockwise to the point east of the eye of the hurricane (Fig. 5.18).

Going from the NE to the NW quadrant (Figs. 5.11 through 5.13), winds are virtually non-existent, and the spectrum has transitioned to a distinct swell configuration, with low frequency energy distributed over narrow bands in frequency and direction. Note that two of the three spectra have issues with normalizing the steepness spectrum as discussed above. Directly behind the hurricane (location cW, Fig. 5.14). the two spectral peaks observed closer to the hurricane in Fig. 5.10 have now fully separated into individual wave fields. In the SE quadrant (Fig. 5.15), these two wave fields are starting to separate, with a clear impact on the nonlinear interactions, whereas south of the eye (location cS, Fig. 5.16) no separation is visible in the spectrum or source term. Finally, leading the hurricane in the SE quadrant and east of the eye (Figs. 5.17 and 5.18) again two wave fields can be distinguished, including a low-frequency swell that represents the "forerunners" of the hurricane. This brings us back to the full swell conditions to the north of the eye.

The only location not yet considered is the eye of the hurricane (Fig. 5.19). The wave height maps in Figs. 5.2 and 5.3 indicate an 'eye' in the wave height

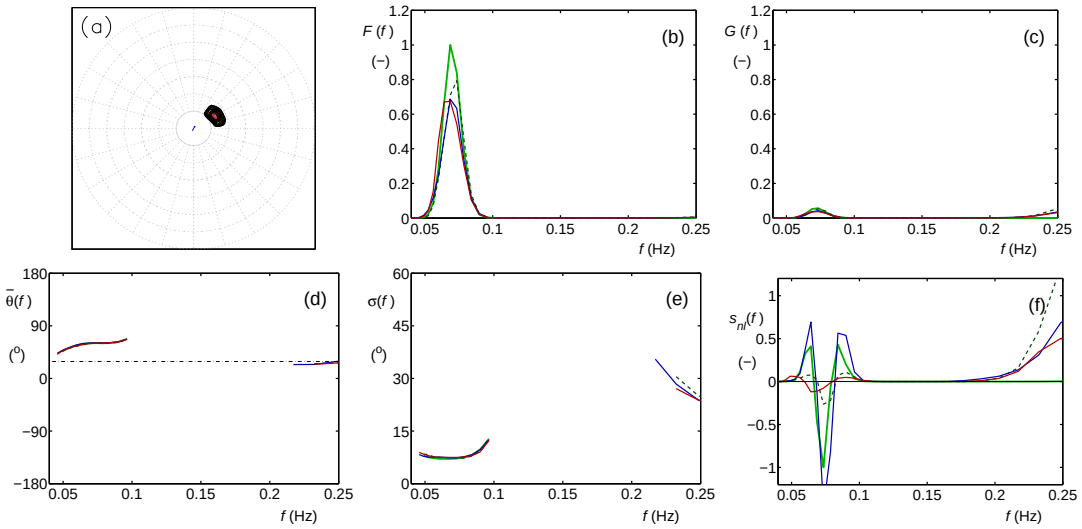

Fig. 5.11 : Like Fig. 5.4 for location cNE

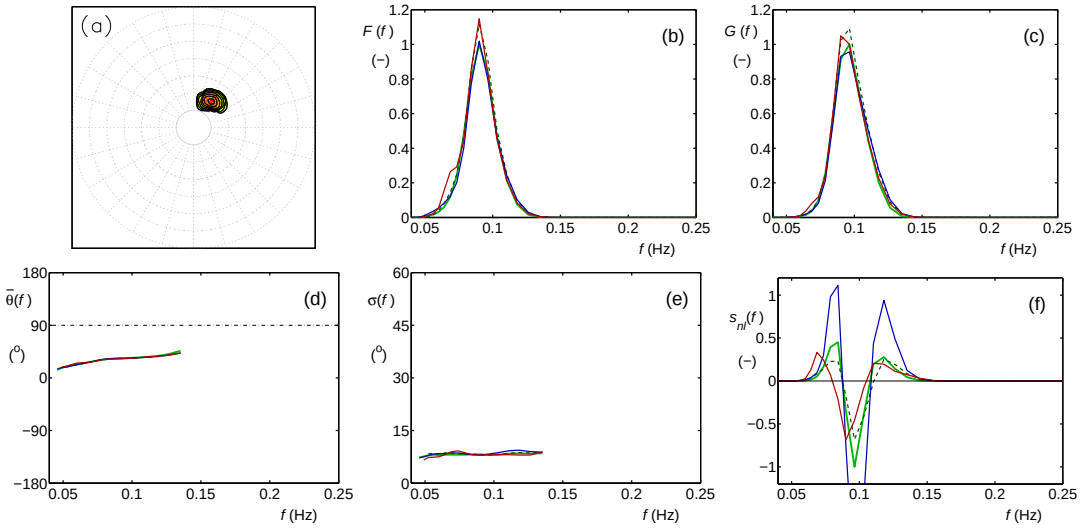

Fig. 5.12 : Like Fig. 5.4 for location cN

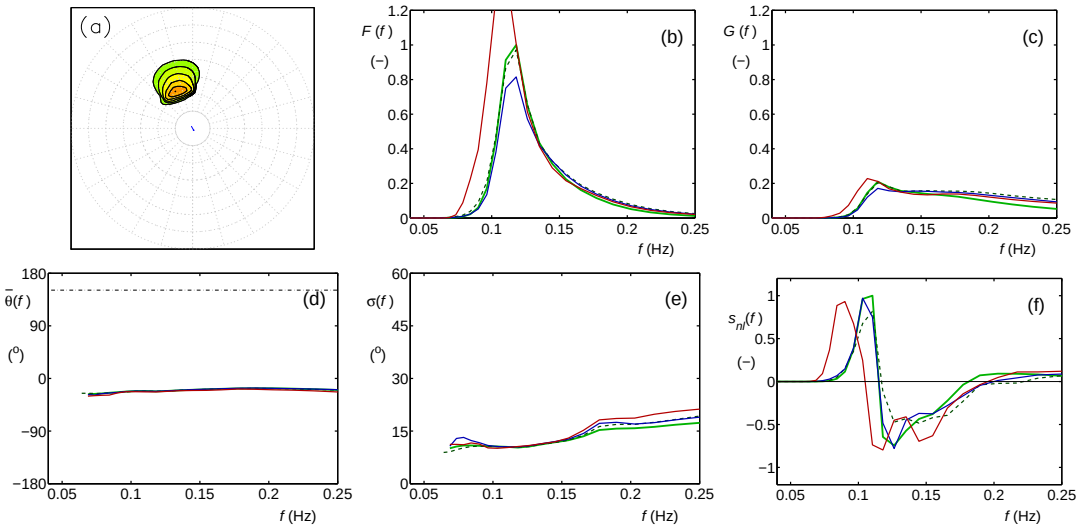

Fig. 5.13 : Like Fig. 5.4 for location cNW

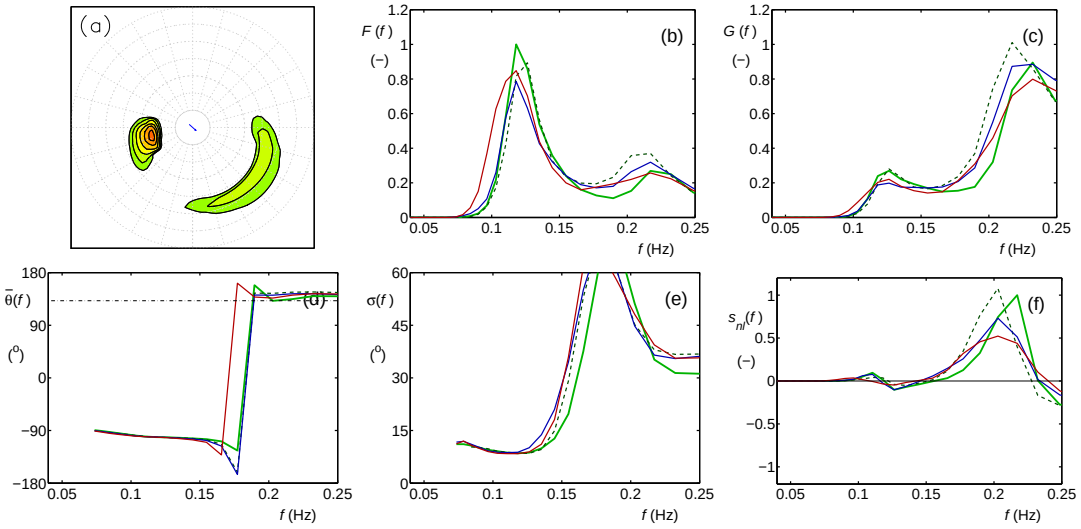

Fig. 5.14 : Like Fig. 5.4 for location cW

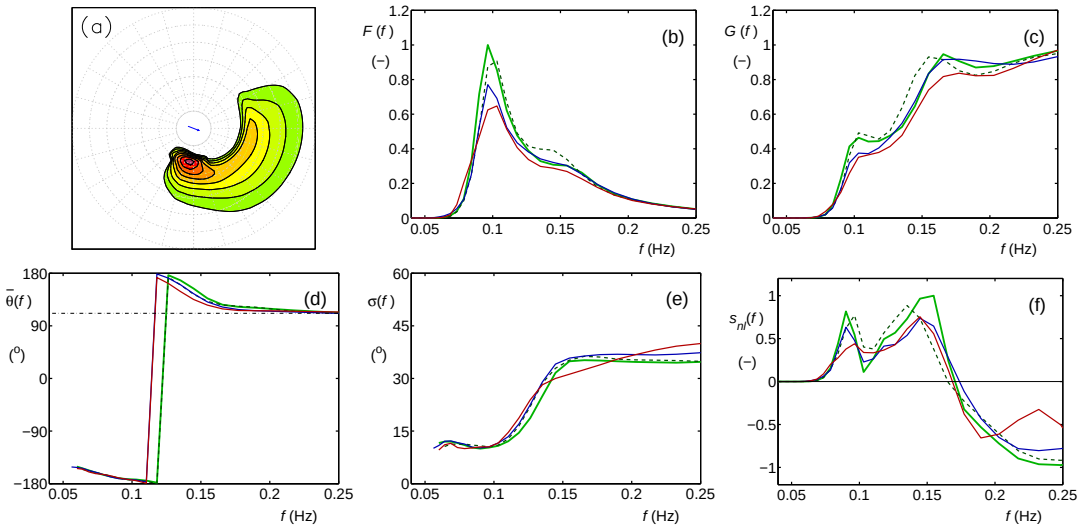

Fig. 5.15 : Like Fig. 5.4 for location cSW

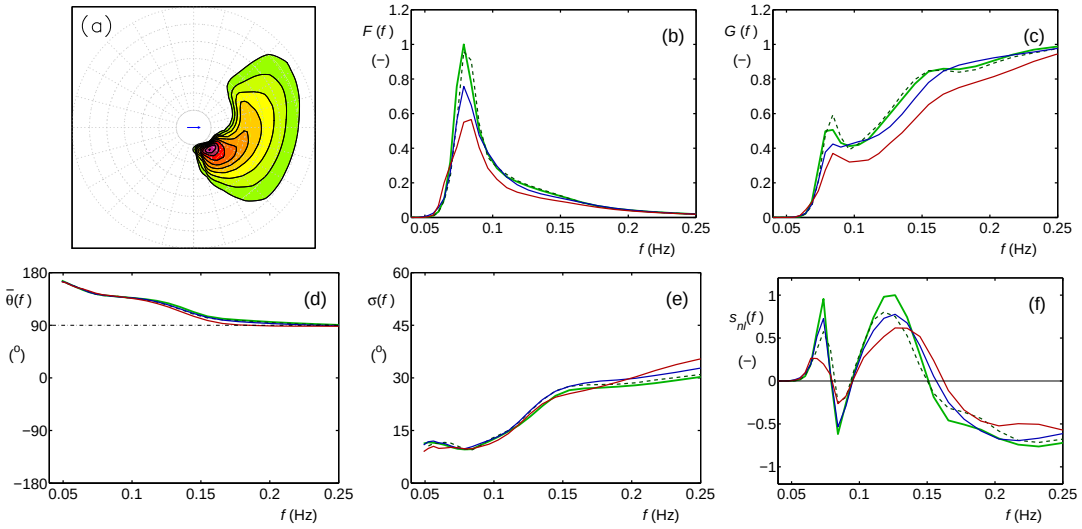

Fig. 5.16 : Like Fig. 5.4 for location cS

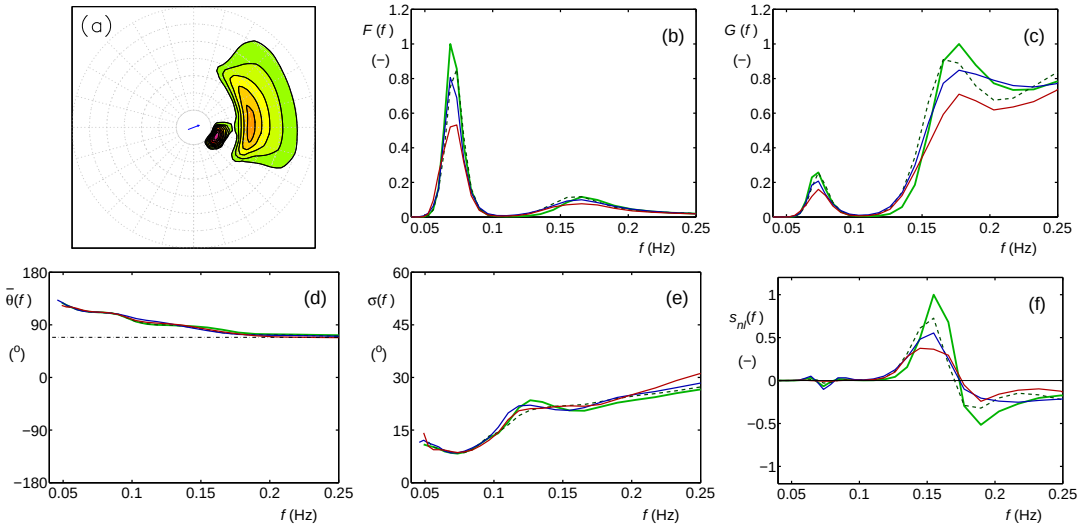

Fig. 5.17 : Like Fig. 5.4 for location cSE

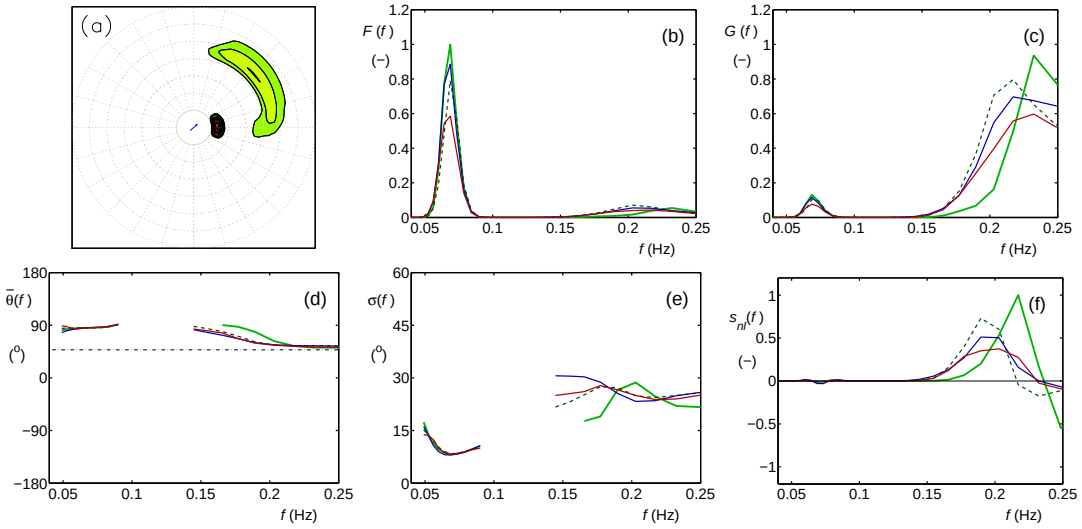

Fig. 5.18 : Like Fig. 5.4 for location cE

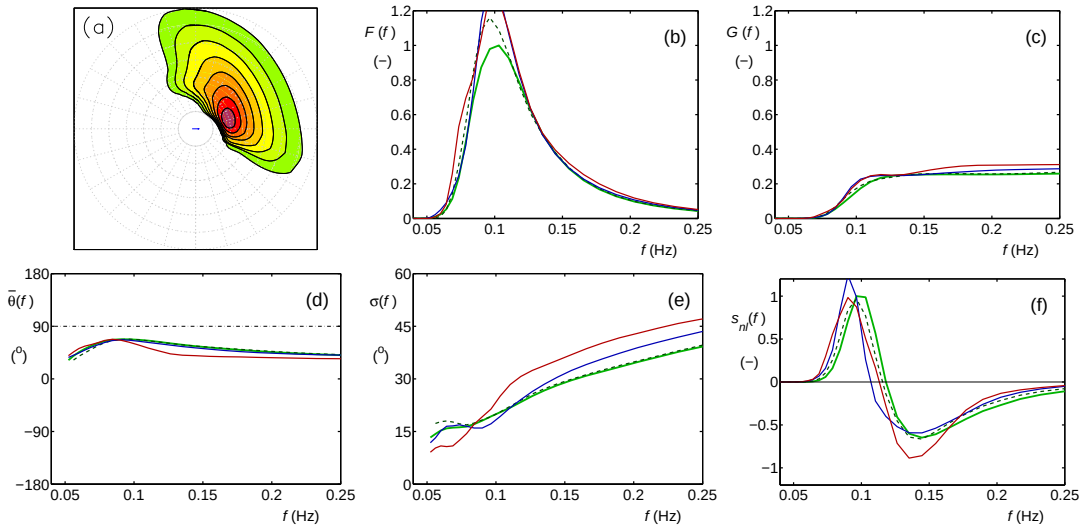

Fig. 5.19 : Like Fig. 5.4 for location eye

field offset from the eye in the wind field, and associated with notable wave height errors. Figure 5.19 indicates that the error is associated with a general overestimation of the spectral energy for the GMD1 and GMD3 configurations, with a moderate overestimation for the G35d configuration. Note that the spectral shape and source term suggest a wind sea spectrum, although the actual local wind speed is virtually nonexistent.

Considering Figs 5.4 through 5.19 this test case represents a large variety of wind wave conditions, including wind seas under turning wind conditions, wind-sea and swell separation, coexisting wind seas and swell, and swell dominated conditions. Uniformly, increasing complexity in the GMD configuration corresponds to better model behavior, with qualitative model improvements fully consistent with the improvement seen in the test cases used for the optimization. Objective error measures for this test are presented in Table 5.1 on page 163. In these error measures, errors for α, β and f_0 are not considered for reasons discussed above. The table shows error measures declining systematically from 27 to 17% with increasing complexity of the GMD configuration. This test case strongly suggests that the findings from the dependent test cases for the optimization of the GMD can be applied to more general cases. Furthermore, this test case quantifies that practical errors in wave height for hurricane conditions incurred due to errors in the DIA can be as large as 25%, and show systematic differences for the various quadrants of the hurricane relative to its propagation direction. Due to this systematic nature of the errors, it is expected that they will also occur in a well-tuned model.

5.2 A storm on Lake Michigan

The second realistic test considers a a real time forecast problem for Lake Michigan. The grid is extracted from the operational Great Lakes wave models at NCEP, and has a resolution of 0.05° in latitude and 0.0035° in longitude (or approximately 4km). The grid consist of 66×133 grid points with 41% (3598) wet grid points. For this test, the spectral range is expanded to 60 frequency grid points and out to 2.17Hz, to avoid issues with unresolved spectra for low winds as encountered with the WRT methods in the previous section. A two day period around a storm on October 6 and 7, 2009 is considered, During these two days, a strong wave event with rapidly turning wind and wave conditions occurred in the southern part of Lake Michigan. For this period hourly spectra are saved at buoy location 45007. Winds for this model run are provided by the Great Lakes Environmental Research Laboratory (GLERL), and consist of analysis based on in-situ observed winds only. The model is spun up with a one day model integration, for which results are not considered here.

Wave height maps for various dates are presented in Fig. 5.20 through 5.27, together with relative differences in wave heights for the five GMD configurations considered here. These figures represent the beginning and ending times of the period considered. The discussion will mostly focus on the southern part of Lake Michigan around buoy 45007 (identified by the black square in th figures).

At the beginning of the period considered (Fig. 5.20), weak southeasterly winds cover the southern half of Lake Michigan, with accompanying wave heights between 0.3 and 0.6m. Wind and wave conditions in the north are generally weaker. The GMD configurations equivalent to the traditional DIA (WW3, WAM and GMD1, Figs. 5.20b through d) show fairly systematic errors throughout the basin, with the WW3 configuration overestimating wave height H_s by typically 5-10%, the WAM configuration underestimating H_s by 10-15%, and the GMD1 configuration underestimating H_s by 5-10%, For both the GMD3 and G35d configurations, mean wave heights are well represented, with more localized errors generally smaller than 5%.

In the next several hours, winds and waves in the southern part of the basin slowly increase while wind and wave conditions in the northern part slowly decrease. At 14z (Fig. 5.21). Error patterns are generally unchanged, although WW3, GMD3 and G35d configurations have become more accurate. Note that positive errors in Green Bay (upper left) are at least partially due to the low normalizing wave height in the WRT approach.

By 18z (Fig. 5.22) winds and wave height have increased throughout the basin, and the errors in Green Bay have disappeared. Otherwise, error patterns have generally remained the same. In the next three hours (Fig. 5.23) winds in the south turn to the southwest and higher waves travel from the west to the center of the lake. An area of moderate errors is starting to grow in the center of the lake in the G35d configuration.

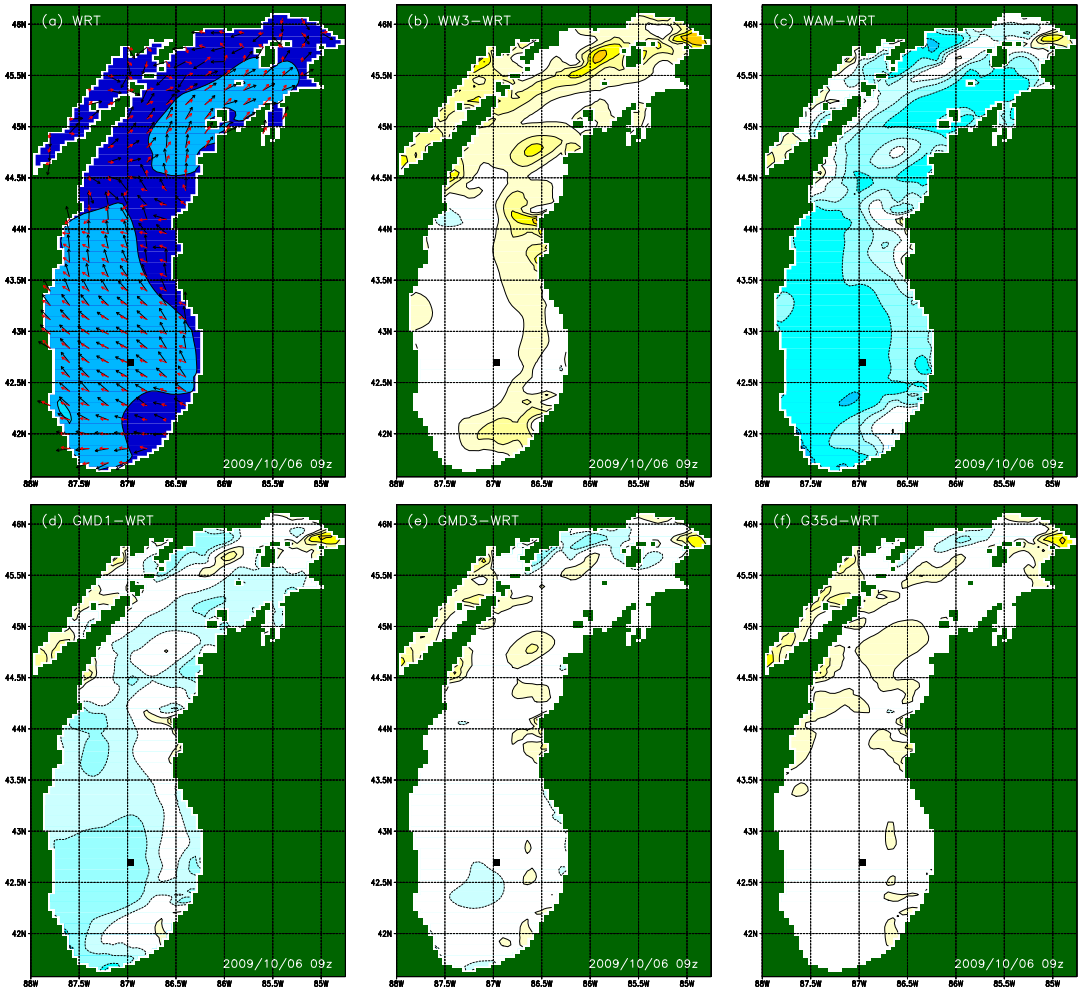

Fig. 5.20 : (a) Significant wave height H_s at Oct. 06 09z for the Lake Michigan test test_LM *and the WRT approach. Contour intervals at 1/3 m. Black arrows identify peak wave direction. Red arrows identify wind direction. (b-f) Relative ave height difference in % for indicated approaches. Contour levels at 4%. Reds indicate positive difference. 0% difference contour not plotted. The symbol represent the location of buoy 45007.*

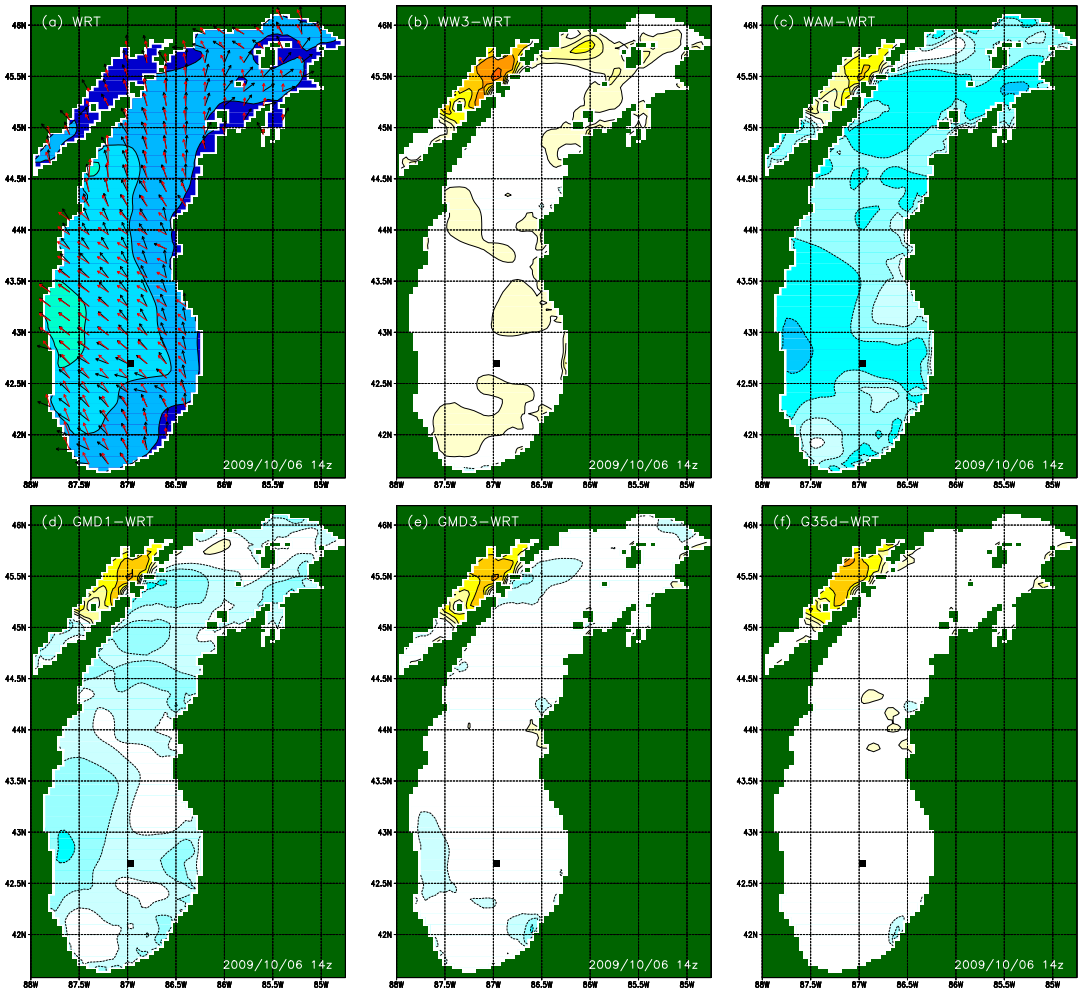

Fig. 5.21 : Like Fig. 5.20 at Oct. 06 14z.

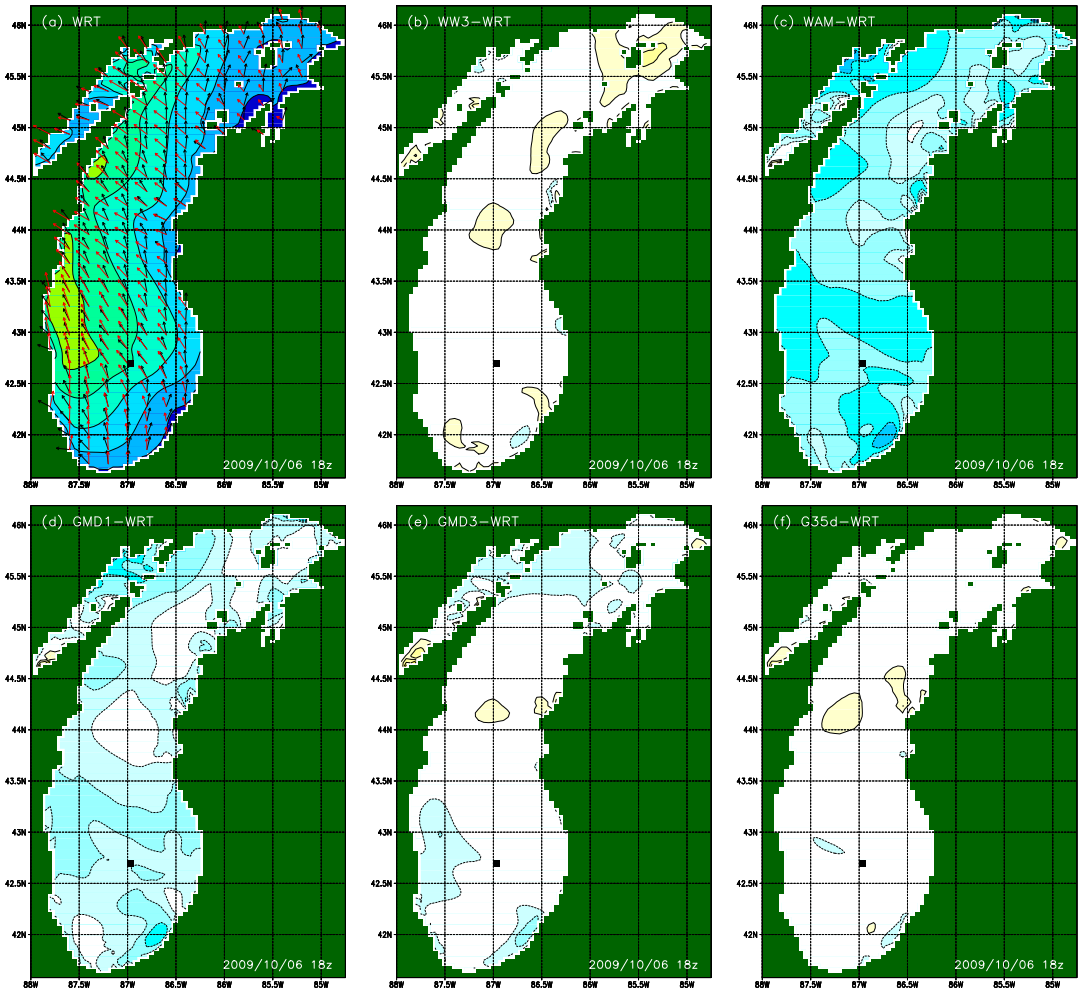

Fig. 5.22 : Like Fig. 5.20 at Oct. 06 18z.

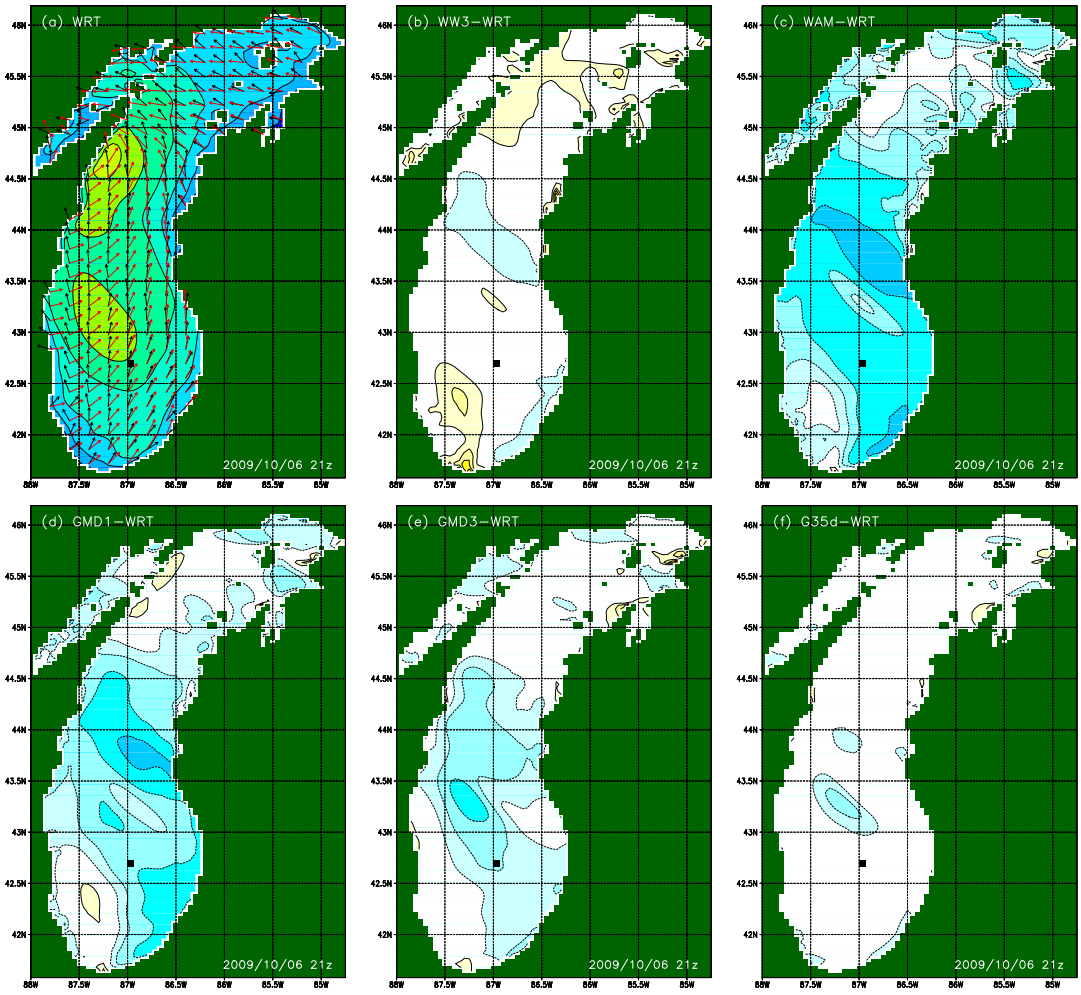

Fig. 5.23 : Like Fig. 5.20 at Oct. 06 21z.

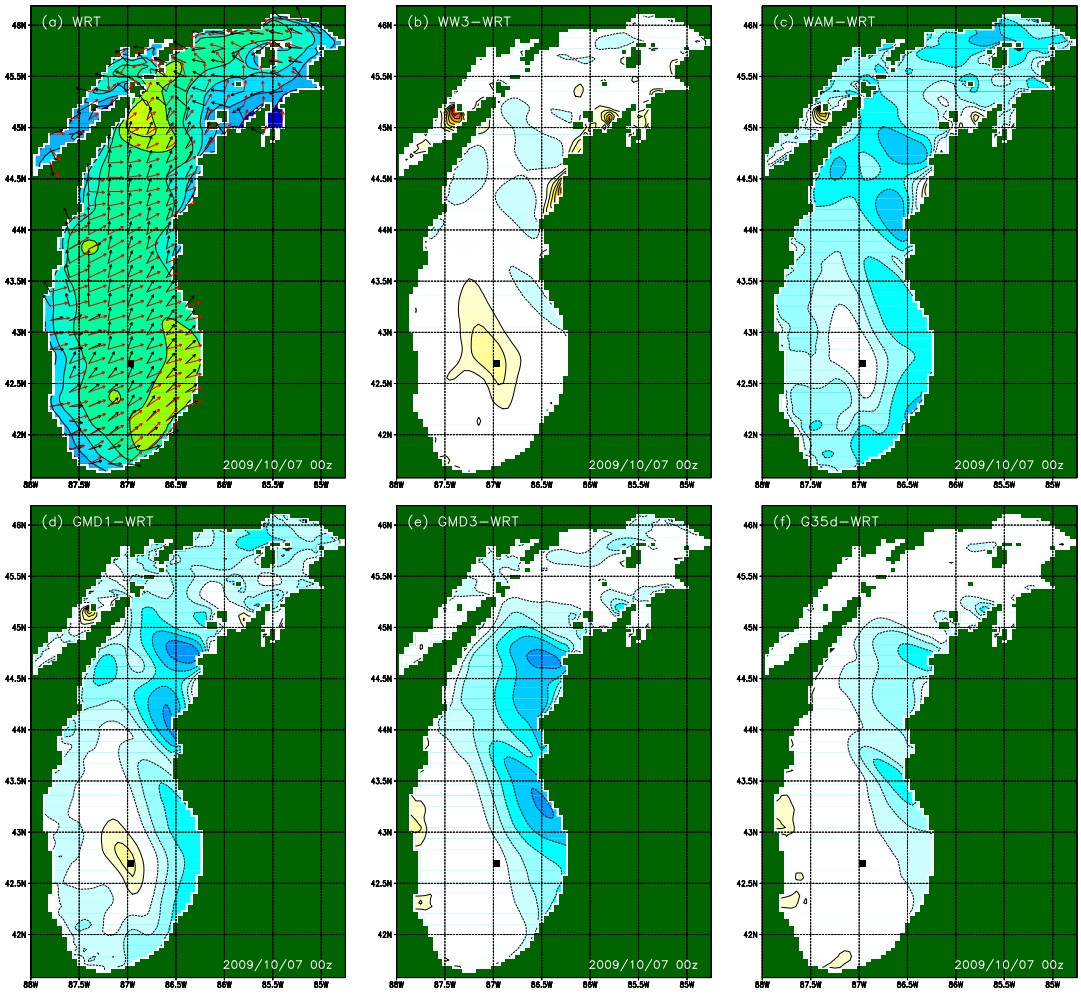

Fig. 5.24 : Like Fig. 5.20 at Oct. 07 00z.

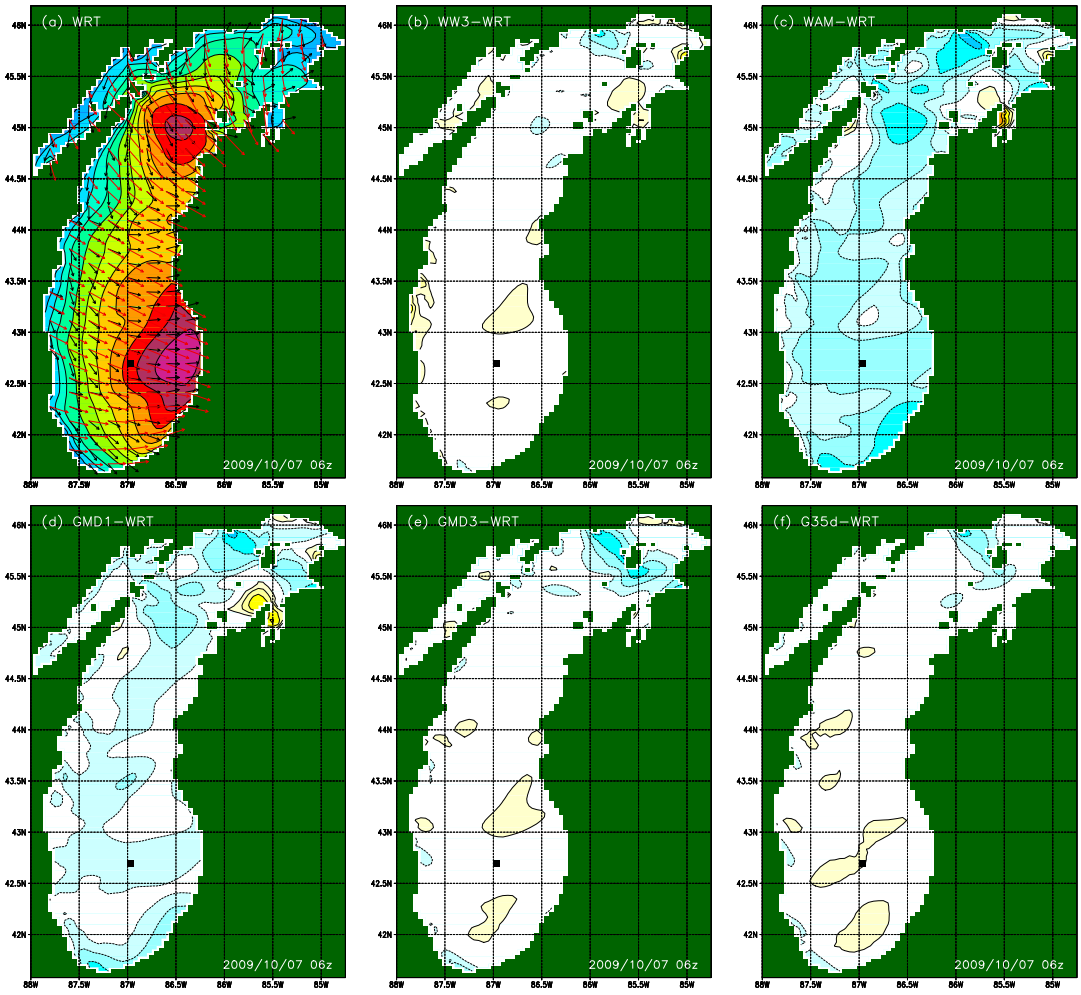

Fig. 5.25 : Like Fig. 5.20 at Oct. 07 06z.

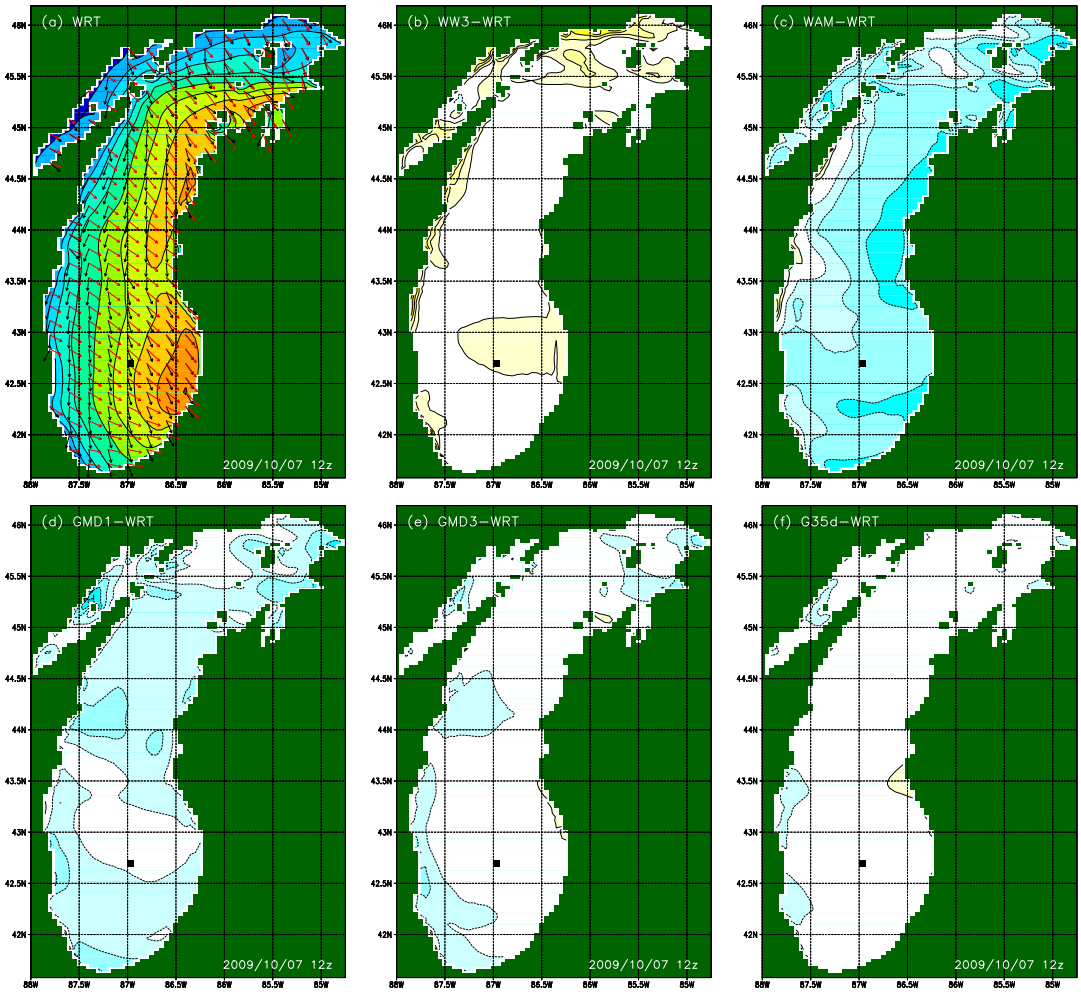

Fig. 5.26 : Like Fig. 5.20 at Oct. 07 12z.

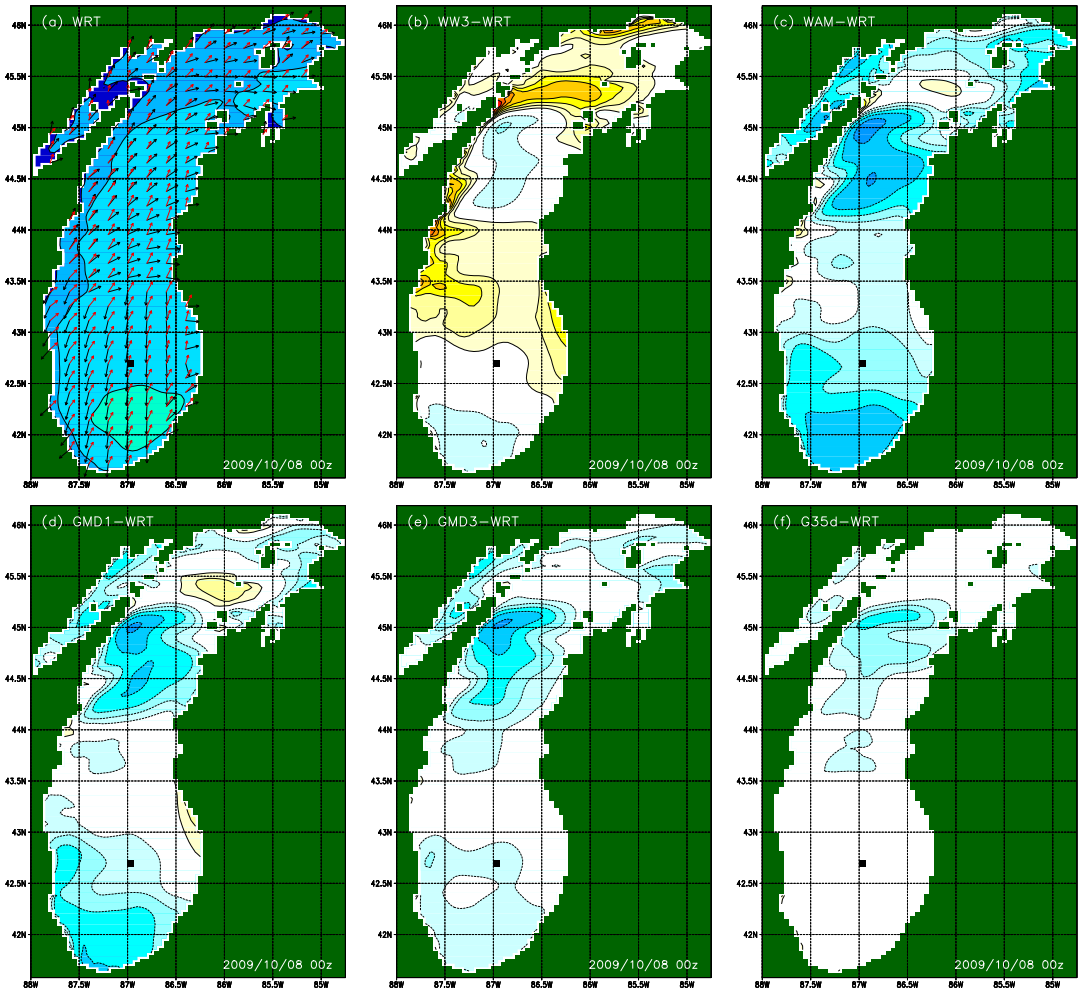

Fig. 5.27 : Like Fig. 5.20 at Oct. 08 00z.

By 00z on Oct. 7 (Fig. 5.24), winds are still in the southwest, and the highest waves have reached the eastern side of the lake, with relatively larger errors for the GMD3 and G35d configurations. Over the next 6 hours, the winds gradually turn to the northwest and increases, until the maximum wave heights occur for this storm in the southern part of the lake (Fig. 5.25). By this time, the relatively larger errors for the GMD3 and G35d configurations have subsided to smaller values as observed earlier in the storm, and as consistent with the expected increased accuracy for increased complexity of the GMD configuration.

As in previous figures, the wave height errors as incurred by the WW3 configuration are surprisingly small. In fact wave height errors for this configuration suggest a very high model accuracy for this GMD configuration. As will be shown below, the low wave height errors for this configuration are associated with large errors in spectral shape, so that the suggestion of accuracy based on wave height error alone is misleading.

During the next 6 hours, winds remain northwesterly over the entire basin, but gradually decrease in strength. This results in a similar wave height distribution, but lower wave heights in general (Fig. 5.26). For the GMD configurations consistent with the DIA, in particular the WW3 configuration, some systematic positive errors occur for short fetches and offshore winds at the western side of the basin. The G35d configuration now results in near-prefect wave height fields. Over the next 6 hours up to 18z on the October 7, these wind and wave conditions (including wave height errors) largely persist with slowly diminishing wind speeds and wave heights (no figures presented here). Waves in the southern part of the basin travel in more southerly directions as they start displaying swell rather than wind sea conditions. For the last six hours of the period considered, winds turn to the southeast, and start building moderate wind seas (Fig. 5.27). In the southern part of the basin, this creates conditions of winds and swells in opposing directions. At the end of the simulation, wave height errors incurred by the WW3 configuration have become the largest as observed during the simulation (Fig. 5.27).

This concludes the assessment of model errors due to the interaction computations based on wave height maps. The next step is to assess the quality of the different GMD configurations based on the detailed error metrics computed from model spectra at buoy location 45007. Figure 5.28 presents the wave height H_s, peak frequency f_p, mean direction $\overline{\theta}$, and directional spread σ_θ as a function of the time for buoy location 45007. Presented are the results of the WRT method (solid green line), G35d configuration (dashed green line), GMD3 (blue line) and the DIA equivalent approaches (WW3, WAM and GMD1; dashed, sold and dotted red lines, respectively).

Consistent with the results of the wave height maps, the WW3 configuration shows an excellent representation of the wave height H_s of the computations

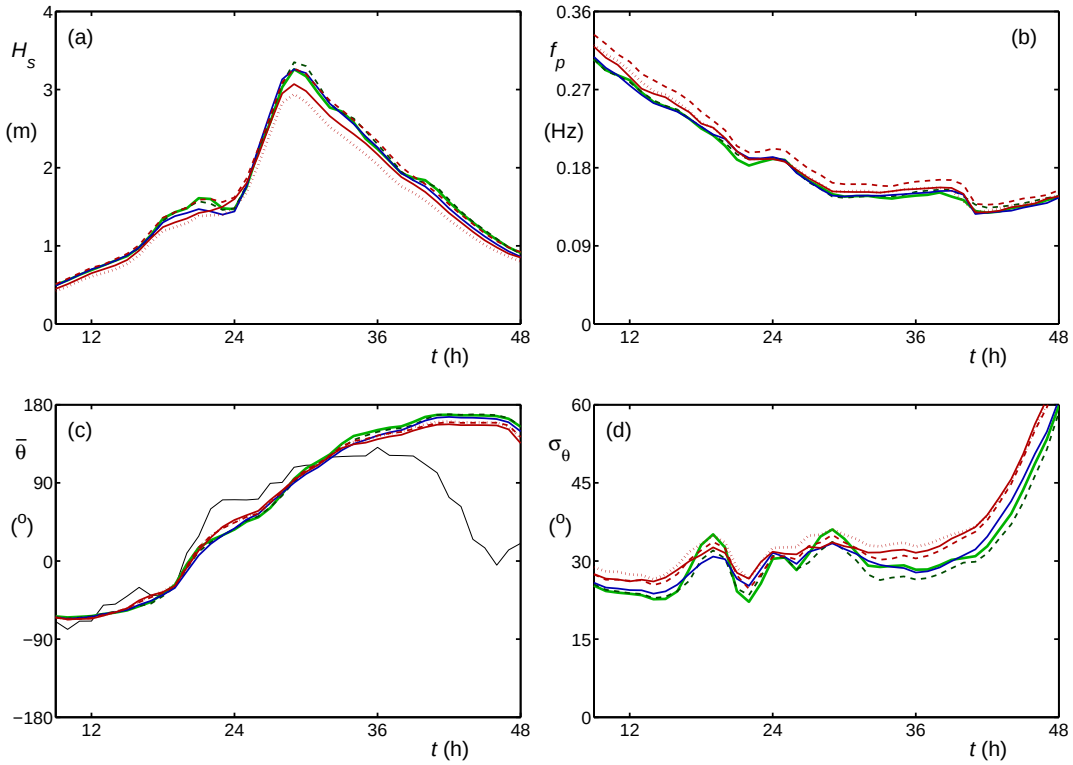

Fig. 5.28 : Evolution in time of a) significant wave height H_s, b) peak frequency f_p, c) mean direction $\overline{\theta}$, and d) directional spread σ_θ at location 45007 for the Lake Michigan test case. Time in h from Oct. 6, 2009, 00z. Solid green line; WRT. Dashed green line: GMD in G35d configuration. Blue line: GMD3 configuration. Red solid line: GMD1. Red dashed line: WW3. Red dotted line: WAM. Solid black line in panel c represents wind direction.

with the WRT approach (Fig. 5.28a). This however, goes at the expense of a rather poor representation of the peak frequency (Fig. 5.28b) underestimating it by roughly 10%. This is consistent with earlier assessment of behavior of the WW3 configuration (Tolman and Krasnopolsky, 2004). All DIA equivalent configurations (all three red lines) introduce some errors in the mean direction in the swell dominated period (after 30h in Fig. 5.28c), and systematically overestimate the directional spread (Fig. 5.28d).

Finally, some examples of one and two dimensional spectral behavior will be presented in Figs. 5.29 through 5.32. From the start of the test period (Oct. 6, 09z) through the middle of Oct. 7, the spectra remain mostly unimodal, with distinct characteristics of wind seas. This is illustrated here in Figs. 5.29 and 5.30. The wind sea character of the spectrum is evident in the large range of directions and frequencies with distinct wave energy, and in the typical shape

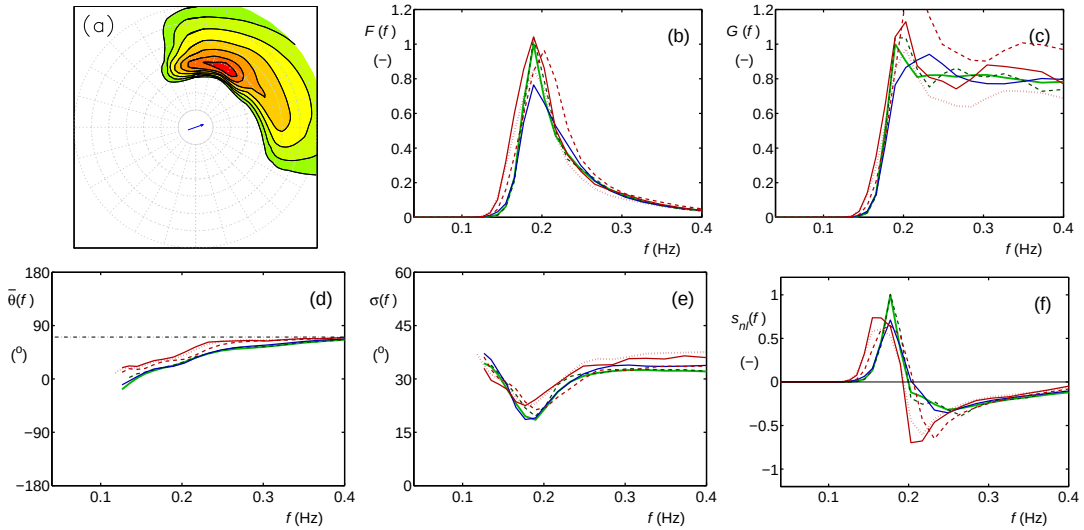

Fig. 5.29 : Spectral behavior of various nonlinear approaches for output point 45007. (a) Two-dimensional spectrum $F(f,\theta)$. (b) One-dimensional spectrum $F(f)$. (c) Steepness spectrum $G(f)$.(d) Spectral direction $\overline{\theta}(f)$. (e) Directional spread $\sigma_\theta(f)$. (f) Source term $s_{nl}(f)$. Green line: exact (WRT) solution. Dashed green line: G35d. Blue line: GMD3. Red lines: GMD1 (solid), WW3 (dashed) and WAM (dotted).

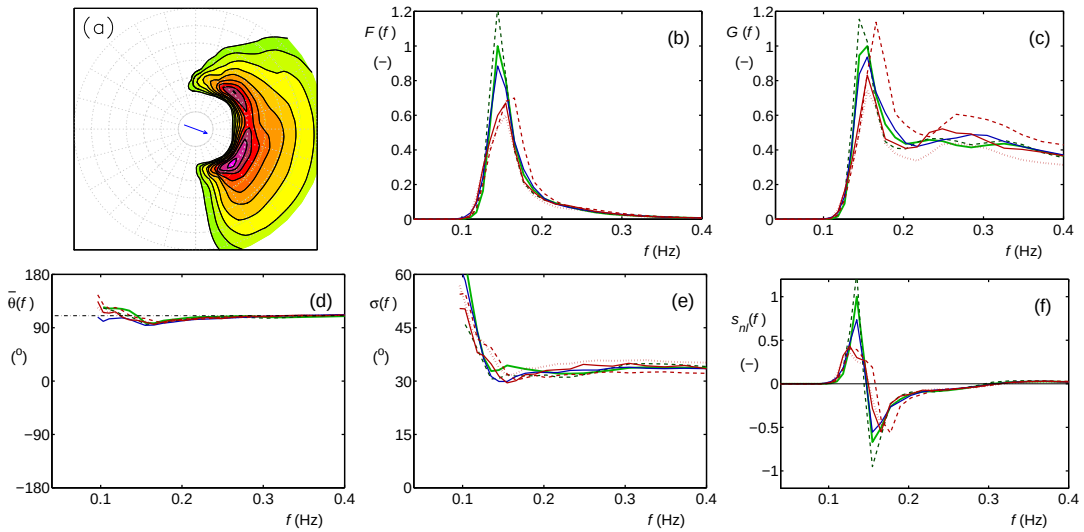

Fig. 5.30 : Like Fig. 5.29 for Oct. 07, 06z

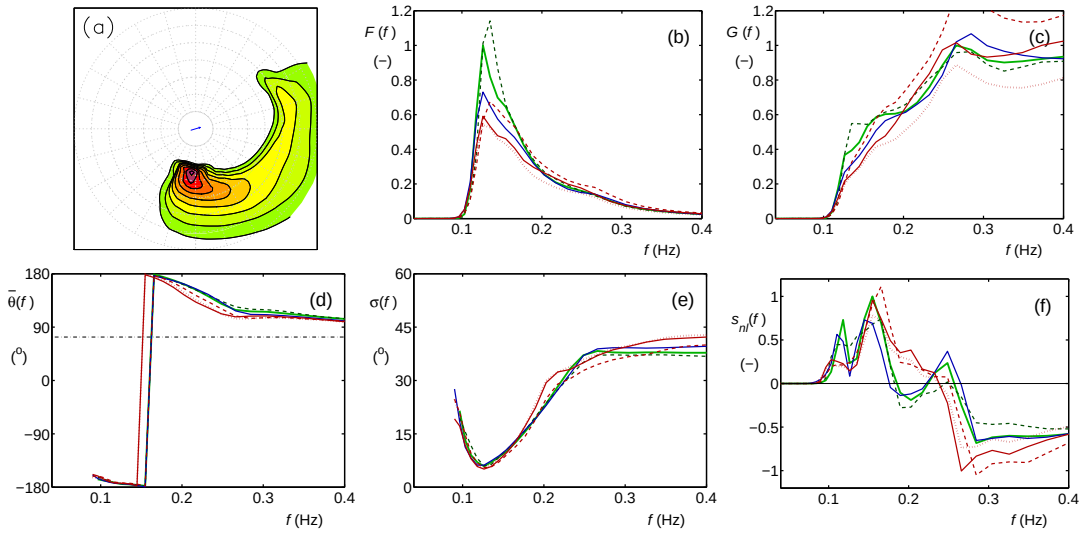

Fig. 5.31 : Like Fig. 5.29 for Oct. 07, 18z

for nonlinear interactions for wind seas. The configurations equivalent to the traditional DIA (red lines), result in spectra that are not sufficiently peaked (b panels), that are too broad in directions (e panels), and have interactions that are generally to weak or to broad in frequency space. The default setting for the WAVEWATCH III model (WW3) results in spurious shift of the spectral peak to higher frequencies (b and c) panels, corresponding to the error in f_p as displayed in Fig. 5.28, and as previously reported as an undesired feature of the default WAVEWATCH III model (e.g., Tolman and Krasnopolsky, 2004).

During the second half of Oct. 7, wave conditions at location 45007 display a separation of swell and wind sea. Early in this period, the swell is sufficiently young and steep to produce a notable signature in the nonlinear interactions, as is illustrated in Fig. 5.31 for 18z. The steepness spectrum (Fig. 5.31c) clearly indicates that the lowest energy in the spectrum has lost some of its steepness while transitioning to swell, particularly due to a directional narrowing of this wave field due to dispersion (Fig. 5.31a,e), resulting in a more complex nonlinear interaction than generally observed for a wind sea (Fig. 5.31f). Whereas the GMD3 (blue line) and G35d configurations (dashed green line) by no means represent the exact interactions (solid green line) perfectly, they are much more realistic than the three traditional DIA configurations (red lines). At the end of the test period (Fig. 5.32, Oct. 8 00z), the wind sea and swell have fully separated (Fig. 5.32a). Whereas the energy density of the swell is much larger than that of the wind sea, its steepness is much lower (Fig. 5.32b,c). Hence, the wind seas dominate the nonlinear interactions, with a signature more representative for wind waves, and a signature of swell at lower frequency showing up at almost negligible intensity.

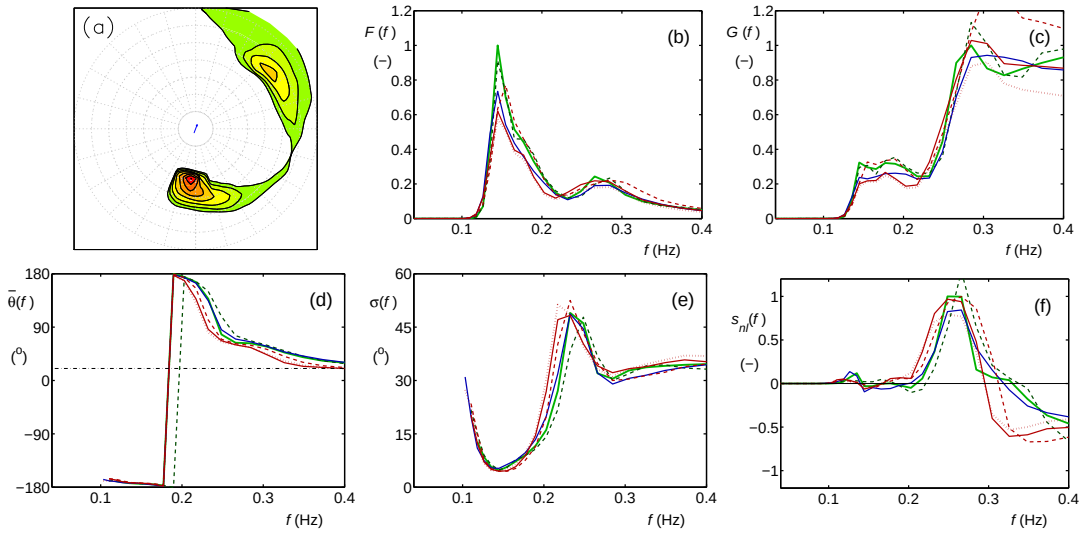

Fig. 5.32 : Like Fig. 5.29 for Oct. 08, 00z

The high accuracy of wave height maps combined with the large errors of many other parameters for the WW3 configuration clearly indicate that a traditional wave-height-only model validation can be highly misleading. This is particularly true in enclosed basins, where swell does not propagate over sufficiently long distances to generate wave height errors in space associated with spectral shape errors in the area of wave generation. A full error assessment using the error metrics from the genetic optimizations (Table 5.1) more realistically shows the G35d and GMD3 approaches far superior, with an error evolution with increasing complexity of the GMD consistent with those found in the optimization tests.

5.3 Model economy

Finally, the numerical economy of the different GMD configurations is presented in Table 5.1. All timing results are obtained on an IBM P6 supercomputer, using 32 processes for the computation. Only for the WRT computations, more processes are used, and hence the normalized run time T_n can only be estimated. For comparison, results are also obtained with an 64 bit Opteron cluster. Generally, timing results on the cluster are more favorable for more complex GMD configurations, as the less effective cluster communications make the relative contribution of source terms to the run times smaller. Cluster run times are not presented here.

The normalized run time T_n is obtained by dividing the run time obtained with the GMD configuration by the run time obtained with the default wave model, that is, using the WW3 configuration with the traditional DIA implementation. When γ is defined as the fraction of the computing time used by the DIA in the

Table 5.1: Synopsis of model performance for practical test cases for various GMD configurations. T_n is the normalized model run time. All computations performed with GMD parameterization. T_n is normalized with the default model settings in WAVEWATCH III, corresponding to the traditional DIA in WW3 configuration. Weights for errors in α, f_0 and β set to 0 for hurricane run.

	Hurricane		L. Michigan	
configuration	T_n (-)	ϵ_{tot} (%)	T_n (-)	ϵ_{tot} (%)
WW3	1.28	27.1	1.16	23.5
WAM	0.98	27.3	1.09	24.9
GMD1	1.15	26.6	1.10	21.8
GMD3	1.82	19.3	1.45	16.8
G35d	5.08	17.1	4.04	14.1
WRT	2800 *	—	370 *	—

*: Estimated; additional resource needed to make model runs feasible.

default wave model configuration, the normalized run time can be estimated as

$$T_n = (1-\gamma) + \gamma X_{GMD} \quad , \tag{5.1}$$

where X_{GMD} is the expected factor of increase in run time for a single call to the GMD routine compared to a single call to the traditional DIA routine, as assessed in Part 3. For the WW3 configuration in Table 5.1, Part 3 suggest that $X_{GMD} \approx 2$, and assuming that the corresponding integrations with the DIA and GMD are identical for all practical purposes, γ can be estimated from (5.1) as

$$\gamma = \frac{T_n - 1}{X_{GMD} - 1} \quad . \tag{5.2}$$

Thus, $\gamma \approx 0.28$ or 0.16 for the hurricane and Lake Michigan cases, respectively. The smaller relative importance of the nonlinear interactions (smaller γ) in the latter case corresponds to a more modestly forced situation, combined with the dynamic source term integration scheme of WAVEWATCH III. In this scheme, the time step of integration for the source terms depends on the rate of change of the spectrum. Strong forcing corresponds to rapid rates of change and small time steps. The more weakly forced Lake Michigan case is therefore expected to have larger source term integration time steps and hence a smaller relative contribution of the source terms to the integration efforts (i.e., a smaller γ).

For other configurations of the GMD consistent with the DIA (i.e., the WAM and GMD1 configurations in Table 5.1) identical computation effort is expected for each individual source term computation. Nevertheless, different model run

times may be found, because the dynamic source term integration scheme results in shorter model run times for interactions that result in smoother spectral integration. For the WAM configuration, run times are 6-23% shorter than for the WW3 configuration, and for the GMD1 configurations, run times are 5-10% shorter, suggesting the the WAM and GMD1 configurations result in significantly smoother model integration than the WW3 configuration.

For the GMD3 configuration, Part 3 indicates that $X_{GMD} \approx 6$, resulting in estimated values of T_n from Eq. (5.1) of 2.40 and 1.80, respectively. Table 5.1 shows that actual model integration times are 24 and 20% faster, respectively. For the G35d configuration Part 3 indicates that $X_{GMD} \approx 20$, resulting in estimated values of T_n from Eq. (5.1) of 6.34 and 4.04, respectively. Table 5.1 shows that actual model integration times are 20 and 32% faster, respectively, indicating that the GMD1 and G35d configurations result in the smoothest model integration.

Note that a large difference are found in relative run times for the WRT method. This appears to be associated with the limited spectral frequency range in the hurricane test, which results in a strong shock in the spectrum for high frequencies and low winds. In the Great Lakes test, the frequency range is extended, effectively eliminating this shock. Thus, by using a larger spectral (frequency) domain computations using WRT are in fact cheaper and more realistic. Hence, the timing results for the Great Lakes test should be considered more realistic, and the G35d approach should be considered roughly 2 orders of magnitude cheaper than the WRT method in terms of the total model run times.

6 Summary and conclusions

The present study addresses the optimization of the Generalized Multiple DIA (GMD) as defined in Tolman (2008b). Using initial optimization experiments reported in Tolman (2009a), the GMD is expressed in terms of the traditional variance spectrum, instead of in terms of an action spectrum, as the former proved to be more accurate when objectively optimized. Also considered is the nonlinear high-frequency filtering tool introduced in Tolman (2008b). This technique is used only after optimization for selected GMD configurations (i.e., the G25d configuration), but is not explicitly optimized, nor considered during the optimization.

In previous studies (Tolman and Krasnopolsky, 2004; Tolman, 2005) it has been shown that a traditional optimization of a nonlinear parameterization based on interactions for individual spectra does not guarantee good model behavior. In fact, more accurate interaction approximations than the DIA were found to result in unstable model integration behavior. Considering this, a 'holistic' optimization was introduced in the latter papers where results of model integration are optimized rather than interactions for individual spectra. In this approach, spectra are saved from model integrations with the WRT methods, as well as from model integrations with various configurations of the GMD. From these spectra, errors in various parameters are computed. Form these errors a 'cost function' is defined, which is then dynamically optimized.

A wide range of test parameters is used in this study, including mean (integral) wave parameters (significant wave height, peak frequency, mean direction, directional spread), parameters associated with the one-dimensional spectrum (energy and steepness spectra, direction and directional spread per frequency, one-dimensional source term $s_{nl}(f)$, zero-flux frequency, and energy levels in the equilibrium and tail section of the spectrum), and two-dimensional spectral parameters (energy and steepness spectrum and nonlinear source term). Errors for individual parameters are combined into a single error metric, favoring the accuracy of the mean wave parameters (in particular H_s) most.

The test metrics are computed for a set of up to 9 idealized test cases. Six of these cases consider deep water, three consider shallow water. Most cases consider wave growth, since the critical aspect of the interactions to be reproduced is wave growth with appropriate and stable spectral shapes. The deep water cases consist of traditional time- and fetch-limited cases, two cases with turning winds, a slanting fetch case, and a case with wave growth in the presence of swell. The shallow water test cases consist or a wave growth in rapidly decreasing water depths in homogeneous conditions, and either a wind sea of a swell dissipating on a beach. These nine tests produce a rich set of spectra, including effects of wave growth, shearing spectra, swells, conditions approaching wind-sea swell separation (in turning wind cases) and some limited interactions

between wind sea and swell. It is expected that these cases are representative for more complex conditions in nature. After optimization of the GMD for these test cases, it is necessary to asses model errors for validation cases. Such cases need to be independent of the optimization tests, and should cover more realistic (two-dimensional) wind and wave conditions. Note that optimization has been done incrementally here. Good shallow water behavior can only be expected if the deep water behavior (boundary conditions) are accurate. Hence, it is sensible to treat deep and shallow water optimization separately, and to consider deep water cases first.

For simple GMD configurations with a small number of free parameters, it is economically feasible to map the model error in the full parameter space of the GMD. For instance, considering a conventional DIA configuration in deep water, only the λ parameter of the quadruplet and the proportionality constant C_d need to be optimized. A course optimization of this two-dimensional parameter space would consider $O(10^2)$ parameter configurations to be considered, a more accurate mapping requires $O(10^3 - 10^4)$ configurations. This kind of mapping has been performed here to establishes valid ranges of parameters, and to assess the error behavior of the various parameters considered. Such an experiment has shown that there are optimum areas rather than a single location in parameter space for many parameters, and that not all parameters can be optimized simultaneously in a traditional DIA configuration (consistent with results from Tolman and Krasnopolsky, 2004). Such a mapping experiment has also been used here to validate more advanced optimization techniques.

Full mapping of the error in parameter space rapidly becomes economically unfeasible for more complex GMD configurations. For instance, a traditional DIA configuration with 3 representative quadruplets in deep water has 6 free parameters, requiring roughly $O(10^6)$ parameter configurations for a coarse description of parameter space. On the presently available supercomputer at NCEP, using 5 nodes and 320 parallel processes to compute, such a volume of computations takes several days up to a week to compute, and hence is still feasible. A better resolution of parameter space will require $O(10^9)$ configurations to be assessed, or of the order of several years to compute, and hence is not economically feasible. For an extended three-parameter quadruplet definition with 5 representative quadruplets the number of free parameters becomes 20, and the number of configurations to be considered in a full mapping exercise can be roughly estimated as $O(10^{30})$, or, conservatively $O(10^{20})$ years to complete. Even the largest super computer presently available completely dedicated to this problem would require at least $O(10^{12})$ years for this computation to be completed.

The inability to fully map errors in parameter space requires more directed search algorithms to be used to estimate optimum parameter settings for the GMD. A traditional method would be a steepest descent method. Previous studies have shown that such methods do not work well for complex GMD con-

figurations, because errors are not well-behaved in parameter space with some discontinuities of errors and many local minima.

In Tolman and Krasnopolsky (2004) and Tolman (2005) a genetic optimization approach was used to objectively estimate near-optimal parameter setting for predecessors of the present GMD with up to 15 free parameters, This method has been expanded upon in the present study, and the resulting genetic optimization approach has been shown to be able to produce near-optimum GMD configurations with more than 20 free parameters by considering typically $O(10^6)$ configurations. This makes the genetic optimization approach a very powerful tool to optimize the GMD; without this approach, it would not be possible to objectively optimize the GMD with such a level of complexity.

A genetic optimization approach can be interpreted as a directed random search, loosely based on principles of natural selection. A realization of a GMD configuration is defined with a string of numbers defining its free parameters, A population is generated defining each member of the population by it own string of numbers, or 'genetic material'. For each member of the population a 'fitness' is computed, in this case based on the error metric for all test cases and parameters considered. The fittest members of the population are allowed to remain in the population and/or 'procreate'. 'Offspring' of these fit members are generated by combining the genetic information of parents using both genetic crossover and mutation. For the new generation, the fitness for each member is computed, and the process is repeated until a set number of generations is reached, or until no further convergence to fitter populations is found.

A genetic optimization estimates rather than obtains the optimum solution. Due to its inherent random nature, it is prudent to repeat each experiments with a range of different random initial conditions. This will indicate the ability of the population size, number of generations, and general setting of the genetic optimization to reach a reasonable solution. It will also indicate if multiple near-optimum solutions can be found. A key element in successful genetic optimization is retention of genetic diversity in the population. Counter-intuitively, a better initial population and/or large initial population may lead to rapid initial convergence, but at a cost of rapid loss of diversity and a loss of capability to continuously improve populations. Similarly, too small a population may have insufficient diversity to sustain improvement. Hence, genetic optimization by itself requires some trial and error to obtain reasonable population sizes and parameters settings. Considering this, it is prudent to incrementally increase the complexity of the GMD to be optimized. Furthermore, a genetic optimization approach is generally efficient to obtain near-optimum results, but may not be efficient to achieve final convergence to the (local) optimum solution. It is therefore prudent and efficient to augment a genetic optimization experiment with a steepest descent optimization starting from the best configurations(s) obtained with the genetic optimization. A final reason to incrementally increase the com-

plexity of the GMD is to find the optimum balance between cost and accuracy of a GMD, and to assess if there is a saturation point where additional complexity does not result in additional accuracy.

Considering the above, the first optimization experiments for the GMD consider the traditional DIA configuration with one or more quadruplets. Deep water optimization in such conditions is expected to produce results similar to the deep water optimization for such a DIA configuration in Tolman and Krasnopolsky (2004) and Tolman (2005). The first experiments considered optimization of λ and C_d for an increasing number of quadruplets $n_q = n_{q,d}$. As in the latter papers, it is found that increasing n_q to 2 and 3 significantly increases the accuracy of the GMD, but that beyond this range of n_q additional increase of accuracy of the GMD is small or non-existent. Due to the simplicity of the quadruplet layout, this GMD configuration allows for a systematic way to use the quadruplet to sample phase space in the spectrum, by selecting values of λ and then optimizing C_d only. Such an approach is similar to the SRIAM approach (e.g., Komatsu, 1996; Tamura et al., 2008), but has not been tried before in the context of a holistic genetic GMD optimization. Here, experiments have been performed by sampling the phase space with 7 or 13 preset values of λ. These experiments have shown that the most accurate GMD in such a configuration switches off many preset quadruplets and leaves no more than 5 quadruplets active and contributing. This results in a configuration with the same accuracy as a GMD with three quadruplets where both λ and C_d are optimized. Hence, the saturation of improvement is clearly related to the GMD, and not to the optimization approach. Furthermore, freely optimized quadruplets reach the same accuracy as preset quadruplets with smaller n_q, and are therefore preferable for reasons of model economy. Whereas these results are obtained for the traditional quadruplet configuration only, it will be assumed that they hold for more complex quadruplet configurations too.

Attempting to optimized the GMD with a traditional quadruplet configuration for shallow water has never been attempted before, and hence breaks new ground. It is shown that a properly optimized shallow water GMD indeed improves the quality of the model results, and is able to reproduce the shallow water spreading of swell in frequency space. However, this spreading in extremely shallow water does generally result in spurious spectral peaks, making this approach not yet sufficiently mature for practical wave models. Sampling spectral space makes it possible to suppress the spurious behavior somewhat, but cannot easily be applied to more complex quadruplet layouts. Sampling of spectral space indicates that no additional accuracy can be gained from using more than 5 or 6 shallow water quadruplets, but that all parameters of these quadruplets should be independently optimized, and should not be based on optimum deep water quadruplets. Note that the spurious behavior described above only occurs in extremely shallow water ($d \leq 3$m, for waves with $f_p \leq 0.06$Hz), and may well be improved by a more detailed assessment of scaling considerations.

The natural next step in optimizing the GMD considers more complex quadruplet definitions. Based on previous work, it is known that such configurations with a single quadruplet generally do not result in stable model integration. Hence, optimization for deep water started with $n_{q,d} = 3$. Economy of the optimization for now has limited the maximum number of deep or shallow water quadruplets to 6. Adding complexity to the quadruplet has little impact on mean wave parameters in the test cases, but has a large impact on errors in the spectral shape. The two-parameter quadruplet definition is less accurate than the three parameter definition. Furthermore, the two-parameter definition needed additional filtering to suppress spectral noise in some deep water tests (unlike the three-parameter definition). Combined with near-identical costs for the computation of an individual interaction, this makes a three-parameter quadruplet definition more suitable to use. The optimum deep water GMD configuration chosen here consist of 5 deep water quadruplets with the full three-parameter quadruplet definition. This configuration proved extremely accurate. The only identified shortcoming for the test cases in the genetic optimization is the tendency to produce minor spurious bi-modality in steepness spectra, and the presentation of multi-modality in spectra at extremely short fetches.

The optimized GMD with the full quadruplet definition and 5 deep water quadruplets is also used as the starting point for the shallow water optimization. Going from the single parameter to the three parameter quadruplet definition again improved the quality of the wave model in shallow water. Some improvement is found by adding an optimized C_s to each deep water quadruplet, but, as before, much more improvement is obtained when separate shallow water quadruplets are defined. Diminishing gain is obtained for $n_{q,s} \approx 5$. Whereas the improvements are clear, and occur for a large range of depths, some spurious behavior remains in extremely shallow water. This identifies the shallow water GMD as a major step forward in shallow water wave modeling, but not quite ready for operational wave modeling.

Testing the present GMD with conditions used in the genetic optimization creates dependent tests, that may not be representative for practical wave model applications. For this reason, some selected GMD configurations have been tested /validated against more realistic forecast conditions. Considering the above, it is sufficient for now to consider only realistic deep water tests. Since the present GMD for deep water ($C_s \equiv 0$) and the previous DIA naturally 'switch off' in shallow water, such an approach can be used directly in a practical wave model. The two deep water tests considered here are an artificial hurricane modeled with three telescoping and moving nests (Tolman and Alves, 2005; Tolman, 2008a), and a storm system on Oct. 6-7, 2009 on Lake Michigan.

Both practical test cases show that the findings from optimizing the GMD and the corresponding results of test cases implicit to the optimization apply directly to practical wave modeling cases. GMD configurations consistent with the

traditional DIA show notable errors in mean wave parameters. The GMD3 configuration with three traditional quadruplets greatly reduces the errors in mean parameter, but leaves significant errors in the spectral parameters. The G35d configuration with 5 quadruplets using the full three-parameter quadruplet definition is accurate in mean wave parameters as well as spectral wave parameters, albeit with the potential for minor spurious bi-modality in the steepness spectra. The realistic test cases also identify and quantify errors incurred by a traditional DIA approach in practical applications, and the level up to which they can be removed by more accurate GMD configurations.

The hurricane case shows that DIA configurations systematically overestimate wave heights H_s to the left front of the hurricane, while systematically underestimating H_s to the right and in front of the hurricane. Depending on the configuration of the DIA, overestimations can be as large as 30%, and underestimations as large as 20%. These errors in H_s are large enough to be observed in practical conditions (see, e.g., Chao and Tolman, 2010), even with significant errors in hurricane wave forcing in operational wave models. The tradition DIA configuration with three representative quadruplets (GMD3) also results in wide spread errors in H_s, but with errors generally well below 10%. The most complex GMD configuration considered here (G35d, with five three-parameter quadruplets) displays localized wave height errors, with errors generally well below 5%. In the hurricane test case wave height errors are fairly representative for all error behavior, although spectral errors more clearly show a distinction in model accuracy between the GMD3 and G35d configurations of the GMD.

In the Lake Michigan test case, wave height errors associated with the DIA configurations of the GMD are somewhat smaller, but still of the order of $\pm 15\%$. In general such errors should be notable in a full model validation. Somewhat surprisingly, the Lake Michigan test suggest that the traditional DIA configuration used as the default model setting in the WAVEWATCH III model (GMD configuration WW3) results in highly accurate wave heights. These wave height errors, however, are accompanied by large errors in other mean parameters and in the spectral shape. This makes a traditional validation of a wave model based on H_s only highly misleading, specially in enclosed basins.

In Part 3 it was shown that the more complex implementation needed for the GMD is typically twice as expensive to compute as an optimum traditional DIA implementation for a similar configuration. Using an extended quadruplet definition doubles the number of quadruplet realizations for a single configuration, and hence is four times as expensive to compute. Adding representative quadruplets has a simple cumulative impact on computational costs. Thus, for a single interaction to be computed, the WW3, WAM and GMD1 configurations are 2 times as expensive to compute compared to the traditional DIA, the GMD3 configuration is 5 times as expensive, and the G35d approach is 20 times as expensive. Estimating that the nonlinear interactions are responsible for roughly 20% of the

computational costs of a wave model, a first estimate of corresponding increases in model run times are factors of 1.2, 2.0, and 5.0, respectively.

However, the total computational cost of the WAVEWATCH III model is also influenced by the dynamic time stepping scheme used to integrate the source terms (Tolman, 1992). In this scheme, smoother source terms will result in longer integration time steps and hence shorter computational times. The practical test cases have been used to assess the practical economy of the new GMD configurations, including the effects of smoothness of integration. The WAM and GMD1 configurations are shown to be computationally cheaper than the traditional WW3 approach, suggesting a smoother model integration. Computational costs of the GMD3 and G35d configurations are also less than predicted based on costs of individual interactions, and hence also represent smoother integration than in the default wave model.

The GMD3 configuration increases the computational cost for the more typical Lake Michigan case by a factor of 1.5, and the G35d approach increases the corresponding computational costs by a factor of 4. Whereas the latter is a significant increase in computational costs, it represents feasible configurations for operational wave models at NCEP, and more importantly perhaps, it results in a model that is typically two orders of magnitude cheaper to run than a model using the WRT implementation. Note that the G35d approach could tentatively be sped up by combining it with a Neural Network approach, as suggested in Tolman and Krasnopolsky (2004).

Even with these positive results, this is only a first attempt at fully optimizing a GMD for practical wave model applications. Particularly the shallow water aspects need more attention, to ensure robust model behavior even for the smallest water depth and longest frequencies in the model. Some improvements that could be considered are

- Revisit scaling function to get more realistic behavior in the most shallow water, and possibly identify more individually scalable regimes.
- Consider optimizing m and/or n per quadruplet.
- Combine deep and shallow test to get better overall results; this may introduce deep water quadruplets that have Little impact on deep water but may impact results for intermediate water depths.
- Consider adding the high-frequency filter to the optimization, either to make spectra smoother, or to enforce β behavior in the G35d and similar configurations.
- Look at details of genetic optimization, particularly a) saving a smaller part or of existing generation or none at all, and b) use smarter initializa-

tion where more good quadruplets from $n_q = n - 1$ are used for $n_q = n$ experiment.

- Add triad interactions in shallow water tests, either as part of the optimization, or as a another non-optimized source term.

References

Alves, J. H. G. M. and M. L. Banner, 2003: Performance of a saturation-based dissipation-rate source term in modeling the fetch-limited evolution of wind waves. *J. Phys. Oceanogr.*, **33**, 1274–1298.

Battjes, J. A. and J. P. F. M. Janssen, 1978: Energy loss and set-up due to breaking of random waves. in *Proc. 16th Int. Conf. Coastal Eng.*, pp. 569–587. ASCE.

Bretherthon, F. P. and C. J. R. Garrett, 1968: Wave trains in inhomogeneous moving media. *Proc. Roy. Soc. London*, **A 302**, 529–554.

Chao, Y. Y. and H. L. Tolman, 2010: Performance of NCEP regional wave models in predicting peak sea states duting the 2005 North Atlantic hurricane season. *Wea. Forecasting*, **25**, 1543–1567.

Eiben, A. E. and J. E. Smith, 2003: *Introduction to Evolutionary Computing*. Springer, 299 pp.

Hanson, J. L. and R. E. Jensen, 2004: Wave system diagnostics for numerical wave models. in *8 th international workshop on wave hindcasting and forecasting, JCOMM Tech. Rep. 29, WMO/TD-No. 1319*.

Hanson, J. L., B. A. Tracy, H. L. Tolman and D. Scott, 2006: Pacific hindcast performance evaluation of three numerical wave models. in *9 th international workshop on wave hindcasting and forecasting, JCOMM Tech. Rep. 34*. Paper A2.

Hasselmann, K., 1960: Grundgleichungen der seegangsvoraussage. *Schiffstechnik*, **1**, 191–195.

Hasselmann, K., 1962: On the non-linear transfer in a gravity wave spectrum, Part 1. General theory. *J. Fluid Mech.*, **12**, 481–500.

Hasselmann, K., 1963: On the non-linear transfer in a gravity wave spectrum, Part 2, Conservation theory, wave-particle correspondence, irreversibility. *J. Fluid Mech.*, **15**, 273–281.

Hasselmann, K., T. P. Barnett, E. Bouws, H. Carlson, D. E. Cartwright, K. Enke, J. A. Ewing, H. Gienapp, D. E. Hasselmann, P. Kruseman, A. Meerburg, P. Mueller, D. J. Olbers, K. Richter, W. Sell and H. Walden, 1973: Measurements of wind-wave growth and swell decay during the Joint North Sea Wave Project (JONSWAP). *Ergaenzungsheft zur Deutschen Hydrographischen Zeitschrift, Reihe A(8)*, **12**, 95 pp.

Hasselmann, S. and K. Hasselmann, 1985: Computations and parameterizations of the nonlinear energy transfer in a gravity-wave spectrum, Part I: A new method for efficient computations of the exact nonlinear transfer integral. *J. Phys. Oceanogr.*, **15**, 1369–1377.

Hasselmann, S., K. Hasselmann, J. H. Allender and T. P. Barnett, 1985: Computations and parameterizations of the nonlinear energy transfer in a gravity-wave spectrum, Part II: parameterizations of the nonlinear energy transfer for

application in wave models. *J. Phys. Oceanogr.*, **15**, 1378–1391.

Herterich, K. and K. Hasselmann, 1980: A similarity relation for the nonlinear energy transfer in a finite-depth gravity-wave spectrum. *J. Fluid Mech.*, **97**, 215–224.

Holland, J. H., 1992: *Adaptation in natural and artificial systems.* MIT press, Cambridge, MA.

Komatsu, K., 1996: Development of a new generation wave forecast model based on a new schema of nonlinear energy transfer among wind waves (in Japanese). Ph.D. thesis, Kyoto University, 155 pp.

Kuik, A. J., G. Ph. Van Vledder and L. Holthuijsen, 1988: A method for the routine analysis of pitch-and-roll buoy wave data. *J. Phys. Oceanogr.*, **18**, 1020–1034.

Phillips, O. M., 1958: The equilibrium range in the specrum of wind-generated waves. *J. Fluid Mech.*, **4**, 426–434.

Resio, D. T. and W. Perrie, 1991: A numerical study of nonlinear energy fluxes due to wave-wave interactions. Part 1: Methodology and basic results. *J. Fluid Mech.*, **223**, 609–629.

Tamura, H., T. Waseda, Y. Miyazawa and K. Komatsu, 2008: Current-induced modulation of the ocean wave spectrum and the role of nonlinear energy transfer. *J. Phys. Oceanogr.*, **38**, 2262–2684.

Tolman, H. L., 1990: The influence of unsteady depths and currents of tides on wind wave propagation in shelf seas. *J. Phys. Oceanogr.*, **20**, 1166–1174.

Tolman, H. L., 1991a: Effects of tides and storm surges on North Sea wind waves. *J. Phys. Oceanogr.*, **21**, 766–781.

Tolman, H. L., 1991b: A third-generation model for wind waves on slowly varying, unsteady and inhomogeneous depths and currents. *J. Phys. Oceanogr.*, **21**, 782–797.

Tolman, H. L., 1992: Effects of numerics on the physics in a third-generation wind-wave model. *J. Phys. Oceanogr.*, **22**, 1095–1111.

Tolman, H. L., 2003: Optimum Discrete Interaction Approximations for wind waves. Part 1: Mapping using inverse modeling. Tech. Note 227, NOAA/NWS/NCEP/MMAB, 57 pp. + Appendices.

Tolman, H. L., 2004: Inverse modeling of Discrete Interaction Approximations for nonlinear interactions in wind waves. *Ocean Mod.*, **6**, 405–422.

Tolman, H. L., 2005: Optimum Discrete Interaction Approximations for wind waves. Part 2: Convergence of model integration. Tech. Note 247, NOAA/NWS/NCEP/MMAB, 74 pp. + Appendices.

Tolman, H. L., 2008a: A mosaic approach to wind wave modeling. *Ocean Mod.*, **25**, 35–47.

Tolman, H. L., 2008b: Optimum Discrete Interaction Approximations for wind waves. Part 3: Generalized multiple DIAs. Tech. Note 269, NOAA/NWS/NCEP/MMAB, 117 pp.

Tolman, H. L., 2009a: Practical nonlinear interaction algorithms. in *11th international workshop on wave hindcasting and forecasting & coastal hazards symposium, JCOMM Tech. Rep. 52, WMO/TD-No. 1533*. Paper J2.

Tolman, H. L., 2009b: User manual and system documentation of WAVEWATCH III ^{TM} version 3.14. Tech. Note 276, NOAA/NWS/NCEP/MMAB, 194 pp. + Appendices.

Tolman, H. L., 2010: A genetic optimization package for the Generalized Multiple DIA in WAVEWATCH III ®. Tech. Note 288, NOAA/NWS/NCEP/MMAB, 21 pp.

Tolman, H. L. and J. H. G. M. Alves, 2005: Numerical modeling of wind waves generated by tropical cyclones using moving grids. *Ocean Mod.*, **9**, 305–323.

Tolman, H. L. and D. V. Chalikov, 1996: Source terms in a third-generation wind-wave model. *J. Phys. Oceanogr.*, **26**, 2497–2518.

Tolman, H. L. and V. M. Krasnopolsky, 2004: Nonlinear interactions in practical wind wave models. in *8 th international workshop on wave hindcasting and forecasting, JCOMM Tech. Rep. 29, WMO/TD-No. 1319*. Paper E1.

Tracy, B. and D. T. Resio, 1982: Theory and calculation of the nonlinear energy transfer between sea waves in deep water. WES Report 11, US Army Corps of Engineers.

Van Vledder, G. Ph., 2002: A subroutine version of the Webb/Resio/Tracy method for the computation of nonlinear quadruplet interactions in a wind-wave spectrum. Report 151b, Alkyon, The Netherlands.

Van Vledder, G. Ph., 2006: The WRT method for the computation of non-linear four wave interactions in discrete spectral wave models. *Coastal Eng.*, **53**, 223–242.

Vincent, L. and P. Soille, 1991: Watersheds in digital spaces: An efficient algorithm based on immersion simulations. *IEEE Transactions of Pattern Analysis and Machine Intelligence*, **13**, 583–598.

WAMDIG, 1988: The WAM model – a third generation ocean wave prediction model. *J. Phys. Oceanogr.*, **18**, 1775–1809.

Webb, D. J., 1978: Non-linear transfers between sea waves. *Deep-Sea Res.*, **25**, 279–298.

This page is intentionally left blank.